Magmatic and volcanic evolution of a silicic large igneous province (SLIP): the Gawler Range Volcanics and Hiltaba Suite, South Australia

By
Andrea Agangi
(M.Sc. University of Turin, 2003)

Submitted in fulfilment of the
requirements for the Degree of
Doctor of Philosophy (Geology)

June 2011

STATEMENT

This thesis contains no material which has been accepted for a degree or diploma by the University or any other institution, except by way of background information and duly acknowledged in the thesis, and to the best of the candidate's knowledge and belief no material previously published or written by another person except where due acknowledgement is made in the text of the thesis, nor does the thesis contain any material that infringes copyright.

This thesis may be made available for loan and limited copying in accordance with the Copyright Act of 1968.

Andrea Agangi
University of Tasmania
May 2011

Abstract

The Gawler Range Volcanics (GRV) and the co-magmatic Hiltaba Suite (HS) granite form a Mesoproterozoic Silicic-dominated Large Igneous Province (SLIP) cropping out over a vast area in the central Gawler craton, South Australia. Only a few SLIP have been recognised in the world; they occur throughout geological history and in both intraplate and plate margin settings. The igneous province in question, or Gawler SLIP, was emplaced in an intracontinental setting during assembly of the supercontinent Laurentia. Since emplacement, the Gawler craton remained an area of positive relief, allowing a good preservation of the Gawler SLIP. Emplacement of the Gawler SLIP is associated with a major mineralising event in the Gawler craton which includes the super-giant Cu-Au-U Olympic Dam deposit. This thesis focuses on the lower part of the Gawler Range Volcanics.

By definition, SLIP are formed by large volumes of magma (≥100000 km^3) emplaced over a short time, in the order of the millions of years. The emplacement mechanism of large volumes of felsic magma in a short time span is one of the open questions in the study of these igneous manifestations. In this thesis, the volcanic facies in the lower part of the Gawler Range Volcanics have been described in detail, in order to assess the emplacement mechanism of the rocks. The rock units include moderately extensive (up to tens of km in diameter) felsic lavas, associated with pyroclastic deposits (ignimbrite) of comparable extent. Lavas are characterised by evenly porphyritic texture, with medium grained phenocrysts of feldspar ±pyroxene ±quartz in a fine microcrystalline quartzo-feldspathic groundmass. Flow bands and flow folds, autobreccia domains, elongate vesicles and lithophysae are also present. Some of these large units may be composite lavas, separated by thin breccia layers of possible pyroclastic origin. Ignimbrites are compositionally and texturally homogeneous, and contain mm-scale crystals of feldspar and quartz in fine grained, eutaxitic and vitriclastic matrix. Some of the lavas have previously been interpreted as pyroclastic flow deposits in which all evidence of clastic origin have been concealed by welding. This interpretation was mainly based on the extent of the units and inferred high viscosity of felsic lavas. Volumetrically minor mafic and intermediate lavas are also present and locally form thick piles.

The chemical composition of the lower Gawler Range Volcanics has been determined, including major and trace elements. Whole-rock analyses are complemented by melt inclusion analyses, which allowed measuring volatile components (halogens in particular). The rocks are characterised by increasing trends of K_2O, REE, Y, Zr, Th and Nb with increasing SiO_2, and decreasing trends of CaO, FeO, MgO and TiO_2. Fluorine is present in high concentrations in melt inclusions (F ≤1.3 wt.%, more than 20 times the average upper continental crust), whereas Cl has moderate concentrations. High microprobe totals of melt inclusions are compatible with low water contents, in agreement with the anhydrous parageneses and previous estimates based on petrological considerations (method of Nekvasil, 1988). Plots of Zr and the Zr/Hf ratio versus indicators of magma fractionation (e.g. SiO_2 and incompatible elements) indicate that source magmas of the most felsic rocks (SiO_2 >68 wt.%) were zircon-saturated. Application of the zircon saturation model (Watson and Harrison, 1983) on these samples yields temperatures up to 950-990°C for the lower GRV. The combination of high magmatic temperatures, high F and low water in the magma creates conditions of low viscosity and low explosivity.

These conditions are favourable for the effusive emplacement of the units, and help explaining how extensive units were emplaced as lavas.

Comparison of whole-rock and melt inclusion analyses allowed assessing the degree of alteration of the rock units. Major element compositions are similar in whole-rock and melt inclusion analyses, with the local exception of Na, which showed low concentration in a few whole-rock samples. This indicates that alteration did not affect substantially concentrations of the most “mobile”, water-soluble major elements. This is also true for most trace elements, and whole-rock analyses can be considered as indicative of the magma composition. Notable exceptions are Pb, U and Sn, which were selectively mobilised and variously depleted. Alteration of Pb, U and Sn is evident from scattered whole-rock compositions and lack of correlation between these elements and other elements. In contrast, melt inclusion compositions show good correlations and indicate incompatible behaviour.

Quartz textures and trace element content in the lower Gawler Range Volcanics and Hiltaba Suite were studied by scanning electron microscopy cathodoluminescence (CL) and electron microprobe. Mineral zones retain a record of crystallisation conditions through time (“crystal stratigraphy”). Comparisons were made between volcanic units, shallow and deeper intrusions (dykes and granite). Quartz in volcanic units and dykes has sharp-edged CL zones in which CL brightness correlates with Ti content, whereas the granite quartz has “smudged” zones with gradational contacts. This difference is interpreted as the result of poor preservation of Ti zones in the granite, for which slow cooling allowed solid-state diffusion of Ti in the quartz lattice. Intra-granular textures in volcanic units and dykes also include truncation of growth textures and reverse zoning (rimwards increase of Ti content). Intra-granular textures indicate a complex history of crystallisation and resorption, and trace elements suggest varying temperature. These results point to pulsating magmatic conditions, compatible with a non-linear evolution of the lower Gawler Range Volcanics magma chamber(s). The volcanic units have contrasting (non-correlatable) zoning patterns among quartz crystals, each pattern indicating different crystallisation conditions. The juxtaposition of quartz crystals with contrasting zoning patterns are consistent with a dynamic regime (convection, stirring, overturning) of the GRV magma chamber. These results point to pulsating magmatic conditions, compatible with a non-linear evolution of the GRV magma chamber. In contrast, quartz crystals in the dykes have similar zoning patterns, suggesting that all the crystals in each dyke experienced a similar crystallisation history.

In some rhyolite samples, aggregates of minerals (including fluorite, epidote, REE-F-carbonate, titanite, anatase, and zircon) have crystallised in “pockets” such as vesicles, micro-miarolitic cavities and lithophysal vugs. These aggregates of minerals contain significant amounts of rare earth (RE), high-field strength (HFS) elements, and base metals (Cu and Mo). In average, concentration of these elements is higher in these aggregates than in the surrounding host rock. These aggregates are interpreted to have crystallised from a late-stage magmatic volatile (F, CO_2, H2O, ±S, ±P)-bearing fluid that exsolved and infilled pockets during the final stages of emplacement and crystallisation. The presence of complexing agents such as F and CO_2 can explain how low-solubility, “immobile” trace elements were transported in solution. A magmatic, primary origin for this fluid appears likely, given the F-, REE-, and HFSE-rich composition of the melt

shown by melt inclusions. Conversely, the hypothesis of a post-magmatic, secondary origin is considered less likely because of the absence of alteration, mineralisation and veins in these rocks. Magmatic accessory minerals, the alteration of which would have been necessary for secondary remobilisation of RE and HFS elements, appear fresh and unaltered. These data testify the mobility of RE and HFS elements in the lower Gawler Range Volcanics and can have implications in the formation of associated mineral deposits in the Gawler craton, including the Olympic Dam deposit. This deposit is also characterised by high concentrations of F, RE and HFS elements, and a similar F-rich fluid as the one hypothesised here might have been active in the mineralisation process.

Acknowledgments

This work was funded by the Australian Research Council Centre of Excellence in Ore Deposits (ARC-CODES). Supervisors Jocelyn McPhie, Vadim Kamenetsky and Sharon Allen provided invaluable support and discussion during both data gathering and writing stages of this thesis. The Primary Industries and Resources of South Australia, and in particular Martin Fairclough and Stacey Curtis, are thanked for providing field assistance, equipment and GIS, geochemical and geological data. Dr. Isabelle Chabefort and Dr. Paul Davidson are warmly thanked for providing continuous discussion and advice. Dr. Karsten Gömann, Simon Stephens, Philip Robinson, Katie McGoldrick (University of Tasmania) have offered analytical assistance throughout the work.

TABLE OF CONTENTS

List of figures

List of Tables

CHAPTER 1

Introduction

Large igneous provinces (LIP) represent vast amounts of magma erupted onto the Earth's surface and injected into the crust, emplaced in pulses of activity of relatively short duration (<10 Ma), and at high emplacement rates (Coffin and Eldholm, 1994; Ernst et al., 2005; Bryan and Ernst, 2008). Emplacement of LIP has occurred throughout geological time in both intraplate and plate margin settings, although the best preserved examples are Phanerozoic (e.g. Mahoney and Coffin, 1997; Hamilton and Buchan, 2010). Large igneous provinces include continental flood basalt provinces, volcanic passive margins, oceanic plateaus, ocean basin flood basalts, seamount chains, and giant continental dolerite dyke swarms, and are distinct from seafloor spreading and subduction-related magmatism (Head and Coffin, 1997).

The composition of these igneous provinces is mainly mafic, but the silicic and ultramafic components can be conspicuous (e.g. felsic rocks associated with the Paraná-Etendeka continental flood basalt province of Western Africa and South America, Milner et al., 1992; Peate, 1997; Ewart et al., 1998a). Silicic-dominated provinces of similar dimensions to the mafic provinces ($\geq 10^5$ km^3) are uncommon, although are being increasingly recognised. Examples occur throughout the geological record, and include the Mesoproterozoic Gawler Range Volcanics of South Australia (McPhie et al., 2008), the Early Cretaceous Whitsunday Volcanic Province of Australia (Bryan et al., 2000; 2002; Bryan, 2007), the Early to Late Jurassic Chon-Aike Province of South America and Antarctica (Pankhurst et al., 1995; 1998; 2000; Riley et al., 2001), the Mid-Tertiary Sierra Madre Occidental of Mexico (Cameron et al., 1980; Ferrari et al., 2002; Bryan et al., 2008), the Eocene Trans-Pecos volcanic field of the USA (Henry et al., 1988; Parker and White, 2008), and the Miocene Snake River Plain of the USA (Branney et al., 2008).

1.1 Key research questions

The study of silicic-dominated large igneous provinces (SLIP), including both volcanic and plutonic rocks, is important because SLIP are significant components of the continental crust. It is largely accepted that the formation of such large amounts of felsic magma and the associated mafic magmas ultimately requires a mantle source of heat (Hildreth, 1981; Bryan et al., 2000). Therefore, the study of SLIP and the associated mafic magmas is important for understanding the formation of continental crust, and the interaction between crust and mantle.

The emplacement of large-volume, extensive felsic volcanic units introduces questions regarding the mechanisms of eruption and final emplacement. The very definition of (S)LIP implies higher-than-normal eruption rates, and the literature does not give univocal indications on how large volumes of felsic magma can be emplaced in a relatively short lifespan. Explosive eruptions are commonly recognised as an effective way to emplace large volumes of silicic magma, and some of the largest felsic volcanic units known are pyroclastic flow deposits originated during extremely

voluminous caldera-forming eruptions. Among felsic units formed by these eruptions, also termed “supereruptions” (Self, 2006), are the 4500 km^3 dense rock equivalent Fish Canyon Tuff, Colorado, USA (Bachmann et al., 2002); the 2700 km^3 Younger Toba Tuff, Sumatra, Indonesia (Rose and Chesner, 1987); and the 2200 km^3 Huckleberry Ridge Tuff, Yellowstone caldera, Whyoming, USA (Christiansen, 1984; Lowenstern et al., 2006; also see Mason et al., 2004). However, it has been noted that some extensive, low aspect-ratio felsic units lack textural evidence for an explosive eruption and show characteristics reconcilable with emplacement as lava. Examples of these extremely extensive silicic lavas are the Star Mountain Rhyolites, Trans-Pecos (Henry et al., 1988), the Keweenawan Midcontinent Rift plateau volcanic units (Green and Fitz, 1993), the Yardea Dacite, Gawler Range Volcanics (Allen and McPhie, 2002; Allen et al., 2003) and the quartz-latite units of the Etendeka Province, Namibia (Ewart et al., 1998b; Marsh, 2001). The size of these units is up to thousands of km^3, comparable with flood basalts. The Springbok quartz-latite of the Etendeka Province has been correlated with units in the Paraná, Brazil, for a total estimated volume of ~6000 km^3 (Ewart et al., 1998b), thus amounting to one of the largest eruptive units known.

A key research question for this thesis and for SLIP research in general is: are SLIP erupted explosively or effusively? If extensive felsic units are emplaced effusively (flood rhyolites), how can lava flow for tens of km?

The Gawler Range Volcanics and Hiltaba Suite (GRV-HS) constitute a Mesoproterozoic silicic-dominated large igneous province (the Gawler SLIP) cropping out over a vast area in the Gawler craton, South Australia. The preserved (minimum) volume of the province is estimated to be in the order of 100 000 km^3 (McPhie et al., 2008). The GRV include some very extensive felsic volcanic units (several hundreds of km^3 and a few hundreds of km across) and the entire succession was emplaced over a few million years in an intracontinental setting (Blissett et al., 1993; Fanning et al., 1998). Although the GRV are mainly felsic in composition, mafic units are present and reflect direct (mafic lavas) and indirect (mantle heat causing melting of the crust) mantle input to the succession. The igneous province shows no signs of deep burial, deformation and metamorphism and preserves primary volcanic textures and compositions. Hence, the Gawler SLIP offers an excellent opportunity to explore the eruption and emplacement mechanisms and a number of key research questions posed by voluminous silicic magmas in intracontinental settings. Other more recent and well studied volcanic provinces that include large felsic lavas (e.g. Yellowstone-Snake River Plain, Paraná-Etendeka) are mentioned as useful comparisons.

The eruption and emplacement mechanisms of volcanic units are determined by the interplay of several parameters, including magma composition (especially silica content, Al/alkalis ratio and volatile content), magma temperature, total volume erupted, and eruption rate. Bulk composition, temperature and dissolved volatile components are important controls on viscosity. Constraining these three parameters is very important to describe the eruptive behaviour of magmas. Volatile components also play a fundamental role in triggering volcanic explosions through exsolution of a fluid phase and vesiculation of magma.

Although for most felsic magmas water is the main volatile component, and has a huge impact on magma viscosity and explosivity (e.g. Holtz et al., 1999; Romano et al., 2001), other volatiles – and F in particular – may be similarly influential (Manning, 1981; Dingwell et al., 1985; Giordano et al., 2004). Some units in the GRV are known to contain

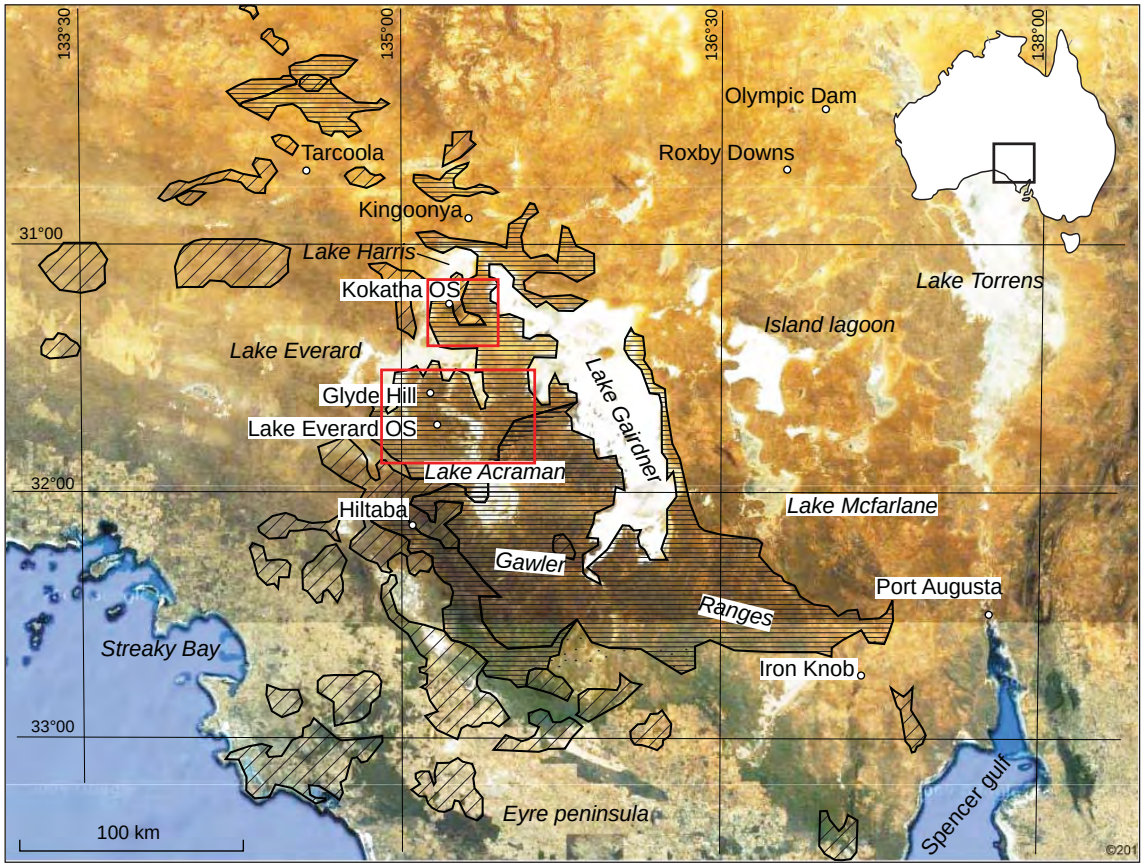

Fig. 1.1. Satellite view of central South Australia and the study areas at Kokatha and Lake Everard Outstations (rectangles). Outcrop areas of the Gawler Range Volcanics (horizontal lines) and Hiltaba Suite granite (oblique lines) are indicated (satellite image from Google maps).

pristine melt inclusions in quartz (Kamenetsky et al., 2000; Bath, 2005), representing a good opportunity to document pre-eruptive melt compositions in detail, including volatile elements.

Another point of longstanding discussion is the nature of crustal magma storage, which includes magma chamber geometry and dynamics, residence time of crystals before eruption, formation of new crystals vs. recycling of older crystals. Recent studies have proposed complex models involving zoned magma chambers with variable melt to solid ratio and non-continuous (“waxing and waning”) production of melt (Hildreth, 1981; Lipman et al., 1997; Hildreth, 2004; Charlier et al., 2005). Addition of heat and new magma from the mantle can result in “rejuvenation” of the magma chamber (e.g. Hildreth and Wilson, 2007), causing temperature increase, magma mixing, and remelting of crystal mush (largely solid marginal portions of plutons). These variations in magma composition and temperature are potentially recorded by zoned crystals (e.g. Streck, 2008). The study of these processes can add to the understanding of silicic magma chambers. This thesis is an attempt to address some of these issues.

A further motive of interest is that the emplacement of the Gawler SLIP was coincident with two major mineralising events, which gave origin to the Olympic Fe oxide Cu-Au-U (IOCG) province (Skirrow et al., 2002) and the gold-dominated central Gawler gold province (Budd and Fraser, 2004). The formation of ore deposits requires a source of ore elements, a medium able to transport these elements, and a process to precipitate

them. By virtue of their size, SLIP can provide large amounts of ore elements, fluids, and heat necessary for transport. The relation between large felsic volcanic systems and mineralisation has been postulated for other provinces (e.g. John, 2008). This thesis discusses the possible role of the Gawler SLIP magmatism as a source of elements, and the role of magmatic fluids in the transport of lithophile elements (especially rare earth and high-field strength elements) that are enriched in the Olympic Dam deposit, providing a possible link between Mesoproterozoic magmatic and hydrothermal activity in the Gawler craton.

1.2 Aims and methods

The aims of this study and the methods used to achieve them are:

• Describe in detail the textures and field characteristics of the lower part of the Gawler Range Volcanics, and evaluate the features indicative of eruption style and emplacement mechanism. Field investigations and microtextural analysis (optical and electron microscopy) were undertaken to address this task.

• Characterise the lower Gawler SLIP magmas in terms of major and trace elements, and compare those compositions with the rest of the province and with other similar provinces. Whole rock X-ray fluorescence (XRF) and inductive coupled plasma mass spectrometry (ICP-MS) were used to obtain major and trace element compositions of the rock units.

• Study the nature and abundance of volatile components in the pre-eruption melts, with a focus on halogens (F and Cl). Electron microprobe and laser ablation ICP-MS analyses of quartz-hosted melt inclusions were used for this task.

• Study quartz phenocrysts as an indicator of magma crystallisation conditions. Despite its simple chemical composition, quartz can record a wealth of information in its growth zones: intragranular textures give information on growth-resorption events, and trace element content can be used to estimate the crystallisation temperature. Quartz was chosen for this study because of the weak but widespread alteration of other phenocryst phases in the studied rocks. Quartz zones were studied by different microbeam methods, including cathodoluminescence and microprobe analysis.

1.3 Structure of the thesis

Chapter 2 presents the geological setting of the Gawler SLIP and briefly describes the tectonic phases that led to the present crustal configuration of the Gawler craton.

Chapter 3 includes field and petrographic descriptions of the units in two areas where outcrop of the lower GRV is extensive: the Glyde Hill Volcanic Complex at Lake Everard and the Chitanilga Volcanic Complex at Kokatha. Subdivision of the units in these two areas is based on the latest PIRSA (Primary Industries and Resources of South Australia) 1:250 000 maps. During field work (spring 2006 and winter 2007), geological boundaries on these maps have proved to be fundamentally correct. The descriptions are presented in data sheets, each containing unit name, compositional classification (total alkali versus silica according to Le Bas et al., 1986, and trace elements according to Pearce, 1996), rough outcrop distribution, field photographs and photomicrographs, and where deemed relevant, a detailed log. These descriptions constitute a database for the

following discussion and analyses. The second part of the chapter discusses the volcanic facies and interprets the emplacement mechanism of the units. The chapter shows that felsic lavas and volumetrically minor ignimbrites coexist in the studied successions, and small and moderately-large volume units (up to more than 100 km^3) alternate without a clear pattern.

Chapter 4 describes the whole rock and melt inclusion compositions. New XRF and high-precision, low-detection limit ICP-MS whole-rock data complement and complete datasets already published in the past (e.g. Giles, 1988; Stewart, 1994). Comparisons are made across the compositional spectrum from mafic-intermediate to felsic compositions. The melt inclusion study is the first of this kind in the area, and is aimed at determining the melt composition, including nature and abundance of volatile components, with a focus on halogens. A previous study (Stewart, 1994) has detected the presence of F in minerals (apatite, amphibole) in the GRV, but due to the poorly constrained crystal-melt distribution coefficients, estimates of F concentrations in the melt are not possible. Further, because whole-rock volatile element compositions are affected by degassing and alteration, melt inclusion analysis is the only direct way of measuring pre-eruptive magmatic volatile elements. Dissolved volatile elements are important controls on the magma rheology and ultimately on the eruption style (Manning, 1981; Dingwell, 1996). Melt inclusions are irreplaceable in addressing problems encountered by any study dealing with whole-rock data, including alteration of the most “mobile”, water-soluble elements (e.g. alkalis, Ca), and accumulation of crystals with a high density contrast with the melt (thus affecting, for instance, Zr and Hf). In addition, after showing that the melt in felsic GRV rocks (SiO_2 >68 wt.%) are zircon-saturated, the zircon-saturation model of Watson and Harrison (1983) can be applied to estimate magmatic temperatures.

Chapter 5 describes quartz textures. Quartz is the best preserved mineral in these rocks, due to the alteration of feldspar and ferromagnesian minerals. Scanning electron microscope cathodoluminescence (SEM-CL) is used to identify growth textures, and electron probe micro-analysis (EPMA) is used to measure trace element concentrations. Growth zones of quartz preserve a history of crystallisation conditions, or “crystal stratigraphy”. Trace element content is controlled by intensive parameters (temperature, pressure, melt composition), and truncation relationships of growth textures can be used to identify growth and dissolution events. These data are the basis for inferences on the changing conditions of crystallisation and the dynamics of the magma chamber. Titanium content of different quartz zones is used in this chapter for geothermometric estimates (Wark and Watson, 2006). These crystallisation temperature estimates are compared with other estimates presented in this thesis (melt inclusion homogenisation temperatures and zircon-saturation temperatures) and in other investigations (e.g. two-pyroxene equilibration; Creaser and White, 1991). Chapters 4 and 5 are currently under revision for publication.

Chapter 6 reports the presence of aggregates of volatile (F, H_2O, CO_2)-rich and lithophile-rich minerals (e.g. fluorite, rare earth element-fluoro-carbonate, Nb-anatase, titanite, epidote) and their textures. These minerals occur in “pockets” or cavities and are interpreted to have crystallised from a magmatic fluid in the last stages of magma solidification. The hypothesis of alteration of magmatic accessory minerals and re-mobilisation of these elements by much later hydrothermal fluids (“secondary” origin) is considered less likely because of the absence of veins, alteration, and hydrothermal activity in general. Whole-rock and melt inclusion data presented in chapter 4 show that rare earth and high field strength elements, as well as F, are enriched in the GRV magma,

suggesting a magmatic origin for these elements. Thus, these pockets of minerals attest to the mobility of elements such as rare earth and high field strength elements, Y, Th, U, and Cu in late-stage volatile (H_2O, F, CO_2, SO_4^{2-})-rich (fluid) phases. This chapter was published in May 2010 (Agangi et al., 2010, Chemical Geology 273, 314-325).

Chapter 7 contains a review of the main results of the previous chapters. Then the major implications of these results on the evolution of the Gawler SLIP and SLIP in general are discussed. In particular, the discussion touches on petrogenesis, emplacement of extensive felsic lava units, and ore genesis.

1.4 Previous investigations of the Gawler Range Volcanics

Gold discovery in 1893 at Tarcoola prompted interest in this remote area of the South Australian outback, and the first reports on the geology of the region were made by the South Australia Department of Mines and Energy (SADME), part of the Geological Survey of South Australia (Blissett, 1985). The magmatism of the area was first systematically studied by the Geological Survey and the University of Adelaide in the 1970s and 1980s (Blissett, 1975; 1980; 1985; Giles, 1977; Branch, 1978). All these studies describe the volcanic province as a series of welded ashflow tuffs associated with volumetrically minor mafic lavas and felsic domes. The petrogenesis has been investigated in a few key studies (Giles, 1988; Creaser and White, 1991; Stewart, 1994). More recently, studies have been carried out by the University of Tasmania (Garner and McPhie, 1999; Kamenetsky et al., 2000; Morrow et al., 2000; Roache et al., 2000; Allen et al., 2002; Allen and McPhie, 2003; Allen et al., 2008; McPhie et al., 2008) and the styles of volcanism have been reconsidered on the basis of field data and microtextures. Further work on the tectonic circumstances and the origin of magmatism in the Gawler Range Volcanics has been recently produced (e.g. Hand et al., 2007; Betts et al., 2009).

Mapping of the area is currently being conducted by the Primary Industries and Resources of South Australia (PIRSA). The 2006 version of the 1:250 000 Childara and Gairdner sheets (SH 53-14 and 53-15) and 1:100 000 Childara, Everard and Kokatha (5834, 5935 and 5934) maps were used as the basis for the present study. The two study areas of this thesis are located at Lake Everard, and at Kokatha (Fig. 1.1), where the lower part of the volcanic province is exposed.

CHAPTER 2

The Gawler Range Volcanics and the Hiltaba Suite: a Mesoproterozoic intracratonic silicic large igneous province

The Gawler Range Volcanics and the comagmatic Hiltaba Suite form a Mesoproterozoic dominantly silicic large igneous province (SLIP) situated in the central part of the Gawler craton, South Australia (Fig. 2.1).

2.1 Gawler Range Volcanics

The Gawler Range Volcanics (GRV) outcrop for over 25 000 km^2, and the estimated erupted volume exceeds 25 000 km^3 (Creaser, 1989; Blissett et al., 1993). To the east, they are partially concealed by younger Proterozoic and Phanerozoic sedimentary formations of the Stuart Shelf (Blissett et al., 1993). Rocks correlated with the GRV are known from the subsurface on the eastern side of the Adelaide Geosyncline, more than 100 km to the east, and clasts interpreted to be derived from the GRV have been found in moraines in Terre Adelie Land in Antarctica (Peucat et al., 2002), indicating that the igneous activity extended far beyond present outcrop limits (Allen et al., 2008). Furthermore, the area remained land for most of the Phanerozoic and was subjected to erosion and weathering, therefore the original extent of the province is larger than presently preserved (Blissett et al., 1993; Daly et al., 1998).

The GRV overlie Archaean and Palaeoproterozoic granitoid suites, metamorphic complexes and metasedimentary formations of the Gawler craton and were emplaced in a subaerial intracontinental setting (Blissett et al., 1993). A short emplacement interval (a few million years) is suggested by U-Pb zircon dating of the oldest and youngest units exposed, at 1592±3 and 1591±3 Ma, respectively (Fanning et al., 1988; Creaser, 1995).

The volcanic province has been subdivided into lower and upper sequences (Blissett, 1987) based on a structural discordance between small- to moderate-volume, gently to moderately dipping older units (lower GRV) and extensive, gently dipping to flat-lying younger units (upper GRV). Although that discontinuity is nowadays considered of local importance (Blissett et al., 1993), such subdivision has been supported by geochemical and isotopic data of Stewart (1994), who adopted the names of “developmental” and “mature” for the two magmatic phases that produced the two main parts of the GRV.

Several different volcanic centres have been identified in the lower GRV (or developmental phase). The Chitanilga Volcanic Complex at Kokatha (Blissett, 1975; Branch, 1978; Blissett et al., 1993), and the Glyde Hill Volcanic Complex at Lake Everard are the best exposed successions (Blissett, 1975; Blissett et al., 1993) and are the subject of the present thesis (Fig. 2.2). In addition, the Menninnie Dam volcanic

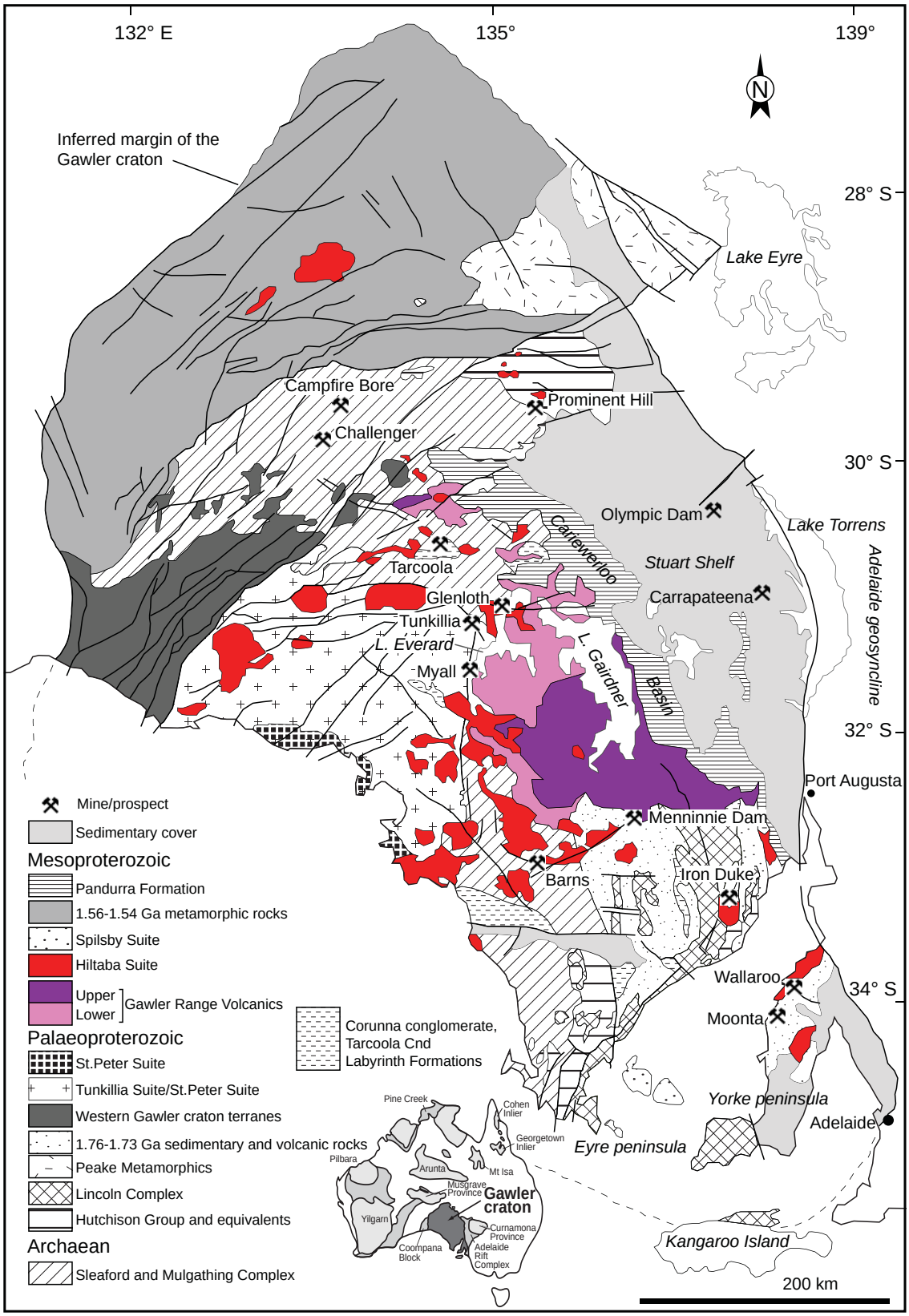

Fig 2.1. Geology of the Gawler craton (after Daly et al., 1998; Betts and Giles, 2006, Hand et al., 2007). Inset shows the location of the Gawler craton and distribution of Proterozoic.

centre at Nonning (Roache et al., 2000) in the southern GRV, and volcanic successions at Tarcoola-Kingoonya and at Myall Creek (Daly, 1985; Blissett, 1993) on the eastern margin were intersected during drilling. Products of the lower GRV volcanic centres are also exposed at Tarcoola (northwest of the province), and within inliers beneath the upper GRV at Lake Acraman (Allen et al., 2008). All successions in the lower GRV consist of compositionally heterogeneous, small- to moderate-volume (up to tens of km^3), gently to moderately dipping units, containing low to moderate phenocryst content (Giles, 1988; Stewart, 1994). These successions are 0.5 to 3 km thick and dominated by felsic compositions, although thick basalt and basaltic andesite lavas occur at the base of the Chitanilga Volcanic Complex (Branch, 1978). The felsic rocks in the Chitanilga Volcanic Complex and Glyde Hill Volcanic Complex range from dacite to rhyolite, and have been interpreted to be moderately to intensely welded ashflow tuffs, and minor flow-banded rhyolite lavas (Giles, 1977; Blissett et al., 1993). The Menninnie Dam volcanic centre includes porphyritic rhyolitic intrusions, pyroclastic deposits and minor lava; it was interpreted as a small hydroexplosive centre (Roache et al., 2000). Scattered outcrops at Tarcoola include welded ignimbrite and basalt lavas (Blissett et al., 1993).

The upper GRV (or mature phase), exposed in the southern and central part of the province, are represented by extensive (tens to a few hundreds km across), flat-lying massive dacite and rhyolite units. The upper GRV units are characterised by evenly porphyritic textures, compositional homogeneity, and well-defined fractionation sequences (Giles, 1988; Stewart, 1994). The units in this portion of the province are up to 250–300 m-thick, in excess of 500 km^3 in volume and they crop out for up to 12 000 km^2 (Blissett, 1975; Giles, 1988; Blissett et al. 1993; Allen et al., 2003, Allen et al., 2008). The upper GRV includes two main units, the Eucarro Rhyolite and the Yardea Dacite (Allen et al., 2008). The Chandabooka Dacite at Kokatha and the Carnding Rhyodacite (Tarcoola area) were also included in the upper GRV and correlated with the Yardea Dacite by Blissett et al. (1993). The Yardea Dacite is composed of two members, the Pondanna Rhyolite and the Moonaree Dacite member, both showing evidence of having been emplaced as lava flows (Allen et al., 2003).Common mineral assemblages are essentially anhydrous and include phenocrysts of plagioclase, K-feldspar and pyroxene in a fine grained quartz-feldspar groundmass. The Yardea Dacite, having an area of exposure of 12 000 km^2 and a total erupted volume of 3 000 km^3, is one of the largest felsic volcanic units known (Creaser and White, 1991).

The widespread extent and the enormous volume of the felsic units suggested to several authors that these units are intensely welded ignimbrite sheets (e.g. Giles, 1977; Blissett, 1985). However, the lack of vitriclastic textures (pumice, shards, broken crystals, lithic clasts) was noted more recently (Creaser and White, 1991). A combination of fieldwork and petrography, and considerations of textural characteristics, including characteristics indicative of non-particulate flow (flow bands, mingling textures, textural homogeneity, orientation of phenocrysts, and presence of megablocks as inclusions), led to the interpretation of these units lavas (Garner and McPhie, 1999; Morrow and McPhie, 2000; Allen and McPhie, 2002; Allen et al., 2003; 2008; McPhie et al., 2008).

Pyroxene compositions in the felsic units of the upper GRV indicate equilibration temperatures as high as 1000-1100°C (Creaser and White, 1991; Stewart, 1994). Based on experiments (Johnson and Rutherford, 1989), very low water contents are required to

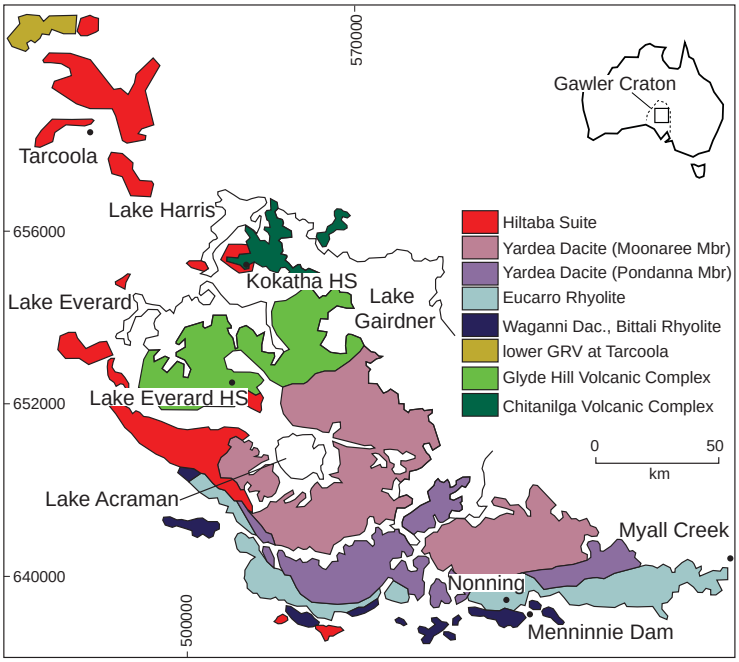

Fig. 2.2. Simplified geological map of the Gawler Range Volcanics (modified from Blissett et al., 1993; Allen et al., 2008).

obtain the observed mineral assemblages and crystallisation sequence in the upper GRV (Stewart, 1994). Maximum magma water contents of 1–2 wt.% have been estimated by Creaser and White (1991) given the mineral assemblage and the estimated temperature of the Yardea Dacite (method of Nekvasil, 1988). Stewart (1994) also reported high concentrations of halogen in amphibole and apatite in the Yardea Dacite and Eucarro Rhyolite.

The GRV have been intruded by the Hiltaba Suite Granite and by rhyolitic and andesitic to dacitic porphyritic dykes. These dykes are up to several m wide and have been mapped for several km along strike. Porphyritic, quartz-feldspar-phyric rhyolite dykes are common at Glyde Hill, where they are termed Moonamby Dyke Suite, and at Kokatha (Giles, 1977; Blissett et al., 1993). Some of the andesitic to dacitic dykes are thought be feeders from which the volcanic units were erupted (Branch, 1978; Blissett, 1985; Allen et al., 2008).

2.2 Hiltaba Suite

The Hiltaba Suite consists of a series of equigranular to porphyritic, medium to coarse-grained, massive plutons. The plutons show variable mineral composition and a bimodal chemical distribution. Granites predominate but monzodiorite, quartz monzonite and granodiorite are also present (Flint, 1993; Ferris, 2001). The most common assemblage comprises K-feldspar (either perthitic orthoclase or microcline), plagioclase, quartz (locally showing graphic intergrowths with K-feldspar) and biotite as the main phases and fluorite, magnetite, titanite, zircon and apatite as accessory phases; muscovite and amphibole can be also present. The less silicic lithologies (SiO_2 < 65%) contain plagioclase, augite, hornblende, and minor K-feldspar and quartz; apatite and zircon are common accessory phases (Blissett, 1985; Flint, 1993).

The Hiltaba Suite plutons are compositionally similar to, and broadly coeval with the GRV. U-Pb zircon ages of the Hiltaba Suite plutons range from ca. 1600 to ca. 1580 Ma (Flint, 1993; Ferris, 2001). The Hiltaba Suite plutons intrude the Tarcoola Formation, the Corunna Conglomerate and the GRV, and are unconformably overlain by Pandurra Formation (Flint, 1993). Intrusive contacts between the Hiltaba Suite and the GRV can be observed at various localities and have been described as sharp and free of metamorphic overprint in the host volcanic rocks, locally coinciding with fracture planes in the volcanic units (e.g. Blissett, 1985; Giles, 1988). Hiltaba Suite granite xenoliths occur in the Yardea Dacite, the youngest unit of the upper GRV (Garner and McPhie, 1999) and testify that early-crystallised portions of the Hiltaba Suite predate the emplacement of the Yardea Dacite.

2.3 Composition and petrogenesis of the GRV and Hiltaba Suite

The GRV – Hiltaba Suite province has a distinctive chemical signature including high K, rare earth element (REE), and high field strength element (HFSE) concentrations and low Ca, Mg, Cr, and Ni abundances compared with Phanerozoic calc-alkaline rocks and average crustal values (e.g. Hu and Gao, 2008). These characteristics are shared with A-type granites (Collins et al., 1982; Whalen et al., 1987; Giles 1988; Creaser and White, 1991).

The GRV range in silica from 50 to 80 wt.%, although there are no analyses around SiO_2 55 wt.% (Fig. 2.3), and silicic compositions are by far the most abundant (Blissett et al., 1993). The GRV exhibit silica-saturated to slightly undersaturated compositions with respect to alkaline elements in the total alkali versus silica (TAS) diagram. The rocks are alkali-calcic according to Peacock (1931), metaluminous (alumina saturation index, ASI =0.8-1, Al>Na + K) to peraluminous (ASI =1-1.3), with ~8% of analyses, n ~450, ASI >1.3, and mainly plot in the high-K and ultra-K series fields in the K_2O versus SiO_2 diagram (Fig. 2.3). Major and trace elements variations with increasing silica show broad common trends throughout the volcanic province, although there is more scatter in the data from the lower part of the sequence (Giles, 1988; Stewart, 1994). A negative correlation with increasing silica is shown by Al_2O_3, FeO(tot), CaO, MgO, TiO_2 and MnO, and a positive correlation is shown by K_2O, FeO/MgO, K, Ba, HFSE (Zn, Nb, Ga, Y) and REE. Light REE are enriched compared to heavy REE in normalised plots.

The Hiltaba Suite granites show quite considerable compositional variation, in both major and trace elements and each pluton has distinctive characteristics in terms of trace element patterns and abundances (Flint, 1993). Silica content ranges from 67-79 wt.%, but is locally as low as 57 wt.% (Flint, 1993). Total alkalis increase with silica content and decrease with silica for the more felsic compositions (SiO2 ≥68 wt.%). A negative trend is recognisable in FeO(tot), Al_2O_3, TiO_2, MgO, CaO and P_2O_5 versus silica plots. The Hiltaba Suite granites are metaluminous to peraluminous (ASI =0.9-1.4, and higher in ~10% of analyses) and have high-K to ultra-K affinity in silica versus K_2O plots (Ferris, 2001). The granite plots in the alkali-calcic and calc-alkalic fields in the MALI index versus silica plot, and across the boundary between magnesian and ferroan fields according to Frost and Frost (2001). Chondrite-normalised REE trends are rather consistent in different plutons, and characterised by steep LREE-enriched patterns, relatively flat HREE and significant

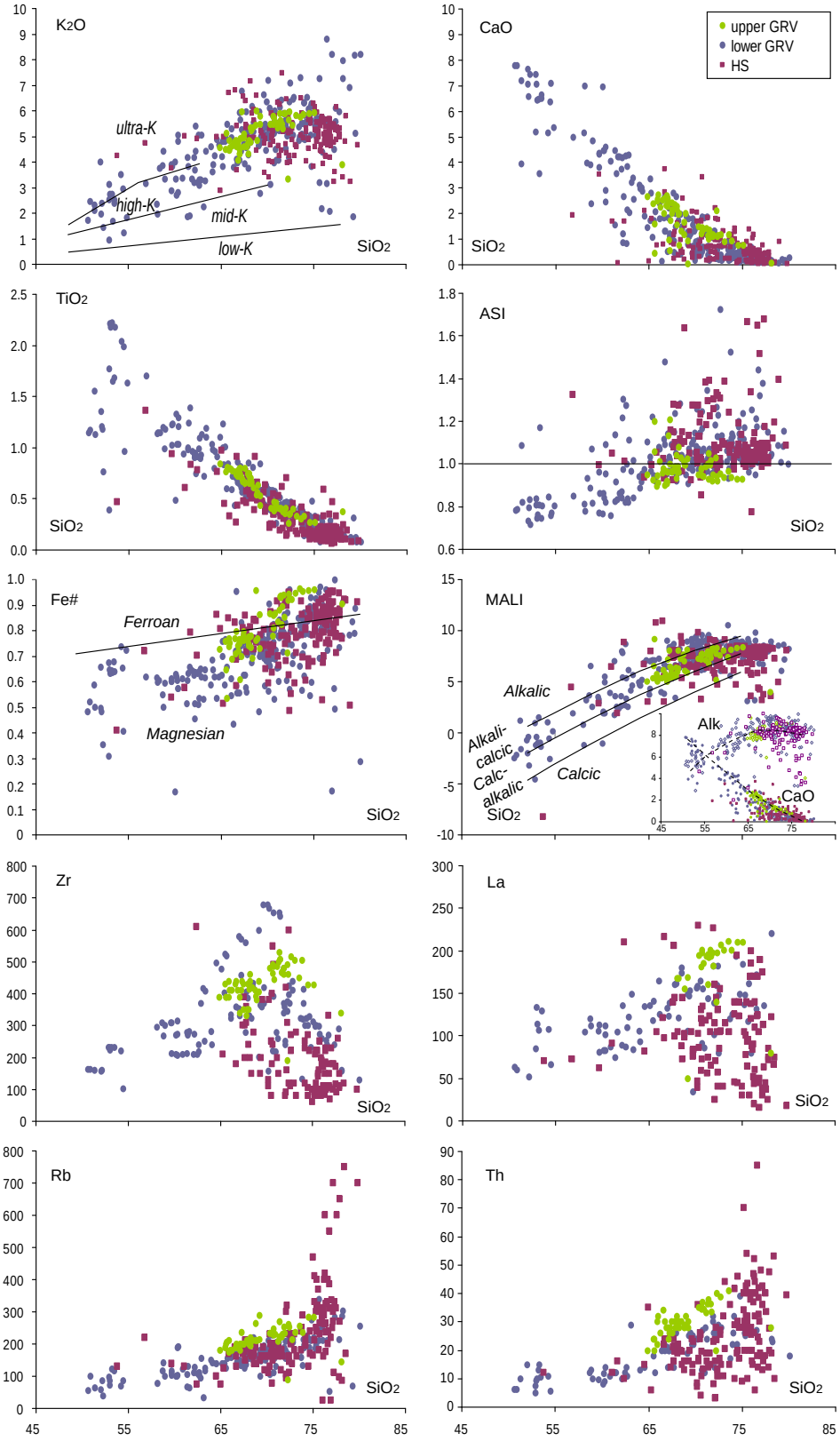

Fig. 2.3. Whole-rock composition of the Gawler Range Volcanics–Hiltaba Suite igneous province. Recalculated to anhydrous, oxides as wt.%, elements as ppm. Data from Giles (1988); Stewart (1994); Ferris (2001); PIRSA Dataset (2006). Fields in the K_2O vs SiO_2 plot from Peccerillo and Taylor (1976).

negative Eu anomalies (Ferris, 2001).

Based on petrologic and isotopic evidence, the GRV and Hiltaba Suite magmas are thought to be derived from source rocks in the mantle and the lower granulitic crust (Giles, 1988; Creaser, 1989; Stewart, 1994). The basalts and basaltic andesites of the lower GRV have been interpreted as products of different degrees of melting and mixing of enriched lithospheric and asthenospheric mantle (Stewart, 1994). These magmas then rose into the crust initiating crustal melting. The huge volume of felsic magma was interpreted as the result of extensive partial melting of Archaean and Palaeoproterozoic continental crust, the heat source being mantle-derived mafic magmas (Giles, 1988; Creaser, 1995).

2.4 Evolution of the Gawler craton

The Gawler craton has been affected by two major phases of tectonic activity, or megacycles, between the Archaean and the Palaeoproterozoic (e.g. Betts and Giles, 2006). Each of these megacycles was concluded by an orogenic cycle: the Sleaford Orogeny (Late Archaean – Palaeoproterozoic) and the Kimban Orogeny (Palaeoproterozoic).

The first megacycle is represented by granulite facies gneiss, mafic granulite and granite belonging to the Sleaford Complex in the south (Fanning et al., 1988; Parker et al., 1986), and gneiss, mafic volcanic units and banded iron formation belonging to the Mulgathing Complex in the northern portion of the Gawler craton (Daly et al., 1988). These complexes began as Late Archaean to Palaeoproterozoic sediments and volcanic units, all of which were metamorphosed to upper amphibolite-granulite facies and intruded by granitoids during the Sleafordian Orogeny (2480–2420 Ma, Daly et al., 1998).

The second megacycle involved deposition of a sequence of mixed clastic and chemical sediments on the basement metamorphic complexes. This succession is represented by the Hutchison Group (Fig. 2.1), and includes calc-silicate, quartzite, dolomite, iron formation, amphibolite, and various schist types (Parker and Lemon, 1982; Creaser, 1989). The sedimentary cover was metamorphosed by the high-temperature metamorphism and polydeformation of the Kimban Orogeny (1740–1690 Ma) that affected the whole Gawler craton (Parker and Lemon, 1982; Betts et al., 2003b; Betts and Giles, 2006). Felsic and mafic plutonism accompanied different phases of this orogenic phase. The earliest intrusions are represented by the Donington Granitoid Suite, and occur in the southeastern portion of the craton.

Subsequent to the Kimban Orogeny, the tectonic development of the Gawler craton was dominated by widespread magmatism, including the St. Peter Suite (ca. 1620–1610 Ma), interpreted as arc-related (Ferris et al., 2002), followed by formation of voluminous GRV and Hiltaba Suite. The emplacement of the GRV and the Hiltaba Suite is the expression in the Gawler craton of the ca. 1600–1560 Ma continental-scale high-temperature thermal event referred to as the Hiltaba Event (Betts et al., 2002). Coincident magmatism occurred in the Curnamona Province (Robertson et al., 1998). The high-temperature episode caused amphibolite to granulite facies metamorphism (ca. 1600–1580 Ma) in the Mount Isa Inlier (Rubenach and Barker, 1998), Curnamona Province (Clarke et al., 1986), Coen and Yambo Inliers (Blewett et al., 1998) and in the Harts Range in the Arunta Inlier (Rubatto et al., 2001, see inset in Fig. 2.1).

The emplacement of the GRV was accompanied by minor sedimentation, restricted to the Corunna Conglomerate and Labyrinth Formation (Daly, 1993).

The GRV and Hiltaba Suite magmatism has widely been considered to have developed in an anorogenic or extensional setting. This magmatic event is interpreted to record the arrival of a mantle plume, resulting in intra-cratonic extension, partial melting of the lower crust and emplacement of shallow plutons and voluminous volcanic units (Blissett et al., 1993; Flint et al., 1993; Creaser, 1995). This interpretation is supported by the volume of magma emplaced and the undeformed state of the succession (Giles, 1988; Creaser and White, 1991; Daly et al., 1998). This explanation is also consistent with the A-type affinity and the bimodal composition of the magmas, and with the high magmatic temperatures (Whalen et al., 1987; Creaser et al., 1991). However, evidence of the significance of tectonic events in the wider Gawler craton during magma emplacement has been pointed out (e.g. Betts and Giles, 2006). Hand and co-workers (Hand et al., 2007; 2008) noted that the magmatism occurred during a time of compression in the adjacent Curnamona province and suggested an overall compressional regime. An active geological setting at the southern end of the Gawler craton during magma emplacement is also suggested by the presence of foliated granites of the Yorke Peninsula (Betts and Giles, 2006). After emplacement, the GRV have formed a stable platform, largely unaffected by subsequent deformation. There is no indication of deep burial of the province and the rocks are unmetamorphosed and only slightly deformed (Fanning, 1988; Giles, 1988; Blissett et al., 1993; Allen et al., 2008).

2.5 Mineralisation in the Gawler craton

Emplacement of the GRV and Hiltaba Suite was coincident with a major mineralising interval in the Gawler craton. Two regional metallogenic provinces are distinguished: the Olympic iron oxide Cu-Au (IOCG) province (Skirrow et al., 2002) along the eastern margin of the craton and the gold-dominated central Gawler gold province (Budd and Fraser, 2004). The spatial distribution of IOCG versus Au-dominated mineral provinces appears to correspond to regional variations in crustal composition, Hiltaba Suite petrogenesis and heat flow still recorded today (Hand et al., 2007). The world-class Olympic Dam IOCG Cu-U-Au-Ag deposit (Fig. 2.1) contains approximately 40 percent of the world's known U resources, as well as world-class resources of Cu and Au (Oreskes and Einaudi, 1990; Haynes et al., 1995; Skirrow et al., 2007). The Olympic Dam deposit is hosted by the Roxby Downs Granite, associated with the GRV - Hiltaba Suite SLIP. Recently discovered Carrapateena and Prominent Hill deposits (Belperio et al., 2007) are also included in the Olympic IOCG province. The central Gawler gold province includes Pb–Zn–Ag mineralisation at Menninnie Dam, hosted in a small GRV volcanic centre (Roache et al., 2000), and Au mineralisation at Glenloth and Tarcoola (Daly, 1993; Budd and Skirrow, 2007; Fig. 2.1). Recently, more gold prospects have been discovered at Tunkillia, Barns, and Nuckulla Hill (Budd and Fraser, 2004 and ref. therein). These gold prospects and deposits are hosted in rocks of different age, but they share similar timing, mineralisation style and fluid characteristics (Fraser et al., 2007). Mineralisation dating (Budd and Fraser, 2004; Skirrow et al., 2007) indicates that both the IOCG and gold hydrothermal systems were broadly coeval with magmatism of the Hiltaba Suite and GRV.

CHAPTER 3

The lower Gawler Range Volcanics at Lake Everard and Kokatha: stratigraphy and volcanic facies

3.1 Introduction

The Glyde Hill Volcanic Complex at Lake Everard and the Chitanilga Volcanic Complex at Kokatha are the best exposed successions identified in the lower Gawler Range Volcanics (GRV, chapter 2). Volcanic units in the Glyde Hill Volcanic Complex (>2000 km^2) and the Chitanilga Volcanic Complex (>200 km^2) mainly range in composition from basalt to rhyolite with a compositional gap between ~52-56 wt.% SiO_2. The successions are dominated by felsic to intermediate, massive to banded volcanic rocks, with localised mafic lavas and very minor bedded volcanogenic sedimentary units. Small- to moderate-volume units (Tables 3.1, 3.2) are numerically predominant, but large volume (>100 km^3) extensive felsic units are present.

Most of the felsic units in the Glyde Hill Volcanic Complex and Chitanilga Volcanic Complex have been previously interpreted as variably welded ashflow tuffs (ignimbrites), mainly on the basis of their wide extent and low aspect ratio (Giles, 1977; Blissett, 1975; 1985; Branch, 1978). However, as pointed out by Allen et al. (2008), textural evidence in some of these units does not support such an origin and the lack of pyroclastic textures (shards, broken crystals, fiamme, lithic fragments) may not be simply the result of intense welding.

The aim of this chapter is to describe the Glyde Hill and Chitanilga Volcanic Complexes, focussing on field characteristics and microtextures that can give insight into the eruption and emplacement mechanisms, distinguishing between explosive and effusive processes, expecially for the contentious felsic units. These field, textural and petrographic data also provide the context for geochemical and petrological information presented in chapters 4, 5 and 6.

Rock unit descriptions are presented as “data sheets”, each including field and microscale description, chemical classification, distribution of the unit, and interpreted emplacement mechanism. Detailed logs are also presented for several units. Descriptions include mineral compositions and textures, groundmass/matrix components and textures, flow deformation structures at the meso- to micro-scale, and presence of lithic clasts, glass shards and broken crystals. Optical microscopy, scanning electron microscope back-scattered electron images (SEM-BSE) and energy dispersive spectroscopy (EDS) were used for the petrographic descriptions. Part of such information is useful in the interpretation of the eruption and emplacement mechanisms of the lower GRV and is discussed in this chapter. Parageneses and mineral textures are instrumental to the petrological discussion and magma evolution and will be discussed in the following

chapters.

Published names of units were introduced by Blissett (1975; 1977a; 1977b) and Giles (1977) and then used on the most recent maps produced by the Primary Industries and Resources of South Australia (PIRSA). These names were retained in this chapter, with some modifications justified on a compositional basis. Whereas previous nomenclature was based on silica content only (Blissett, 1975; Branch, 1978; Stewart, 1994), a comparison between total alkali and silica is used here, according to the official IUGS nomenclature for volcanic rocks (Le Bas et al., 1986), supported by trace element classification (Pearce, 1996).

3.2 Felsic lavas and pyroclastic deposits. Characteristics and key distinguishing features

Because of the different eruption and emplacement mechanisms, most lavas and pyroclastic flow deposits are readily distinguished on the basis of textures and geometry of the units. However, some extensive felsic units show features compatible with both lavas and rheoignimbrites (e.g. Snake River Plain, Bonnichsen and Kauffman, 1987; Trans-Pecos volcanic field, Henry et al., 1988), implying that pyroclastic rocks cannot be distinguished from lavas exclusively on the basis of geometrical characteristics.

3.2.1 Felsic lavas

Lavas are erupted during mostly effusive volcanic activity and are emplaced as coherent flows. The geometrical characteristics of a lava are controlled by several parameters, including intrinsic characteristics and “external” factors: initial viscosity of the lava, total volume extruded, rate of effusion, and slope of the underlying topography (Walker, 1973). Viscosity is considered the main control on aspect ratio (ratio between the diameter of the circle with equal area and the thickness of the lava), whereas effusion rate is the most important parameter in determining the length of a lava (Walker, 1973).

Typical aspect ratios for felsic lavas and domes are between 1 and 100 (Henry et al., 1988). Rhyolitic lavas are usually <1 km^3 in volume and <a few km in length (Walker, 1973, Clough et al., 1982), whereas large volumes (tens to thousands of km^3) of silicic magmas are typically erupted explosively and deposited as ignimbrites. Significantly larger rhyolite lavas are uncommon, but have been described in both recent and ancient successions (Rooiberg Felsite, Twist and French, 1983; Snake River Plain-Yellowstone, Bonnichsen and Kauffman, 1987; Keweenawan Midcontinent Rift plateau, Green and Fitz, 1993). Recognition of these extensive felsic units as lavas has been relatively recent, and until then large felsic units were assumed to have a pyroclastic origin.

Typical outcrop characteristics of lavas include flow bands and flow folds, elongate vesicles, autobreccia and vitrophyre (Henry et al., 1988). Autobreccia (monomictic, clast-supported and poorly sorted aggregate of blocky or irregular-shaped lava clasts) is a common by-product of lava flow in a subaerial environment (McPhie et al., 1993). It can occur at the top, at the bottom and at the front of the flow, causing a rough surface, typical of felsic lavas. Vitrophyre occurs as a chilled carapace around lavas and can be interlayered with microcrystalline horizons. At the micro-scale, the even distribution of phenocrysts throughout the unit, the lack/paucity of broken crystals, the alignment

of phenocrysts and vesicles and microcrystalline or glassy groundmass textures are considered as indicative of lava flows (Henry et al., 1988; Bonnichsen and Kauffman, 1987; Allen and McPhie, 2003). Felsic lavas commonly include vesicular-pumiceous domains above and below a poorly vesicular centre. The non-vesicular centre typically comprises combinations of spherulites, micropoikilitic texture and other crystalline groundmass textures, and glass (Fink and Manley, 1987).

3.2.2 Felsic pyroclastic flow deposits

Pyroclastic flows are produced during explosive eruptions and are composed of a high-concentration mixture of juvenile and lithic clasts (pyroclasts) dispersed in a continuous gas phase. Pyroclastic flow deposits predominantly comprise a poorly sorted mixture of juvenile and lithic blocks and lapilli supported in a crystal fragment-rich ash matrix. Ignimbrites are pyroclastic flow deposits dominated by pumice clasts in a matrix of bubble-wall shards and crystal fragments. As a general rule, pyroclastic flows are topographically controlled. The aspect ratio of ignimbrites is typically between 100 and 1000, but can be as high as 200 000 and the lateral extent can be in the order of the tens, or rarely hundreds, of km (Walker et al., 1980; Wilson et al., 1995). Such variable geometrical characteristics are attributed to the eruption column height, the erupted volume and the magma discharge rate, since a high dispersal of the deposits is favoured by the collapse of a high column and by a high discharge rate (Walker, 1983). Pyroclastic flow deposits can be up to several thousands of km^3 in volume (Branney and Kokelaar, 2003). Although mostly massive, pyroclastic flow deposits can show sharp to diffuse stratification, cross-stratification and grading (Branney and Kokelaar, 2003). They may be loose and uncompacted, or partly to entirely welded and indurated (Branney and Kokelaar, 2003). Hot welding compaction can also result in a bedding-parallel texture (eutaxitic texture) defined by variably compacted, elongate, aligned pumice clasts (fiamme). Other typical outcrop-scale and micro-scale textural characteristics of pyroclastic flow deposits include elutriation pipes and abundant broken crystals, lithic fragments and glass shards (Henry and Wolff, 1992; McPhie et al., 1993).

Low-grade versus high- and extremely high-grade ignimbrite

Ignimbrites display variable degrees of welding (coalescence of juvenile components) and welding compaction, depending on the viscosity of the juvenile components, the thickness of the deposit, and the ratio between juvenile and non-juvenile components. A complete spectrum exists between low-grade, non-welded and high-grade, welded ignimbrites (Wright et al., 1980; Wolff and Wright, 1981; Walker, 1983). Low- to moderate-grade ignimbrites show non-welded or partially welded zones and tend to preserve textural evidence of particulate eruption and emplacement mechanism.

High- and extremely high-grade ignimbrites are mostly to completely welded and compacted. Welding and compaction are favoured by low viscosity of the juvenile components, in turn promoted by high temperature, high alkali and high dissolved volatile content. High- and extremely high-grade ignimbrites record a transition from particulate to non-particulate (lava-like) flowage (rhemorphism) (e.g. Bonnichsen and Krauffman, 1987; Branney et al., 1992). If such intense welding and coalescence start during deposition (Branney and Kokelaar, 1992; Branney et al., 1992) and the long-distance transport is dominated by non-particulate flow, then textures of the resulting units will

reflect the latter mode of transport and evidence of a pyroclastic origin will be obscured. As a result of viscous deformation, textures in lava-like ignimbrites can mimic textures of lavas, including flow-folded flow bands, aligned vesicles and breccia zones (Henry and Wolff, 1992; Branney et al., 2004; Andrews et al., 2008).

3.2.3 Key distinguishing features between lava-like ignimbrites and true lavas

A combination of field and textural characteristics can be used to distinguish high- and extremely high-grade felsic ignimbrites from lavas. Units emplaced as lavas have been distinguished based on the presence of steep unit margins, abundant basal and marginal autobreccias, and pervasive steep flow bands, combined with the absence of lithic and pumice fragments, whereas pyroclastic flow deposits may show local preservation of clastic texture, abundant broken phenocrysts, internal subhorizontal ash-emplacement layering, and subparallel flow marks (Henry and Wolff, 1992; Branney and Kokelaar, 2003; Branney et al., 2008). Geometrical characteristics of the units, such as thinning at the edges and infilling of the underlying topography, are also diagnostic for pyroclastic flow deposits (e.g. Henry et al., 1988). Branney et al. (1992) proposed an pyroclastic origin for the Bad Step Tuff, England, based on the evidence of gradation between unambiguous vitriclastic matrix at the base of the unit to a flow-laminated, non-vitriclastic matrix in the centre of the unit.

In the lower GRV, the original geometry of the units cannot be observed due to incomplete preservation and to the discontinuous outcrop, and cannot be used to discern the emplacement mechanisms. Meso-scale and micro-scale textures give the most information and were used in this chapter.

3.3 Glyde Hill Volcanic Complex, Lake Everard

Figure 3.1 shows a schematic stratigraphic log and the total alkali versus silica (TAS) chemical classification (Le Bas et al., 1986) for the Glyde Hill Volcanic Complex, Lake Everard. Rhyolite, dacite and trachyte are the most represented compositions. Because alteration can cause remobilisation of some elements (alkalis in particular), a proxy for the TAS diagram using immobile elements is also presented (Zr/Ti versus Nb/Y, Winchester and Floyd, 1977; Floyd and Winchester, 1978; fields modified by Pearce, 1996). In both diagrams, the compositions plot in the high end of the subalkaline field or straddle the line between the subalkaline and alkaline fields. Based on these diagrams, and on an overall good agreement of major elements in whole-rock and melt inclusion analyses (cf. chapter 4), the use of the TAS diagrams appears justified as a classification tool.

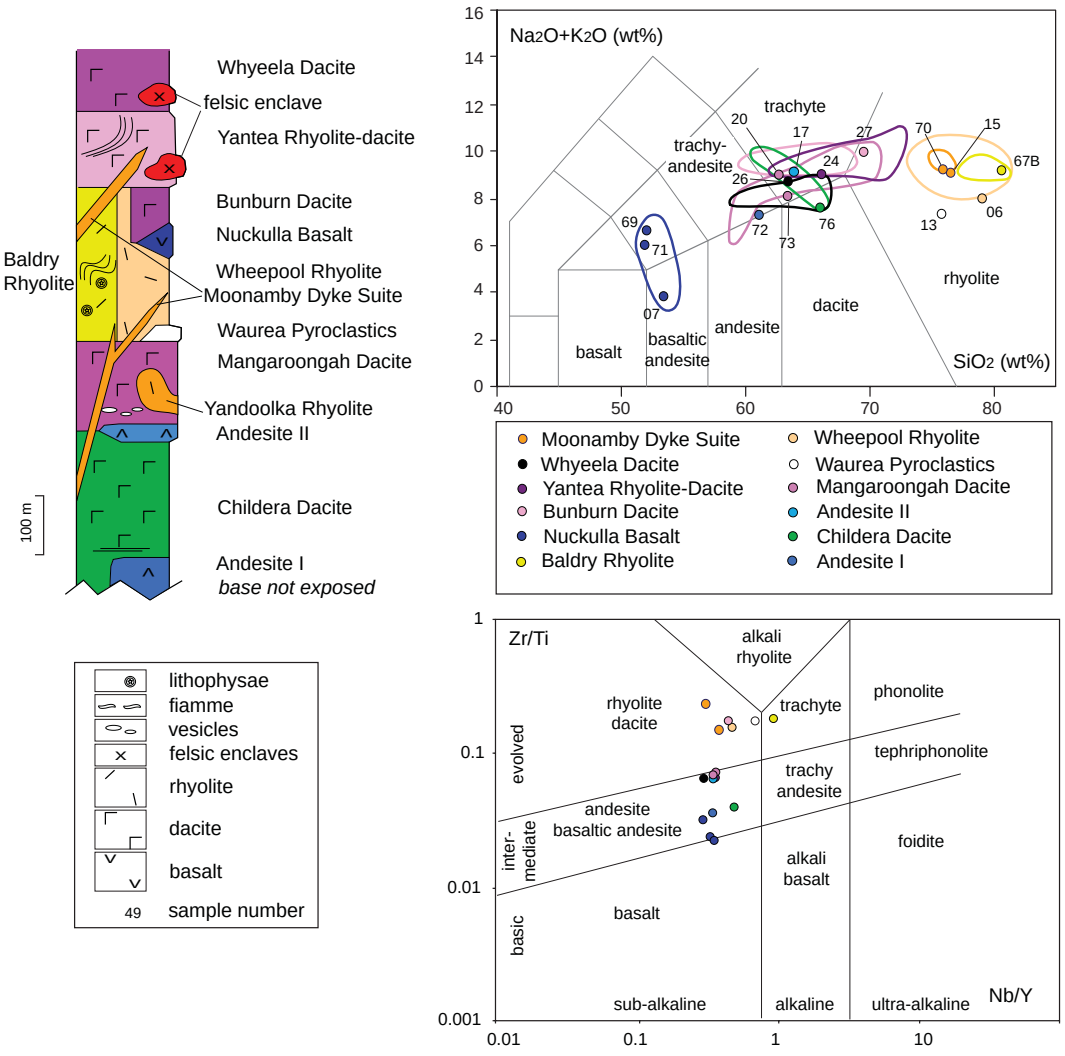

Fig. 3.1. Simplified log and rock classification plots for the Glyde Hill Volcanic Complex, Lake Everard. Total alkali versus silica (TAS) plot from LeBas et al. (1986) and Zr/Ti versus Nb/Y plot from Winchester and Floyd (1977), fields modified by Pearce (1996). Data recalculated to 100% anhydrous. Literature data (lines, same colour as spot symbols) are also shown for comparison (data from PIRSA, 2006; Stewart, 1994).

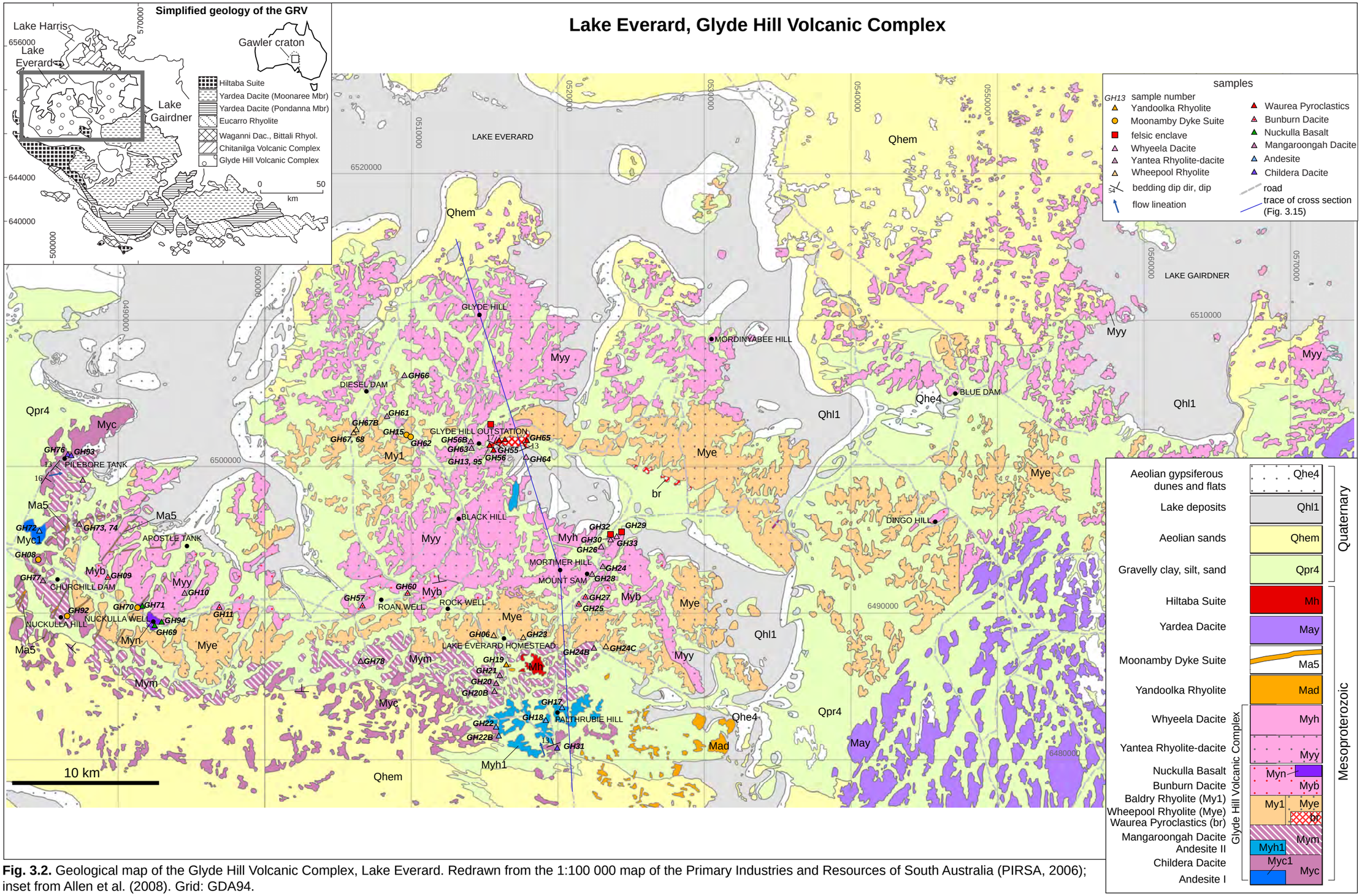

Fig. 3.2. Geological map of the Glyde Hill Volcanic Complex, Lake Everard. Redrawn from the 1:100 000 map of the Primary Industries and Resources of South Australia (PIRSA, 2006); inset from Allen et al. (2008). Grid: GDA94.

Glyde Hill Volcanic Complex, Lake Everard - Data sheets

CHILDERA DACITE (Childera Dacite of Giles, 1977) and ANDESITE I

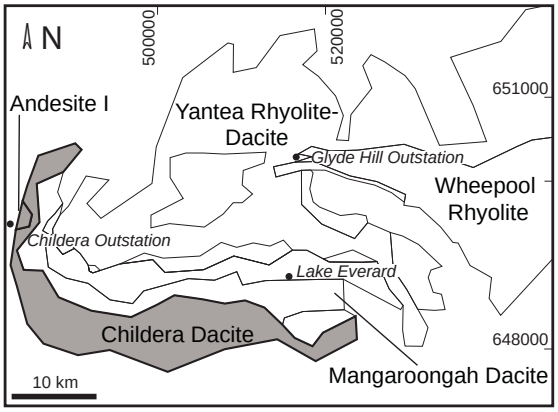

CHILDERA DACITE

Field description

The unit includes purple to purplish-brown, weathered to brick-red, porphyritic rocks. Scattered cream feldspar phenocrysts (<1 vol.%, 2-3 mm), a minor prismatic ferromagnesian phase and very minor quartz are set in an aphanitic groundmass. The rock is mostly massive, but locally (1.5 km southwest of Pilebore tank, GR 0485508-6499533) shows a cm-spaced planar foliation dipping to the southeast at a gentle angle (dip direction 130-146, dip 13-16). A lineation, plunging east-northeast at a gentle angle, is contained on this plane (Fig. 3.3 A). Next to Pilebore tank (GR 0486368-6500557) the Childera Dacite is massive and sparsely feldspar-phyric. Locally, round textures with a dark core and a fine grained brick-red rim, <1 cm across, slightly flattened are present (spherulites?). South of Lake Everard Homestead (GR 0520217-6481443), columnar joints form hexagonal prisms, ~30 cm wide, steeply plunging to the southeast (Fig. 3.3 B). Clast-supported breccia intercalated between massive dacite was observed south of Pilebore tank (GR 0485516-6499641). It includes subangular cm-scale clasts of a dark feldspar-phyric rock in a sand-sized matrix.

Petrographic description (samples 76, 93)

K-feldspar-phyric dacite lava

K-feldspar (perthite) phenocrysts are subhedral to anhedral and angular-shaped. The microcrystalline groundmass (grainsize ≤tens of µm) is mainly composed of K-feldspar, albite and minor quartz. Magnetite, apatite and titanite are present as accessory minerals. Locally, round to irregular textures, <1 cm across, slightly elongate and aligned, are present (spherulites?). They show a brick-red semi-opaque rim composed of fine grained K-feldspar, albite, quartz, titanite, apatite, magnetite (Fig. 3.3 C). The groundmass between globules is darker, green-brown, and is enriched in opaque minerals in comparison with the globule rims. Very fine grained titanite (leucoxene) occurs in the groundmass.

ANDESITE I

Field description

Blissett (1975) reported the occurrence of “Basalt and Andesite” northeast of Childera Outstation. These rocks are green-grey, massive and sparsely porphyritic (Fig. 3.4 A) with scattered phenocrysts (<1 vol.%) of feldspar and pyroxene in an aphanitic groundmass.

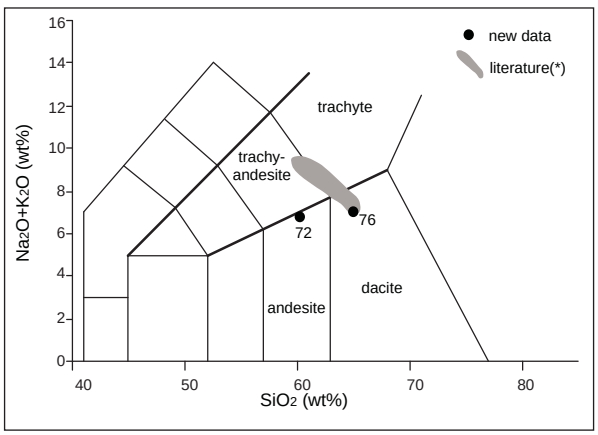

(*) Chemical compositions from PIRSA Dataset (2006) and Stewart (1994).

Petrographic description (sample GH72)

Plagioclase- and clinopyroxene-phyric andesite lava

Phenocrysts of plagioclase and clinopyroxene are set in a fine-grained groundmass (≤20 µm), mainly composed of plagioclase, quartz and Ca-pyroxene. Magnetite, apatite, a REE-F-phase, and ±titanite occur as accessories. Plagioclase (Ca-andesine) forms euhedral unzoned phenocrysts and small (<50 µm) elongate crystals in the groundmass, strongly altered to sericite and fine grained chlorite. Strongly to completely uralitised

Fig. 3.3 Childera Dacite. A- Lineation on cm-spaced sheet-joint surface (Grid Reference GDA94 0485508-6499533). B- Columnar joints (GR 0520217-6481443). C- Perthitic K-feldspar in a microcrystalline, K-feldspar+albite+magnetite groundmass (sample GH93, plane polarised transmitted light, GR 0486689-6500667).

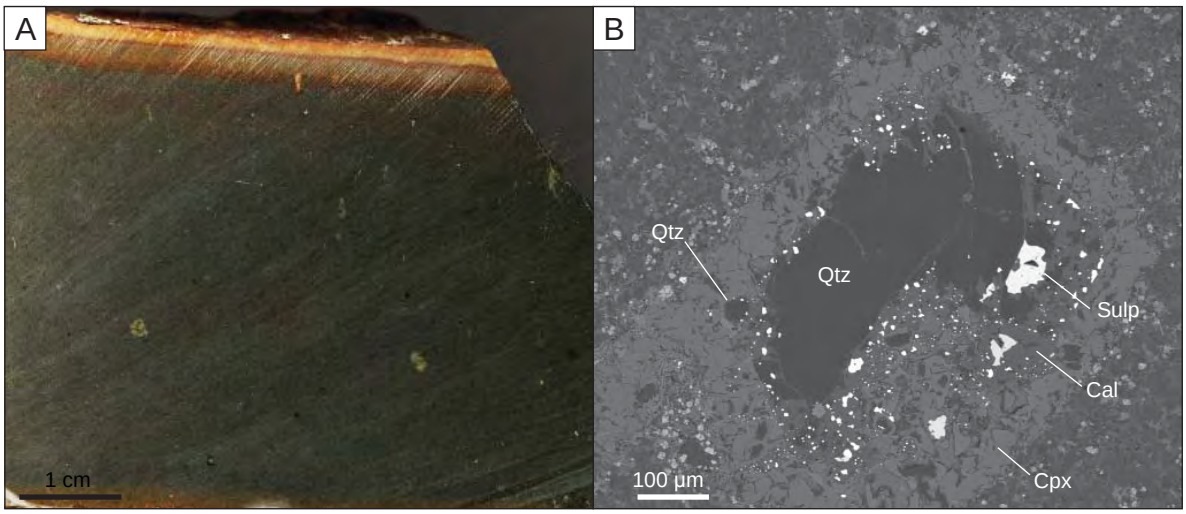

Fig. 3.4 Andesite I. A- Sparsely porphyritic, massive Andesite I (sample GH72). B- Calcite+Ca-pyroxene+opaques-rimmed xenocrystic quartz (sample GH72, BSE). Grid reference (GDA94): 0484559-6495596.

Ca-pyroxene forms prismatic phenocrysts (≤2 mm) and fine grained intergranular crystals in the groundmass. Magnetite and apatite occur as eihedral to subhedral crystals (10-20 µm and <5 µm, respectively) in the groundmass. Aggregates of very fine grained titanite are intergranular between plagioclase in the groundmass. Anhedral quartz grains, a few mm across and showing wavy extinction are locally present (Fig. 3.4 B). These quartz grains are surrounded by a rim (corona) of clinopyroxene, calcite and opaques (Cu-Fe±Zn sulphides).

MANGAROONGAH DACITE (Mangaroongah Dacite of Giles, 1977) and ANDESITE II

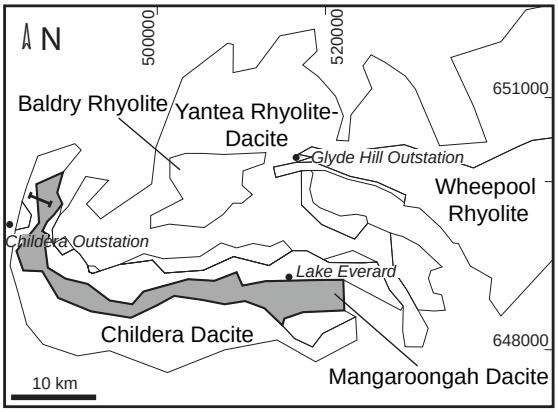

Field description

Rocks In the Mangaroongah Dacite are characterised by a rather homogeneous appearance across the outcrop areas: purplish-red or brown, feldspar- and pyroxene-phyric (~5-10 vol.%) with an aphanitic groundmass. Despite a similar composition, the Mangaroongah Dacite can be distinguished from the underlying Childera Dacite on the basis of the higher abundance of phenocrysts. About 5 km south of Pilebore Dam (GR 0487394-6496160), approximately halfway between the base and the top of the unit, the Mangaroongah Dacite is brecciated into angular clasts, ≤tens of cm across, showing jigsaw-fit texture, surrounded by a dark green or black, fine grained groundmass. The clasts are porphyritic and contain elongate and aligned amygdales, ≤a few cm in size. Levels of amygdaloidal autobreccia, with angular to lobate and flow-banded clasts embedded in a massive, porphyritic and amygdaloidal matrix can be also seen 2 km northwest of Nuckulla Hill (GR 0486138-6490540) and south of Lake Everard Homestead (GR 0515440-6484867) (Fig. 3.5 A). About 1 km west of Pilebore tank, above the contact with the underlying Childera Dacite (GR 0486261-6500298), the Mangaroongah Dacite is vesicular, almost continuously, for approximately 20 m, and the base of the vesicular portion is brecciated: angular and partly flattened fragments, ≤tens of cm across, are embedded in a porphyritic groundmass. Amygdales are round to flattened, up to 3 cm in diameter, filled with quartz and a fine grained chlorite. At the base of the exposed sequence, the amygdales form 5-10 vol.% of the rock and their abundance decreases upwards. Above the amygdaloidal brecciated base, the unit is massive and evenly porphyritic, scattered phenocrysts of feldspar are embedded in an aphyric groundmass. The massive portion of the rock is homogeneous for tens of metres, but is interrupted by thin layers (several cm to tens of cm thick) of breccia composed of mm- to cm-scale angular clasts in a sand-sized matrix.

Petrographic description (Samples GH20, 74, 77, 73)

Plagioclase ±Ca-pyroxene-phyric dacite-andesite lava

Phenocrysts of plagioclase and Ca-pyroxene are embedded in a microcrystalline (<50 μm) groundmass, mainly composed of K-feldspar, tablets of albite, Fe-Ti oxide, apatite, Ti oxide, and very minor quartz. Plagioclase (albite) forms euhedral to anhedral phenocrysts, in some cases grouped in glomerocrysts. The largest crystals (>0.5 mm) are mostly anhedral, sieve-textured (Fig. 3.5 B) and altered to sericite ±epidote, whereas the smaller ones are generally euhedral. Phenocrysts of Ca-pyroxene are anhedral, up to several mm across, and commonly altered to chlorite and only locally preserved (e.g. sample GH77, Fig. 3.5 C). Pyroxene includes Fe-Ti oxide and apatite. In the groundmass, very fine grained (few μm to tens μm across) Fe-Ti±Mn oxides, apatite, and Ti oxide are common in all the samples (Fig. 3.5 D), often occurring in irregular-shaped aggregates. F-apatite forms small euhedral prisms, tens of μm long, and occurs disseminated in the groundmass or included in the phenocrysts and oxides. Fe-Ti oxide occurs as anhedral crystals, ~10 μm to 0.5 mm in size, showing unmixing lamellae (Fig. 3.5 E). Quartz is present in amygdaloidal samples (sample GH74) and occupies an interstitial position in the groundmass or occurs as small aggregates, <0.1 mm in diameter, of fine grained crystals. The amygdales are elongate (up to 5 mm) and aligned (sample GH74). Amygdales include concentrically distributed quartz, chlorite ±Fe oxide ±baryte.

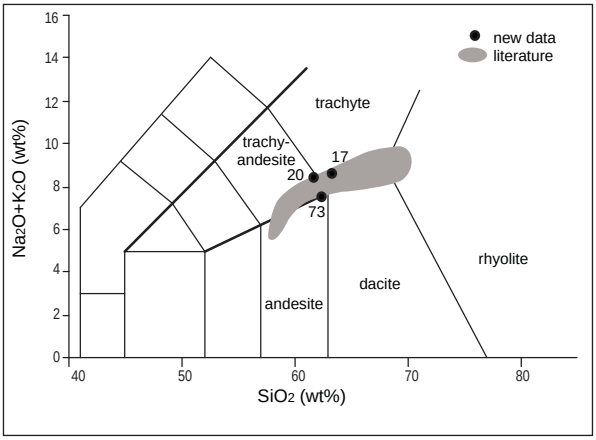

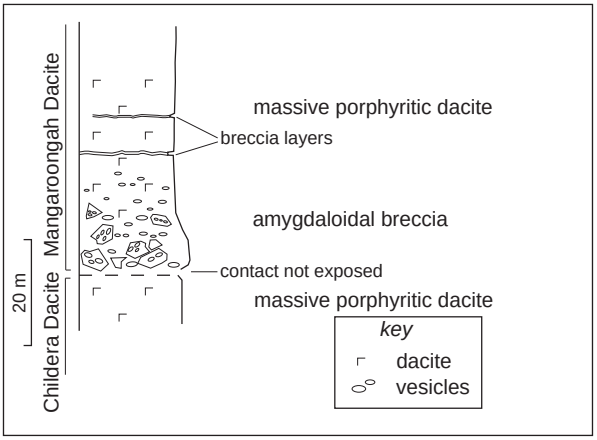

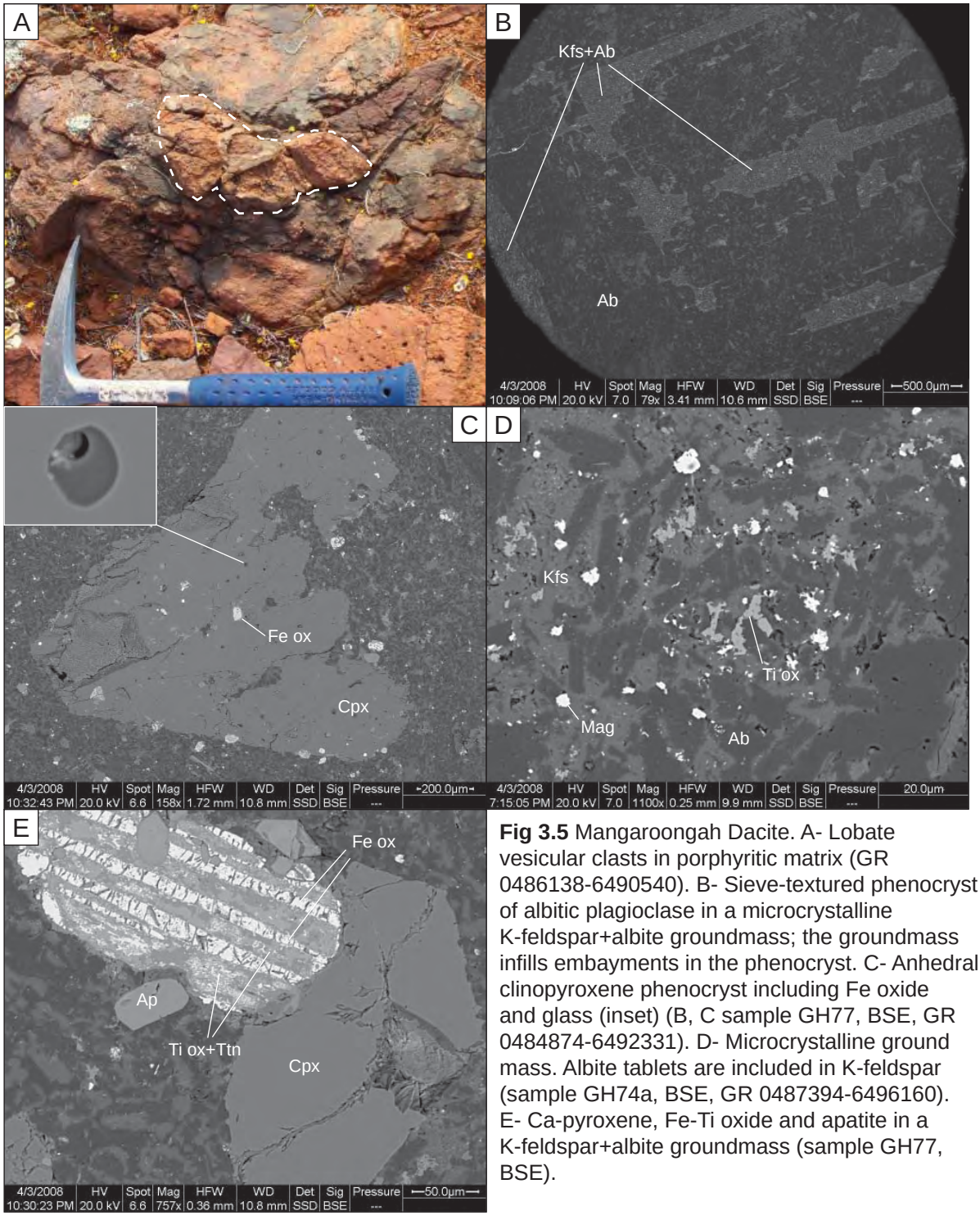

Fig 3.5 Mangaroongah Dacite. A- Lobate vesicular clasts in porphyritic matrix (GR 0486138-6490540). B- Sieve-textured phenocryst of albitic plagioclase in a microcrystalline K-feldspar+albite groundmass; the groundmass infills embayments in the phenocryst. C- Anhedral clinopyroxene phenocryst including Fe oxide and glass (inset) (B, C sample GH77, BSE, GR 0484874-6492331). D- Microcrystalline ground mass. Albite tablets are included in K-feldspar (sample GH74a, BSE, GR 0487394-6496160). E- Ca-pyroxene, Fe-Ti oxide and apatite in a K-feldspar+albite groundmass (sample GH77, BSE).

ANDESITE II

Petrographic description (sample GH17)

Clinopyroxene- and plagioclase-phyric andesite lava

Plagioclase and clinopyroxene phenocrysts, ≤a few mm, are set in a microcrystalline, locally micropoikilitic, groundmass, composed of quartz, K-feldspar, plagioclase, opaque minerals and apatite. Plagioclase (Ca-oligoclase) forms euhedral to anhedral unzoned and sericite-altered phenocrysts, commonly 0.3 to 1 mm in size and in some cases up to 2 mm. The larger plagioclase crystals show the most anhedral habit and are sieve-textured (cavities filled with the groundmass). Plagioclase also occurs as small (<0.1 mm) elongate crystals in the groundmass, together with K-feldspar. Clinopyroxene forms subhedral polysynthetically-twinned crystals (colourless, c^γ≈50°, δ=0.009-0.010). Quartz is present in the groundmass as interstitial to poikilitic crystals.

WHEEPOOL RHYOLITE (Wheepool Rhyolite of Blissett, 1975; 1977a; Arburee Rhyolite of Giles, 1977)

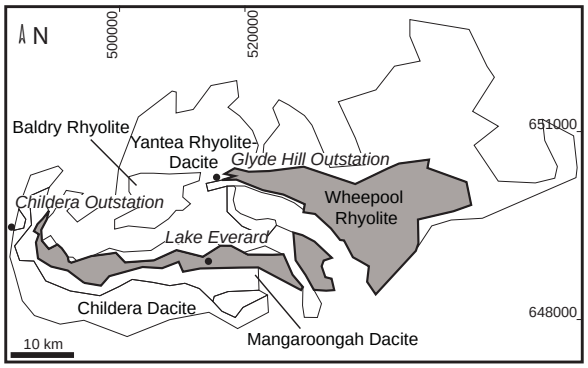

Field description

The Wheepool Rhyolite includes purple or purplish red, weathered to yellow-brown, porphyritic rocks. Phenocrysts (~10 vol.%) of euhedral to subhedral feldspar and minor anhedral quartz are embedded in a fine grained groundmass (Fig. 3.6 A). The rock can be massive or banded at the mm- to cm-scale. The banding is defined by alternating dark (purple) and pale (reddish or cream) discontinuous and lens-shaped to wispy layers: no orientation of phenocrysts is evident. About 10 km east of Lake Everard Homestead, near Roan Well, the Wheepool Rhyolite shows a mm- to cm-scale orientation defined by fiamme, locally wrapping around phenocrysts. The unit also includes brecciated domains: about 1 km west of Lake Everard Homestead the rock is flow banded and fragments of a feldspar- and quartz-phyric rock are incorporated into the base of the unit. The fragments are angular to sub-angular, have variable size (≤a few m) and are commonly flow banded. Brecciated rocks also crop out for several metres about 2 km northeast of Nuckulla Hill, where sub-angular to angular fragments, several cm across, composed of a brick-red, feldspar- and quartz-phyric rock, are embedded in a darker, porphyritic flow-banded matrix. The matrix can be distinguished from the clasts on the basis of a lesser amount of phenocrysts. The flow bands are defined by intercalated brick-red, phenocryst-rich layers (Fig. 3.6 B).

Petrographic description (samples GH06, 23, 59)

Two-feldspar- and quartz-phyric rhyolite lava

The phenocryst assemblage includes plagioclase (albite), K-feldspar (perthite, Fig. 3.6 C) and minor quartz, up to 4 mm in size. Plagioclase occurs as anhedral and locally fractured phenocrysts and small (< 50 µm), anhedral to tabular-shaped crystals in the groundmass. K-feldspar forms anhedral phenocrysts, up to a few mm across. Phenocrysts of quartz are anhedral, round and embayed, up to 1 mm and locally 2-3 mm in diameter. The groundmass is microcrystalline (grain size <10 to 50 µm) and mainly composed of quartz, K-feldspar and plagioclase (albite). In massive samples (sample GH06), micropoikilitic quartz includes euhedral tablets of albite. Quartz also forms wispy microgranular aggregates <1 mm long (Fig. 3.6 D) which probably represent the product of crystallisation of a mm-scale perlitic groundmass. In samples showing an banded texture (sample GH59), the mm-scale bands are defined by K-feldspar+albite lens-shaped domains (fiamme at the hand specimen scale) alternating with K-feldspar+quartz±albite domains. Accessory phases include F-apatite (euhedral elongate prisms, ≤200 µm), zircon (mostly euhedral, includes apatite), and Nb-bearing Ti oxide. Irregular aggregates, up to a few mm in size, include F-bearing apatite, zircon, Nb-Ti-oxide, Fe-Ti oxide, monazite and chlorite (Fig. 3.6 E).

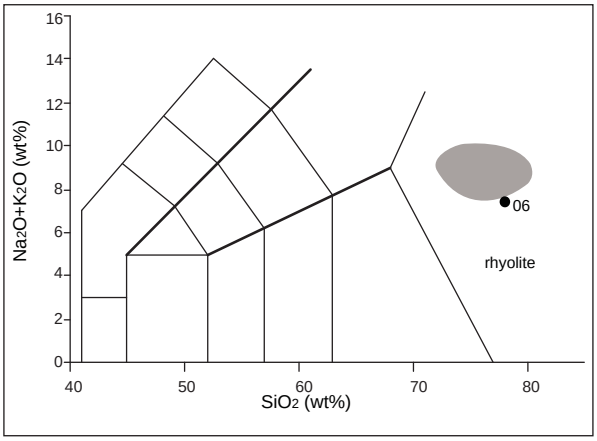

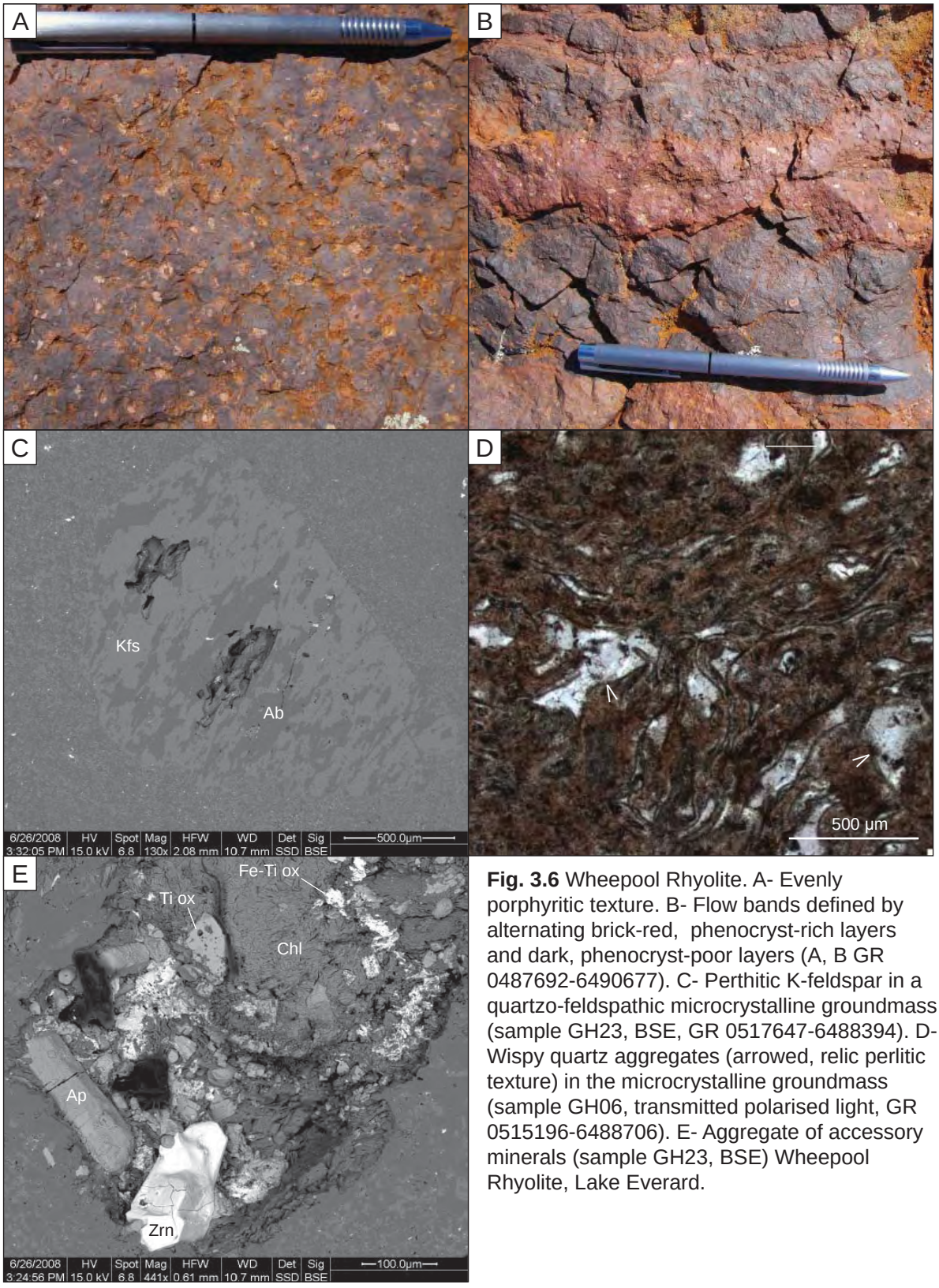

Fig. 3.6 Wheepool Rhyolite. A- Evenly porphyritic texture. B- Flow bands defined by alternating brick-red, phenocryst-rich layers and dark, phenocryst-poor layers (A, B GR 0487692-6490677). C- Perthitic K-feldspar in a quartzo-feldspathic microcrystalline groundmass (sample GH23, BSE, GR 0517647-6488394). D- Wispy quartz aggregates (arrowed, relic perlitic texture) in the microcrystalline groundmass (sample GH06, transmitted polarised light, GR 0515196-6488706). E- Aggregate of accessory minerals (sample GH23, BSE) Wheepool Rhyolite, Lake Everard.

WAUREA PYROCLASTICS (Waurea Pyroclastics by Giles, 1977 and included in the Wheepool Rhyolite by Blissett, 1977a; 1985)

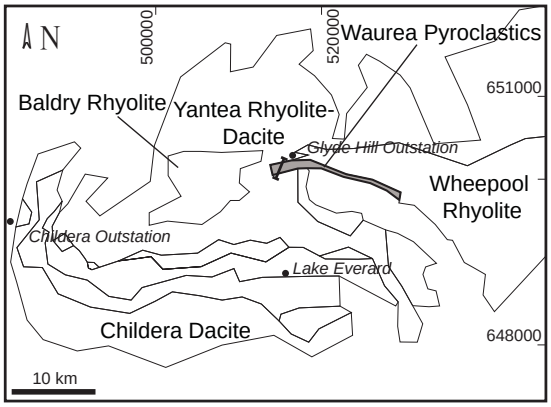

Field description

The rocks mapped as Waurea Pyroclastics by Giles (1977) consist of volcanic breccia in sparse outcrops east of Glyde Hill Outstation (GR 0514624-650153) along the shores of a salt lake. They include several different facies, bedded or massive, with variable clast size, composition and texture. The breccia can be matrix- or clast-supported and the grain size can vary significantly, ranging up to several tens of cm. The clasts include porphyritic (feldspar ± quartz phenocrysts in a brick-red fine grained matrix), finely banded (sub-mm scale contorted banding) or aphanitic massive lithologies. Overall, the colour is reddish-purple, brownish-yellow or pale grey-white; other variations in colour are due to local alteration where the rock is crosscut by fractures. The contacts between different facies were observed only in a few cases and the geometry and lateral continuity cannot be easily ascertained. Bedding is generally north-northeast- to north-dipping at a gentle angle (≤20°) in the westernmost outcrops (~1 km east of Glyde Hill Outstation) and north- to north-northwest-dipping 2 km farther east. The Waurea Pyroclastics are partly concealed under the deposits of the salt lake. Along a soutwest to northeast traverse in the westernmost part of the outcropping area, the sequence is as follows (Fig. 3.7):

1-*Yellow, centimetre-scale bedded sandstone*. Well sorted, clearly stratified deposit (Fig. 5.8 A). Bedding is defined by alternating layers of different grain size or cementation degree. A relatively coarse grained interval occurs within scours in the underlying intervals. The top and base contacts do not crop out, and cannot be precisely indicated. The thickness in outcrop is 5-10 m.

2-*Violet to pale grey, matrix-supported breccia*. The deposit is relatively poorly sorted and contains round to angular quartz grains and crystal fragments, up to a few mm across. Lithic fragments, angular and up to several cm across, are mostly fine grained, and locally thinly banded (Fig. 3.8 B, C). The rock is generally massive, but locally a weak orientation is defined by elongate lens-shaped fragments (fiamme), a few mm long. The matrix is fine grained and volumetrically predominant (>80 vol.%, mainly composed of devitrified coarse ash glass shards). The base is not exposed. The thickness in outcrop is 2-3 m. Facies 1 and 2 are separated by a 1 m-wide cataclastic zone.

3-*Coarse grained polymictic clast-supported breccia*. The breccia is poorly sorted, massive to diffusely stratified, mainly clast-supported and locally shows inverse grading (coarsening upwards). The clasts are up to tens of cm in size. Three types of clasts can be distinguished:

- thinly bedded siltstone;
- brick-red porphyritic rock with feldspar phenocrysts in a fine grained groundmass;

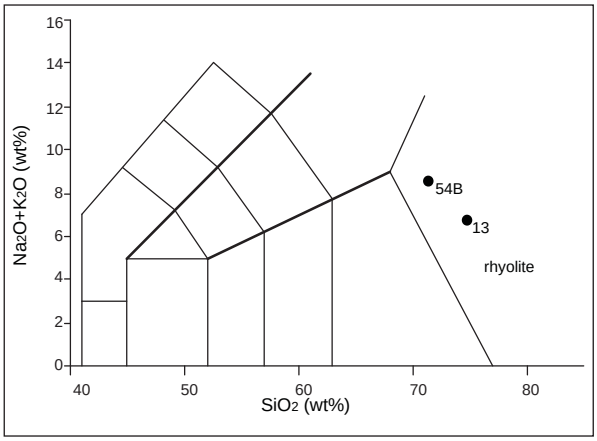

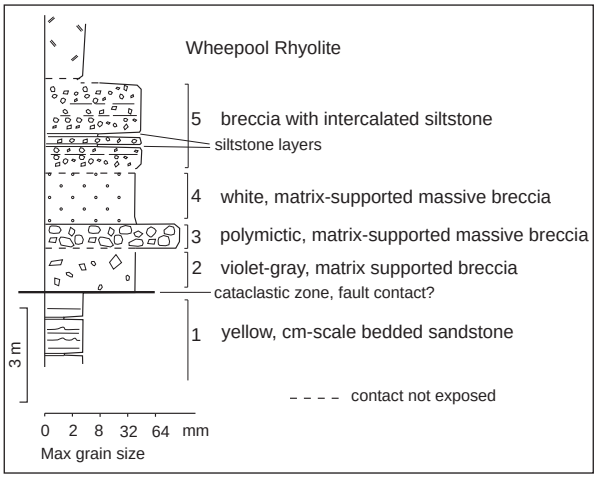

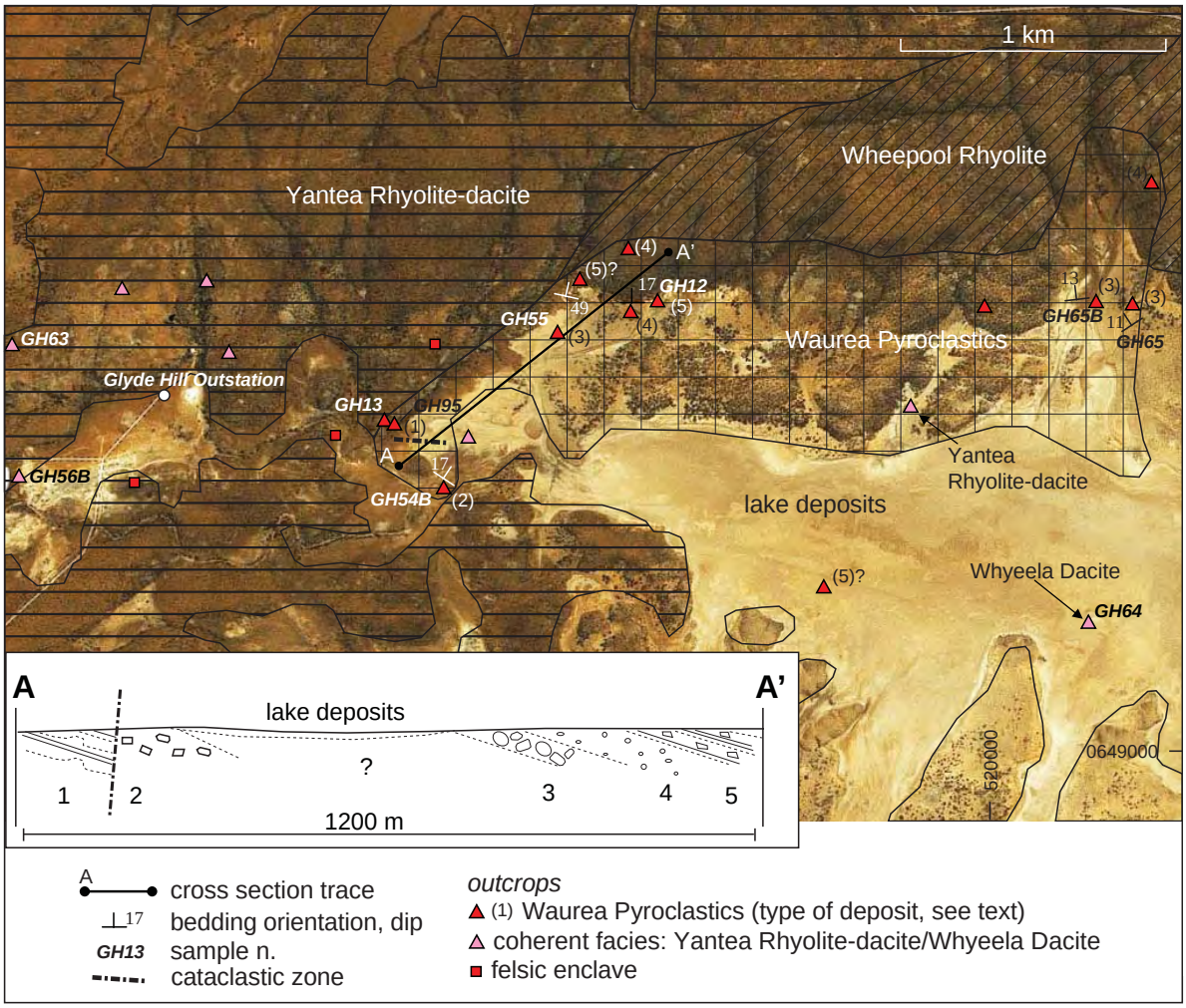

Fig 3.7 The Waurea Pyroclastics east of Glyde Hill Outstation. The reconstruction of the cross section is limited by the discontinuous outcrop conditions and by the presence of a cataclastic zone (fault?). Boundaries between lithologies modified after the Primary Industries and Resources of South Australia 1:100 000 geological map, sheet 5935 (PIRSA, 2006). Grid: GDA94.

– green-grey, massive and aphanitic rock.

The clasts are mainly low-sphericity, angular to sub-angular (Fig. 3.8 D). The matrix of the breccia is green-grey and composed of lithic fragments (grain size ≤a few mm). The outcropping portion of the deposit is several metres thick. A breccia showing the same texture (polymictic, coarse-grained, massive, clast-supported) crops out a few km further east (GR 0517988-6501855, Fig. 3.7), but with a predominance of brick-red porphyritic clasts. The porphyritic clasts are similar in internal texture and mineral composition to the Yantea Rhyolite-dacite.

4-*White, matrix-supported, massive breccia*. This poorly sorted breccia consists of subrounded clasts a few cm in diameter, in a white, sand-sized matrix (Fig. 3.8 E). Minor spherical and round boulders, up to tens of cm in size, are locally present. The clasts consist of fine grained banded or massive porphyritic rocks.

5-*Very thinly bedded breccia with intercalated siltstone.* Angular, low sphericity lithic fragments up to a few centimetres across occur in a sandstone matrix. The breccia is very thinly bedded and intercalated with finer grained layers, up to a few cm thick. These layers are internally massive and show planar contacts (Fig. 3.8 F). In the easternmost part of the outcropping area, this facies conformably overlies the coarse grained breccia (facies 3). The contact with the coarse grained breccia is sharp as the lithology changes in a few tens of centimetres.

WAUREA PYROCLASTICS (cont.)

Petrographic description (sample GH13)

Rhyolitic ignimbrite with quartz and feldspar crystals and lithic fragments (vitric ash tuff)

The massive quartz-bearing facies (facies 2) consists of crystals and crystal fragments of quartz, K-feldspar and minor plagioclase (albite) and lithic fragments embedded in a fine grained (grain size ≤0.3 mm), vitriclastic matrix (Fig. 3.8 C). An orientation, locally visible on the specimen, is defined by few elongate fragments, fiamme and the distribution of a very fine grained opaque mineral (Fe oxide). Fiamme are lens-shaped, up to 1 mm thick and composed of a microgranular aggregate of quartz, strongly altered K-feldspar and an opaque mineral (Fe oxide). Quartz occurs as anhedral, round crystals or angular fragments, up to 1-2 mm in diameter, either as separate grains or included in lithic fragments (Fig. 3.8 C). Transmitted light and CL observations of quartz phenocrysts indicate a high degree of fragmentation. CL in particular reveals that angular grain margins truncate internal concentric growth surfaces. K-feldspar (microperthite) crystals are subhedral to anhedral, up to 1 mm across. Plagioclase (albite) is subhedral, and <1 mm long. Two types of lithic fragments were observed. Angular lithic fragments, ≤3-4 mm across, are composed of a µm-scale banded fine grained rock (Fig. 3.8 C). Lithic fragments of the second type are composed of very fine grained K-feldspar, quartz and minor Fe oxide (aggregates of very fine ash?). Most of the matrix is formed by platy or cuspate glass shards, ≤300 µm long, with vesicle walls partially preserved and generally undeformed. They are completely crystallised and consist of a fine grained quartz core and a K-feldspar rim (Fig. 3.8 C inset). Ti oxide occurs as small euhedral to anhedral crystals in the matrix. Zircon and apatite complete the accessory assemblage.

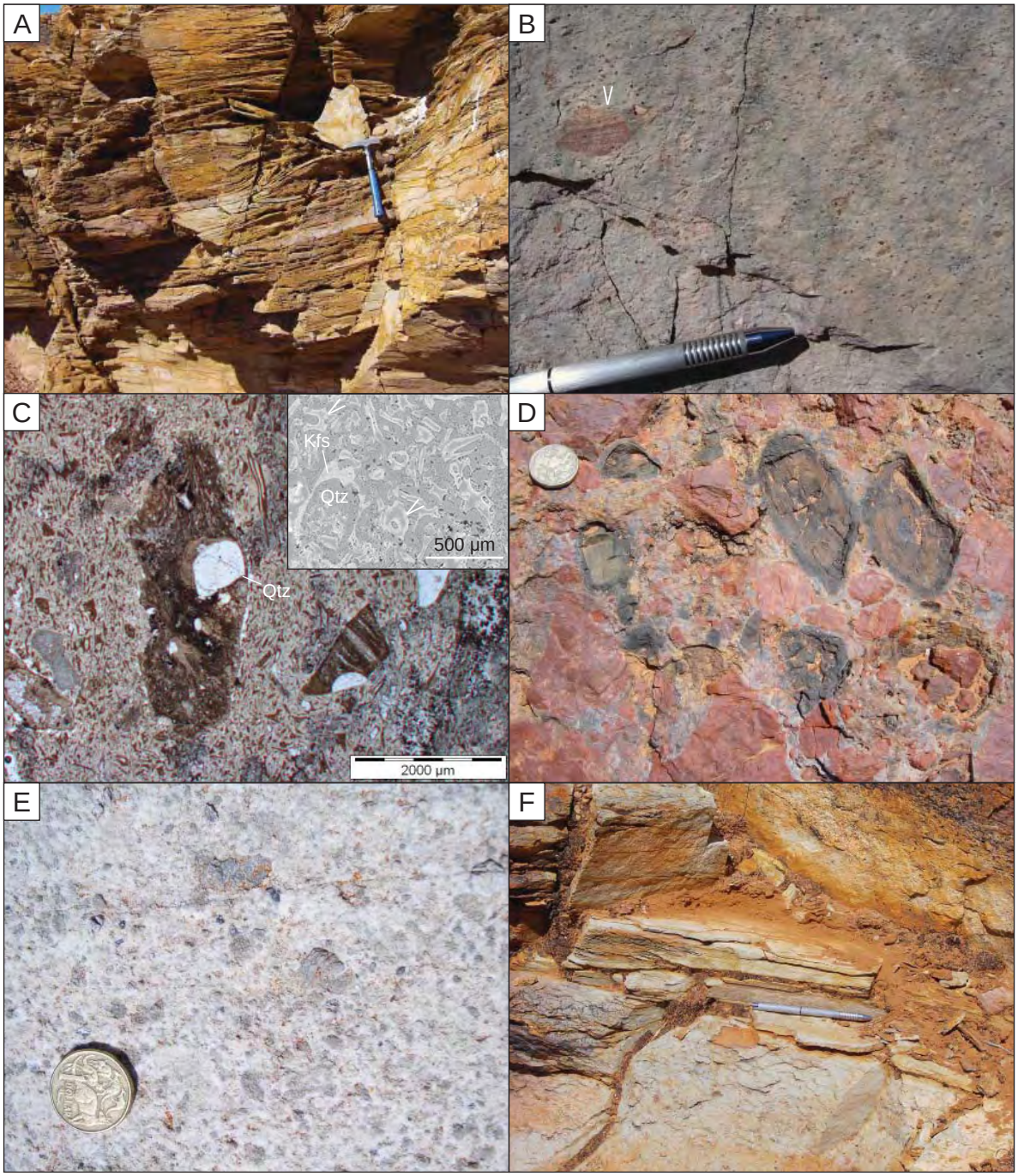

Fig 3.8 Waurea Pyroclastics east of Glyde Hill Outstation. A- Centimeter-scale banded sandstone (facies 1, GR 0515607-6501226). The scour (above the hammer) is filled with slightly coarser sediment. B, C- Matrix-supported massive breccia (facies 2, lithic fragment arrowed, GR 0515415-6501451). C- Quartz-phyric angular clasts in a vitriclastic matrix composed of bubble-wall shards (inset, vesicles arrowed, GR 0515415-6501451). D- Coarse polymctic breccia (facies 3, GR 0517867-6501874). E- Millimetre- to cm-scale clasts in a fine grained matrix (facies 4, GR 0516347-6501868). F- Siltstone intercalation (centre of photo) between breccia layers (facies 5, GR 0517988-6501855).

BALDRY RHYOLITE (Baldry Rhyolite of Giles, 1977)

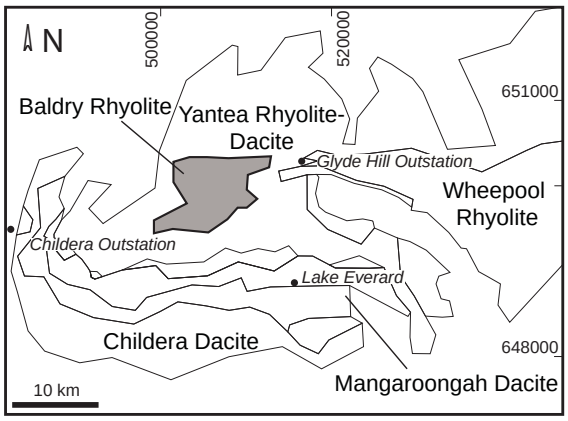

Field description

The Baldry Rhyolite outcrops in the area of Diesel Dam, underlying the Yantea Rhyolite-dacite. It includes pink, porphyritic rocks: scattered phenocrysts of K-feldspar and quartz embedded in a fine grained groundmass. Flow bands, folded in cm- to tens of cm-scale folds, are widespread throughout the unit and show a variable spacing. Domains of closely spaced bands alternate with relatively massive domains, several mm to a few cm thick (Fig. 3.9 A). An elongation lineation on these surfaces, indicating the direction of shear (flow), lies parallel to the fold hinge line. In outcrops cutting perpendicular to the direction of flow the bands describe circular to elongate structures (“eye” structures), representing intersected culminations of hinge lines in non cylindrical folds (sheath folds, Fig. 3.9 B). In the upper part of the unit, the rhyolite is non-foliated and vesicular (Fig. 3.9 C). Vesicles are round and <1 cm in diameter. Locally, the rock has a brecciated texture: cm-scale jigsaw-fit angular fragments are cemented by quartz- and fluorite-bearing veinlets. The clasts are finely banded (less 1 mm to several mm). Bands are defined by alternating white and pink layers. The unit contains abundant lithophysae, ≤tens of cm in diameter, mostly round and statically overgrowing the flow bands (Fig. 3.9 D), although flow-deformed lithophysae were described by Ferris (2003).

Petrographic description (samples GH67, 67B, 68)

K-feldspar- and quartz-phyric lithophysal rhyolite lava

The Baldry Rhyolite includes leucocratic porphyritic, lithophysal rhyolite. Minor amounts (<1 vol.%) of phenocrystic K-feldspar and quartz, up to 2 mm long, are embedded in a fine grained groundmass mainly composed of K-feldspar and quartz (Fig. 3.9 E). K-feldspar (microperthite) occurs as subhedral phenocrysts. In the groundmass, fine grained quartz and K-feldspar form alternating layers, each tens of µm thick (flow bands? Fig. 3.9 E). The accessory assemblage is composed of fluorite, magnetite, Ti-oxide and zircon. Ti oxide contains appreciable amounts of Nb and occurs as small, euhedral to subhedral crystals commonly associated with magnetite.

Lithophysal vugs are partly filled with quartz, amorphous silica, Y-bearing fluorite and minor amounts of Ca-Mg carbonate, Fe-oxide and baryte. The minerals are roughly concentrically arranged, with quartz in contact with the walls and fluorite in the internal portions of the vug (Fig. 3.9 F) (cf. chapter 6 for a more detailed description).

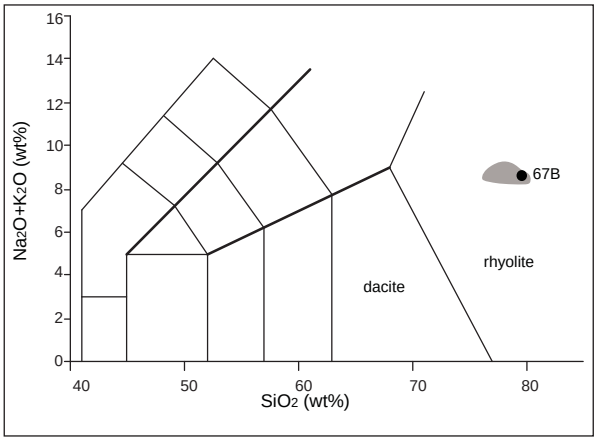

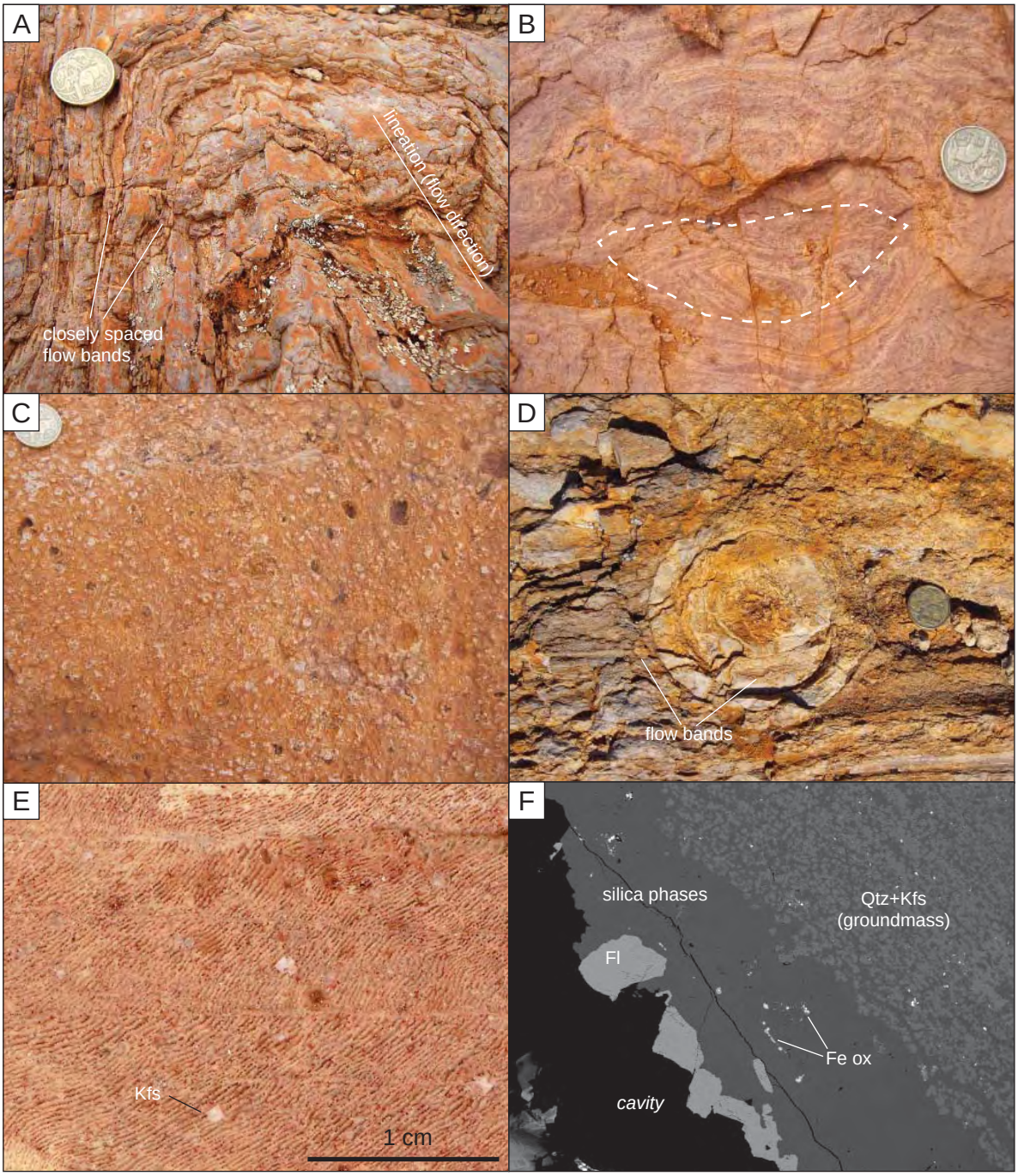

Fig. 3.9 The Baldry Rhyolite at Lake Everard. A- Flow bands form a dm-scale fold (GR 0509831-6501976). Relatively massive domains are evidenced by preferential erosion. Flow direction is parallel to the fold hinge line. B- "Eye" structures observed in a plane lying normal to the flow direction and intersecting the hinge line of a non-cylindrical fold (sheath fold, GR 0509578-6502087). C- Non-foliated, vesicular top of the lava (GR 0509578-6502087). D- Lithophysa overgrowing flow bands. Flow bands can be seen crossing the lithophysa (GR 0509965-6502023). E- Alternated µm- to tens of µm-scale layers of Kfs+Qtz form a "fish bone" texture (sample GH68, BSE, 0506087-6502449). F- Quartz, fluorite and Fe oxide deposited on lithophysal vug walls (sample GH68, BSE).

NUCKULLA BASALT (Nuckulla Basalt of Giles, 1977)

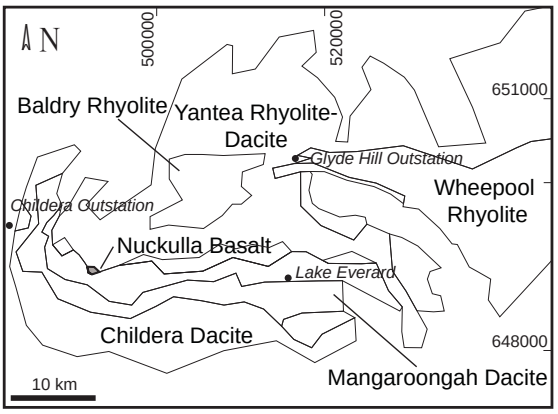

Field description

The Nuckulla Basalt outcrops in a small area (<1 km^2) near Nuckulla Well in a lens-shaped body stratigraphically situated at the base of the Yantea Rhyolite-dacite. These rocks represent the only femic (SiO_2 <53 wt%) lithologies cropping out in the Lake Everard area. The upper and lower contact are not exposed. On fresh surfaces the Nuckulla Basalt is a dark grey-green fine grained, and almost aphanitic, massive rock (Fig. 3.10 A). On weathered surfaces, where the rock alters to orange-brown, small phenocrysts can be locally seen.

Petrographic description (samples GH07, 69, 71)

Clinopyroxene-phyric basalt lava

The Nuckulla Basalt includes sparsely porphyritic to glomerophyric rocks. Phenocrysts of clinopyroxene (<1 vol.%) are embedded in a fine grained groundmass composed of plagioclase, clinopyroxene, Ti-magnetite and F-apatite (Fig. 3.10 B). Phenocrysts are subhedral to anhedral, ≤1 mm in length. They exhibit a concentric zoning with a light yellow to colourless, non-pleochroic core (II order δ, intermediate $2V_\alpha$) and a yellow, slightly to non-pleochroic rim with higher birefringence. Cores and rims are separated by an irregular surface. Cores are anhedral and inclusion-free, whereas rims contain inclusions of opaques (Ti-Cr magnetite) and glass. Plagioclase is partially included (Fig. 3.10 C). Clinopyroxene-hosted inclusions of magnetite are round, ≤20 µm across and homogeneous. Small (<30 µm), round to irregular-shaped and clear (glassy) melt inclusions are mostly homogeneous (Fig. 3.10 D). Fine grained clinopyroxene is evenly distributed throughout the groundmass. It tends to be intergranular between plagioclase and locally includes magnetite. Optical characteristics and composition are similar to the phenocryst rims, with yellow absorption colour, slight pleochroism, II order birefringence. Microprobe analysis (Fig. 3.10 E) of pyroxene indicates a compositional variation between core and rim in terms of most elements (core: Mg# = 0.80-0.82, rim: Mg# = 0.72-0.73). Phenocryst rims and groundmass pyroxenes show overlapping compositions in terms of all the analysed elements (Mg# = 0.70-0.74). Other elements such as Al, Ti, Mn, Cr also show a clear zoning. Plagioclase (Na-oligoclase, EDS) occurs in the groundmass as euhedral tabular crystals, mostly ≤100 µm in length, turbid due to the alteration to a very fine grained sericitic product. An orientation of plagioclase can be identified in small domains, but it is not consistent throughout the thin section. Magnetite in the groundmass is euhedral diamond-shaped to subhedral, ≤50-70 µm in size, and shows µm-scale lamellae overrgrown by very fine grained titanite. F-apatite occurs as anhedral crystals in the groundmass.

Textural relationships suggest the following crystallisation order: Cpx cores – Mag – Pl – Cpx rims and groundmass – Mag+Ap. Magnetite continued to crystallise after clinopyroxene.

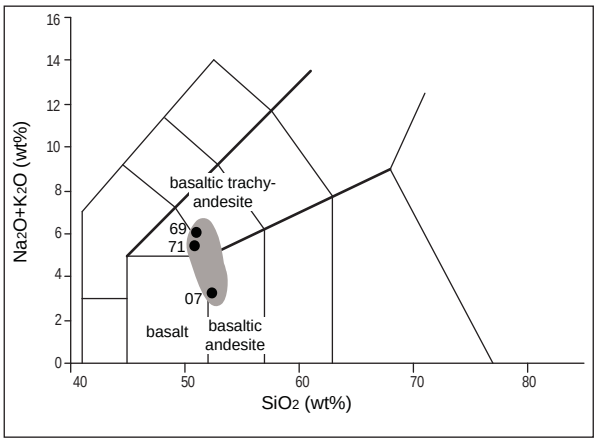

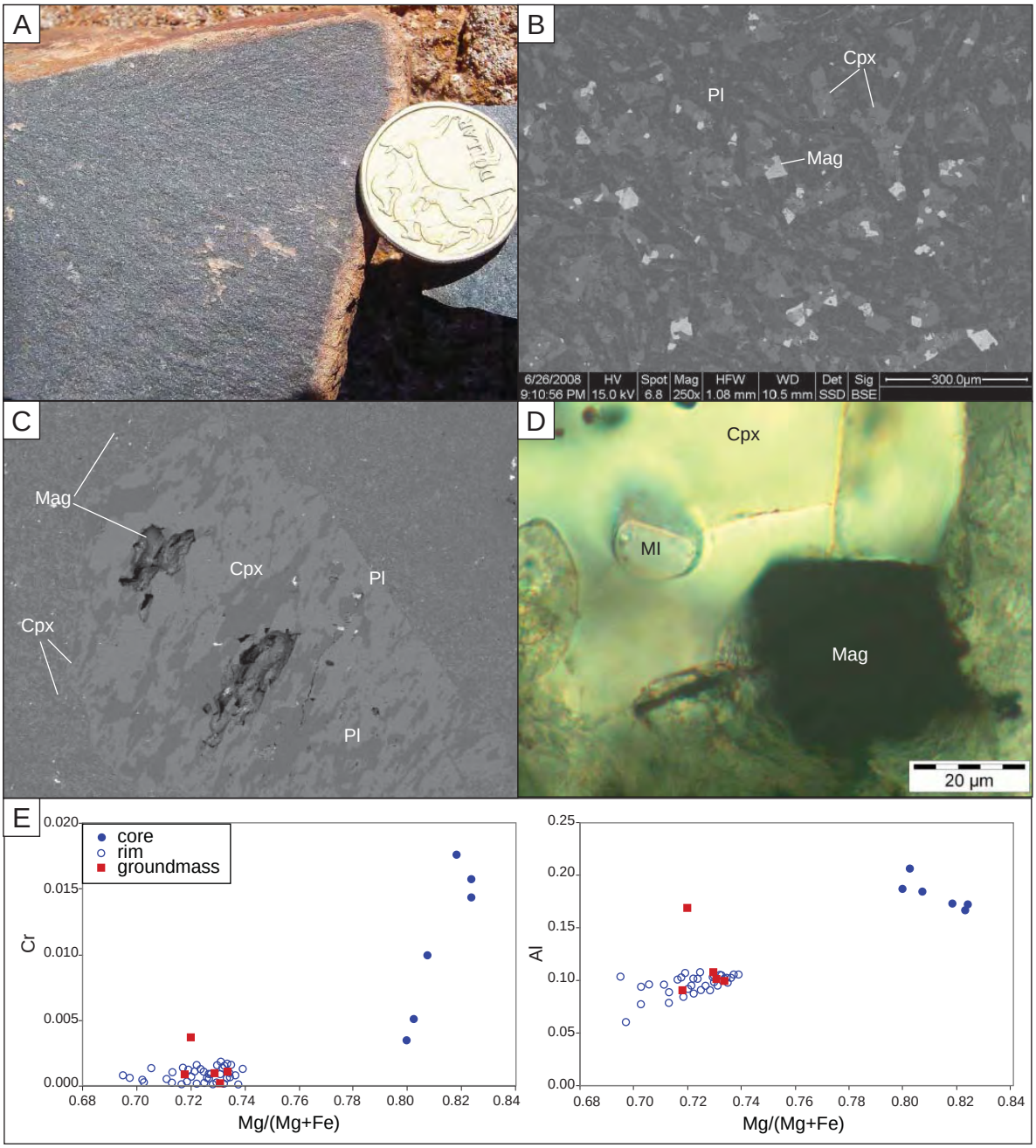

Fig. 3.10 A- Massive Nuckulla Basalt specimen (GR 0493342-6489464). B- Fine grained groundmass. Clinopyroxene is interstitial between plagioclase tablets and Ti-bearing magnetite (sample GH71, BSE, GR 0491465-6490512). C- Zoned phenocryst of clinopyroxene. The BSE-brighter rim grew interstitial between plagioclase and in continuity with the core. Magnetite show two occurrences: relatively coarse grained magnetite occurs in the ground mass and fine grained magnetite is included in pyroxene (sample GH07, BSE, GR 0493342-6489464). D- Clinopyroxene-hosted homogeneous melt inclusion (sample GH07, plane polarised transmitted light). E- Clinopyroxene composition (EPMA*); elements as upf calculated on 6 oxigens.

*Electron microprobe analysis (EPMA) of pyroxene was carried out with a 5-spectrometer Cameca SX100 microprobe. Conditions as follows: 15 kV accellerating voltage, 20 nA beam current, 2µm spot size.

BUNBURN DACITE (Bunburn Dacite of Giles, 1977)

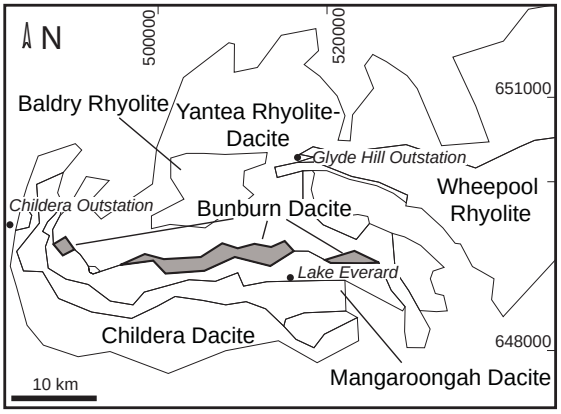

Field description

The Bunburn Dacite forms discontinuous, lens-shaped rock bodies stratigraphically situated between the underlying Wheepool Rhyolite and the overlying Yantea Rhyolite-dacite. It has been observed 4 km East of Childera Outstation, approximately 4 km east-northeast of Nuckulla Well, in the area of Roan Well and south of Mount Sam. The unit is characterised by a homogeneous appearance throughout the outcropping area: purplish-red or purplish-brown, massive, sparsely porphyritic with phenocrysts (<1 vol.%) of feldspar and relicts of a ferromagnesian phase and in a very fine grained (as indicated by the frequently conchoidal fracture), aphanitic groundmass (Fig. 3.11 A). The ferromagnesian phenocrysts are typically altered to a fine grained red-brown product.

Petrographic description (samples GH27, 25)

Oligoporphyritic plagioclase-phyric trachyite-rhyolite lava

Scattered plagioclase (albite) and “ghost” phenocrysts in a micro-crystalline groundmass mainly composed of quartz, K-feldspar and albite. Plagioclase (albite, EDS) forms euhedral elongate, randomly oriented phenocrysts, ≤1 mm long and partially altered to chlorite and sericite (Fig. 3.11 B). Two different kinds of “ghost” phenocrysts are present: the first, possibly a former femic phase (pyroxene?), shows an elongate prismatic habit, ≤0.5 mm long, and is composed of aggregates of fine grained muscovite and Fe-Ti oxide. A second kind of ghost phenocryst, ≤1 mm in size, shows an alteration to Ca-Mg-carbonate, fine grained anhedral Fe-Ti oxide and quartz (Fig. 3.11 C). The microcrystalline quartzo-feldspathic groundmass (grain size <10 µm) is altered to a reddish-brown product (limonite?). Apatite, Ti oxide, zircon and a REE-fluoro-carbonate compose the accessory assemblage. Chlorite, fluorite, Ca-Mg carbonate, Fe oxide and baryte occur as alteration minerals. Apatite occurs as either euhedral crystals in the groundmass or inclusions in albite phenocrysts. A REE-fluoro-carbonate forms extremely anhedral crystals in the groundmass. Baryte veinlets, a few µm thick and scarcely continuous, are locally present.

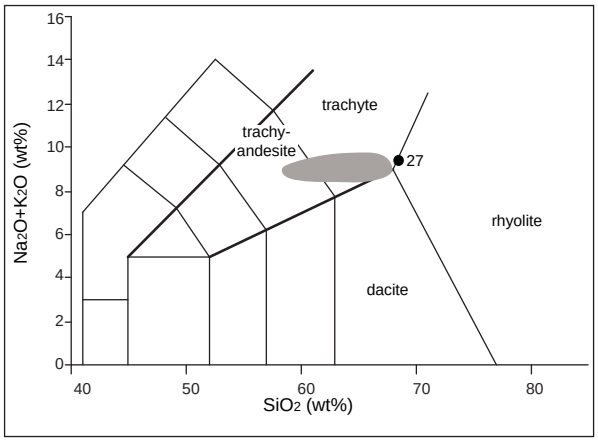

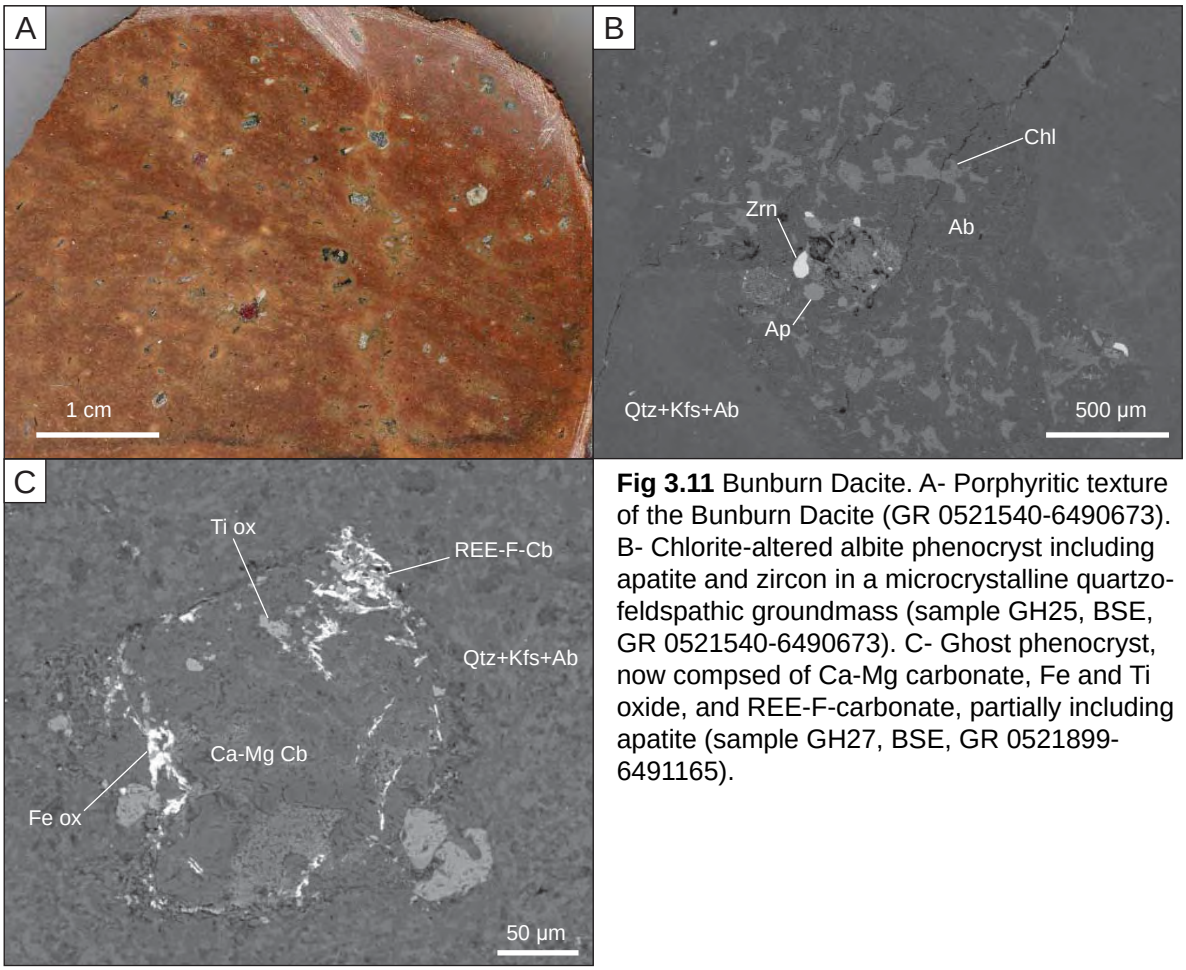

Fig 3.11 Bunburn Dacite. A- Porphyritic texture of the Bunburn Dacite (GR 0521540-6490673). B- Chlorite-altered albite phenocryst including apatite and zircon in a microcrystalline quartzo-feldspathic groundmass (sample GH25, BSE, GR 0521540-6490673). C- Ghost phenocryst, now compsed of Ca-Mg carbonate, Fe and Ti oxide, and REE-F-carbonate, partially including apatite (sample GH27, BSE, GR 0521899-6491165).

YANTEA RHYOLITE-DACITE (Yantea Rhyodacite of Giles, 1977)

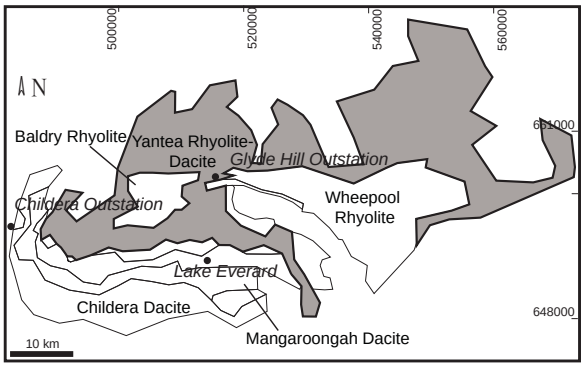

Field description

The Yantea Rhyolite-dacite crops out for a vast area (~90X40 km) and includes feldspar-phyric, massive or foliated lithologies. Feldspar phenocrysts, euhedral to anhedral (≤10 mm in size, 10 vol.%) are ubiquitous and mostly evenly distributed. Round quartz grains are only locally present and in minor amounts. The phenocrysts are embedded in an aphanitic, locally spherulitic groundmass. In the extensive outcrop area of Mount Sam (GR 0523013-6493194), the rock is massive and porphyritic, with euhedral phenocrysts of cream-yellow feldspars, set in a brick-red aphanitic groundmass. Approximately 3 km northeast of Nuckulla Well, on the road to Apostle Tank (GR 0494537-6491393), the rock shows steep flow bands, defined by alternating brick-red and purple-brown layers, ≤tens of cm-thick (Fig. 3.12 A). Feldspar phenocrysts, subhedral to anhedral, are homogeneously distributed through the layers and randomly oriented. Around Glyde Hill Outstation (GR 0514786-6501938), a prominent centimetre-scale foliation is locally present, defined by alternating crystal-rich and relatively fine grained layers, and especially evident in more weathered surfaces. Fiamme (Fig. 3.12 B) and minor lithic fragments are locally present. Three km northwest of Nuckulla Well, <1 km north of the inferred contact with the underlying Bunburn Dacite and Wheepool Rhyolite (GR 0489331-6492457), the dark brown groundmass contains brick-red spherulites, ≤2 cm in size. Approximately 3 km south of Black Hill (GR 0510998-6495085), the unit includes layers of breccia, with cm-scale sub-angular vesicular/amygdaloidal clasts embedded in a porphyritic matrix, separating massive domains. The base contact of the unit outcrops locally, approximately 1 km east of Glyde Hill Outstation. The Yantea Rhyolite-dacite is in contact with a fine grained deposit (clay-silt), possibly a part of the Waurea Pyroclastics. The contact is characterised by irregular inclusions of one rock into the other (fluidal peperite?). The "mingled" contact zone is 1-2 m thick in outcrop and sub-horizontal (Fig. 3.12 C). Approximately 2 km east of Diesel Dam, some outcrops mapped as "unnamed rhyolite" (Baldry Rhyolite of Giles, 1977) by Blissett (1985) and PIRSA (2006) show a porphyritic, massive to mm-scale banded texture with subhedral to anhedral feldspar phenocrysts, ≤1 cm in size, and dark aggregates (a few mm), in a fine grained, brick-red groundmass. On the basis of the absence of quartz and the moderately high feldspar content, they can be attributed to the Yantea Rhyolite-dacite. Massive-textured felsic enclaves, up to a few m in size and composed of medium-grained quartz and feldspar, are included in the Yantea Rhyolite-dacite ~1 km northeast of Glyde Hill Outstation.

Petrographic description (samples GH09, 24, 56B)

Two-feldspar-phyric dacite-trachyte lava

Phenocrysts of plagioclase are set in a microcrystalline groundmass mainly composed of K-feldspar, albite and quartz. Phenocrysts are unzoned (albite), ≤4-5 mm long, and anhedral, mostly altered to a very fine grained red-brown semi-opaque product. They include Fe-Ti oxide and apatite. Locally, silica crystals, round and ≤5 mm in diameter, are present (sample GH56B). The fine grained groundmass (grain size ≤few tens of μm) is composed of tablets of albite surrounded by K-feldspar and quartz (Fig. 3.12 D). Groundmass feldspars are semi-opaque, due to the alteration to a vey fine grained brick-red product. Fe-Ti oxide, apatite and zircon are ubiquitous accessory minerals (Fig. 3.12 E). F-apatite forms euhedral prismatic crystals, commonly occurring as inclusions in albite phenocrysts, Fe-Ti oxide, and zircon. Aggregates of minerals, variable in shape and composition, are common in all the studied samples. Many of these aggregates are rich in trace element- and volatile-bearing mineral phases (zircon, apatite, monazite, REE-fluoro-carbonate, chlorite, Fig. 3.12 F). Other aggregates include: 1) aggregates of chlorite ±Fe-Ti oxide, ±calcite ±quartz, ~2 mm in size, probably mimetic on a previous prismatic ferromagnesian mineral (sample GH24); 2) irregular-shaped aggregates of fine grained epidote (slight pleochroism colourless-light yellow, II order interference colours; clinozoisite-epidote s.s. series) ±fine grained anhedral REE-fluoro-carbonate, rimmed by quartz (sample GH24); and 3) irregular-shaped aggregates of rutile +monazite +chlorite ±zircon (sample GH56B).

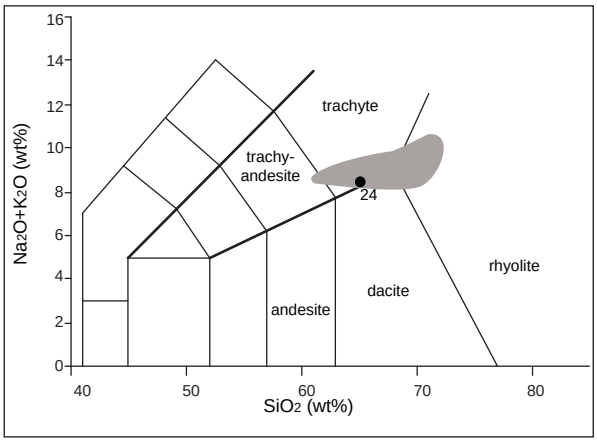

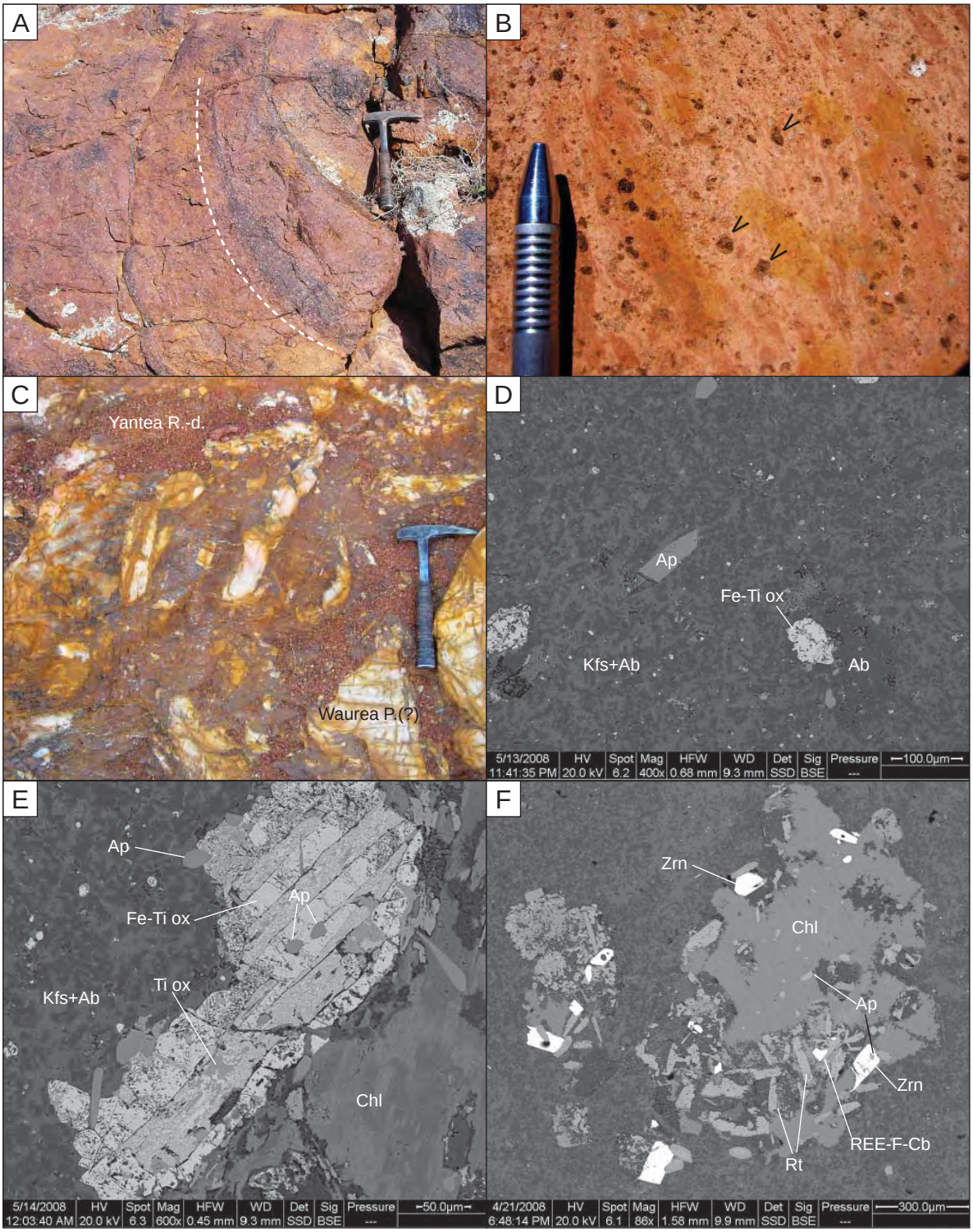

Fig. 3.12 Yantea Rhyolite-dacite. A- Steep flow bands (dashed line, GR 0494537-6491393). B- Fiamme-defined orientation. Partially eroded feldspar phenocrysts are visible (arrowed, GR 0514786-6501938). C- Mingled contact between the Yantea Rhyolite-dacite (brick-red) and a fine grained deposit (white-yellow, Waurea Pyroclastics?, GR 0515415-6501451). D- Albite tablets are included in K-feldspar in the microcrystalline ground mass. Fe-Ti oxide and apatite occur as accessories (sample GH24, BSE, GR 0523013-6493194). E- Fe-Ti oxide including apatite (sample GH24, BSE). F- Chlorite +rutile +zircon +apatite +REE-F-carbonate aggregate. Apatite is included in zircon (sample GH09, BSE, GR 0489331-6492457).

WHYEELA DACITE (Whyeela Dacite of Giles, 1977)

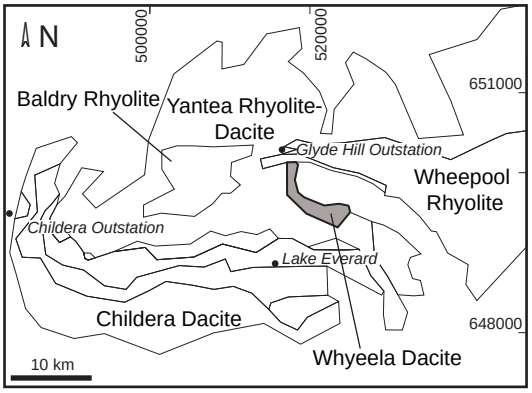

Field description

The Whyeela Dacite outcrops a few kilometres north and northeast of Mortimer Hill, forming a small body (<10 km) that overlies the Yantea Rhyolite-dacite. The unit is composed of brick-red to reddish brown porphyritic rocks, with phenocrysts of feldspar ±relics of a ferromagnesian phase in an aphanitic groundmass. The size and abundance of phenocrysts can vary considerably even between neighbouring outcrops.

East of Glyde Hill Outstation, the Whyeela crops out poorly within a salt lake (GR 0517843-6500771). It includes purplish red, massive and sparsely feldspar-phyric rocks with a fine grained groundmass. The rock is intensely fractured by a mm- to cm-spaced sub-vertical joints. Northeast of Mortimer Hill (GR 0523705-6495238), next to the base contact, Numerous medium to coarse grained, massive, quartz-feldspathic felsic enclaves are present. They are up to several metres in size and show round and gradational borders with the host rock (Fig. 3.13 A). A textural variability of the Whyeela Dacite is associated with the occurrence of these enclaves: domains of higher phenocryst content and phenocryst size alternate with domains of lower phenocryst content and grainsize.

Petrographic description (samples GH26, 33)

Feldspar-phyric trachyte lava

Phenocrysts of plagioclase are set in a microcrystalline, locally granophyric, groundmass. Phenocrysts of plagioclase (albite) are up to 1.5 mm in length, euhedral to anhedral and sieve-textured. Feldspars are frequently fractured and strongly altered to sericite, calcite or very fine grained baryte. Some glomerocrysts (Fig. 3.13 B), a few millimetres across and composed of feldspars with interstitial quartz, baryte and Fe-Ti oxide), are distributed throughout the sample. Quartz crystals, anhedral and up to a few mm in size, are associated with the occurrence of felsic enclaves (sample GH33). The groundmass is mainly composed of K-feldspar and quartz, Fe-Ti oxide, apatite and Ti oxide. Irregular-shaped aggregates, several millimetres in size and containing chlorite, calcite, Fe-Ti oxide ±apatite ±titanite, are also present. Strontium-bearing baryte is fine grained and occurs in anhedral aggregates in the groundmass and as an alteration on feldspars. Epidote and calcite are present in small amounts.

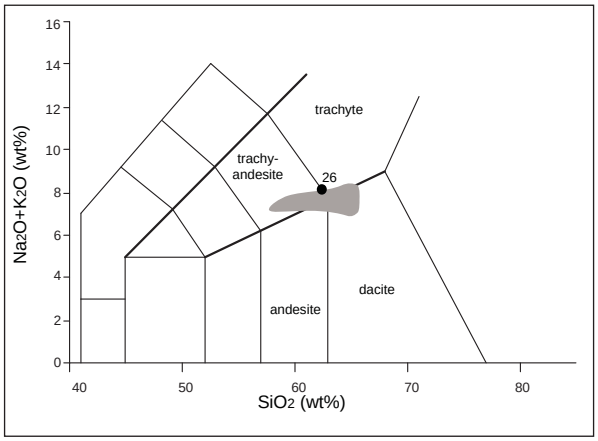

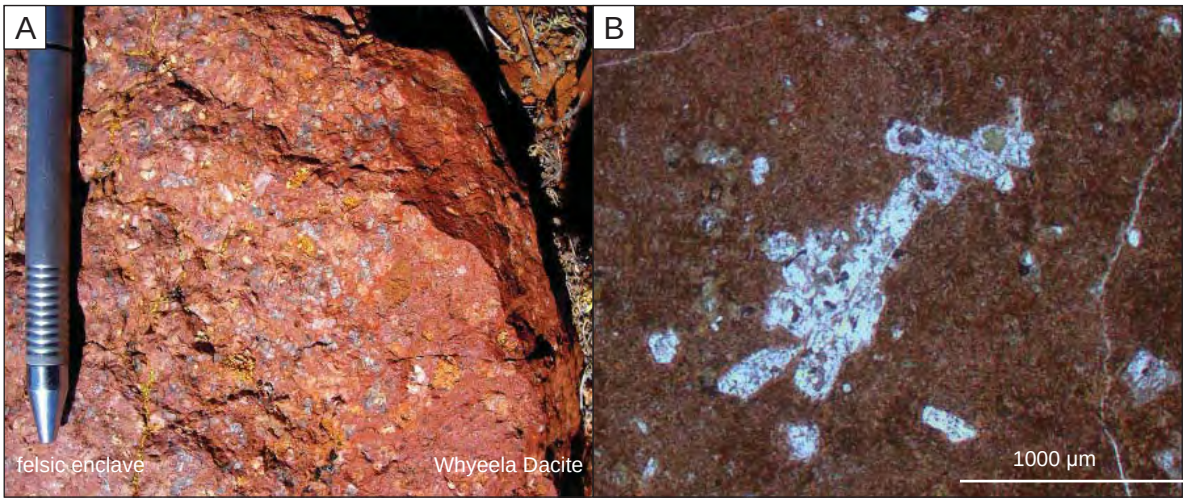

Fig 3.13 Whyeela Dacite. A- Gradational contact between a massive, medium- to coarse-grained felsic enclave (left) and the host rock (GR 0523705-6495238). B- Glomerocrystic plagioclase (sample GH26, plane polarised transmitted light, GR 0522957-6494580).

MOONAMBY DYKE SUITE (Moonamby Suite of Giles, 1977)

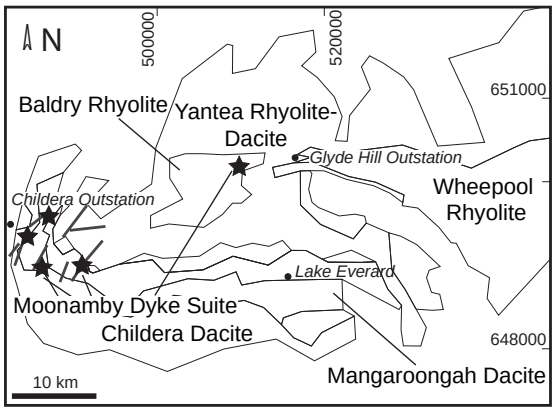

Field description

Porphyritic dykes cross-cut the entire Glyde Hill Volcanic Complex with the exception of the Whyeela Dacite. They appear to be mainly concentrated in the westernmost part of the area (Fig. 3.2). The dykes are up to tens of metres wide and mostly homogeneous in texture. They contain medium to coarse phenocrysts of feldspars and quartz (feldspar can be up to 3-4 cm in size) set in a fine grained, mostly brick-red aphanitic groundmass (Fig. 3.14 A). Phenocrysts are subhedral to anhedral. Quartz grains have round boundaries and show deep embayments. The contact with the country rock is sharp. Textures are homogeneous within single intrusive bodies, but a local reduction in phenocryst abundance can occur at the contacts with the host rock.

The dyke intruded in the Baldry Rhyolite 5 km east of Glyde Hill Outstation (GR 0509965-6502023) is ~7 m thick and crops out in a northwest to southeast direction for 100 m. Phenocrysts of feldspar and quartz are immersed in a light brown, fine grained groundmass. The contact with the country rock is sharp and no chilled margin or textural variations were observed (Fig. 3.14 B). Approximately 5 km east of Nuckulla Hill (GR 0491376-6490439), a porphyritic dyke cuts the Nuckulla Basalt and the Wheepool Rhyolite. The dyke appears to be at least 4-5 m wide, the contacts with the country rock are not exposed. Feldspar phenocrysts are subhedral with round borders and up to 3-4 cm in size. Anhedral phenocrysts of quartz, ≤1 cm in size, are embedded in a fine grained brick-red groundmass. At the contact with the rhyolite and the basalt, the grain size of phenocrysts (both feldspar and quartz) is reduced to a few millimetres. A dyke intruding the Childera Dacite shows a similar texture east of Childera Outstation (GR 484545-6493681), where cream or reddish anhedral phenocrysts of feldspar, up to 1 cm in size, and round phenocrysts of quartz are embedded in a violet-pink or brick-red, fine grained groundmass. The intrusive body is about 5 m wide and southwest-northeast striking. Northeast of Childera Outstation (GR 0487394-6496160), a northeast striking, 15-20 m wide, feldspar- and quartz-phyric dyke intrudes the Mangaroongah Dacite. At Nuckulla Hill (GR 0486550-6489826), two southwest-northeast-striking porphyritic dykes, several metres wide, intrude the Mangaroongah Dacite. No evidence of thermal effect in the country rock was observed and only very locally a reduction of the amount of phenocrysts can be seen in the dykes.

Petrographic description (samples GH15, 70, 70B, 92)

Two-feldspar- and quartz-phyric rhyolite

Phenocrysts of quartz and feldspar show subhedral to anhedral habit and are variable in size (≤a few cm) and in abundance between individual dykes. The groundmass, mainly composed of quartz, K-feldspar and albite, is microcrystalline (grain size ≤50 µm) to poikilitic (Fig. 3.14 C). The accessory assemblage varies between dykes. Opaque minerals (Fe and Fe-Ti oxides), zircon, Ti oxide and titanite are almost ubiquitous, whereas fluorite, F-apatite, REE-fluoro-carbonate, epidote and chlorite are only locally present (sample GH15). In the dyke intruding the Baldry Rhyolite approximately 5 km east of Glyde Hill Outstation (sample GH15, GR 0509965-6502023), K-feldspar occurs as anhedral and embayed phenocrysts, up to 3 mm across. In some cases a double system of twinning is visible (microcline?). Minor plagioclase (albite) occurs as euhedral crystals, <1 mm in size. In some cases, plagioclase is included in K-feldspar. Feldspars are partly altered to chlorite. Embayed quartz phenocrysts are surrounded by a thin (0.1-0.2 mm) rim of fine grained and needle-shaped, radially oriented K-feldspar and albite crystals.

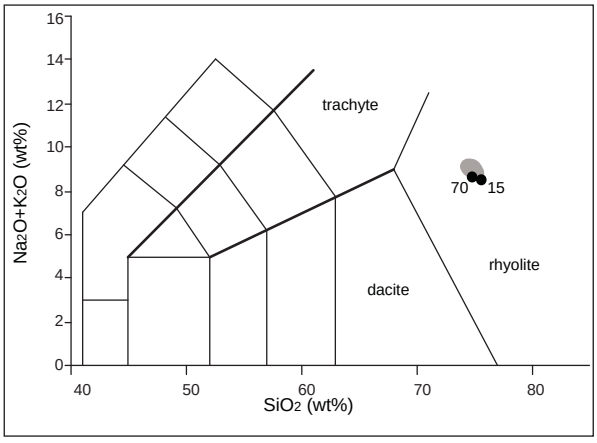

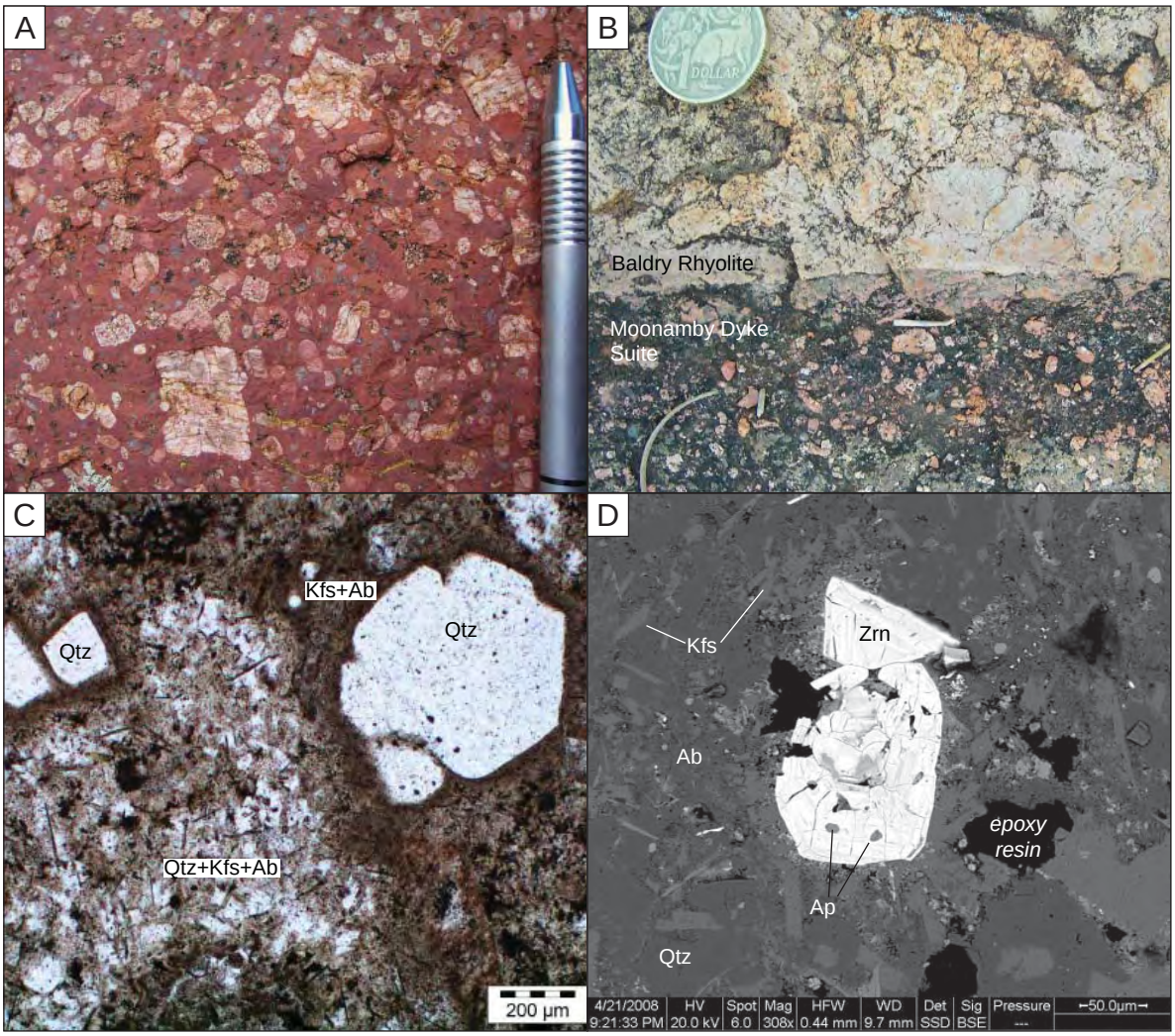

Fig 3.14 Moonamby Dyke Suite. A- Medium to coarse grained feldspar in a porphyritic dyke intruded into the Mangaroongah Dacite (GR 0486550-6489826). B- Sharp contact between a dyke (bottom) and the Baldry Rhyolite (top, GR 0509701-6502089). C- Quartz phenocrysts in a micropoikilitic quartz-K-feldspar-albite groundmass (sample GH15, plane polarised transmitted light, GR 0509965-6502023). D- Zoned zircon crystal including small euhedral crystals of apatite (sample GH15, BSE).

The dyke contains abundant micro-miarolitic cavities, <1 mm in size, including Y-bearing fluorite, quartz, chlorite-altered biotite, zircon, Nb-bearing Ti oxide (anatase), apatite and a REE-fluoro-carbonate. The groundmass is fine grained and contains small (≤0.1 mm) and turbid K-feldspar and albite crystals, included in micropoikilitic quartz. Fluorite forms anhedral crystals showing pink-purple absorption colours and an Y-bearing composition (EDS). REE-fluoro-carbonate (synchysite?) occurs either as small anhedral or needle-like crystals in the groundmass or in aggregates. Apatite is present in minor amounts, and can be included in K-feldspar phenocrysts and in zircon. Zircon occurs as euhedral to anhedral, concentrically zoned crystals including apatite (Fig. 3.14 D). The dyke intruding the Nuckulla Basalt and Wheepool Rhyolite 5 km east of Nuckulla Hill (samples GH70 and 70B, GR 0491376-6490439) has the same phenocryst assemblage, set in a microcrystalline quartzo-feldspathic groundmass. It also includes irregular-shaped aggregates of biotite, zircon and rutile. Minor baryte is present along veinlets. A reduction in phenocryst grain size exists between samples from the inner portion of the dyke and at the contact with the country rock, varying from ≤10 mm in diameter (sample GH70) to ≤3 mm (GH70B), respectively. The dyke intruded into the Mangaroongah Dacite southeast of Childera Outstation (sample GH92, GR 0487394-6496160) contains Al-bearing titanite, zircon and minor fluorite as accessory minerals in addition to K-feldspar phenocryst. Aggregates containing epidote, chlorite, titanite, and apatite are also present.

3.3.2 Summary of volcanology of the Glyde Hill Volcanic Complex, Lake Everard

The Glyde Hill Volcanic Complex includes a flat-lying to gently dipping, 1-km-thick sequence dominated by felsic units with minor andesite and very minor basalt (Fig. 3.15). Felsic to silica-rich intermediate units (SiO_2 >60 wt.%) range in extent from ~10 km to >80 km across and are up to a few hundreds of metres thick (Table 3.1). The volumes, estimated on the basis of the outcrop extent (minimum extent), range between ≤1 km^3 (Whyeela Dacite, Andesite I) and approximately 170 km^3 (Yantea Rhyolite-dacite).

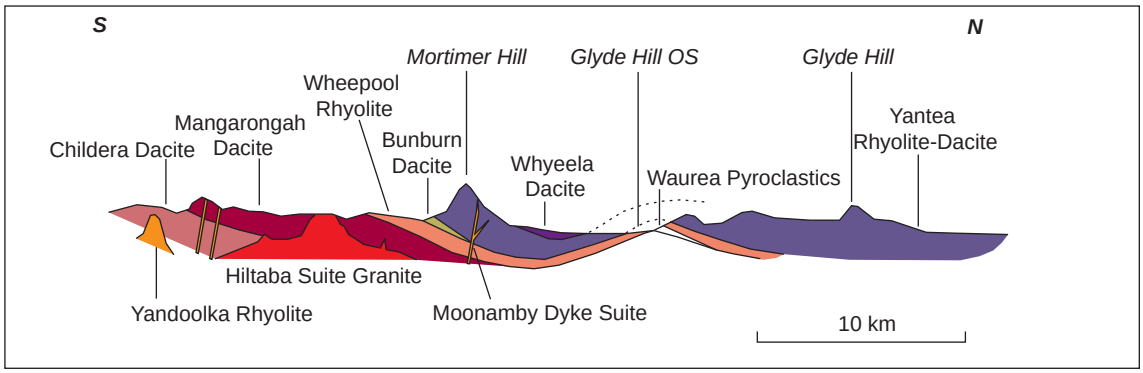

Fig. 3.15. Diagrammatic cross section of the Glyde Hill Volcanic Complex, Lake Everard, illustrating the relations between rock units. The section is approximately north-south-oriented cross-section across Mortimer Hill and Glyde Hill Outstation Vertical scale exaggeration ~25X.

Lavas

All the lava units are evenly porphyritic; phenocrysts of albite, K-feldspar and ±quartz (<1 to >10 vol.%) are set in a microcrystalline groundmass (Fig. 3.16 A-G). Most of the felsic units show cm-scale flow bands, and a lineation is locally contained on such surfaces. Sheet parting, parallel to the flow bands, is common in the Childera Dacite, and is also accompanied by a lineation (Fig. 3.3).

The Baldry Rhyolite shows evidence of intense flow deformation that produced non-cylindrical folds (sheath folds) in the interior of the unit. This unit has a thin non-flow banded vesicular crust (Fig. 3.9 A-C). In other units (Wheepool Rhyolite, Yantea Rhyolite-dacite, Figures 3.6, 3.12 A), flow bands are planar to folded at the m-scale. Development of lithophysae in the Baldry Rhyolite generally post-dated the flow deformation, although elongate lithophysae were described by Ferris (2003). Spherulitic texture is locally present in at least one of the units (Yantea Rhyolite-dacite). Several felsic units (Childera Rhyolite, Mangaroongah Dacite, Wheepool Rhyolite, Baldry Rhyolite, and Yantea Rhyolite-dacite, Table 3.1, Fig. 3.5) contain monomictic breccia zones interpreted as autobreccia. These breccias contain either jigsaw-fit and angular or lobate clasts, set in a porphyritic, flow banded or vesicular/amygdaloidal matrix.

In some cases (Mangaroongah and Childera Dacites), thin breccia layers separate porphyritic and rather massive volumes of rock. The breccia layers are interpreted as pyroclastic deposits separating distinct lava units. The base of the Yantea Rhyolite-dacite

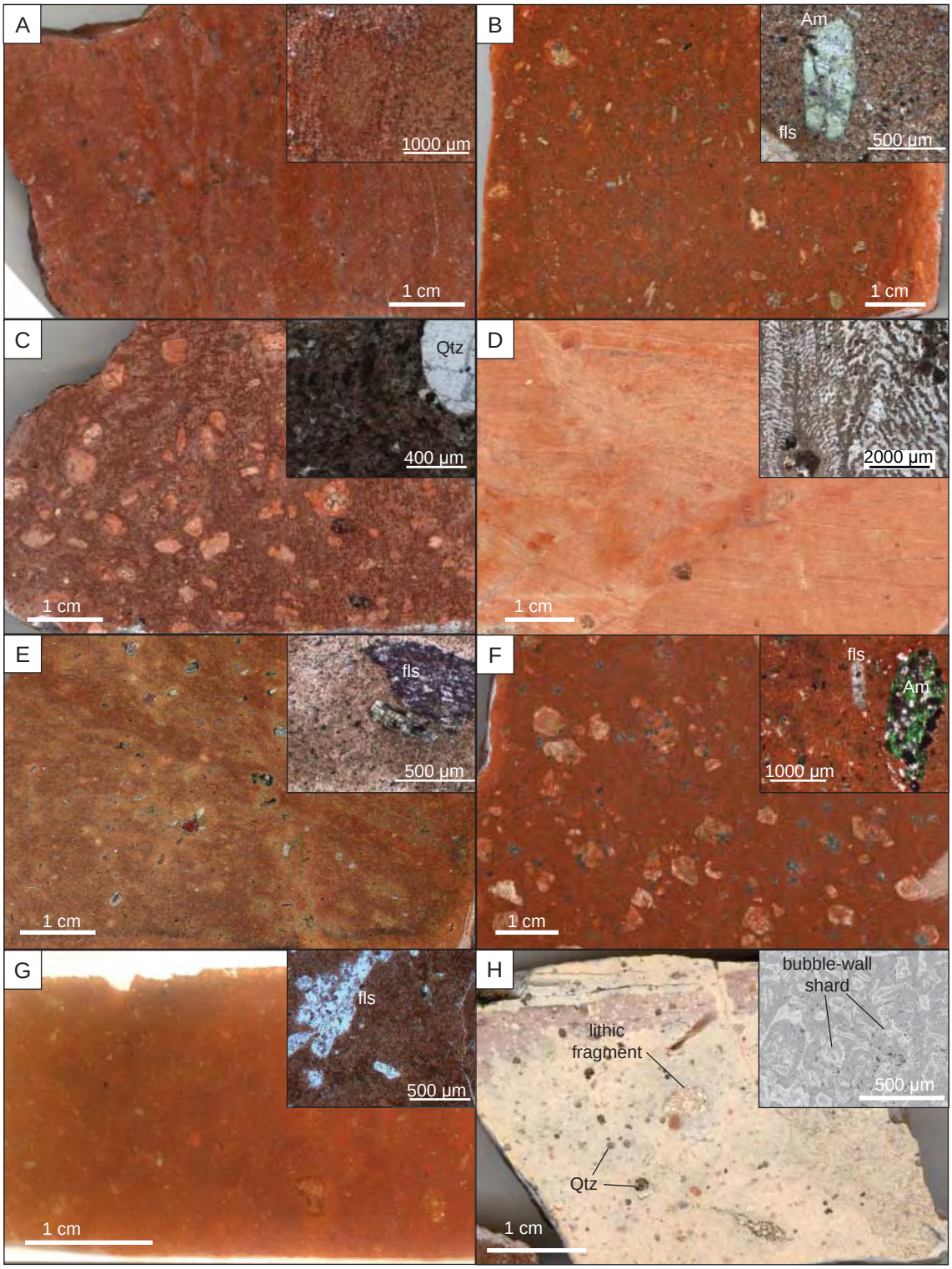

Fig. 3.16. Comparison of textures of lavas (A-G) and pyroclastic rocks (H) in the Glyde Hill Volcanic Complex, Lake Everard. A- Childera Dacite (sample GH31, GR 0520150-6480997). B- Mangaroongah Dacite (GH21, GR 0515440-6484867). C- Wheepool Rhyolite (GH23, GR 0517647-6488394). D- Baldry Rhyolite (GH67, GR 0506205-6502560). E- Bunburn Dacite (GH25, 0521540-6490673). F- Yantea Rhyolite-dacite (GH28, 0522105-6492857). G- Whyeela Dacite (GH26, 0522957-6494580). H- Waurea Pyroclastics (sample GH95, 0515405-6501456). Insets show microtextures (plane polarised transmitted light). GR: Grid reference (GDA94).

is locally peperitic where the dacite has mingled with a fine grained deposit (Fig. 3.12). Elongate and aligned vesicles/amygdales are locally abundant in the Mangaroongah Dacite; aggregates of quartz +chlorite ±barite occur as infilling the vesicles. The lava units contain very minor or no fiamme; the exception is the base of the Yantea Rhyolite-dacite where fiamme (pumice fragments?) are included in a porphyritic groundmass (Fig. 3.12 B).

These units were probably emplaced as lavas based on the evenly porphyritic texture, microcrystalline groundmass, flow bands and lineations, presence and distribution of breccia domains (autobreccia), vesicles/amygdales, and lack or very local presence of fiamme and paucity of fractured crystals.

Intermediate (andesite s.l.: andesite, trachyandesite and trachyte, SiO_2 = 60-62 wt.%) and mafic units (basalt s.l., SiO_2 = 51-53 wt.%) occur in limited areas, <10 km across. These units are mainly massive and evenly porphyritic with phenocrysts of clinopyroxene ±plagioclase in a microcrystalline groundmass. These units are interpreted to have been emplaced as lava flows.

Pyroclastic facies

The Waurea Pyroclastics (Fig. 3.8) includes a variety of pyroclastic facies. The vitric ash tuff (facies 2, Fig. 3.8 B, C) is mainly composed of juvenile bubble-wall fragments, forming most of the matrix, implying an explosive eruption mechanism. The moderate to poor sorting and lack of bedding in most facies within the Waurea Pyroclastics (facies 2-5) suggests that they are pyroclastic flow deposits, rather than fall deposits.

The bedded sandstone (facies 1) is well sorted and shows evidence of local erosion (truncation of beds), which may be due to reworking of an original non-welded pyroclastic deposit by running water and/or wind.

Layers of breccia are also intercalated with lavas in the Mangaroongah and Childera Dacites. These breccias include cm-scale angular pumice or feldspar-phyric clasts in a mm-sized matrix and are interpreted as the products of minor explosive episodes that accompanied the main effusive activity.

Table 3.1. Volcanic textures and emplacement mechanisms of the principal units in the Glyde Hill Volcanic Complex

Unit	Outcrop area* (km^2)	Max estimated thickness (m)	Volume* (km^3)	Aspect ratio	Texture	Groundmass/ matrix	Phenocrysts/ crystals	Breccia domains	Flow deformation	Enclaves, xenocrysts	Emplacement mechanism interpretation	Emplacement, previous interpretation**
Yandoolka Rhyolite	2	?	–	–	coherent	microcrystal-line	euhedral	no	no	no	shallow intrusion (plug)	shallow intrusion (plug)
Whyeela Dacite	12	100	1	39	coherent	microcrystal-line	subhedral	no	no	massive, coarse grained, partially melted Qtz-fls enclaves (granite)	lava flow	welded ash flows
Yantea Rhyolite-dacite	1123	150	168	252	coherent	microcrystal-line, locally fiamme-bear-ing (base)	eu- to anhedral	monomictic breccia domains	flow bands and folds	massive, coarse grained, partially melted Qtz-fls enclaves (granite)	lava flow?	welded ash flows
Nuckulla Basalt	2	-			coherent	microcrystal-line	sub-anhedral	no	no	no	lava flow	lava flows (Giles, 1977)
Bunburn Dacite	67	<100	7	93	coherent	microcrystal-line	sub-euhedral	no	no	no	lava flow?	welded ash flows
Baldry Rhyolite	94	≥50	5	219	coherent	microcrystal-line, µm-scale layering	sub-euhedral	angular jigsaw-fit clasts monomictic breccia domains	folded flow bands, elongation lineation	no	lava flow	welded ash flows, lava dome (Giles, 1977)
Waurea – facies 2	<1	≤3	<1		clastic	glass shards, fiamme-bearing	subhedral, angular fragments	no	no	angular thinly banded lithics	ignimbrite	lapilli tuff (Giles, 1977)
Wheepool Rhyolite	511	300	153	85	coherent	microcrystal-line, locally flow-banded	anhedral	lobate clasts monomictic breccia domains	flow bands	no	lava flow	welded ash flows, lava
Mangaroongah Dacite	136	200	27	66	coherent	microcrystal-line	sub-euhedral or anhedral sieve-textured, glomerocrysts	angular jigsaw-fit or lobate clasts breccia domains and thin (<1 m) breccia layers	deformed vesicles	no	lava flow	welded ash flows, lava
Andesite II	21	–	–	–	coherent	microcrystal-line	eu- to anhedral	no	no	quartz	lava flow	lava flow
Childera Dacite	267	300	81	61	coherent	microcrystal-line	sub-to an-hedral	massive, monomictic breccia domains	flow bands, lineation	no	lava flow	welded ash flows
Andesite I	1	–	–	–	coherent	microcrystal-line	euhedral	no (base not exposed)	no	quartz	lava flow	lava flow

*Outcrop area and volume, calculated by interpolation of outcrops, represent a minimum for the areal extent and, therefore, volume of the unit.
**Blissett (1985) unless otherwise stated

3.4 Chitanilga Volcanic Complex, Kokatha

Figure 3.17 shows a schamatic log and the chemical classification in the TAS (Le Bas et al., 1986) and Zr/Ti vs Nb/Y diagrams (Winchester and Floyd, 1977; Floyd and Winchester, 1978; fields modified by Pearce, 1996) for the Chitanilga Volcanic Complex, Kokatha. In both diagrams, the analyses plot in the high end of the subalkaline field. Rhyolite and dacite are the most represented compositions in the TAS diagram.

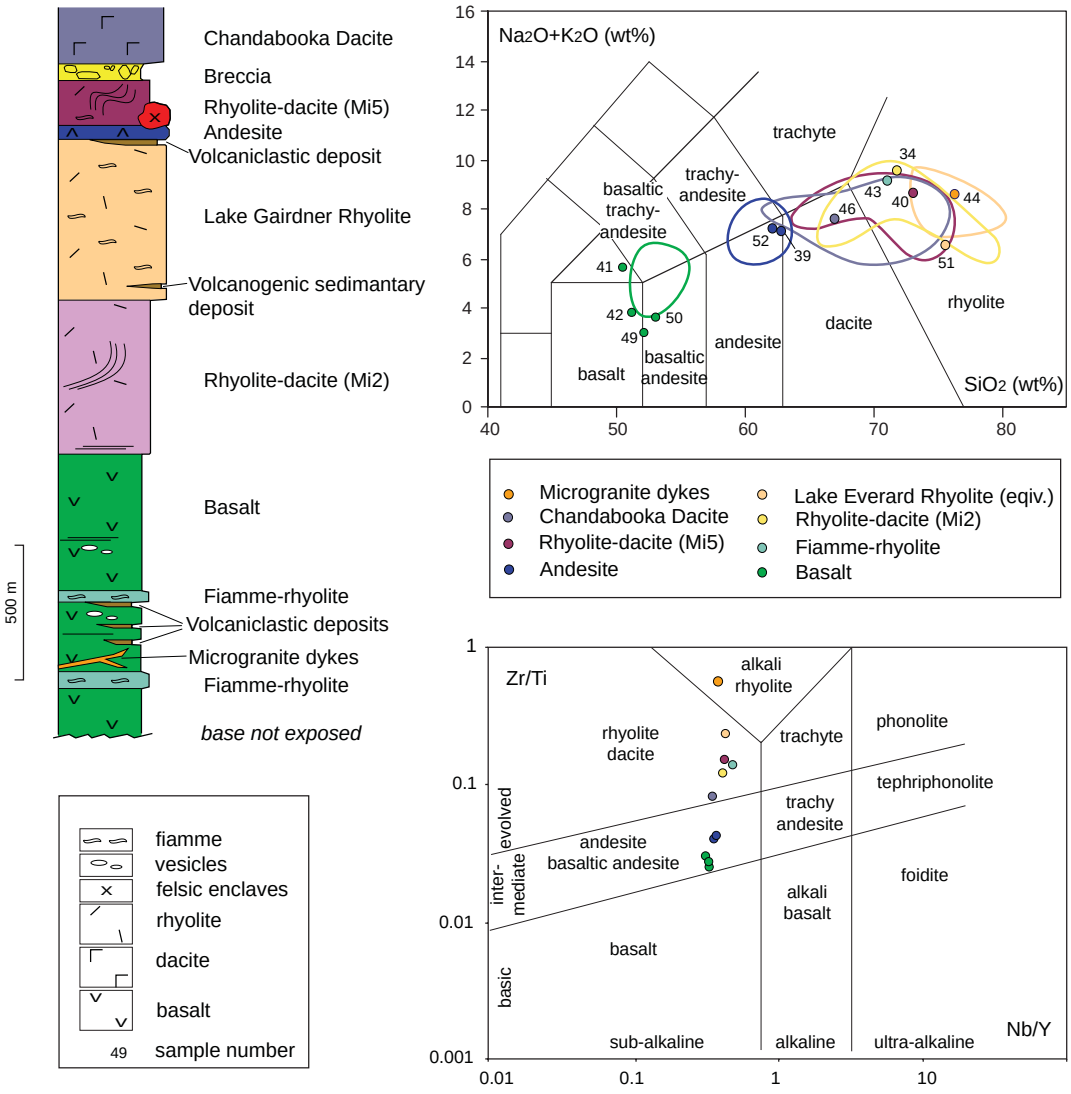

Fig. 3.17. Simplified log and total alkali versus silica (TAS, LeBas et al., 1986) and Zr/Ti versus Nb/Y (Winchester and Floyd, 1977; fields modified by Pearce, 1996) plot for the Chitanilga Volcanic Complex, Kokatha area. Data recalculated to 100% anhydrous. Literature data (lines, same colour as spot symbols) are also shown for comparison (data from PIRSA, 2006; Stewart, 1994).

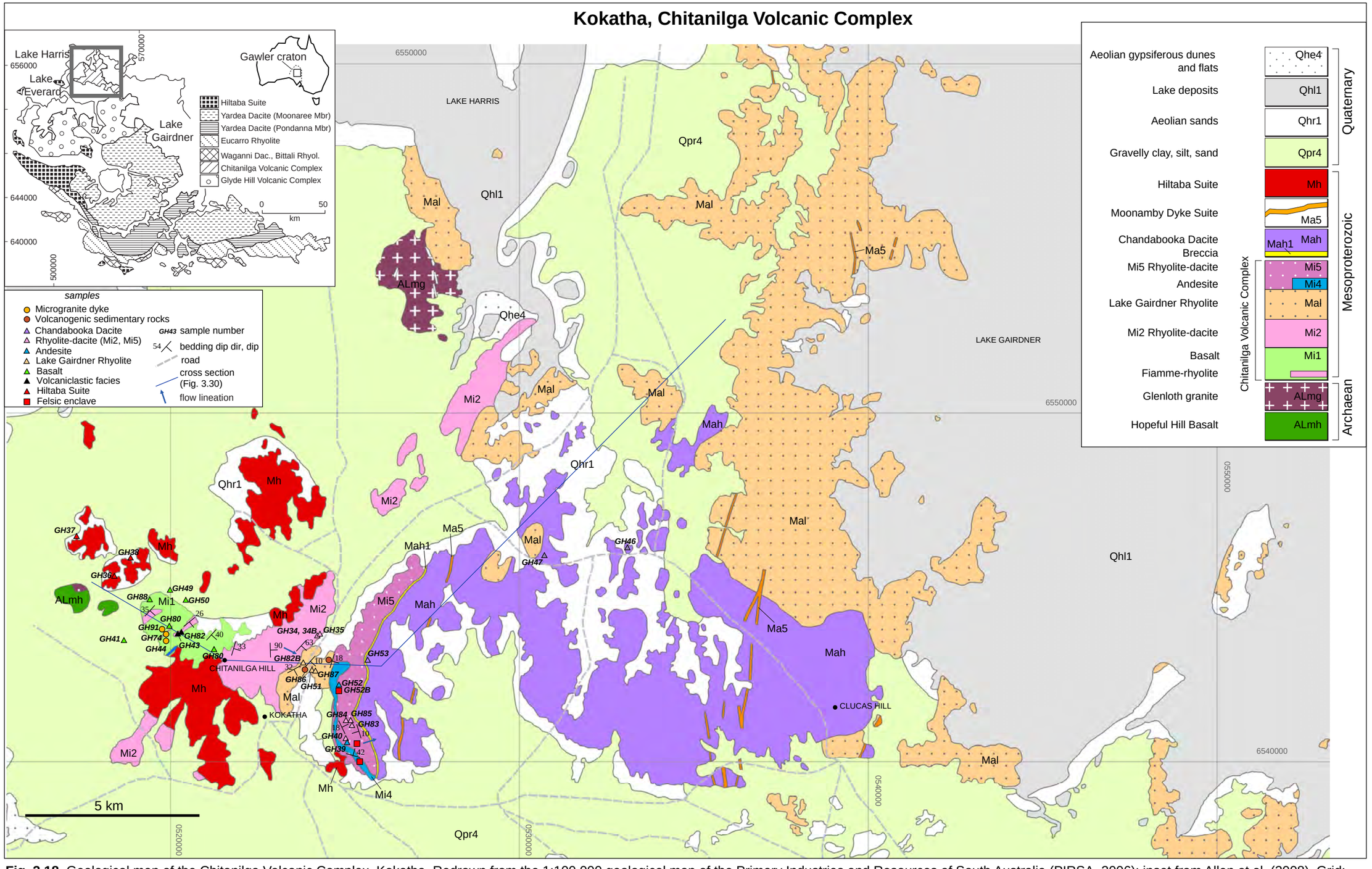

Fig. 3.18. Geological map of the Chitanilga Volcanic Complex, Kokatha. Redrawn from the 1:100 000 geological map of the Primary Industries and Resources of South Australia (PIRSA, 2006); inset from Allen et al. (2008). Grid: GDA94.

Chitanilga Volcanic Complex, Kokatha - Rock data sheets

BASE OF THE CHITANILGA VOLCANIC COMPLEX

The lower part of the Chitanilga Volcanic Complex at Kokatha crops out northwest of Chitanilga Hill and includes a thick (~1 km) sequence of mafic to intermediate lavas (basalt l.s.) and interlayered felsic volcaniclastic facies. It has been subdivided into: 1. Basalt; 2. fiamme-rhyolite; 3. other volcanicalstic facies.

Interlayered felsic rocks provide evidence of mafic and felsic volcanism occurring at the same time, although probably from different volcanic centres, at least in the early stages of the volcanic activity at Kokatha.

1. BASALT

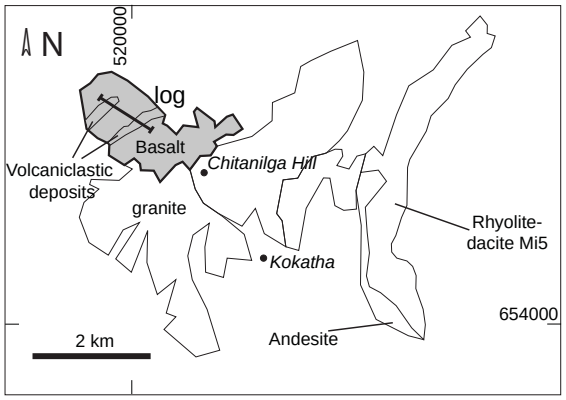

Field description

Basalt crops out extensively northwest of Kokatha Homestead. The base of the unit is not exposed. The outcropping portion of the basalts is approximately 1 km thick. These rocks are greenish-grey to black and aphanitic to sparsely porphyritic with ferromagnesian phenocrysts. Amygdales are ≤1-2 cm long, round or flow-deformed and lobate, and define planar flow surfaces (Fig. 3.19 A), showing a moderately steep, ~southeast-dipping orientation (dip direction 125-150, dip 14-42). Amygdales are concentrated in the upper parts of lavas (flow units). North of Chitanilga Hill, the contact between the basalt and the overlying Rhyolite-dacite (Mi2) is concealed under debris. West of Chitanilga Hill, the granite intrudes the middle-upper part of the basalts. The contact is exposed for ~1.5 km and sharp; angular fragments of basalt are included in the granite. At the contact, the granite shows a reduction in grain size.

Petrographic description (samples GH41, 49, 50)

Amygdaloidal basalt s.l.

The basalt includes equigranular to porphyritic rocks with ghost ferromagnesian phenocrysts, up to a few mm in size, embedded in an aphanitic ground mass (samples GH41, 49). Ghosts of phenocrysts with an equant habit (olivine?) are completely altered to very fine-grained magnetite, distributed around the rim and along fractures, and fine-grained amphibole, quartz and epidote (Fig. 3.19 B). Plagioclase forms

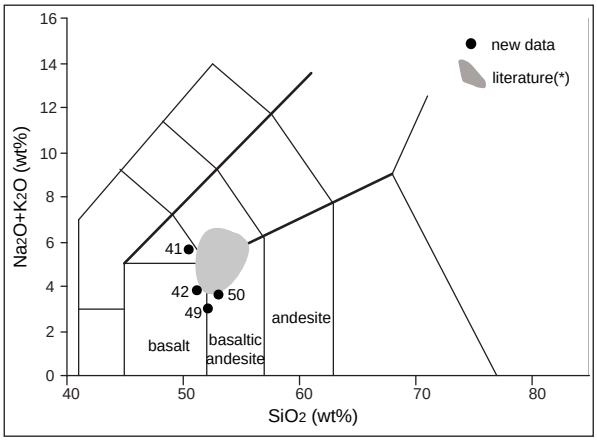

(*) Chemical compositions from PIRSA Dataset (2006) and Stewart (1994).

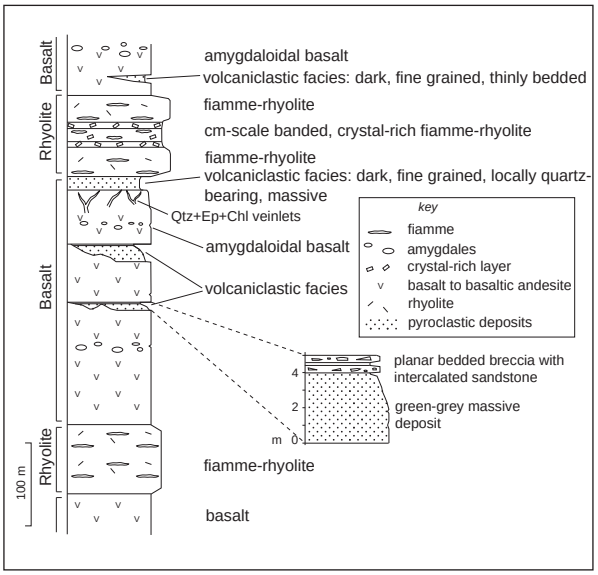

Fig 3.19 Basalt. A- Flow lineation (dashed line) defined by the orientation of vesicles (GR 0520008-6543479). B- Ghost phenocryst (margins arrowed, olivine? Sample GH49, plane polarised transmitted light, GR 0519979-6544918). C- Quartz-epidote-chlorite-amhibole-filled amygdale (sample GH50, plane polarised transmitted light, GR 0520440-6544626).

small (<0.3 mm) unzoned or weakly zoned (core An~40 to rim An~25) euhedral to subhedral crystals, partially altered to sericite. Plagioclase crystals show an alignment at the cm-scale. Opaque minerals occur as either euhedral crystals ≤20 µm in size, disseminated in the groundmass (±Cr ±Mn-bearing magnetite, EDS), or aggregates of very fine-grained crystals interstitial to plagioclase and apparently concentrated along fractures (Fe oxide, EDS). Irregular-shaped and lobate amygdales are up to a few mm in size (samples GH50 and 49) and are filled with amphibole, quartz, ±epidote, ±titanite, ±chlorite (Fig. 3.19 C). Amphibole (pleochroic yellow-light green, c^γ ≈ 25°, II order birefringence, Ca-Al-bearing EDS, actinolite type) occurs as radially oriented needle-like crystals forming single or double rims along the margin of vesicles. Quartz, epidote and chlorite form the amygdales' core. Titanite is present as very fine-grained crystals, interstitial between amphibole.

2. FIAMME-RHYOLITE

Field description

This unit includes dark red or grey, feldspar-bearing bedded rocks, up to several tens of metres thick and laterally continuous. These rocks have been grouped with feldspar-phyric rocks overlying the Basalt in one unit (Pac2 of Blissett, 1977b; 1985, and Mi2 of PIRSA, 2006). Feldspar crystals are a few millimetres in size and partly oriented. The matrix is dark brown and aphanitic. These rocks can be fiamme-poor and mostly massive or fiamme-rich and bedded. Fiamme are few mm to ~10 cm long (Fig. 3.20 A). A cm-spaced, planar and laterally continuous compositional layering, defined by alternating crystal-rich, and crystal-poor ash-rich layers (Fig. 3.20 B), occurs locally.

Petrographic description (samples GH43, 48, 82)

Two-feldspar rhyolite tuff (ignimbrite)

Crystals of K-feldspar, plagioclase and minor quartz and biotite, ≤2-3 mm in size, are set in a microcrystalline matrix. Rare lithic fragments are also present. Apatite, zircon, fluorite and titanite are present as accessories. Plagioclase is up to 1-2 mm across, unzoned (albite), and commonly turbid due to the very fine grained alteration (kaolinite-type and sericite). Biotite, ≤1 mm in size, is partly altered to chlorite, fine grained titanite and Fe-Ti oxide. It locally includes lens-shaped fluorite along the cleavage. Biotite is oriented parallel to the bands of the rock (Fig. 3.20 C). Quartz occurs as rare, anhedral and angular grains, ≤1 mm in size. Opaque minerals occur as both small diamond shaped magnetite crystals (≤0.5 mm) and euhedral to anhedral crystals of Fe-Ti-Mn oxide showing µm-scale Ti-rich exsolutions. The matrix is fine grained (<20 µm), bedded, and composed of K-feldspar, quartz, albite and scattered Fe-Ti-Mn oxide. Bedding is defined by the orientation of lens-shaped quartz-rich domains (fiamme, sample GH43, Fig. 3.20 A, C), and by the orientation of crystals and lithic fragments. In other samples, bands are defined by alternating crystal-rich and crystal-poor, mm- to cm-thick layers (sample GH82, Fig. 3.20 B, D). Crystal-poor layers are mostly composed of devitrified flattened glass shards (now aggregates of very fine grained quartz and K-feldspar). These bands locally wrap around crystals, creating pressure shadows filled with aggregates of fine-grained quartz. At the microscale, fiamme represent well distinct compositional and textural domains, being mainly composed of microgranular aggregates of rounded quartz with a more or less developed granoblastic texture, K-feldspar and minor chlorite, fluorite, biotite and opaque minerals. Round vesicles are locally present (sample GH43). They are a few mm in diameter and filled with radially oriented quartz, epidote, chlorite and Y-bearing fluorite.

3. OTHER VOLCANICLASTIC FACIES

These rocks are too thin to be indicated on the map, but are reported in the detailed log. They include up to 20-25 m of grey or red-purple massive deposits at the base (Fig. 3.21 A). The upper part is composed of 1-2 m of planar bedded deposits. These tops are composed of: 1) well-sorted, thinly laminated buff-coloured mudstone showing a mm-spaced planar bedding (Fig. 3.21 B); or 2) alternating layers of breccia and sandstone (Fig. 3.21 C, D). The breccia is poorly-sorted and contains angular fragments of basalt, up to several centimetres in size, in a sand-grainsized, diffusely bedded matrix. The bedded tops are southeast-dipping at gentle angles (dip 17-30°). The massive basal portions of the deposits show scarce lateral continuity (tens of m) and a concave upwards base contact, whereas the top portions are flat and extend laterally for hundreds of metres and gradually pinch out. Also intercalated between basalts are massive to mm-scale bedded dark grey-black, deposits. These deposits are mostly aphanitic, therefore not easily distinguishable from basalts on the field, but can be locally quartz-bearing.

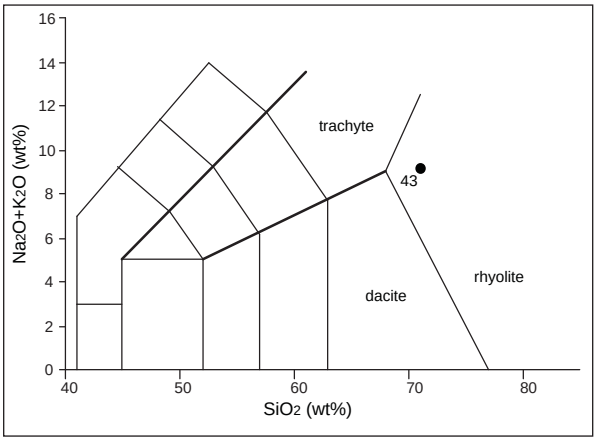

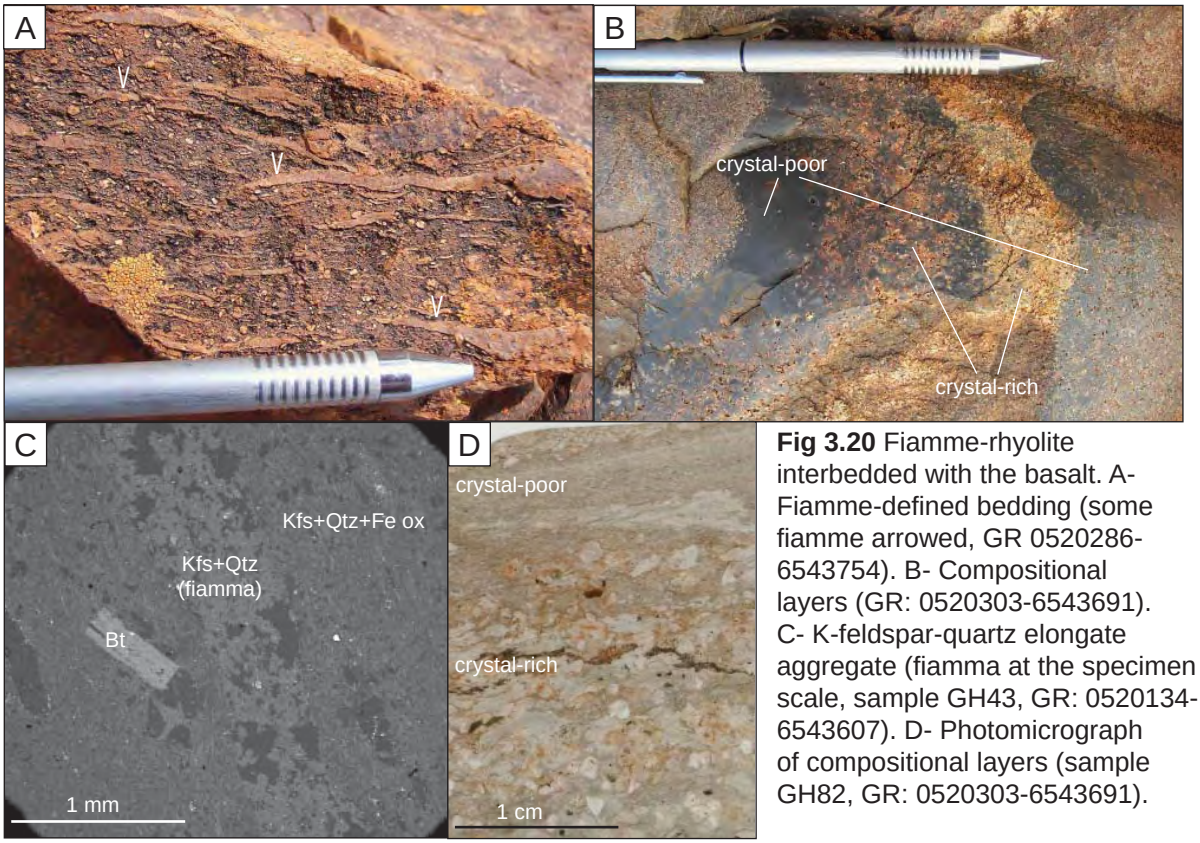

Fig 3.20 Fiamme-rhyolite interbedded with the basalt. A- Fiamme-defined bedding (some fiamme arrowed, GR 0520286-6543754). B- Compositional layers (GR: 0520303-6543691). C- K-feldspar-quartz elongate aggregate (fiamma at the specimen scale, sample GH43, GR: 0520134-6543607). D- Photomicrograph of compositional layers (sample GH82, GR: 0520303-6543691).

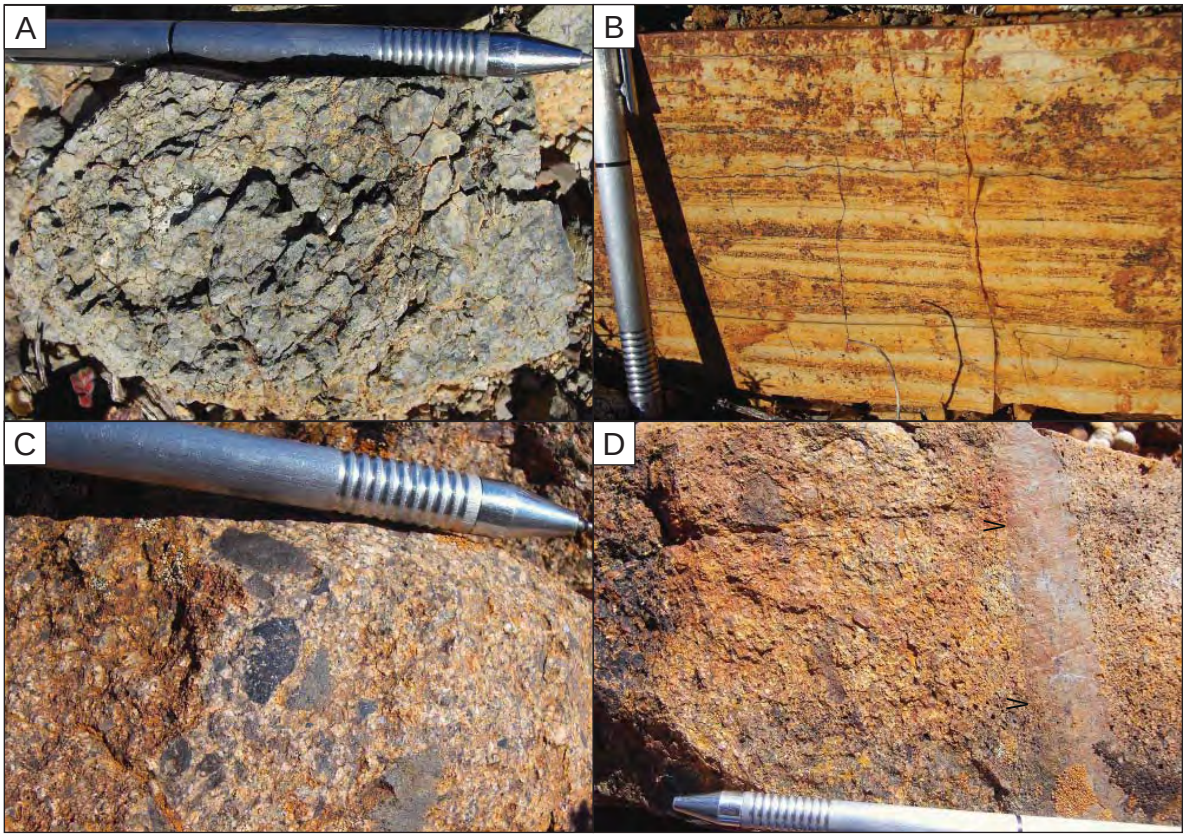

Fig 3.21 Volcaniclastic facies interlayered with the basalt, Kokatha. A massive deposit forms the base of the pyroclastics (A, GR 0520046-6543908). The tops are composed of bedded mudstones (B, GR 0520036-6543898) or interlayering breccia (C) and sandstone (D, sandstone arrowed, GR 0519949-6543953).

RHYOLITE-DACITE Mi2 (*Rhyodacite Pac2* of Blissett, 1977b and *Mi2* of PIRSA, 2006)

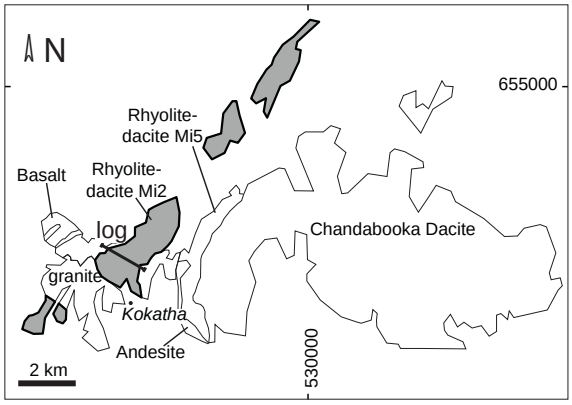

Field description

The unit includes a variety of rocks, generally sparsely feldspar-phyric (<10 vol.%) and massive to banded, stratigraphically situated between the underlying Basalt and the overlying Lake Gairdner Rhyolite. Some of the facies are dark red or purple, porphyritic with feldspar phenocrysts and rare lithic fragments, and locally vesicular/amygdaloidal. Other facies are dark grey, aphanitic, with a conchoidal fracture. Millimetre-spaced flow bands are particularly evident at the top and base of the unit. The bands (Fig. 3.22 A) are defined by alternating reddish, grey (quartz-rich) and black aphanitic layers and locally, by an orientation of phenocrysts. Elongate fiamme are parallel to the bands at the base of the unit. The flow bands show a variable orientation, ranging from low- to moderate-angle at the base of the unit to steep or subvertical in the central part and top of the unit. The flow bands are locally folded at the dm-scale and contain an ~east-southeast-oriented elongation lineation (flow direction Fig. 3.22 B). The base contact with the Basalt is concealed under debris on the northern slopes of Chitanilga Hill. Above the contact, mm-spaced flow bands dip southeast at a moderate to low-angle (dip direction 152-160, dip 14-33), generally consistent with the orientation in the basalts. The top contact is exposed two km east of Chitanilga Hill, where the Rhyolite-dacite Mi2 apparently passes into the overlying Lake Gairdner Rhyolite with an increase in the amount of feldspar and the appearance of ubiquitous quartz phenocrysts (gradational contact?). Below the top contact, the Rhyolite-dacite Mi2 is feldsparphyric and massive to banded. Flow bands are defined by alternating brown-red and grey-black, laterally continuous layers, ≤1 cm thick. Flow bands are generally oriented at a high angle (dip direction 136, dip 63) and bent in open folds. The unit is intruded by granite at two distinct localities. West of Chitanilga Hill, the unit is intruded by the granite at the contact with the Basalt: angular fragments of both the volcanic units, ≤few m in size, are included into the granite. The second intrusive contact crops out discontinuously about 3 km northeast of Chitanilga Hill. Some fragments of Rhyolite-dacite Mi2 are included into the granite and small dykelets of fine grained granite, 1-2 cm thick, are present in the volcanic unit. The contact is sharp, without evident contact thermal effects in the host rock. The granite at the contact is porphyritic to seriate, with phenocrysts of feldspar, ≤5 mm across, in a finer groundmass.

Petrographic description (samples GH34, 35)

Albite-phyric rhyolite-dacite lava

The samples are sparsely porphyritic (phenocryst abundance <5 vol.%) and banded at the mm-scale with phenocrysts of plagioclase (albite), up to 1-2 mm in size, set and in a microcrystalline (grainsize ≤10 μm) groundmass, mainly composed of K-feldspar, albite, quartz and Fe-Ti oxide. Apatite, Ti oxide and minor monazite and REE-fluoro-carbonate (synchysite?) are present as accessories (Fig. 3.22 C). The bands are defined by variations in the relative abundance of very fine grained opaque minerals. The bands are locally deformed, wrapping around phenocrysts. Plagioclase forms anhedral and compositionally

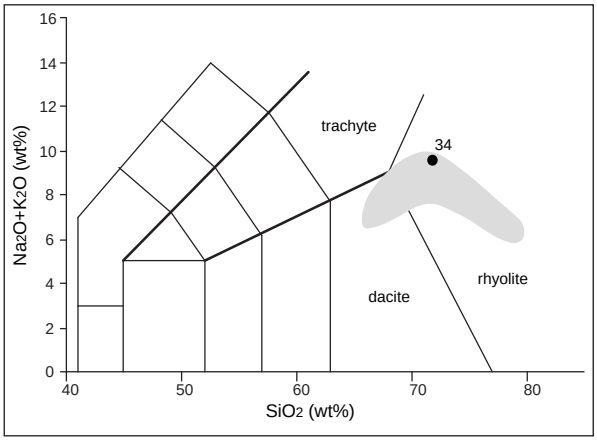

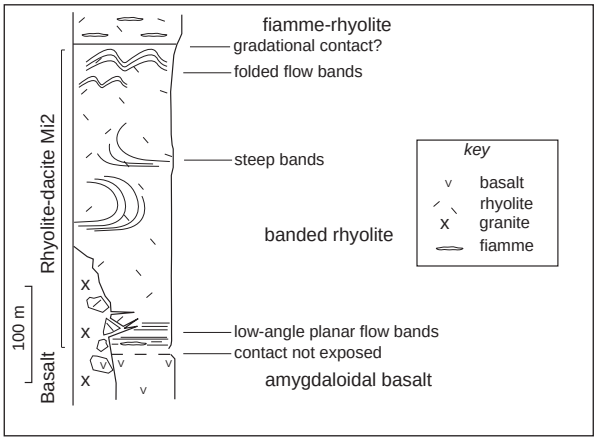

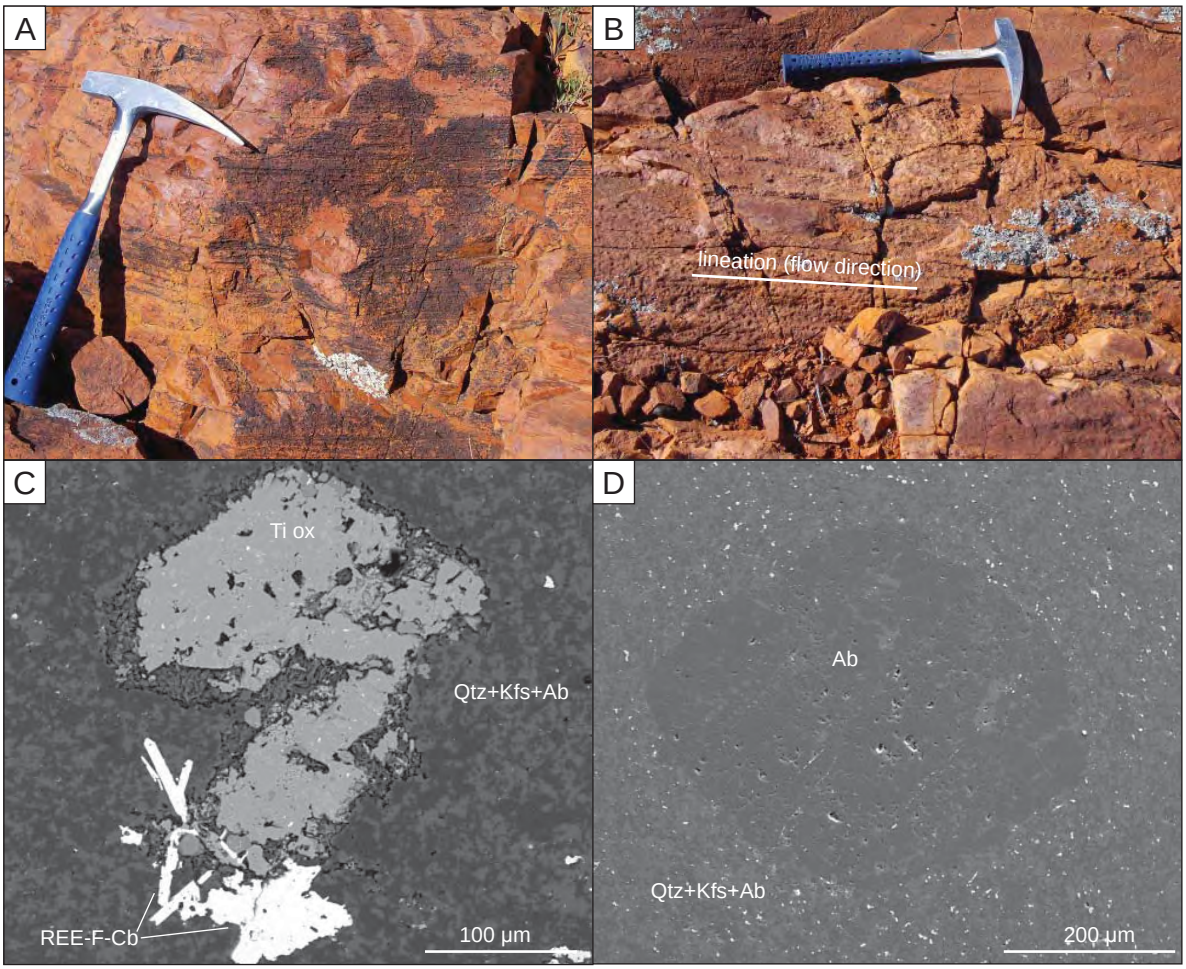

Fig 3.22 Rhyolite-dacite (Mi2). A- Fine planar bands at the base of the unit (GR 0521546-6543190). B- Flow-bands deformed in a decimeter-scale open fold at the top of the unit. An elongation lineation indicates ~west-southwest flow direction (GR 0523557-6542808). C- Ti oxide and REE-fluoro-carbonate (sample GH35, BSE, GR 0524220-6543611). D- Subhedral albite phenocryst in a microcrystalline groundmass (sample GH34, BSE, GR 0524277-6543641).

homogeneous phenocrysts, partly altered to sericite (Fig. 3.22 D). Locally, phenocrysts are partially replaced by pseudomorphic aggregates of quartz and Y-bearing fluorite (sample GH34). Elongate and aligned vesicles are locally present (sample GH35). These vesicles are filled with quartz, epidote, fluorite, chlorite ±titanite ±REE-fluoro-carbonate ±baryte (amygdales). The groundmass surrounding the vesicles is characterised by a concentric zoning defined by an inhomogeneous distribution of quartz, feldspars and Fe-Ti oxides.

LAKE GAIRDNER RHYOLITE (and Equivalent, of Blissett, 1977b, 1985)

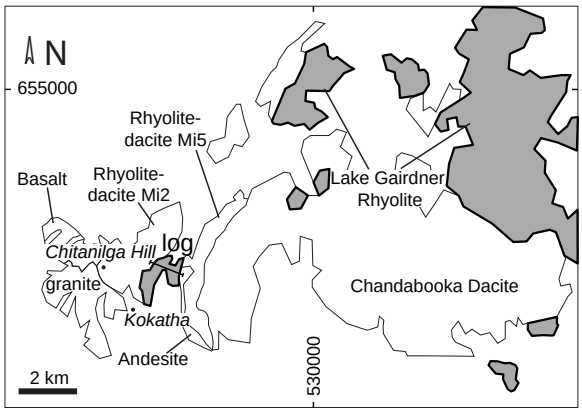

Field description

The Lake Gairdner Rhyolite crops out intermittently over a vast area (>20 km across). Rocks mapped as Equivalent of Lake Gairdner Rhyolite by Blissett (1977b; 1985) are included in the main sequence of the Chitanilga Volcanic Complex and crop out a few km northeast of Kokatha Homestead. These are dark brown to brown-red and contain crystals and crystal fragments of pink feldspar and quartz, up to a few mm in size, set in a dark fine grained matrix. A mm-spaced orientation is mostly defined by fiamme, up to a few cm long (Fig. 3.23A). Minor lithic fragments, up to some tens of cm in diameter and composed of a banded or aphanitic mudstone, are locally present. The unit is approximately 400 m thick and overlies the Rhyolite-dacite Mi2 with an angular unconformity: the fiamme-defined orientation dips south to southeast at a weak to moderate angle (≤38°). At the top, the unit is in contact with the Andesite in the western part of the outcrop area and with the Chandabooka Dacite farther east. Approximately 2 km northeast of Kokatha Homestead, west of the road to Kingoonya (GR 0523942-6542662), a conglomerate crops out intermittently for 200-300 m. This deposit, several m-thick, is massive and clast-supported, with rounded and highly spherical clasts, up to 20 cm in diameter (Fig. 3.23 B). The clasts are mainly composed of a feldspar- and ±quartz-phyric rock, with a dark red-brown aphanitic groundmass, similar to the underlying Rhyolite-dacite (Mi2). The conglomerate is overlain by a thin (<1 m) pack of planar-bedded sandstone to fine breccia, gently dipping to the southeast (dip direction 125, dip 10). At the top of the unit, cm- to dm-thick layers of breccia alternate with thin layers of siltstone and sandstone (Fig. 3.23 C). Breccia layers include mm- to cm-scale angular fragments of feldspar- and quartz-phyric rocks in a sandstone matrix. The fine grained layers show traction structures (ripples). These deposits dip gently towards the east-southeast (dip direction 106-108, dip 16-18). At both base and top of these deposits, the Lake Gairdner Rhyolite is particularly rich in angular lithic fragments, up to a few cm in size and composed of an aphanitic rock.

Petrographic description (samples GH51, 87)

Two-feldspar banded rhyolite tuff (ignimbrite)

Rocks included in the Lake Gairdner Rhyolite are massive to banded and contain quartz, K-feldspar and plagioclase crystals and crystal fragments, ≤2 mm in size, ~20 vol.% of the rock, and minor lithic fragments in a eutaxitic, fine grained matrix (Fig. 3.23 D). The matrix is mainly composed of K-feldspar, quartz and very fine grained Fe-Ti oxide. Titanite and zircon are present as accessory minerals. Feldspar forms subhedral to anhedral crystals, altered to a very fine grained, semi-opaque product (kaolinite-type) or sericite. Rare angular lithic fragments of a very fine grained rock are present. In some cases they contain epidote and an opaque mineral, possibly an altered femic rock. In the matrix, platy and cuspate devitrified bubble-wall shards, <500 µm in size and partly flattened, are recognisable (Fig. 3.23 E). At the microscale, the bedding of the rock is defined by the orientation of shards, by the distribution

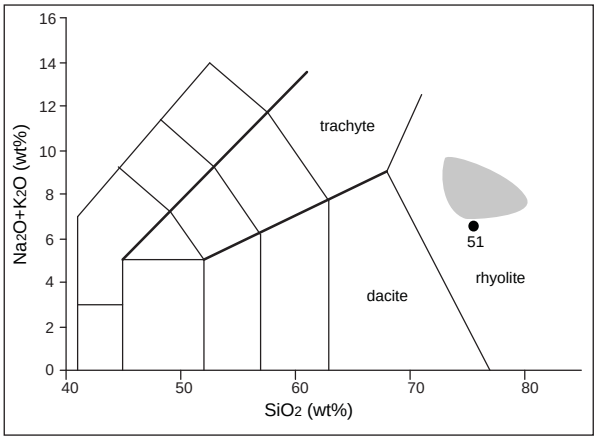

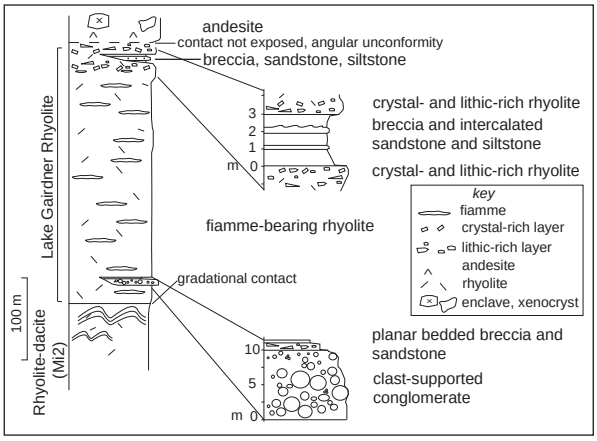

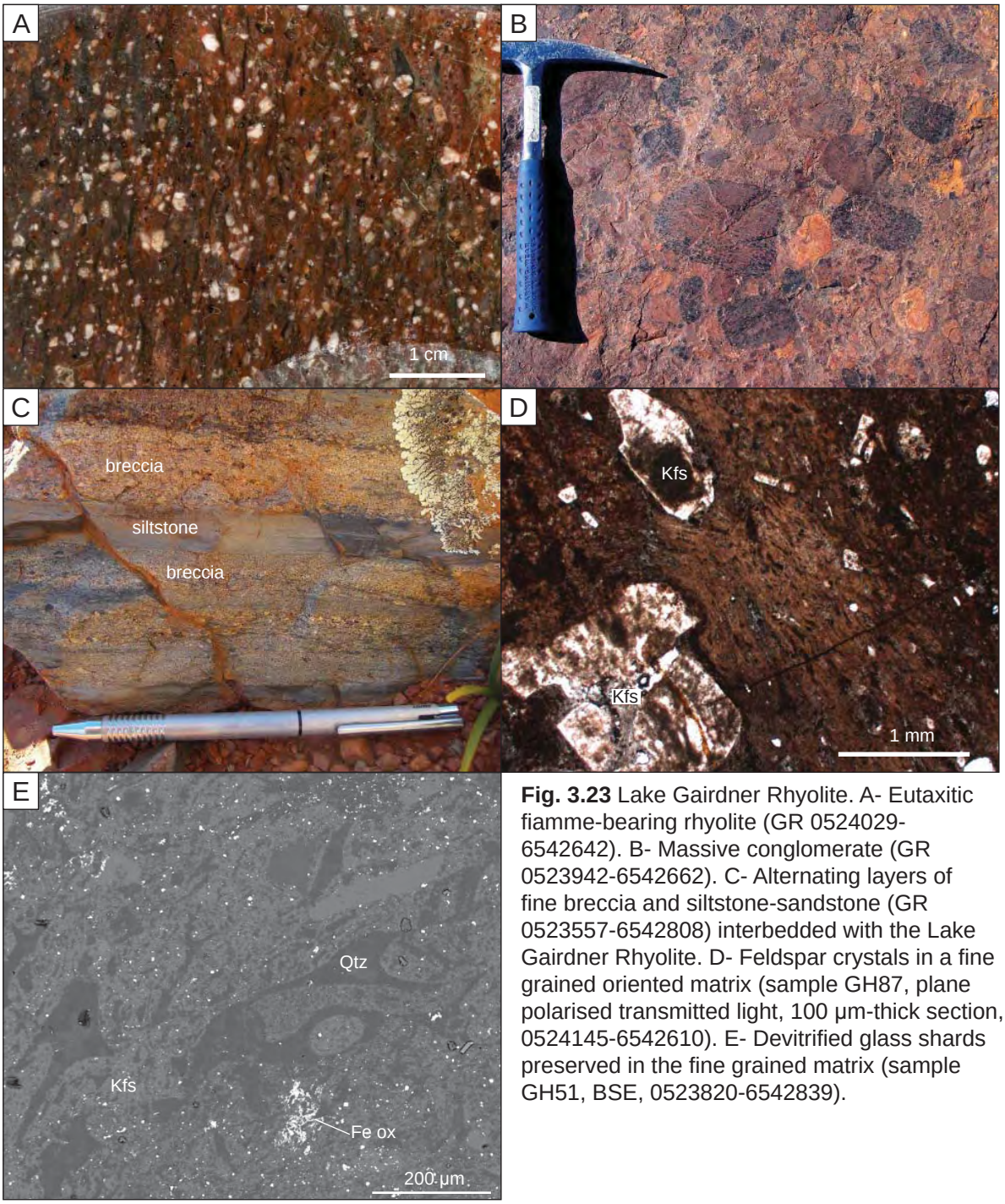

Fig. 3.23 Lake Gairdner Rhyolite. A- Eutaxitic fiamme-bearing rhyolite (GR 0524029-6542642). B- Massive conglomerate (GR 0523942-6542662). C- Alternating layers of fine breccia and siltstone-sandstone (GR 0523557-6542808) interbedded with the Lake Gairdner Rhyolite. D- Feldspar crystals in a fine grained oriented matrix (sample GH87, plane polarised transmitted light, 100 µm-thick section, 0524145-6542610). E- Devitrified glass shards preserved in the fine grained matrix (sample GH51, BSE, 0523820-6542839).

of magnetite and, to a lesser extent, by the orientation of crystals and lithic fragments (Fig. 3.23 D). In some cases, the bands are plastically deformed and wrap around crystals and lithic fragments, thus suggesting a compaction has taken place after deposition.

ANDESITE

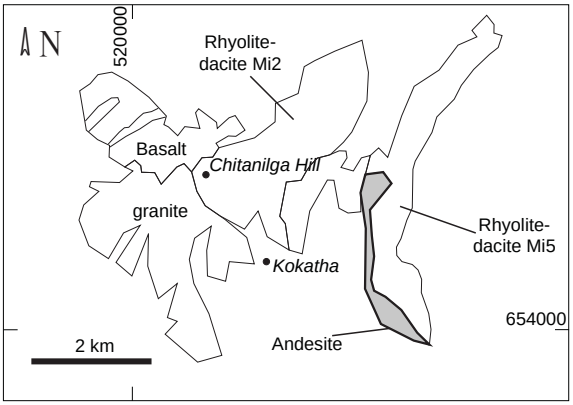

Field description

The Andesite crops out east of Kokatha Homestead in a north-northwest-striking, ~4 km long and 20-30 m thick prominent cliff. The unit dips east to northeast at a moderate angle (~30-40°). These rocks are dark green or greenish-grey, massive and sparsely porphyritic (phenocryst <1 vol.%) with feldspar and femic phenocrysts, a few millimetres in size, set in an aphanitic groundmass.

Near the upper contact, the andesite contains abundant quartz and feldspar xenocrysts and felsic enclaves. Quartz is strongly anhedral (amoeboid), feldspar is euhedral to subhedral and shows a reddish alteration rim (Fig. 3.24 A). Enclaves are up to a few tens of centimetres across, massive or foliated, and composed of medium grained feldspar and quartz (Fig. 3.24 B). The top and base contacts of the Andesite are not exposed. However, the orientation in the underlying unit suggest an angular unconformity exists at the base of the andesite. The overlying Rhyolite-dacite Mi5 shows bedding orientation similar to the andesite.

Petrographic description (samples GH39, 52)

Clinopyroxene-bearing andesite lava with xenocrysts of K-feldspar and quartz

The andesite is porphyritic to glomerophyric with K-feldspar, clinopyroxene and plagioclase phenocrysts, up to a few mm long, in a fine grained groundmass (grain size <50 µm) mainly composed of plagioclase, K-feldspar, quartz and opaque minerals. K-feldspar phenocrysts are mostly fractured, intensely altered to sericite and a very fine grained kaolinite-type product. Larger K-feldspar crystals (>0.5 mm) are anhedral and sieve-textured (possibly of xenocrystic origin), whereas the smaller ones (≤0.5 mm) are mostly euhedral. Plagioclase (oligoclase) forms unzoned phenocrysts, up to 1 mm long. Clinopyroxene (slight pleochroism pale green-pale yellow/colourless, δ≈0.026, c^γ≈45°) forms anhedral phenocrysts up to a few mm across, partially altered to green amphibole. Amphibole (pleochroism γ-green > β-light green > α-light yellow, δ=0.018-20, c^γ≈30°, actinolite type) occurs as an uralitic alteration of pyroxenes and in the groundmass with the same optical characteristics. Plagioclase and clinopyroxene (or uralitic amphibole) also occur as glomerophyric aggregates (Fig. 3.24 C). The groundmass is fine grained and composed of feldspar, interstitial quartz and magnetite. Quartz crystals and fragments showing wavy extinction, surrounded by a rim of green amphibole (possibly of xenocrystic origin, Fig. 3.24 D), are associated with the occurrence of quartz-feldspar enclaves.

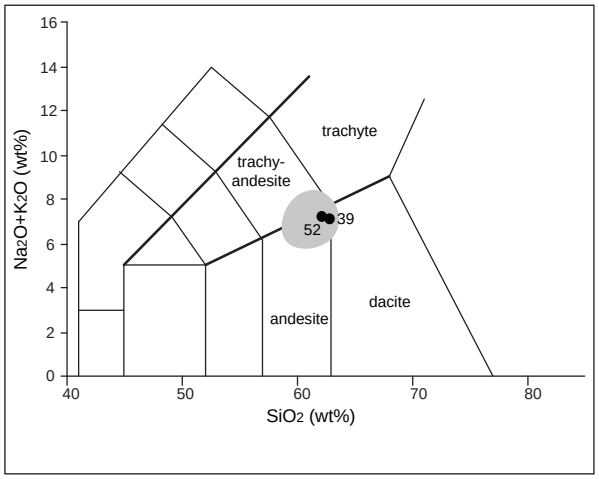

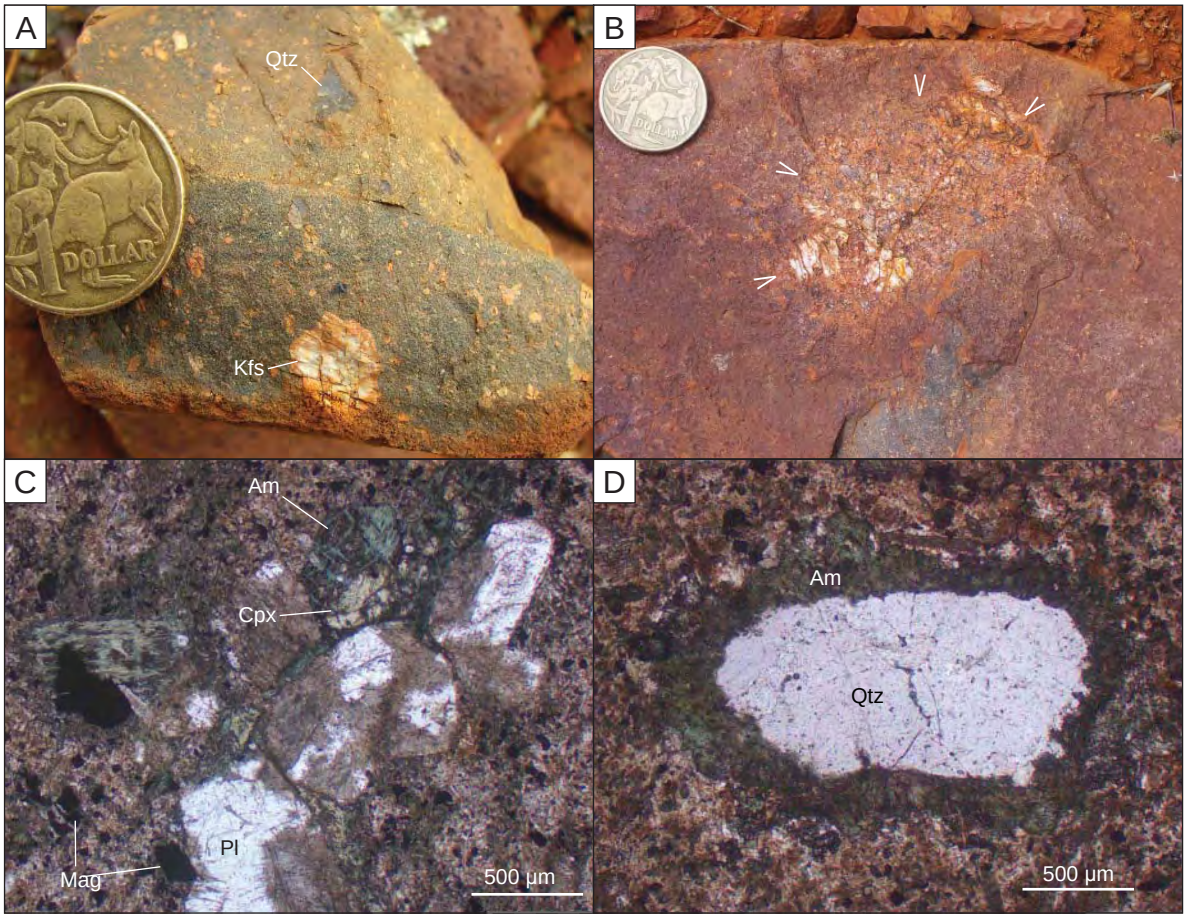

Fig 3.24 Andesite. Quartz and K-feldspar grains (A) and felsic enclaves (B) in porphyritic, massive andesite (margin of enclave arrowed, GR 0524795-6542198). C- Glomerocrystic plagioclase and amphibole-altered clinopyroxene (sample GH39, plane polarised transmitted light, GR 0525051-6540439). D- Amphibole-rimmed quartz (sample GH52, plane polarised transmitted light, GR 0524820-6542202).

RHYOLITE-DACITE (Mi5) (Rhyodacite *Pac5* of Blissett, 1977b, or *Mi5* of PIRSA, 2006)

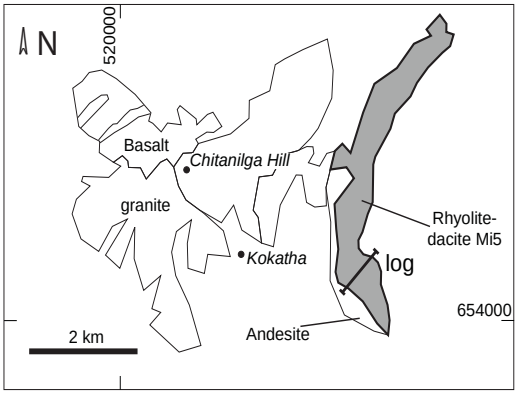

Field description

This unit includes dark red-purple rocks with cream-coloured, anhedral crystals of feldspar, up to a few mm in size, and minor quartz. In the upper portion of the unit the rock becomes progressively nearly aphanitic. The rock shows a banded texture with oriented crystals and millimetre to centimetre-spaced bands. These bands are defined by an alternation of purple-red, crystal-poor layers and brick-red, crystal-rich layers (compositional banding, sample GH83). The oriented texture of the rock is also defined by light-coloured lenses (fiamme), a few mm thick, particularly common in the lower portion of the unit, and evidenced by weathering. The succession, ~300 m-thick, is exposed 2 km east of Kokatha Homestead. The base of the unit (up to ~10 m above the underlying andesite) shows a mm-scale planar lamination (interval A in the log, sample GH40), dipping north to northeast at a moderate angle. Elongate fiamme (≤tens cm long) are parallel to the laminae. This orientation suggests a conformable contact with the Andesite. The central and upper parts (intervals B1 and B2) are layered at the cm-scale and flow folded. Sparsely porphyritic internally banded layers alternate with crystal-rich, massive layers. Fold style varies across the outcrop area from open to isoclinal, and ptygmatic folds are also present (Fig. 3.25 A, B, C). Ptygmatic folds originate in layers having a high viscosity contrast and at high degrees of shortening. Axial surfaces of asymmetric folds are predominantly east-southeast striking and south-southwest-dipping. An elongation lineation, present on some of the folded surfaces, shows a southwest-northeast direction. In the higher portion of the unit (B2), isoclinal folds are predominant. The axial planes of isoclinal folds are southwest-dipping and a southwest-northeast lineation is contained in the folded bands. The lineation is consistently oriented southwest-northeast (Fig. 3.25 D), whereas the angle between lineation and fold hinge line is strongly variable, from high (lineation and hinge line are nearly perpendicular) to very low (sub parallel, Fig. 3.25 C). This suggests that hinge lines are strongly curvilinear, as typical is sheath folds. These cinematic indicators are consistent with a northeastward-directed flow deformation. Medium- to coarse-grained feldspar-quartz cm-scale felsic enclaves and xenocrysts, common in the Andesite, are also locally present in the Rhyolite-dacite Mi5. Enclaves are deformed and flattened in the flow bands.

Petrographic description (samples GH40, 83)

Banded rhyolite tuff with crystals of plagioclase and K-feldspar

Next to the base contact (interval A, sample GH40, GR 0525031-6540512), the Rhyolite-dacite Mi5 contains plagioclase and K-feldspar crystals (<5 vol.%) set in a very fine grained banded matrix composed of quartz, K-feldspar, magnetite and chlorite. Plagioclase (albite) and minor K-feldspar are up to 1 mm across and sericitised. The lamination of the rock is defined by a selective alteration of fine grained feldspar in lens-shaped domains, <1 mm thick (fiamme at the specimen scale). Quartz-magnetite-bearing veinlets, few µm-thick, are parallel to the laminae. Further up in the sequence (interval B, sample GH83, GR 0525046-6541144), the rock shows mm- to cm-scale bands, defined by grain size variations. Very fine grained, crystal-poor and opaque (Fe and Ti oxide)-rich layers alternate with coarser-grained layers containing abundant feldspar crystals and crystal fragments and quartz+opaque aggregates, up to 1-2 mm in size (Fig. 3.25 E-G). The fine grained layers are internally banded at the µm to tens of µm-scale. The internal bands wrap around feldspar crystals and are deformed in sub mm-scale asymmetric folds indicating viscous flow along the bands. Conversely, crystal-rich layers are internally massive and show little evidence of flow deformation.

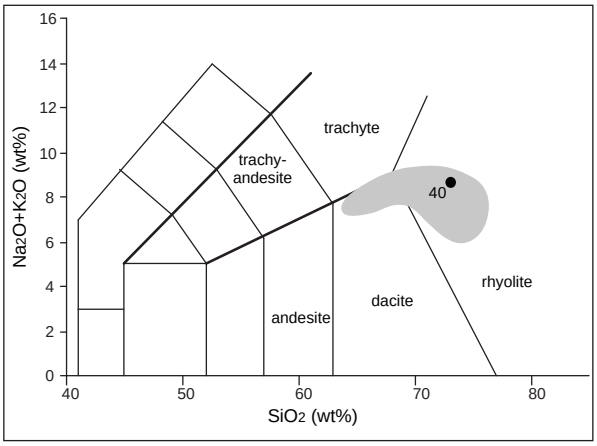

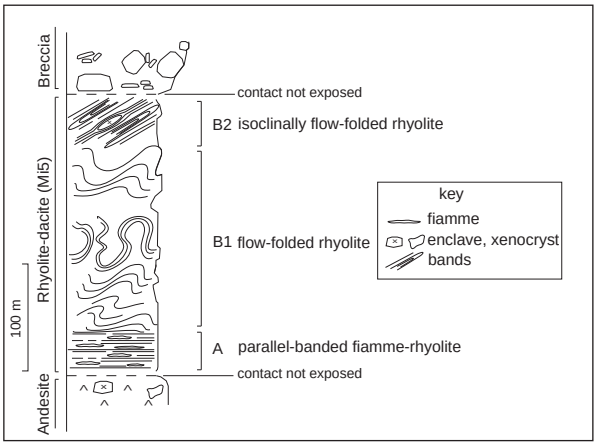

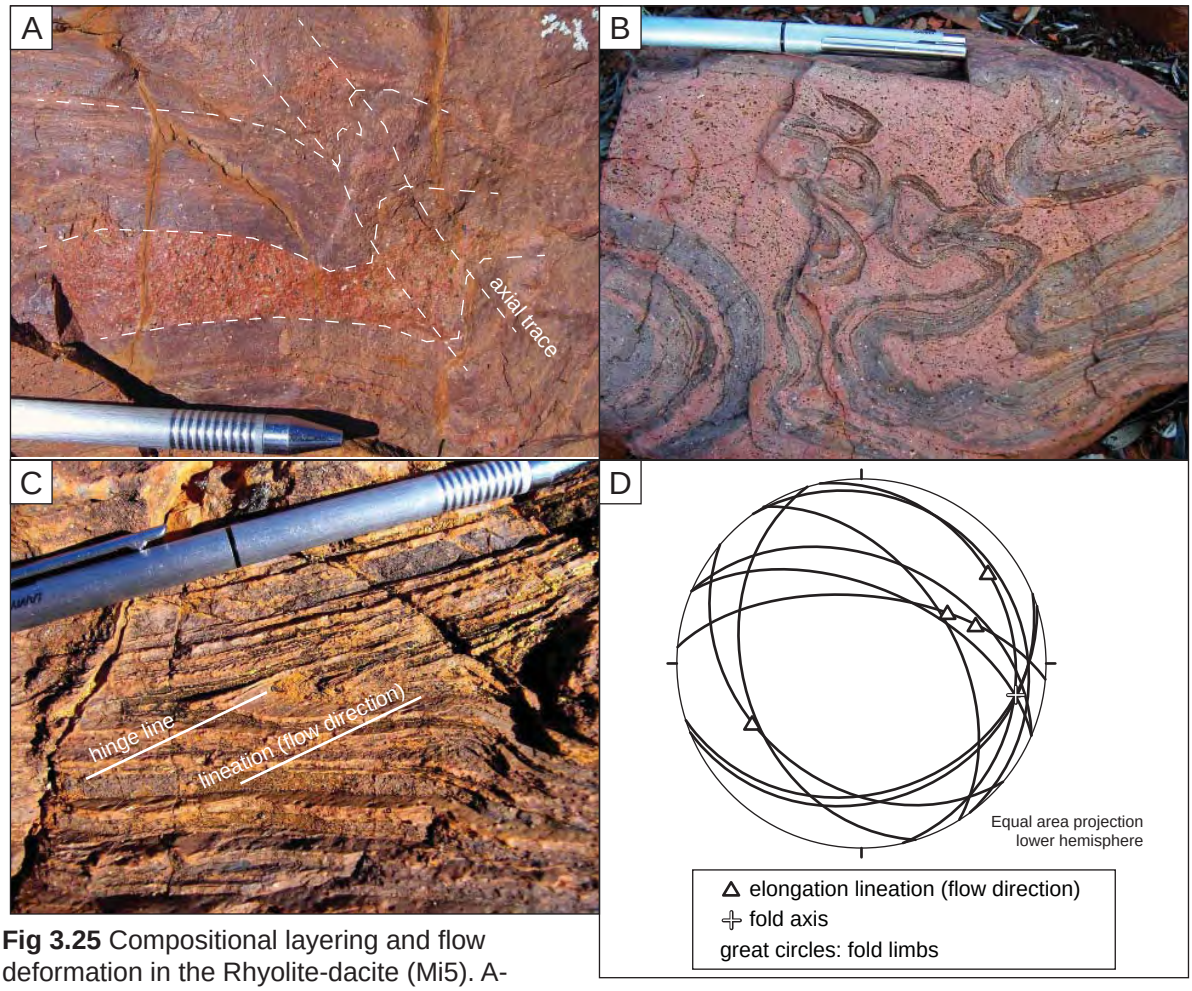

Fig 3.25 Compositional layering and flow deformation in the Rhyolite-dacite (Mi5). A- Open asymmetric folds (GR 0524988- 6541028). B- Ptygmatic folds (GR 0525008-6541038). C- Isoclinal fold showing parallelism between elongation lineation and hinge line (0525170-6541134). D- Stereographic plot of fold limbs, elongation lineation and fold axes. Deformation structures (lineation and fold limbs), together with the orientation of axial surfaces of asymmetric folds indicate a northwest-directed flow.

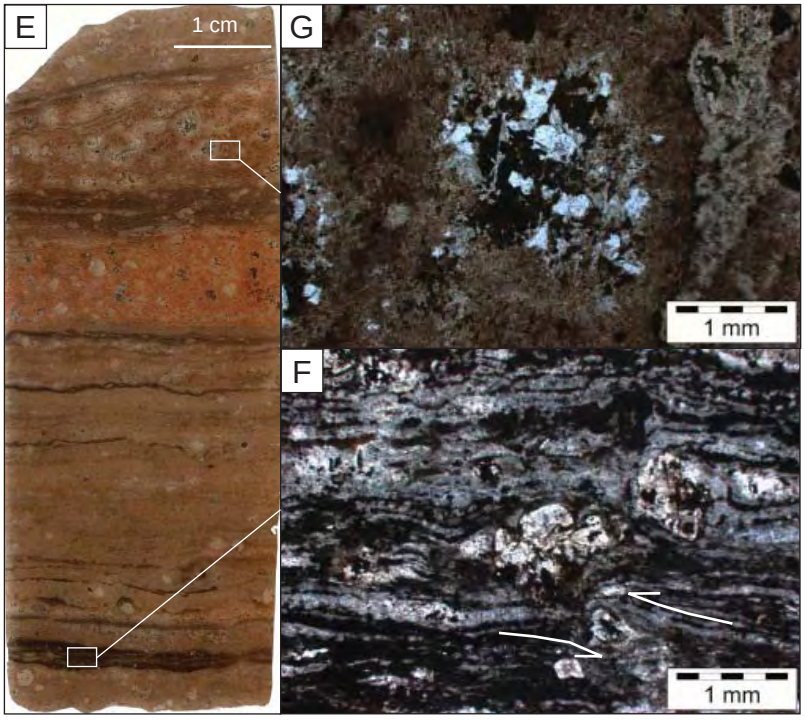

Fig. 3.25 (cont.). E, F, G- Alternating fine grained, crystal-poor, relatively opaque-rich and flow-deformed (arrows) layers (F), and coarser-grained, undeformed layers containing abundant feldspar crystals and quartz+opaque aggregates (G). Rhyolite-dacite (Mi5), Kokatha (sample GH83, plane polarised transmitted light, GR 0525046-6541144).

CHANDABOOKA DACITE

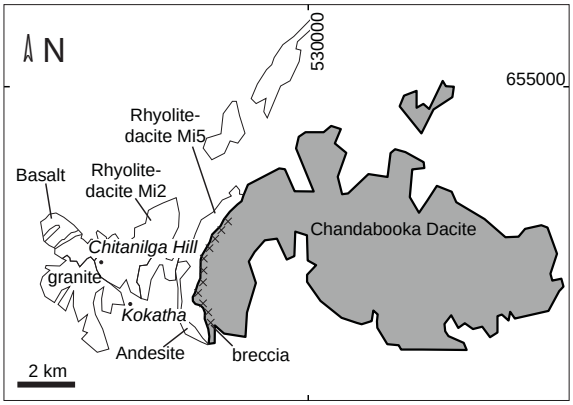

Field description

The Chandabooka Dacite crops out over a vast area east of Kokatha Homestead. It has been correlated with the Yardea unit of the upper GRV (Blissett, 1977b; 1985). The unit is composed of purplish brown evenly porphyritic rocks with cream white phenocrysts (<10 vol.%) of feldspar ±anhedral quartz in an aphanitic groundmass (Fig. 3.26 A). The groundmass locally has an oriented texture with millimetre-thick bands. The base of the unit is marked by laterally continuous breccia, with an apparent thickness of 100-200 m. This breccia is massive, unsorted, mostly clast-supported, and includes angular clasts, ≤tens of cm in size, in a reddish or cream-coloured aphanitic matrix (Fig. 3.26 B). The clasts are composed of massive to banded, sparsely feldspar-phyric rocks. The lithology of the clasts is similar to the Chandabooka Dacite.

Petrographic description (GH46)

Albite-phyric dacite lava

Phenocrysts of plagioclase (albite) and K-feldspar are set in a fine grained oriented groundmass mainly composed of quartz and K-feldspar. Fe oxide, Ti oxide, apatite and F-Ca-REE-fluoro-carbonate are present as accessories. Feldspar forms euhedral to anhedral unzoned, ≤3 mm-long phenocrysts and glomerocrysts, altered to epidote and calcite. K-feldspar phenocrysts show sieve texture. The groundmass is finely banded. The bands, defined by alternating quartz- and K-feldspar-rich layers (Fig. 3.26 C), are slightly deformed and wrap around phenocrysts. Prisms of apatite and very fine grained Ti oxide and a F-Ca-REE-carbonate form rounded aggregates (Fig. 3.26 D). Apatite is also included in feldspar phenocrysts. Baryte (Sr-bearing, EDS) occurs as a late mineral, deposited along thin fractures crossing both phenocrysts and the groundmass.

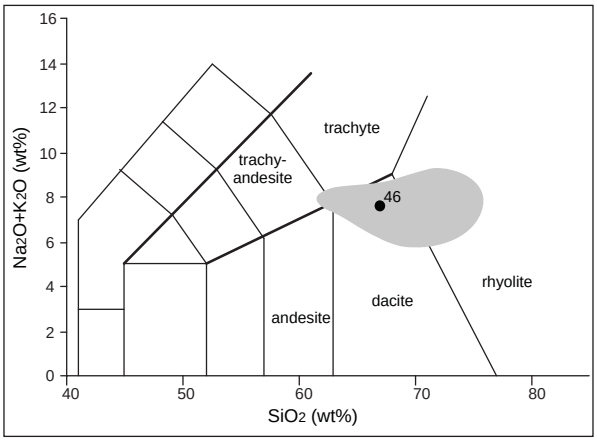

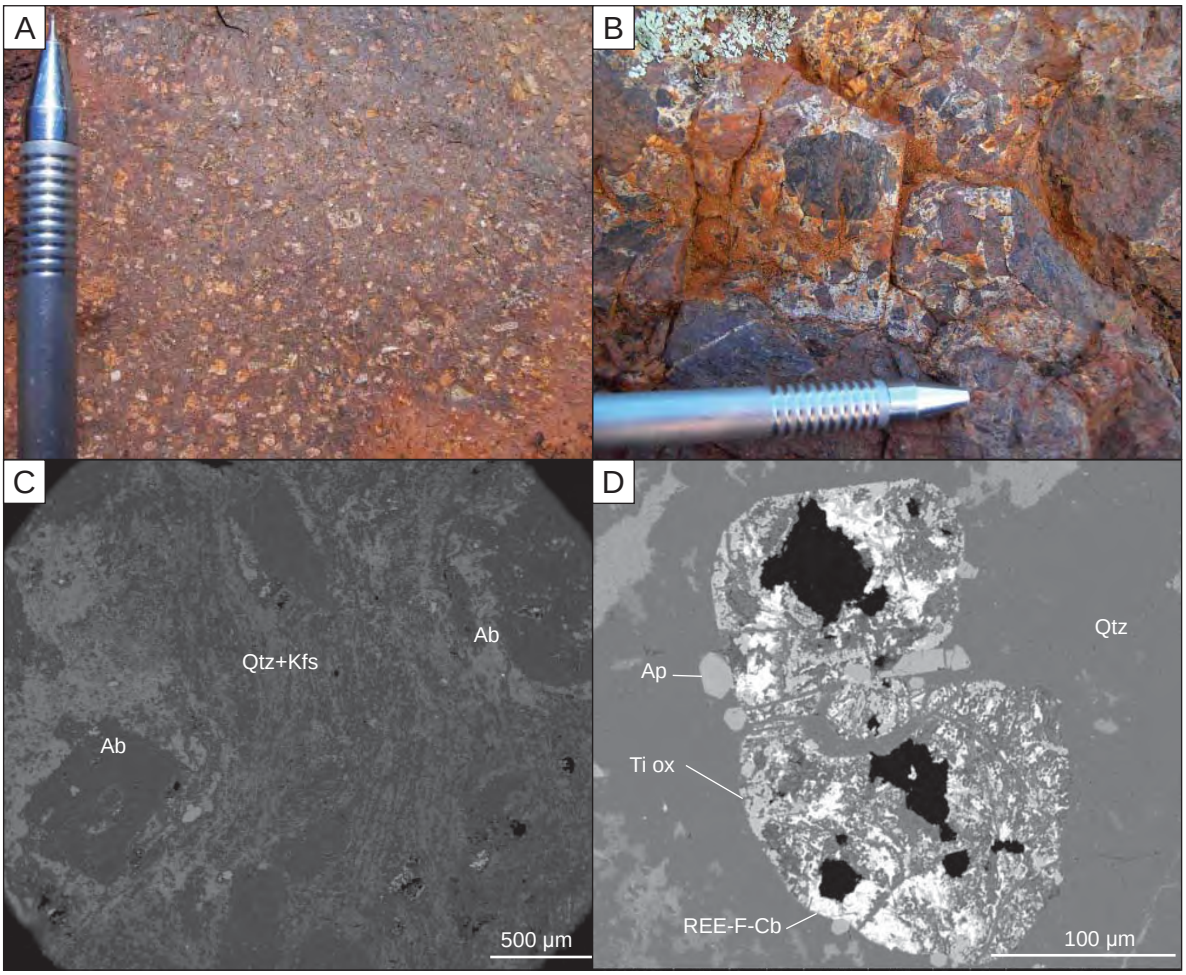

Fig. 3.26 Chandabooka Dacite. A- Feldspar phenocrysts in an aphanitic groundmass (GR 0538919-6541550). B- Massive breccia at the base of the Chandabooka Dacite (GR 0525505-6540980). C- Albite phenocrysts in a thinly banded quartz+K-feldspar groundmass (sample GH46, GR 0533107-6546128). D- Apatite+REE-fluoro-carbonate+Ti oxide aggregate (sample GH46).

MICROGRANITE DYKES

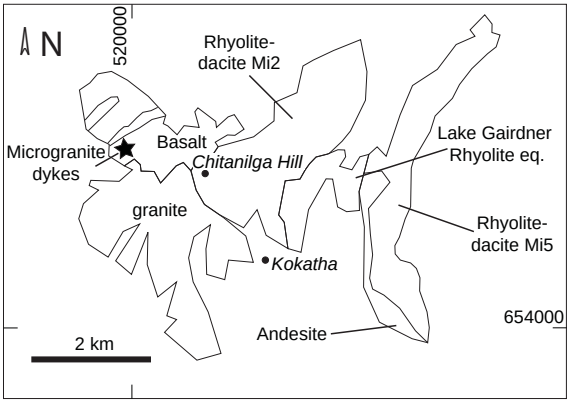

Field description

Microgranite dykes, fine-medium grained (≤3 mm) and seriate-textured, are locally intruded into the Basalt. Feldspar and quartz are the major mineral phases, biotite is a minor constituent (Fig. 3.27 A). The dykes are less than 1 m wide, randomly oriented and show a lateral continuity of several tens of metres. The contact with the host rock is sharp (less than few cm wide) and the texture is homogeneous.

Petrographic description (samples GH44, 91)

Topaz-bearing microgranite

The Microgranite dykes are composed of quartz, K-feldspar, plagioclase (albite) and a complex accessory assemblage including biotite, fluorite, topaz, Fe oxide, epidote, allanite, REE-fluoro-carbonate, monazite, titanite, muscovite and Nb-bearing Ti oxide. Quartz forms anhedral crystals, up to 2-3 mm across, typically showing wavy extinction. K-feldspar (microperthite) occurs as subhedral to anhedral crystals up to 1-2 mm in size. Quartz and K-feldspar locally show micro-granophiric textures. Plagioclase (albite) forms subhedral to anhedral unzoned crystals. Anhedral flakes of chlorite-altered biotite, ≤2 mm long, are interstitial to the major mineral phases. Topaz crystals are anhedral and fractured, ≤1 mm in size, partially altered to fine grained muscovite along fractures. Fluorite forms colourless to violet anhedral crystals, in some cases turbid due to the presence of very fine grained inclusions. It occupies an interstitial position between quartz and K-feldspar and is commonly associated with magnetite. In BSE images, two different types of fluorite can be distinguished: a bright and homogeneous, Y-rich fluorite, and BSE-darker and patchy, low-Y fluorite (Fig. 3.27 B). Epidote (green pleochroism, II order interference colours: epidote s.s.) is locally present (sample GH91) and occurs as anhedral and fine grained crystals distributed along veinlets or disseminated in the rock. Allanite is associated with epidote in aggregates interstitial between quartz and feldspars (Fig. 3.27 C). Monazite shows a rounded habit and is included in most of the major phases. It is surrounded by a pleochroic halo (radiation-damage structure). The REE-fluoro-carbonate occurs as anhedral, fine grained (tens of μm in length) crystals mainly included in fluorite (Fig. 3.27 D). Titanite is also anhedral and interstitial and contains appreciable amounts of Nb (EDS). Minor amounts of Ti oxide and zircon complete the accessory assemblage. Textural relationships suggest the following crystallisation order: Ab, Qtz+Kfs, Fl+Mag+Bt. Due to alteration, it is impossible to establish the textural relationship between topaz and the other mineral phases.

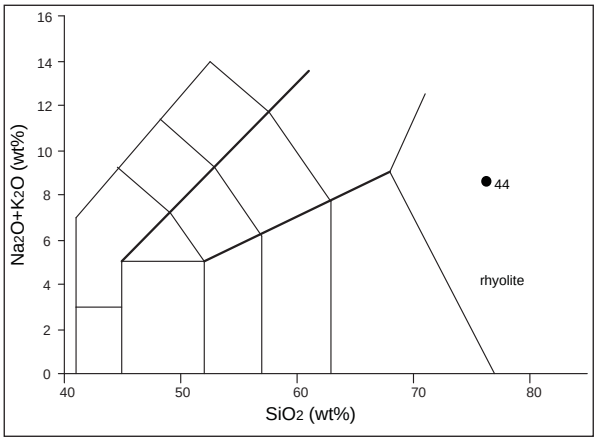

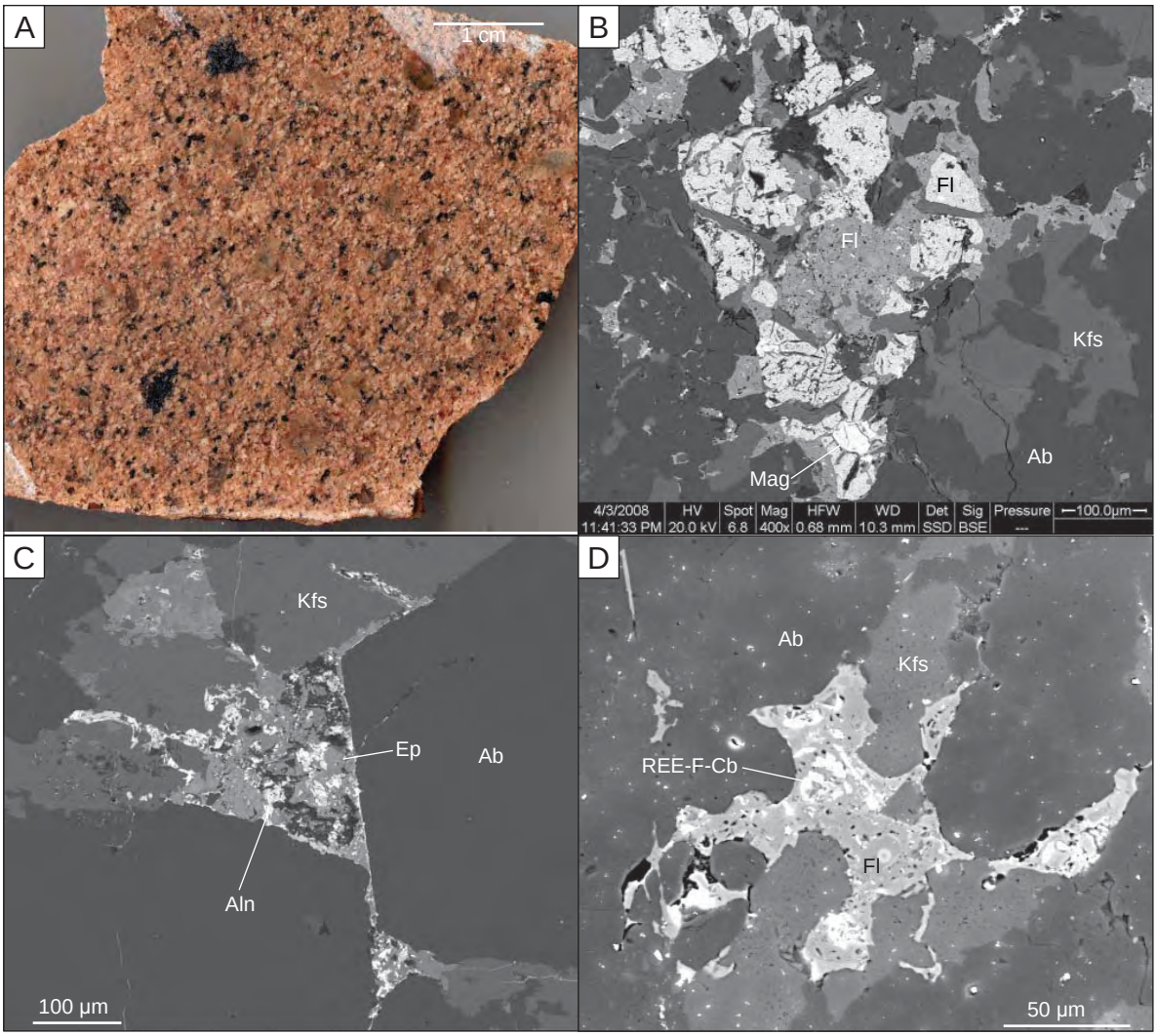

Fig. 3.27 Microgranite dykes intruded into the Basalt, Kokatha. A- Handspecimen of Microgranite dyke showing the seriate texture (sample GH79, GR 0519933-6543460). B- Interstitial fluorite+magnetite aggregate. An Y-rich (BSE-bright) and a Y-poor (BSE-dark) variety of fluorite can be distinguished (sample GH44, GR 0519864-6543748). C- Interstitial epidote and allanite (sample GH91, GR 0519948-6543638). D- Trace element- and volatile element-bearing minerals are concentrated in late, interstitial aggregates. Fluorite includes a REE-fluoro-carbonate (sample GH44).

HILTABA SUITE AT KOKATHA

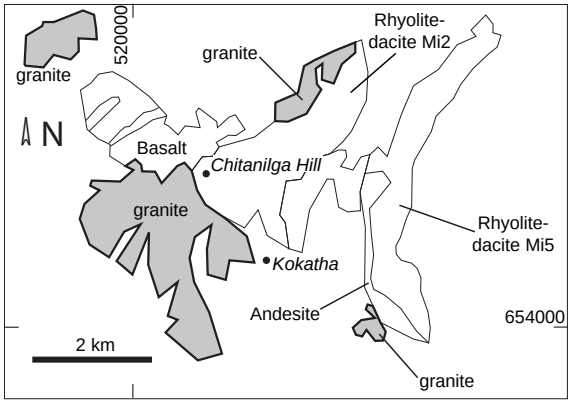

Field description

Granite of the Hiltaba Suite (Blissett, 1985) crops out at several localities in the Kokatha. The granite consists of pink, equigranular to seriate, massive, mostly medium-coarse grained rocks. The main components are feldspar, quartz and minor biotite. Locally, a fine grained and seriate facies of granite (microgranite) with the same colour and mineral assemblage is present. The microgranite forms dyke-like intrusions, up to several m thick, in the medium-coarse granite. Sharp contacts separate the two facies of granite (Fig. 3.28A). Rare thin (1-2 cm) quartz-bearing veins are present, laterally continuous for a few metres. Intrusive contacts with the volcanics can be observed at the base of the Chitanilga Volcanic Complex northwest of Chitanilga Hill, where fragments of basalt are included in the granite (Fig. 3.28 B), and 3 km northeast of Chitanilga Hill, where the contact cuts the flow bands in the Rhyolite-dacite (Mi2) and small dykelets are intruded into the host rock.

Petrographic description (samples GH37, 38)

Two-feldspar granite and microgranite

The granite includes leucocratic, equigranular- to seriate rocks, mainly composed of quartz, K-feldspar, plagioclase and biotite. The granite is mostly medium to coarse-grained (≤10 mm, sample GH37), and locally finer grained (≤2 mm, sample GH38). Fluorite, zircon, opaque minerals and apatite are common accessory mineral phases. Quartz and K-feldspar show relationship of mutual inclusion and intergrowth (granophyric) textures are also present. K-feldspar (string perthite) is altered to a very fine-grained, turbid alteration product. K-feldspar locally shows composite albite-pericline twinning (microcline). Plagioclase, minor compared to quartz and K-feldspar, shows albitic composition with a slight direct zoning. In some cases, albite is rimmed by K-feldspar. Biotite occurs as small (<0.5 mm) anhedral flakes, interstitial between feldspar and quartz (Fig. 3.28 C). Biotite includes lens-shaped quartz and violet fluorite oriented along the (001) plane. Other than biotite-hosted inclusions, fluorite forms anhedral colourless crystals, <1 mm across, interstitial to quartz and K-feldspar (Fig. 3.28 D).

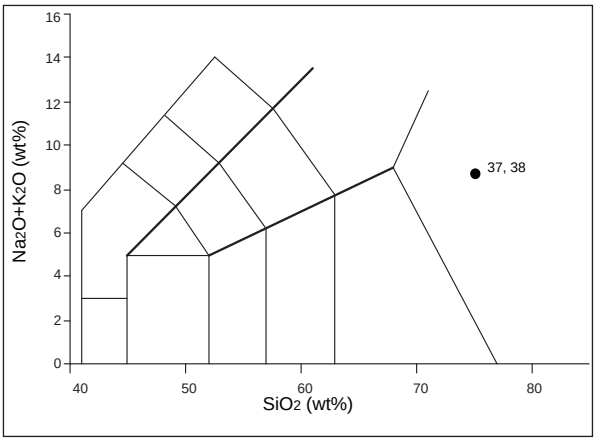

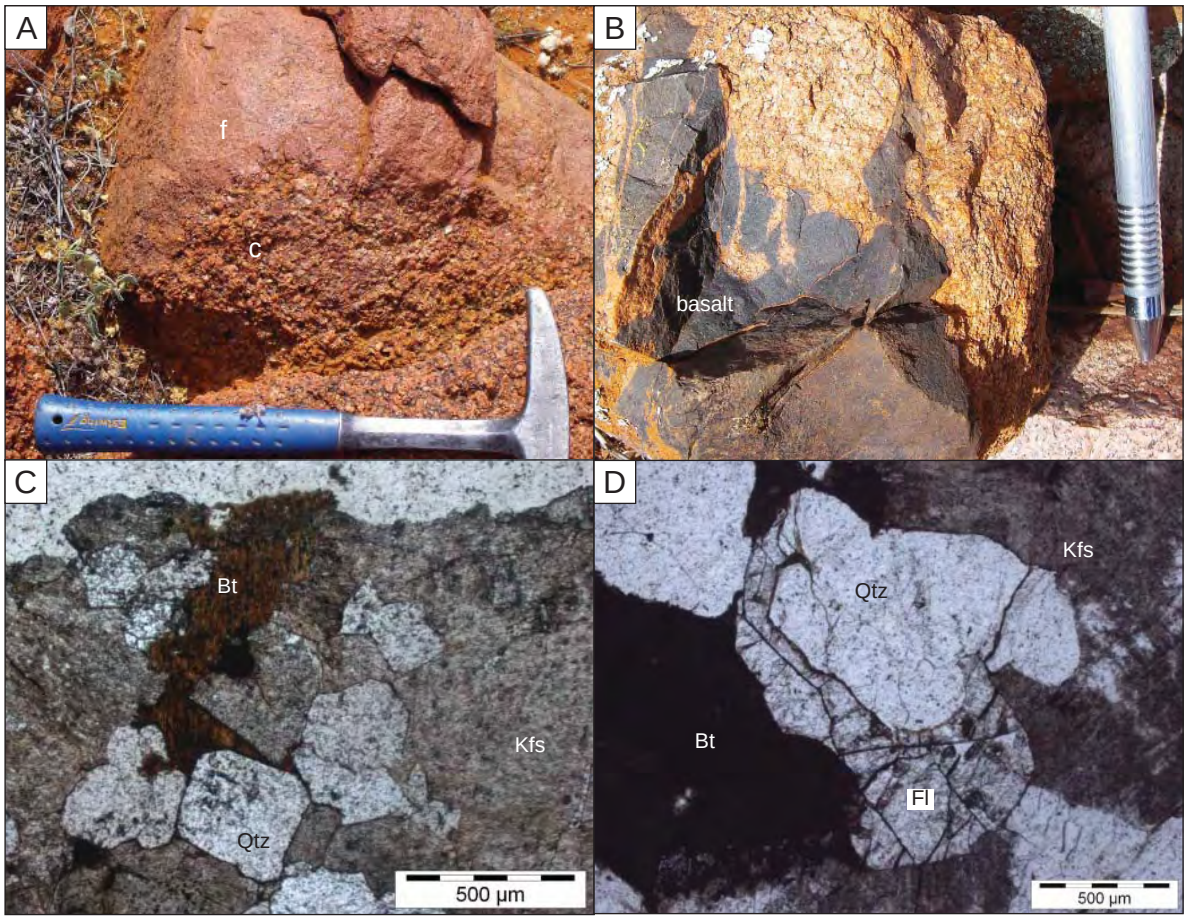

Fig 3.28 Hiltaba Suite granite at Kokatha. A- Contact between a medium-coarse grained (c) and fine grained (f) facies of granite (GR 0518870-6545808). B- Fragment of basalt included in the granite (GR 0520311-6543239). C- Biotite in an interstitial position between quartz and feldspar (sample GH38, GR 0518870-6545808). D- Fluorite interstitial between the other mineral phases (sample GH37, GR 0517317-6546439).

FELSIC ENCLAVES

Medium to coarse grained quartz-K-feldspar enclaves occur at Lake Everard, next to the base of the Yantea Rhyolite-dacite (GR 0515581-6501718) and in the Whyeela Dacite northeast of Mortimer Hill (GR 0523705-6495238), and at Kokatha, in the Rhyolite-dacite Mi2 and in the Andesite. The enclaves are centimetres to several metres in size, massive (Fig. 3.29A) or foliated (Fig. 3.29B), and are composed of medium to coarse grained anhedral K-feldspar and quartz. The enclaves are associated with the occurrence of anhedral quartz and K-feldspar grains, up to 2 cm in size, in the host rocks. Amoeboid quartz was also found in the Andesite I and II at Lake Everard, although not associated with enclaves (Fig. 3.4B).

Massive enclaves

Massive-textured enclaves show round and gradational margins with the host rock, and contain crystals of K-feldspar and amoeboid quartz, separated by a microcrystalline quartz +K-feldspar +albite matrix (Fig. 3.29A). Feldspar crystals are commonly surrounded by a granophyric rim, up to 0.5 mm-thick, formed by an intergrowth of elongate K-feldspar and quartz (Fig. 3.29C). Quartz crystals in the granophyric textures show optical continuity. These intergrowths make up 10-20 vol.% of the matrix and only occur around K-feldspar. Quartz can be found as single crystals, rounded and <0.5 mm across (“magmatic” quartz) or in round to lobed aggregates, 0.5 to 1 mm in size, associated with epidote and minor, fluorite, chlorite and titanite (“late” quartz, Fig. 3.29D). Accessory minerals include zircon, magnetite, fluorite and Ti-oxide.

Foliated enclaves

Foliated quartz- and feldspar-bearing enclaves occur in the Andesite at Kokatha. These inclusions are up to a few tens of centimetres across, foliated at the mm-scale (gneiss, Fig. 3.29B), and crop out near the upper contact of the unit. Quartz in these enclaves shows wavy extinction and triple junction contacts. The occurrence of anhedral crystals of quartz and K-feldspar in the host rock is,ll, associated with these enclaves (Fig. 3.22 A).

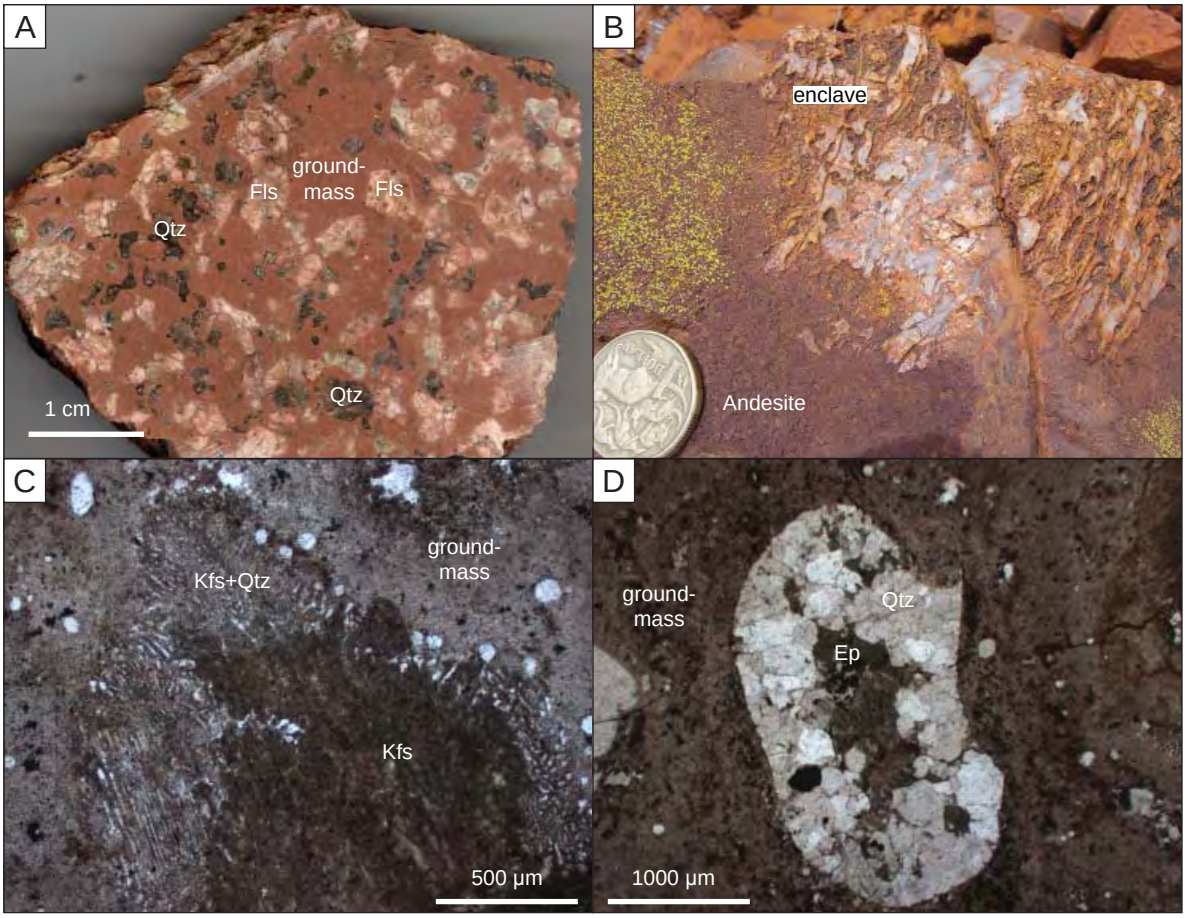

Fig. 3.29 Felsic enlaves in the lower GRV at Lake Everard and Koktha. A- Partially melted coarse grained massive enclave in the Whyeela Dacite (sample GH29, GR 0524305-6495515). B- Foliated enclave in the Andesite, Kokatha (GR 0524825-6542207). C- A K-feldspar crystal in a partially melted felsic enclave is surrounded by a granophyric quartz-K-feldspar rim and a microcrystaline groundmass (sample GH32, GR 0523705-6495238). D- Round aggregate of quartz and epidote (sample GH32).

3.4.1 Summary of volcanology of the Chitanilga Volcanic Complex, Kokatha

The Chitanilga Volcanic Complex includes a thick sequence of alternating lavas and pyroclastic units. The sequence is approximately 3 km thick and dips to the southeast at a gentle to moderate angle (mostly ≤30°). The base is concealed under Quaternary deposits and the unexposed portion can be inferred to be a few hundreds of metres thick, based on the outcrop of Archaean basement (Fig. 3.18). Apart from this concealed base, the complete sequence is exposed in a northwest-southeast oriented 10-km-long traverse, approximately centred on Chitanilga Hill (Fig. 3.30). The lower part of the exposed sequence is composed of m-thick mafic lava units (vesicular/amygdaloidal basalt and basaltic andesite) forming a ~1-km-thick pile, and interlayered ignimbrite and other volcaniclastic units, each up to several tens of metres thick. The upper part of the sequence is dominated by felsic lava and ignimbrite units, and also includes minor intermediate lava. The orientation of some sandstone and conglomerate units within the succession suggests that the complex has undergone tilting of ~10-18° to the southeast.

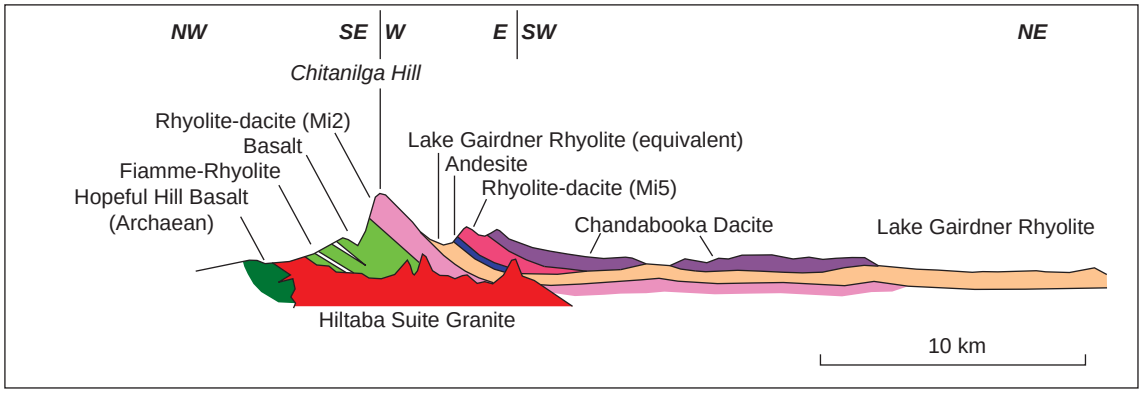

Fig. 3.30. Cross section of the Chitanilga Volcanic Complex, Kokatha. Vertical scale exaggeration ~15X.

Intermediate to felsic lavas

Intermediate to felsic lava units are up to several hundreds of metres thick and extend in outcrop for up to 20 km or more. The volumes, estimated on the basis of the outcrop extent, are extremely variable, from <<1 km^3 (Andesite) to >20 km^3 (Chandabooka Dacite, Table 3.2). They are all evenly porphyritic and include 5-10 vol.% phenocrysts of alkali feldspar and, locally, minor quartz. Local variations in mineral abundance and grain size are associated with granitoid enclaves. Phenocrysts are mostly anhedral (feldspar is sieve-textured and quartz is round or embayed), but unbroken. The groundmass is microcrystalline and composed of K-feldspar, albite and quartz. Bedding-parallel fiamme are locally present at the base of one unit (Rhyolite-dacite Mi2). Felsic units interpreted to be lavas have evenly porphyritic texture, widespread flow bands and lack of vitriclastic texture (Fig. 3.31 A-B).

The 600-m-thick Rhyolite-dacite (Mi2) conformably overlies the mafic lavas, and shows gently to steeply dipping flow folded flow bands, flow lineation and, locally, aligned

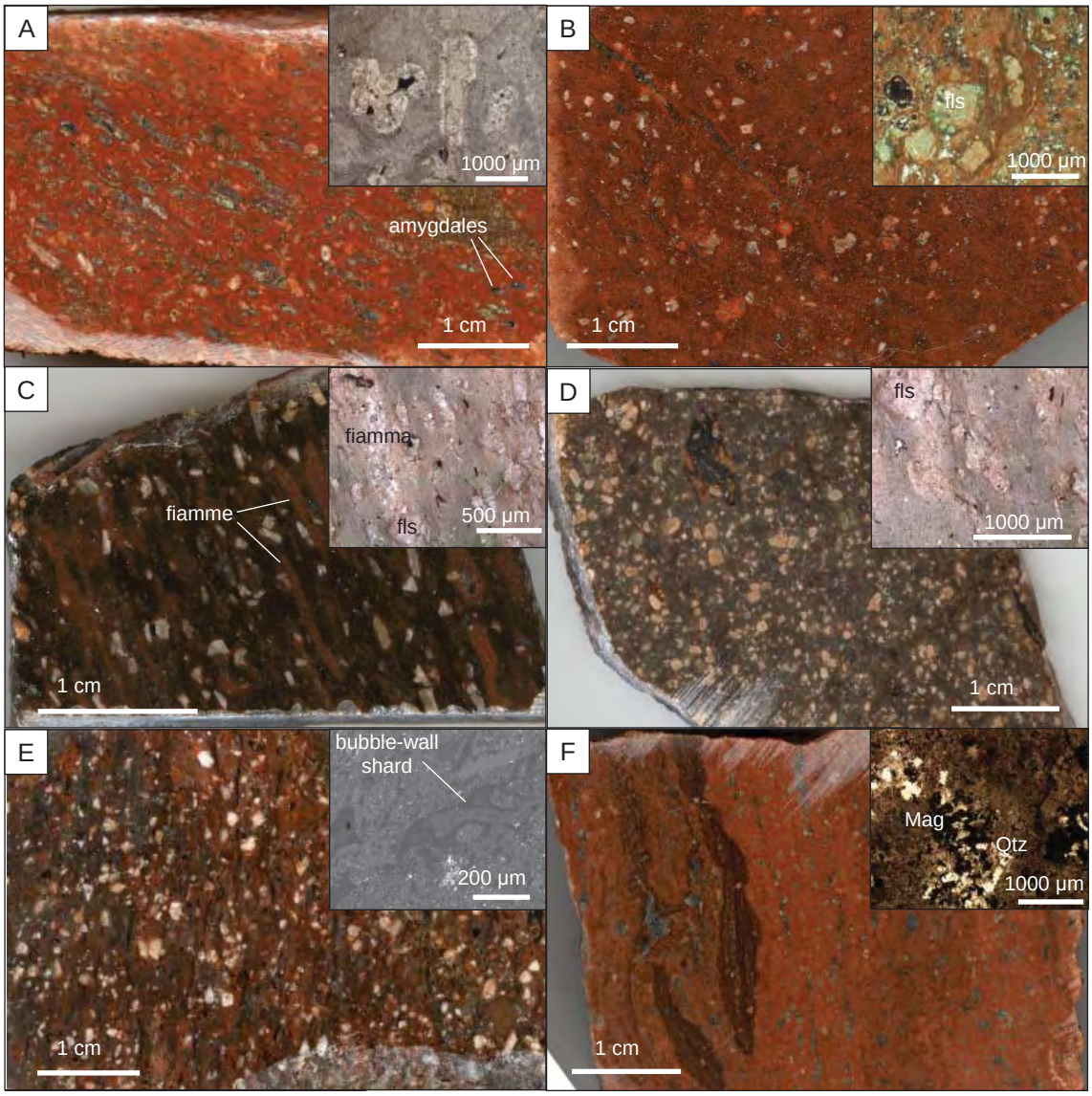

Fig. 3.31. Comparison of textures in lavas (A, B) and pyroclastic rocks (C-F) in the Chitanilga Volcanic Complex, Kokatha. A- Rhyolite-dacite (Mi2) (sample GH35, 0524220-6543611), B- Chandabooka Dacite (GH53, GR 0519933-6543460). C, D- Volcaniclastic units interbedded with Basalt (C: GH43, GR 0520134-6543607; D: GH48, GR 0519533-6433203), E- Lake Gairdner Rhyolite (GH87, GR 0523820-6542839), F- Rhyolite-dacite (Mi5) (GH85, GR 0525157-6541152). Note the paucity of lithic clasts and the massive to crudely oriented texture of most samples. Insets show microstructures (plane polarised transmitted light and BSE). GR: Grid reference (GDA94).

amygdales. Phenocrysts of feldspar are set in a microcrystalline groundmass.

The Chitanilga Volcanic Complex also includes a 20-m-thick, 4-km-across, massive and evenly porphyritic andesite, interpreted as a lava. The unit dips to the east or east-northeast at a moderate angle. Eutaxitic texture measured in the underlying unit and laminations in the overlying unit suggest the presence of an angular unconformity at the base of the Andesite and a conformable contact at its top.

The Chandabooka Dacite lies at the top of the succession and has been correlated with the Yardea Dacite of the upper GRV (Blissett, 1985). It extends for at least 15 by 10 km and is at least 300 m thick. However, outcrops of the same rock were also mapped east of Lake Gairdner (Blissett, 1975, 1985), implying an extent of >40 km. It is locally flow banded at the mm-scale and contains phenocrysts of albite in a microcrystalline quartzo-feldspathic groundmass. This unit is separated from the rest of the sequence by a thick and laterally continuous, massive, clast-supported breccia zone. The Chandabooka Dacite has been interpreted as an intracaldera ignimbrite and the breccia as a caldera rim fault zone by Branch (1978). However, textures of the Chandabooka Dacite are better explained by emplacement as a lava.

Pyroclastic facies

The pyroclastic units are up to 400 m thick and extend for up to a few tens of km. These rocks are massive (Fig. 3.31 D) to bedded/foliated (fiamme-bearing or compositionally layered at the mm- to cm-scale, Figures 3.20, 3.31 C-E). They contain a variable amount of feldspar and quartz crystals or crystal fragments (average 20 vol.%) set in a very fine-grained eutaxitic or banded matrix. Devitrified glass shards and flattened pumice fragments (fiamme) are preserved in moderately welded, non-rheomorphic ignimbrites or better preserved parts of rheomorphic ignimbrites (Fig. 3.31 C-E). Lithic fragments are scarce to absent.

Some small-volume pyroclastic units are interbedded with the basalt at the base of the Chitanilga Volcanic Complex, indicating coeval felsic and mafic magmatic activity, although probably from different sources. These pyroclastic units are up to 100 m thick and laterally continuous and include non- to relatively welded, fiamme-bearing or cm-scale layered ignimbrites. The matrix is fine grained, eutaxitic and locally vitriclastic, to microcrystalline (Fig. 3.20, 3.31). Rare vesicles/amygdales are present. Other less conspicuous volcaniclastic units are mostly massive, non-welded and have thin, bedded tops (Fig. 3.21). The flat tops and concave upwards bases suggest that they are confined in palaeo-valleys.

The Lake Gairdner Rhyolite is a 400-m-thick multiple-flow-unit ignimbrite with a massive to eutaxitic texture, defined by fiamme or by flattening of clastic components in the matrix (Fig. 3.23 D). It contains approximately 20 vol.% of K-feldspar, albite and quartz crystals and crystal fragments, and very minor lithic fragments, set in a variably deformed (compacted) bubble-wall shard matrix (Fig. 3.23).

The 200-m-thick Rhyolite-dacite (Mi5) overlies the Andesite and, locally, the Lake Gairdner Rhyolite east of Kokatha.

The base of the unit shows a cm-scale, planar discontinuous (fiamme-defined) bedding/lamination, conformable with the underlying Andesite. The middle and top parts of the unit are bedded and flow-folded. The mm- to cm-scale beds are defined by alternating crystal- and aggregate-rich, internally massive layers, and crystal-poor, internally finely banded and flow-deformed layers (Fig. 3.25 E-G). The beds are variably flow deformed in open to tight, isoclinal, and sheath folds, reflecting an increase of viscous deformation from the base to the top of the unit. Ptygmatic folds are also locally present, and indicate vertical shortening, possibly where the flow was ponded. The orientation

Table 3.2. Volcanic textures and emplacement mechanism of the principal units in the Chitanilga Volcanic Complex

Unit	Outcrop area* (km^2)	Max estimated thickness (m)	Volume* (km^3)	Aspect ratio	Texture	Groundmass/ matrix	Phenocrysts/ crystals	Breccia domains	Flow deformation	Enclaves, xenocrysts	Emplacement mechanism interpretation	Emplacement mechanism, previous interpretation**
Chandabooka Dacite	77	300	23	33	coherent	microcrystalline	anhedral-euhedral	extensive clast-supported breccia at the base	mm-scale flow bands	no	lava flow	welded ash flows (Branch, 1978; Blissett, 1985)
Rhyolite-dacite (Mi5)	4	200	1	12	coherent	locally fiamme-bearing, eutaxitic/ compositionally layered	subhedral-euhedral	no	mm- to cm-sclae folded compositional/ flow bands, elongation lineation	massive, (granitoid) enclaves	lava-like ignimbrite?	lava flows, welded ash flows (Blissett, 1975)
Andesite	<1	20	<1	44	coherent	microcrystalline	euhedral	no	no	foliated or massive (granitoid) enclaves	lava flow	lava flow
Lake Gairdner Rhyolite	120	400	48	31	clastic	eutaxitic, devitrified glass shards, fiamme-bearing	anhedral, fractured	no	no	–	ignimbrite	ash flows, lavas, breccia (Blissett, 1975)
Rhyolite-dacite (Mi2)	11	600	7	6	coherent	microcrystalline	anhedral	no	folded flow bands, elongation lineation, deformed vesicles	–	lava flow	welded ash flows, lava
Volcaniclastic facies interbedded with the Basalt	<1	<30 m	1	–	clastic	compositional layering	anbhedral-subhedral	angular clast breccia layers	no	–	reworked pyroclastic facies?	tuffs
Fiamme-rhyolite	<1	<100 m	<1	–	clastic	glass shards, locally compositionally layered	anhedral-euhedral	no	no	–	ignimbrite	tuffs
Basalt	3	1000	3	–	coherent	microcrystalline	subhedral-euhedral relic phenocrysts	no	deformed vesicles	no	lava flow	lava flows

*Outcrop area and volume, calculated by interpolation of outcrops, represent a minimum for the areal extent and, therefore, volume of the unit. **Blissett (1985) unless otherwise stated

of east-southeast-striking axial planes of asymmetric and isoclinal folds and their predominantly northwards vergence, together with east-northeast-trending lineation (Fig. 3.25), indicate that folds formed during a east-northeastwards-directed flow. Widespread sparsely porphyritic texture and the outcrop characteristics (flow-folded flow bands and lineation) indicate long-distance transport as a non-particulate flow (lava). Nevertheless, the unit is interpreted as a pyroclastic flow deposit because of the abundant fiamme at the base of the unit and the locally preserved clastic texture of some of the less deformed crystal-rich layers in the central part of the unit.

Volcanogenic sedimentary rocks

Volcanogenic sedimentary rocks are very minor in the Chitanilga Volcanic Complex. Massive, clast-supported conglomerate with well rounded clasts (most likely of fluvial origin) crops out within the Lake Gairdner Rhyolite (Fig. 3.23 B). It is several m thick and is overlain by a thin (~1 m) interval of bedded fine breccia and sandstone, dipping to the southeast at a gentle angle.

3.5 Discussion and conclusions

The Glyde Hill and Chitanilga Volcanic Complexes are thick successions (~1 km and ~3 km, respectively) of lavas and pyroclastic rocks; sedimentary facies are very minor. Both the successions were intruded by shallow intrusions (dykes, granite stocks and plugs). Units in the Glyde Hill and Chitanilga Volcanic Complexes are confined to the Lake Everard and Kokatha areas, respectively. Despite significant geochemical similarities (chapter 4), the two successions cannot be correlated on either textural or compositional grounds.

3.5.1 Glyde Hill Volcanic Complex, Lake Everard area

The Glyde Hill Volcanic Complex is dominated by felsic (dacite to rhyolite) lavas, with minor intermediate lavas and very minor basalt. Volumetrically subordinate pyroclastic rocks occur interbedded with the lavas. Units of the Glyde Hill Volcanic Complex have roughly radial dip directions centred on the Glyde Hill Outstation area, resulting in the upper unit of the sequence (Whyeela Dacite) being exposed at the centre of the outcrop area. This centripetal arrangement of units has been attributed to subsidence following magma chamber evacuation (Giles, 1977).

The lavas in the Glyde Hill Volcanic Complex are evenly porphyritic and some of them contain breccia domains interpreted as autobreccia. Vesicles and amygdales are only abundant in the Mangaroongah Dacite, and occur locally in the Yantea Rhyolite-dacite and Baldry Rhyolite. Fiamme are very locally present at the base of the Yantea Rhyolite-dacite (Fig. 3.12 B). Fiamme can result from incorporation of pumice fragments in the flow, presence of vesicular domains within otherwise dense lava, welding of clasts in basal autobreccia and inhomogeneous shear during laminar flow, and their presence does not disprove the emplacement of a unit as a lava (Manley, 1996; Bull and McPhie, 2007). All the extensive felsic units in the area have previously been interpreted as ashflow tuffs and the coherent textures have been justified as a result of intense welding (Tables 3.1, 3.2, Giles, 1977; Blissett, 1985).

Intermediate and felsic lavas with small to moderate volume and areal extent are interpreted to have not flowed far from the source and to be located very near to their vents (Giles, 1977; Allen et al., 2008). Other units (the Childera and Mangaroongah Dacites, the Yantea Rhyolite-dacite, and the Wheepool Rhyolite) are up to several tens of km in size. These units have unusually large extent and low aspect ratio for silicic lavas, although the presence of pyroclastic layers between massive porphyritic domains may indicate that some of the units were not emplaced as single flows.

Giles (1977) regarded the Yantea Rhyolite-dacite as a pyroclastic flow deposit locally infilling palaeovalleys, namely southeast of Mount Sam (Fig. 3.2). Thus, the base contact of the Yantea Rhyolite-dacite has been interpreted as an unconformity recording a major erosional event. However, because the contact in that area is not in outcrop, its precise nature cannot be ascertained, and other relationships cannot be ruled out. A simple explanation for the distribution of the Yantea Rhyolite-dacite is that the underlying rhyolite was emplaced as multiple lava lobes, resulting in an irregular topography (Fig. 3.32).

The outcrop of Wheepool Rhyolite next to Lake Everard Homestead and further north at Glyde Hill Outstation (Fig. 3.2) can be due either to repetition by faults (Blissett, 1985) or to very gentle folding of the units (Fig. 3.15).

3.5.2 Chitanilga Volcanic Complex, Kokatha area

The Chitanilga Volcanic Complex is gently tilted towards the southeast and the succession is nearly continuously exposed on a ~east-west-oriented traverse. The bottom 1 km of the succession is composed of mafic lavas, overlain by a thick thick sequence (~2 km) of alternating felsic lavas and ignimbrites.

The ignimbrites in the Chitanilga Volcanic Complex range in volume from <1 km^3 to several tens km^3 (Lake Gairdner Rhyolite). The Fiamme-rhyolite unit is composed of small-volume ignimbrites intercalated between Basalt, indicating that felsic and mafic volcanism were active at the same time in the area, although likely erupted from different volcanic centres (Fig. 3.33). The Lake Gairdner Rhyolite crops out within the main sequence, east of Kokatha, for approximately 2 km between the underlying Rhyolite-dacite Mi2 and the overlying Andesite. The unit crops out more extensively farther to the east, where it is overlain by the Chandabooka Dacite. These stratigraphic relationships indicate that the Andesite and the Rhyolite-dacite Mi5 are laterally discontinuous (Fig. 3.18, 3.30).

One of the two felsic lavas in the Kokatha area is the extensive Chandabooka Dacite. The unit has a roughly elliptical outcrop shape, and was interpreted to be an intracaldera welded ignimbrite by Branch (1978). The laterally continuous breccia at its base contact was interpreted to be a fault breccia related to the postulated caldera rim. However, the textural characteristics of the unit (evenly porphyritic texture, flow bands, microcrystalline groundmass, paucity of broken crystals) appear more consistent with emplacement as a lava flow. In the interpretation of Branch (1978), the feldspar-phyric rocks overlying the Basalt (Rhyolite-dacite Mi2) represented the extra-caldera equivalent of the Chandabooka Dacite. However, later workers (Blissett, 1985; Blissett et al., 1993; PIRSA, 2006) interpreted the Lake Gairdner Rhyolite to extend across the

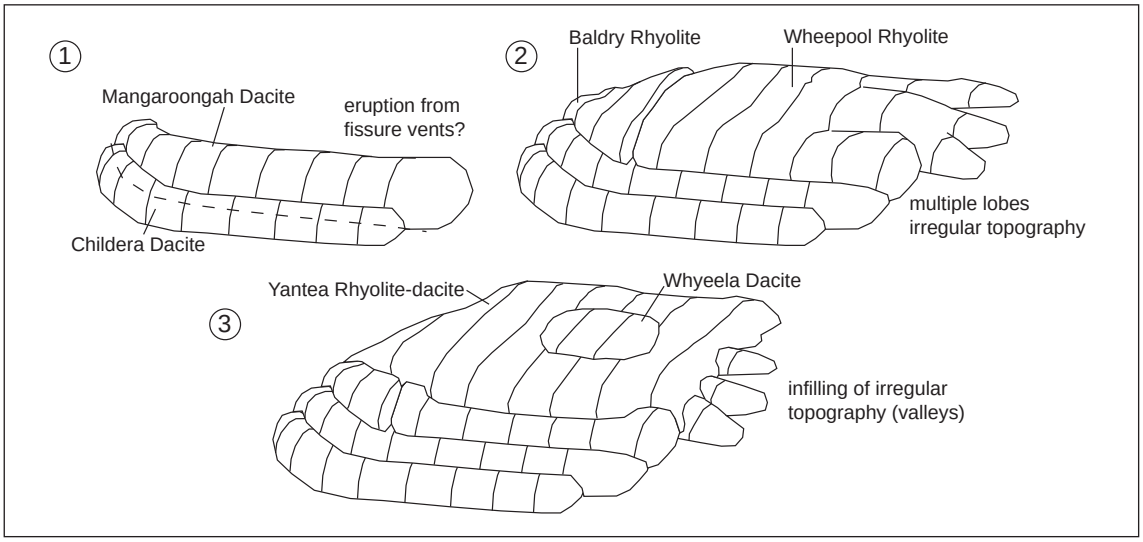

Fig. 3.32. Temporal evolution of the main units in the Glyde Hill Volcanic Complex, Lake Everard. Not in scale.

Kokatha area from west, where it overlies the Rhyolite-dacite Mi2, to east, where it underlies the Chandabooka Dacite (Fig. 3.30). Evidently, this interpretation contrasts with the interpretation of Branch (1978). The Rhyolite-dacite Mi2 is here interpreted not to be the equivalent of the Chandabooka Dacite, based on textural (Fig.3.31 A and B) and compositional (major and trace elements, Fig. 3.17, chapter 4) characteristics of the units.

Source vents have not been precisely located at Lake Everard or Kokatha. However, lavas are considered to have been erupted from volcanos located within or near the current outcrop areas. In particular, some of the less extensive units at Lake Everard (Baldry Rhyolite, Whyeela Dacite) and Kokatha (Rhyolite-dacite Mi2, Andesite) are considered to lie on their source vents. Kinetic indicators in the Rhyolite-dacite Mi5 at Kokatha indicate flow towards west- to northwest, suggesting that the source of this unit was located to the east. Flow folds and lineation in the Rhyolite-dacite Mi2 (Fig. 3.22 B) also indicate a east-southeast flow direction, although the way was not determined. The elongate shape od some units at Lake Everard might be due to eruption from fissure vents or discrete vents locate along liear structures (faults?). Mafic lavas at Kokatha have been interpreted as the remnant of a cone (Branch, 1978). For the ignimbrites, in the absence of textural variation (e.g. grain size variation of lithic fragments), location of the vent remains uncertain.

3.5.3 Comparison with other large-volume felsic units

The lower GRV shows some of the characteristics that distinguish Snake River-type felsic volcanism (Branney et al., 2008), including 1) large-volume and extensive felsic lavas (Childera, Mangaroongah and Chandabooka Dacites, Yantea Rhyolite-dacite and Wheepool Rhyolite), 2) lithic-poor ignimbrites with scarce pumice lapilli, and 3) bimodal association of felsic and mafic units (chapter 4). The lower GRV and the Snake River Plain volcanic rocks were both produced by low-water, metaluminous (chapter 4), high-temperature low-viscosity (Creaser and White, 1991; Stewart, 1994) source magmas.

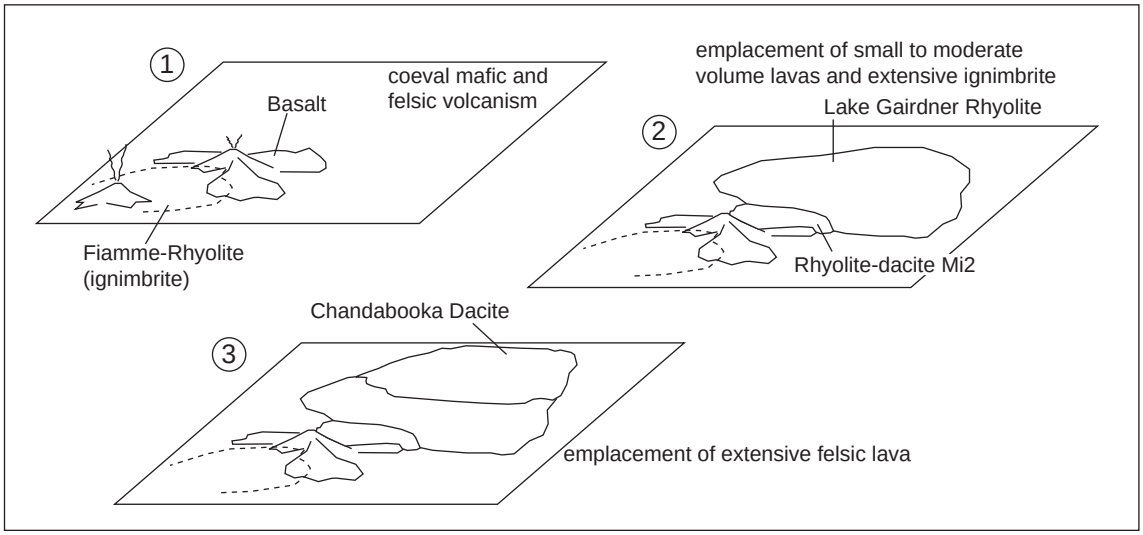

Fig. 3.33. Temporal evolution of the main units in the Chitanilga Volcanic Complex, Kokatha. Not in scale.

Similar geochemical characteristics and the presence of large-volume extensive felsic lavas are also shown by the upper GRV (Allen et al., 2003).

The association of large, low-aspect-ratio felsic lavas with large-volume ignimbrites has been described in the Snake River Plain, Idaho and Nevada, USA (Bonnichsen and Kauffman, 1987; Manley, 1996; Branney et al., 2008), Trans-Pecos, Texas, USA (Henry et al., 1988) and Keweenawan Midcontinent Rift, Minnesota, USA (Green and Fitz, 1993).

Another distinguishing characteristic of Snake River-type volcanism is the widespread evidence of emplacement in a lacustrine-fluvial environment. The GRV was almost entirely emplaced in a subaerial environment. However, evidence of local water-magma interaction in the GRV is shown by the presence of a small hydroexplosive centre at Menninnie Dam (Roache et al., 2000). Further, some of the volcaniclastic deposits intercalated with Basalt at the base of the sequence have been interpreted as water-settled fallout or pyroclasts reworked by fluvial and lacustrine processes (Allen et al., 2008), and accretionary lapilli were described east of Glyde Hill Outstation (Ferris, 2003; Allen et al., 2008).

Mineral assemblages in the lower GRV are consistent with low water contents in the source magmas. Primary (magmatic) ferromagnesian mineral phases in both the volcanic units of the Glyde Hill and Chitanilga Volcanic Complexes are anhydrous. Andesites and dacites contain well preserved clinopyroxene and no primary amphibole or biotite are present. Biotite occurs in interstitial position in intrusive units (Hiltaba Suite granite and Microgranite dykes). Mostly anhydrous parageneses (pyroxene predominant over minor biotite and amphibole) have been reported in other felsic units of LIP in both intracratonic and plate margin settings, including the Sierra Madre Occidental (Cameron, 1980) the Keweenawan Midcontinent Rift plateau (Green and Fitz, 1993), the Goboboseb and Springbok quartz latites (Ewart et al., 1998b; 2004b), and the Snake River Plain (Christiansen and McCurry, 2008).

The interpretation of large-volume (up to >100 km^3), relatively low-aspect-ratio (>100) felsic units as lavas inevitably rises the issue of how a felsic lava could have flowed for several km or tens of km. The length of a lava flow is dependent on the erupted volume and eruption rate (Walker, 1973), on the viscosity and on the heat retention (Bonnichsen and Kauffman, 1987). Composition and temperature can have an important role on viscosity. In the GRV, the combination of relatively low water and high fluorine contents, indicated by the anhydrous mineral assemblages and by melt inclusion compositions (cf. Chapter 4), would offer a low explosivity and a reduced viscosity (e.g. Manning, 1981; Dingwell et al., 1985; Giordano et al., 2004). High magmatic temperatures were invoked for the upper GRV by some authors for the Yardea Dacite of the upper GRV, based on the anhydrous paragenesis and pyroxene geothermometry (Creaser and White, 1991; Stewart, 1994).

CHAPTER 4

Geochemistry of the lower Gawler Range Volcanics: whole rock and melt inclusion study

4.1 Introduction: melt inclusion study applied to ancient successions, the Gawler Range Volcanics case study

Melt inclusions are droplets of silicate melt trapped within crystals growing in a magma. If preserved, they represent a sample of pristine magmatic silicate liquid (melt) unaffected by modifications occurring as the magma approaches the Earth's surface. These modifications may include loss of the volatile component as a result of decompression (degassing), or subsequent alteration of the igneous rock unit. In ancient rocks, in particular, alteration introduces uncertainty in the interpretation of whole-rock geochemical data. Melt inclusions have been extensively studied to assess the pre-emplacement volatile content of a magma (e.g. Lowenstern and Mahood, 1991; Métrich and Clocchiatti, 1989; Lowenstern, 1995) and to reconstruct the magma composition in altered (e.g. Chabiron et al., 2001). Other applications of melt inclusions include the study of co-trapped melt and aqueous fluid as an indication of immiscibility in the magma (Kamenetsky et al., 2004; Lowenstern, 1994), homogenisation thermometry as an indication of crystallisation temperature, and estimates of minimum trapping pressure based on water and CO_2 solubility models (Anderson et al., 1989).

It is known that dissolved volatile elements can affect both physical and chemical characteristics of magmas. Volatile elements strongly control liquidus and solidus equilibria by depressing the eutectic temperature, and reduce density and viscosity of magmas (Tuttle and Bowen, 1958; Dingwell et al., 1985; Manning, 1981), thus affecting volcanic eruption processes and emplacement mechanisms. Water and fluorine in particular, have important and similar effects in reducing viscosity and density of magmas (Giordano et al., 2004). Volatile components also drive magma ascent, vesiculation and expansion, and play a crucial role in explosive eruptions.

In the Gawler Range Volcanics (GRV), melt inclusions are commonly well preserved, despite the Mesoproterozoic age. Glass-bearing melt inclusions are particularly well preserved in quartz phenocrysts in the rhyolites, and apparently uncompromised crystalline inclusions were found in a hypabyssal intrusion. The volatile content of these magmas is of particular interest since some extensive felsic units in the GRV have been recently interpreted as lavas (Garner and McPhie, 1999; Allen et al., 2003; 2008), contrary to the common notion that felsic lava flows do not cover long distances (e.g. Walker, 1973).

The GRV show evidence of weak but widespread deuteric alteration of feldspar to sericite and groundmass oxidation, the latter probably happened during cooling of the units and is made evident by a brick-red colour. This alteration implies that whole-rock

data, particularly the most mobile elements (Na, K), should be considered with caution. Thus, melt inclusions are used here as a useful tool for validating whole-rock data.

The objectives of this chapter are to:

1. obtain an estimate of pre-emplacement volatile components of the lower GRV magmas, with a particular attention to fluorine;

2. assess whether or not alteration has affected whole-rock compositions through a comparison of whole-rock and melt inclusion analyses. The role of magmatic processes on compositional variability can then be evaluated; and

3. compare melt inclusion compositions of the lower GRV with equivalent data from the Eucarro Rhyolite of the upper GRV (Kamenetsky et al., 2000; Bath, 2005).

4.2 Sample preparation and analytical techniques

Whole-rock analysis

Rock samples selected for whole-rock analysis were crushed and reduced to powder in a tungsten carbide mill for X-ray fluorescence (XRF) and inductively coupled plasma mass spectrometer (ICP-MS) analysis. The samples are representative of all the volcanic units in the Chitanilga and Glyde Hill Volcanic Complexes and include three dykes that intrude the volcanic successions; two samples from the Hiltaba Suite Granite at Kokatha and one granitic enclave in the Glyde Hill Volcanic Complex were also analysed. Major elements and some minor elements (Ti, Mn, Ba, P, S) were measured by XRF. Trace element analyses were carried out on 30 samples. Samples were digested in HF/H2SO4 with the PicoTrace high pressure digestion equipment and analysed with a Philips PW1480 X-ray Fluorescence Spectrometer and an Agilent 4500 ICP-MS. Detection limits for trace elements in ICP-MS are ≤ 0.01 ppm (REE) and ≤ 0.5 ppm for other elements, except As (5 ppm). A comparison of XRF and ICP-MS trace element data indicates a good correlation between the two methods, the difference being <20% relative. Some elements (V, Cr, Ni, Cu, Zn, Rb, Sr, Y, Zr, Nb, Ba, La, Pb) were also analysed by XRF to test the effectiveness of the digestion process.

Melt inclusion preparation and heating experiments

Heating experiments were conducted on quartz-hosted melt inclusions from five units from the lower GRV. The experiments were aimed at obtaining homogeneous glass suitable for microanalysis. Quartz grains were separated and heated from the following units:

1. the Lake Gairdner Rhyolite and the microgranite dykes intruded into the basalt in the Chitanilga Volcanic Complex at Kokatha;

2. the Wheepool Rhyolite, the Waurea Pyroclastics and the Moonamby Dyke Suite in the Glyde Hill Volcanic Complex at Lake Everard.

Successful results (dissolution of vapour bubble and solids in an homogeneous silicate liquid phase and quenching to glass) were obtained in the Wheepool Rhyolite,

the Waurea Pyroclastics and the Moonamby Dyke Suite. The present chapter describes inclusions from these units. Melt inclusions from the other units, compromised by fractures, failed to homogenise even at temperatures as high as 1050°C and are not further discussed.

Samples were crushed in a steel mortar and sieved to separate different grain size intervals. Quartz grains were hand-picked under a binocular microscope from the fractions 0.4-1 mm. Batches of quartz grains were heated in a furnace at 1 atm pressure to temperatures between 800° and 1100°C at 50°C intervals. Heating runs were performed for 24 hours. During heating sessions, quartz grains were wrapped in platinum foil (Kamenetsky and Danyushevsky, 2005). After heating, the grains were water-quenched. Then the grains were glued on a double-sided sticky tape and mounted in 1-inch epoxy resin mounts. The mounts were then polished with 0.3 µm corundum powder. The inclusions were observed with a petrographic microscope in transmitted light. After inspection, selected quartz grains were extracted from the epoxy mounts with a soldering iron, glued on double sticky tape and mounted again in single grain mounts moulded in brass or aluminium tubes. Then the inclusions were exposed using abrasive paper and corundum powder and the mounts polished. Additional observations were carried out with an electron microscope equipped with a cathodoluminescence detector (SEM-BSE and SEM-CL).

Melt inclusion analysis

Major, volatile and minor element analyses of 65 melt inclusions were carried out by electron microprobe (EPMA). A number of studies have pointed out a diffusivity of volatile elements (e.g. Chabiron et al., 2001) and metals (Kamenetsky and Danyushevsky, 2005) during heating experiments. Therefore, unheated inclusions were also analysed for comparison with heated inclusions. Analyses were performed using a 5-spectrometer SX-100 Cameca WDS microprobe. Operating conditions of 15 kV acceleration voltage, 10 nA beam current, 5 µm spot size, and counting time between 10 and 30 s were used. Since a heat-induced diffusion of elements under the electron beam can result in an underestimation of some components, the most volatile elements (K, Na, F) were analysed first and the variation in signal intensity was monitored during analyses. No significant loss in signal intensity was observed. As a reference material, USGS glass BSR-2G was chosen. Standard analyses were run at the beginning and at the end of each session. Detection limits were estimated by counting statistics as follows (element ppm): Si=411, Ti=410, Al=236, Fe=759, Mg=206, Mn=729, Ca=505, Na=708, K=509, F=1078, P=275, S=212, Cl=308. Standard deviations are as follows: Si=5419, Ti=493, Al=1758, Fe=1717, Mg=353, Ca=1160, Na=3122, K=2874, F=1002, P=262, S=181, Cl=332. Major element analyses on the standard glass show good agreement (differences <10% relative) with the data published by GeoRem and USGS.

Even though H_2O and CO_2 cannot be directly measured by electron microprobe, the difference between the total of all the analysable elements and 100%, being due to the unmeasured elements, can be equated to these dissolved components (difference method or summation deficit, Devine et al., 1995). The precision and accuracy of totals are affected by cumulative errors on single elements and by diffusion of the most volatile elements under the electron beam. A comparison between totals measured on the reference glass and the published values (USGS, GeoRem) indicates a high relative

precision (~1 %) and a low 2σ uncertainty (≤0.8 wt.%). The validity of the method has also been supported by comparisons with other methods such as FTIR and SIMS (Straub and Layne, 2003; Gurenko et al., 2005; Chabiron et al., 2001).

Eighteen melt inclusions were also analysed for trace elements by laser ablation inductively coupled plasma mass spectrometry (LA-ICP-MS). Trace elements were measured using a New Wave UP-213 Laser Ablation System coupled with an Agilent 4500 inductive coupled plasma mass spectrometer. Energy was 2 J/cm2 at 5 Hz repetition frequency. Spot size (20 - 60 μm) was comparable to slightly larger than melt inclusion size, but the relatively low laser energy allowed ablating only the glass inclusions and not the host quartz. Ablation time was 60 s per inclusion. Glass NIST 612 was used as a standard material and glass BCR-2G was used as a secondary standard. Aluminium, measured by microprobe analysis, was used as the internal standard. During measurements, the signal was stable to steadily decreasing and lacked peaks, indicating that the glass was homogeneous. A steeper decrease of signal intensity at the end of some measurements is attributed to the progressive ablation of melt inclusions and was not included in the integration interval. A comparison with published standard compositions (Georem) indicates an error within 20% relative.

4.3 Results

4.3.1 Whole-rock compositions

Whole-rock compositional data are presented in Figures 4.1 to 4.7 and in Table 4.1.

Major elements

Silica content spans a wide compositional range, from ~50 to ~80 wt.%. A compositional gap, or “Daly gap”, (SiO_2 = 53-60 wt.%) separates mafic compositions from the intermediate-felsic ones. Analyses with SiO_2 ≤70 wt.% show increasing total alkalis (TAS diagram of Le Bas et al., 1986) and plot approximately along the boundary between the silica-undersaturated (sub-alkaline) and silica-saturated (alkaline) fields (series basaltic trachyandesite to trachyte and basaltic andesite to dacite, respectively). The more silica-rich samples (SiO_2 >70 wt.%) show a slightly decreasing alkali trend (Fig. 4.1). Similarly, Na_2O content increases with increasing silica for silica values up to 70 wt.% and decreases. A few rhyolite samples show lower Na_2O (<2 wt.%) in comparison with the other samples of similar silica content. Potash increases almost constantly with silica. Analyses plot mainly in the high-K and ultra-K series of Peccerillo and Taylor (1976). Alumina has a generally decreasing trend, although there is little variation in intermediate compositions. Iron has a rather steadily decreasing trend; CaO decreases steeply for silica values ≤65 wt.% (Fig. 4.1). Rocks with silica >65 wt.% have CaO ≤1 wt.%, in agreement with the presence of low-Ca plagioclase (albite-oligoclase). On the contrary, intermediate rocks (SiO_2 = 60-65 wt.%), containing Ca-pyroxene and apatite, show CaO ≤4.4 wt.%. Phosphorus oxide content sharply decreases from 0.8 to less than 0.1 wt.% between silica 60 and 70 wt.%. This pattern is in agreement with the presence of apatite, included in quartz and feldspar phenocrysts, and in zircon, implying early crystallisation. The modified Fe number (Fe* number = FeOtot/(FeOtot +MgO),

Table 4.1: Whole-rock major (XRF, as wt.%) and trace element (ICP-MS/XRF, ppm) analyses

Sample	GH06	GH07	GH13	GH17	GH20	GH24	GH26	GH27	GH67B	GH71	GH72
Volcanic complex	Glyde Hill	Glyde Hill	Glyde Hill	Glyde Hill	Glyde Hill	Glyde Hill	Glyde Hill	Glyde Hill	Glyde Hill	Glyde Hill	Glyde Hill
Locality	Lake Everard	Lake Everard	Lake Everard	Lake Everard	Lake Everard	Lake Everard	Lake Everard	Lake Everard	Lake Everard	Lake Everard	Lake Everard
Unit	Wheepool Rhyolite	Nuckulla Basalt	Waurea Pyroclastics	Andesite II	Mangaroongah Dacite	Yantea Rhyolite-dacite	Whyeela Dacite	Bunburn Dacite	Baldry Rhyolite	Nuckulla Basalt	Andesite I
SiO2	78.16	52.48	74.85	62.82	61.74	65.18	62.63	68.57	79.66	50.90	60.07
Al2O3	11.23	16.02	11.93	14.50	14.50	14.51	14.23	15.37	9.99	16.86	14.10
Fe2O3	1.24	9.41	2.10	5.95	6.10	4.61	5.50	1.94	0.19	9.84	7.83
MnO	0.03	0.14	0.03	0.16	0.14	0.11	0.15	0.08	0.01	0.14	0.20
MgO	0.53	7.17	0.83	2.14	1.69	2.29	2.98	1.17	0.36	5.01	2.44
CaO	0.11	8.95	0.17	2.72	2.79	0.99	1.07	0.77	0.31	7.60	4.41
Na2O	3.47	2.65	1.04	3.93	3.95	3.79	3.32	3.85	1.06	3.79	3.35
K2O	4.00	0.58	5.68	4.60	4.45	4.59	4.90	5.61	7.50	1.64	3.37
P2O5	0.04	0.29	0.02	0.39	0.37	0.34	0.39	0.13	0.02	0.25	0.77
S	<0.01	<0.01	<0.01	<0.01	<0.01	<0.01	0.13	0.02	0.01	<0.01	<0.01
LOI	0.97	1.27	2.81	1.32	3.00	1.91	3.22	2.09	0.94	2.66	2.04
Total	100.19	99.85	99.62	99.93	100.08	99.69	100.46	100.44	100.12	99.87	100.19
Li	10.0	16.2	14.5	18.8	17.6	42.9	28.5	12.3	5.1	42.2	23.1
Be	2.00	0.98	2.41	2.30	2.27	2.57	2.08	1.95	1.59	0.97	2.58
Sc	4.6	24.4	3.3	16.4	15.9	15.8	16.3	6.7	2.2	21.2	19.7
Ti	1805	4762	767	6239	5524	6025	6370	2618	516	6449	7877
V (XRF)	14	175	6	78	80	78	87	5	3	197	108
Cr (XRF)	2	486	2	10	9	9	10	1	2	43	7
Mn	231	1055	203	1232	1018	888	1211	604	72	1082	1490
Ni (XRF)	4	161	3	14	13	11	23	2	3	90	12
Cu (XRF)	1	19	3	18	11	6	39	5	2	52	15
Zn (XRF)	29	84	43	97	89	78	89	59	4	99	115
Ga	10.6	16.6	13.6	18.4	19.2	18.7	18.0	14.8	4.4	18.8	19.9
As	<5	<5	10.4	<5	<5	<5	<5	<5	<5	<5	<5
Rb	117.4	20.3	211.0	130.3	119.7	122.8	114.7	155.2	291.9	75.1	108.2
Sr	49.9	705.3	28.3	318.7	261.3	191.2	317.9	206.8	19.2	509.1	394.1
Y	33.7	22.8	29.2	37.9	40.4	37.7	45.5	37.4	17.5	25.8	45.4
Zr	299	148	139	420	402	442	412	460	95	163	282
Nb (XRF)	19	6	22	15	15	15	15	18	17	9	17
Mo	0.14	0.30	0.54	0.75	0.62	0.61	0.96	1.12	0.34	0.56	1.13
Ag	0.03	0.05	0.05	0.11	0.13	0.06	0.15	1.07	0.03	0.08	0.12
Cd	<0.23	0.1	<0.23	<0.23	0.1	<0.23	<0.23	<0.23	<0.23	0.1	0.4
Sn	2.87	1.17	2.50	2.42	2.83	2.39	2.55	2.35	1.55	1.64	2.83
Sb	0.21	0.13	0.54	<0.06	0.07	0.56	0.23	0.16	0.14	0.28	0.09
Te	<0.37	<0.09	<0.37	<0.37	<0.09	<0.37	<0.37	<0.37	<0.37	<0.09	<0.09
Cs	1.27	1.17	3.33	2.64	2.60	1.52	0.92	2.41	2.19	4.38	1.90
Ba (XRF)	584	430	199	2390	2270	2362	6324	2691	193	503	1587
La	39.8	28.0	40.4	52.2	57.8	54.4	54.3	57.1	16.4	24.3	45.1
Ce	131.0	56.3	71.5	116.7	120.9	120.8	123.7	127.0	38.1	50.2	95.3
Pr	10.99	7.05	8.05	14.64	14.54	15.15	16.91	15.48	3.82	6.31	12.23
Nd	43.3	28.5	27.7	58.8	56.5	60.7	68.6	60.3	12.6	26.2	51.1
Sm	8.85	5.51	4.76	10.83	10.64	11.05	12.36	10.53	2.54	5.59	10.32
Eu	1.00	1.50	0.52	2.97	2.93	3.02	3.34	2.25	0.23	1.54	2.78
Gd	7.04	4.76	4.20	9.28	9.10	9.17	10.69	8.53	2.59	5.17	9.26
Tb	1.08	0.72	0.76	1.38	1.36	1.36	1.58	1.25	0.46	0.83	1.40
Dy	6.12	4.17	4.85	7.49	7.62	7.48	8.68	6.93	2.70	4.80	8.04
Ho	1.23	0.83	1.02	1.43	1.51	1.43	1.63	1.35	0.54	0.96	1.62
Er	3.79	2.35	3.28	4.08	4.16	4.04	4.52	3.95	1.69	2.68	4.48
Tm	0.57	0.35	0.53	0.57	0.61	0.58	0.62	0.58	0.26	0.39	0.67
Yb	3.66	2.14	3.58	3.63	3.75	3.55	3.75	3.66	1.77	2.41	4.15
Lu	0.57	0.32	0.56	0.56	0.55	0.53	0.57	0.57	0.28	0.36	0.62
Hf	8.40	3.51	5.59	10.28	9.61	10.54	9.90	11.11	3.88	4.19	7.23
Ta	1.51	0.51	1.28	1.00	0.90	0.80	0.81	1.00	1.75	0.67	0.99
Tl	0.64	0.10	1.01	0.58	0.59	0.64	0.57	0.75	1.60	0.29	0.55
Pb (XRF)	10	10	11	24	18	14	11	4	6	19	25
Bi	0.16	0.25	0.01	0.08	0.07	0.12	0.11	0.03	0.07	0.10	0.11
Th	17.8	3.9	21.8	9.7	11.3	8.9	8.2	12.3	16.4	4.4	11.7
U	2.69	0.60	1.31	1.91	1.81	2.74	0.60	0.99	1.38	5.25	4.88

Table 4.1: Whole-rock major (wt.%) and trace element (ppm) analyses (cont.)

Sample	GH73	GH76	GH15	GH70	GH32	GH39	GH34	GH40	GH41	GH43	GH46
Volcanic complex	Glyde Hill	Glyde Hill	-	-	Glyde Hill	Chitanilga	Chitanilga	Chitanilga	Chitanilga	Chitanilga	Chitanilga
Locality	Lake Everard	Lake Everard	Lake Everard	Lake Everard	Lake Everard	Kokatha	Kokatha	Kokatha	Kokatha	Kokatha	Kokatha
Unit	Mangaroongah Dacite	Mangaroongah Dacite	Moonamby Dyke Suite	Moonamby Dyke Suite	Felsic enclave (Whyeela Dacite)	Andesite	Rhyolite-dacite (Mi2)	Rhyolite-dacite (Mi5)	Basalt	Fiamme-rhyolite interbedded with basalt	Chandabooka Dacite
SiO2	62.36	65.10	75.60	75.16	74.66	62.92	71.65	73.20	52.28	71.00	67.11
Al2O3	14.92	13.79	11.88	12.19	12.95	13.96	13.87	12.66	15.87	14.45	14.34
Fe2O3	6.73	5.44	1.56	2.03	1.25	7.58	2.98	2.80	9.63	2.03	5.08
MnO	0.12	0.18	0.06	0.01	0.05	0.12	0.03	0.07	0.14	0.06	0.14
MgO	2.82	3.17	0.44	0.34	0.31	2.15	0.21	0.41	7.35	0.69	1.55
CaO	1.40	1.40	0.69	0.14	0.54	4.00	0.55	0.81	9.05	0.93	0.83
Na2O	2.98	4.77	2.54	2.93	3.22	3.90	3.84	3.64	2.60	4.33	4.30
K2O	4.64	2.28	5.95	5.63	6.08	3.14	5.73	4.96	0.53	4.82	3.36
P2O5	0.38	0.49	0.02	0.05	0.02	0.22	0.06	0.05	0.31	0.04	0.20
S	<0.01	<0.01	<0.01	0.01	<0.01	<0.01	<0.01	<0.01	<0.01	<0.01	0.01
LOI	2.04	2.25	1.37	1.00	0.82	0.70	0.36	0.43	1.20	0.61	1.95
Total	99.81	99.87	100.34	99.90	100.17	99.78	100.06	99.60	99.95	99.63	99.87
Li	32.2	31.9	13.0	7.6	5.2	17.4	4.1	8.1	25.0	12.1	21.0
Be	2.62	3.08	4.35	3.64	3.72	2.03	3.13	2.78	1.11	2.72	3.37
Sc	17.2	14.3	3.4	4.1	4.2	17.4	6.2	6.8	23.4	7.0	10.7
Ti	6279	5289	986	1509	1113	5282	2681	2151	6639	2861	4371
V (XRF)	82	73	2	9	4	160	4	12	202	16	33
Cr (XRF)	9	5	2	3	1	5	2	2	58	3	4
Mn	970	1427	458	101	421	911	221	544	1111	472	1118
Ni (XRF)	14	8	5	5	4	9	3	4	92	3	6
Cu (XRF)	23	10	2	2	2	11	3	4	26	5	6
Zn (XRF)	91	129	37	28	18	91	55	60	97	52	104
Ga	17.9	19.0	15.3	14.9	17.0	20.6	19.7	18.0	19.5	18.4	19.8
As	<5	<5	<5	<5	9.1	<5	<5	<5	<5	<5	<5
Rb	159.9	79.3	312.1	271.6	259.3	94.3	177.8	154.8	69.7	143.8	118.7
Sr	586.4	217.6	27.3	77.5	172.8	336.1	134.1	116.7	461.1	164.1	209.8
Y	37.3	34.2	60.4	44.1	45.3	27.0	35.2	29.2	26.3	32.4	45.2
Zr	437	208	231	233	194	216	321	329	165	393	355
Nb (XRF)	15	19	22	20	32	11	18	15	9	19	18
Mo	0.30	0.84	1.11	0.46	16.38	1.41	1.48	0.93	0.47	4.42	0.76
Ag	0.09	0.05	0.04	0.05	1.52	0.08	0.09	0.07	0.07	0.14	0.06
Cd	<0.23	0.2	<0.23	<0.23	<0.23	0.1	<0.23	<0.23	0.1	<0.23	<0.23
Sn	2.38	2.95	7.21	4.19	1.75	2.10	3.05	2.39	1.68	2.91	2.86
Sb	0.07	0.13	0.44	0.11	0.10	<0.05	0.12	<0.06	<0.05	0.14	0.21
Te	<0.37	<0.37	<0.37	<0.37	<0.37	<0.09	<0.37	<0.37	<0.09	<0.37	<0.37
Cs	6.17	1.27	3.47	2.38	3.40	1.97	1.61	1.22	3.41	1.80	1.07
Ba (XRF)	2363	708	175	983	456	1045	1871	1353	502	1315	1925
La	53.5	30.1	112.0	79.9	83.3	44.0	63.8	49.6	24.3	67.4	82.8
Ce	120.0	67.3	202.5	164.7	163.5	85.6	136.5	104.1	52.7	139.3	145.6
Pr	14.91	8.87	23.62	17.63	18.46	9.71	16.53	12.00	6.61	16.16	19.55
Nd	59.1	37.5	80.0	58.8	67.5	35.9	62.4	44.1	27.1	59.6	72.7
Sm	10.98	7.61	13.70	9.89	12.37	6.43	11.07	7.60	5.76	10.13	11.78
Eu	2.98	1.85	0.33	0.87	0.87	1.56	2.49	1.17	1.55	1.86	2.28
Gd	9.32	6.87	10.96	8.09	10.05	5.46	8.95	6.45	5.36	7.58	9.87
Tb	1.36	1.05	1.73	1.33	1.53	0.84	1.33	0.99	0.83	1.12	1.43
Dy	7.52	6.05	10.14	7.80	8.26	4.82	7.12	5.59	4.86	6.03	8.22
Ho	1.42	1.22	2.05	1.56	1.57	0.98	1.32	1.09	0.97	1.16	1.63
Er	4.01	3.66	6.21	4.90	4.50	2.75	3.70	3.21	2.70	3.42	4.76
Tm	0.56	0.56	0.94	0.76	0.66	0.41	0.52	0.47	0.41	0.51	0.68
Yb	3.44	3.69	5.97	5.05	4.09	2.55	3.29	3.07	2.42	3.22	4.23
Lu	0.53	0.57	0.91	0.78	0.62	0.37	0.51	0.46	0.36	0.50	0.65
Hf	10.45	6.47	8.21	7.59	6.77	5.44	8.75	8.45	4.24	9.86	9.27
Ta	0.73	1.33	2.50	2.35	2.84	0.86	1.62	1.29	0.61	1.38	1.24
Tl	0.93	0.37	1.43	1.25	1.31	0.63	0.95	0.81	0.25	0.76	0.68
Pb (XRF)	26	6	7	8	21	30	34	31	9	37	16
Bi	0.15	0.15	0.06	0.09	0.01	0.05	0.17	0.04	0.02	0.23	0.07
Th	10.0	13.4	47.1	45.7	40.9	10.1	18.7	11.8	4.4	19.5	18.2
U	1.89	2.77	9.17	2.47	0.93	2.15	0.76	2.21		4.59	3.79

Table 4.1: Whole-rock major (wt.%) and trace element (ppm) analyses (cont.)

Sample	GH49	GH50	GH51	GH52	GH69	GH44	GH37	GH38
Volcanic complex	Chitanilga	Chitanilga	Chitanilga	Chitanilga	Chitanilga	-	-	-
Locality	Kokatha	Kokatha	Kokatha	Kokatha	Kokatha	Kokatha	Kokatha	Kokatha
Unit	Basalt	Basalt	Lake Gairdner Rhyolite	Andesite	Basalt	Microgranite Dyke	Hiltaba Suite	Hiltaba Suite
SiO2	52.12	53.20	75.67	62.35	51.03	76.44	76.25	76.26
Al2O3	15.66	14.37	12.10	14.22	16.95	12.66	12.12	11.55
Fe2O3	9.57	9.81	2.20	7.70	9.90	0.81	1.21	1.60
MnO	0.14	0.17	0.11	0.13	0.15	0.02	0.02	0.03
MgO	7.48	8.25	0.24	2.31	5.30	0.16	0.23	0.22
CaO	9.11	7.55	0.46	3.92	7.41	0.42	0.60	0.27
Na2O	2.62	3.09	1.87	3.66	3.50	3.95	2.91	2.61
K2O	0.51	0.55	6.61	3.50	2.54	4.71	5.83	6.06
P2O5	0.31	0.23	0.02	0.21	0.25	0.03	0.03	0.04
S	<0.01	<0.01	<0.01	<0.01	<0.01	0.01	<0.01	<0.01
LOI	1.16	1.73	0.44	1.21	2.10	0.71	0.50	0.56
Total	99.63	99.75	100.10	100.29	100.36	99.98	99.95	99.54
Li	25.0	18.1	5.7	21.2	23.0	30.0	10.7	10.4
Be	1.48	0.97	2.30	1.78	1.20	6.26	3.27	2.29
Sc	24.5	21.6	6.1	17.4	25.1	2.0	2.7	4.5
Ti	6035	4251	1259	5314	7209	264	931	1940
V (XRF)	162	174	4	163	196	8	2	3
Cr (XRF)	364	780	4	5	80	2	1	2
Mn	1197	1265	931	950	1221	130	172	279
Ni (XRF)	117	306	4	11	103	9	4	4
Cu (XRF)	16	21	6	19	76	1	4	5
Zn (XRF)	96	80	49	92	82	8	23	49
Ga	16.5	16.0	17.3	19.6	19.3	24.6	16.7	15.6
As	<5	<5	<5	<5	<5	<5	<5	<5
Rb	44.0	19.1	226.5	115.6	93.5	798.1	266.9	259.5
Sr	908.1	558.7	49.9	359.5	552.1	15.7	72.8	42.6
Y	24.7	18.4	26.2	26.8	24.3	101.9	35.0	38.9
Zr	169	132	293	209	165	147	162	472
Nb (XRF)	9	6	14	11	8	43	16	22
Mo	0.53	0.22	0.66	0.72	0.77	0.24	0.82	1.33
Ag	0.07	0.06	0.10	0.09	0.05	0.05	0.08	0.15
Cd	0.2	0.1	<0.23	0.1	0.3	<0.23	<0.23	<0.23
Sn	1.84	1.29	2.63	1.92	1.40	10.65	2.94	5.38
Sb	0.35	0.06	<0.06	0.07	0.23	0.24	0.21	0.22
Te	<0.09	<0.09	<0.37	<0.09	<0.37	<0.37	<0.37	<0.37
Cs	2.22	1.23	4.23	1.84	2.95	7.33	3.67	2.88
Ba (XRF)	1405	627	1067	1050	600	181	568	266
La	44.5	26.3	67.0	43.9	24.1	34.2	58.6	53.9
Ce	93.3	51.9	131.8	82.0	52.9	81.1	98.7	150.4
Pr	11.58	6.43	14.59	9.42	6.70	10.18	11.87	12.54
Nd	47.0	25.9	51.5	35.1	27.7	36.9	41.7	43.6
Sm	8.73	5.02	8.21	6.40	5.78	10.20	7.12	7.69
Eu	2.15	1.32	1.14	1.53	1.58	0.05	0.85	0.62
Gd	6.70	4.16	6.33	5.41	5.31	11.11	6.37	6.81
Tb	0.91	0.62	0.93	0.85	0.83	2.42	1.03	1.17
Dy	4.78	3.50	5.13	4.90	4.74	16.41	6.08	6.98
Ho	0.92	0.69	0.98	0.98	0.91	3.52	1.21	1.42
Er	2.46	1.94	2.90	2.79	2.62	11.99	3.65	4.35
Tm	0.35	0.28	0.42	0.41	0.37	2.05	0.55	0.65
Yb	2.12	1.73	2.63	2.55	2.34	14.09	3.46	4.26
Lu	0.31	0.26	0.40	0.38	0.36	2.12	0.53	0.67
Hf	4.22	3.35	7.87	5.36	4.32	9.95	5.54	12.83
Ta	0.63	0.52	1.29	0.74	0.55	7.93	2.26	2.05
Tl	0.23	0.10	1.12	0.72	0.29	2.87	1.40	1.31
Pb (XRF)	14	10	42	49	8	40	37	42
Bi	0.17	0.07	0.12	0.04	0.02	0.06	0.67	0.23
Th	7.8	4.4	19.3	10.0	4.1	48.7	27.1	33.7
U	1.62	1.52	3.84	8.11	0.64	8.25	1.75	0.60

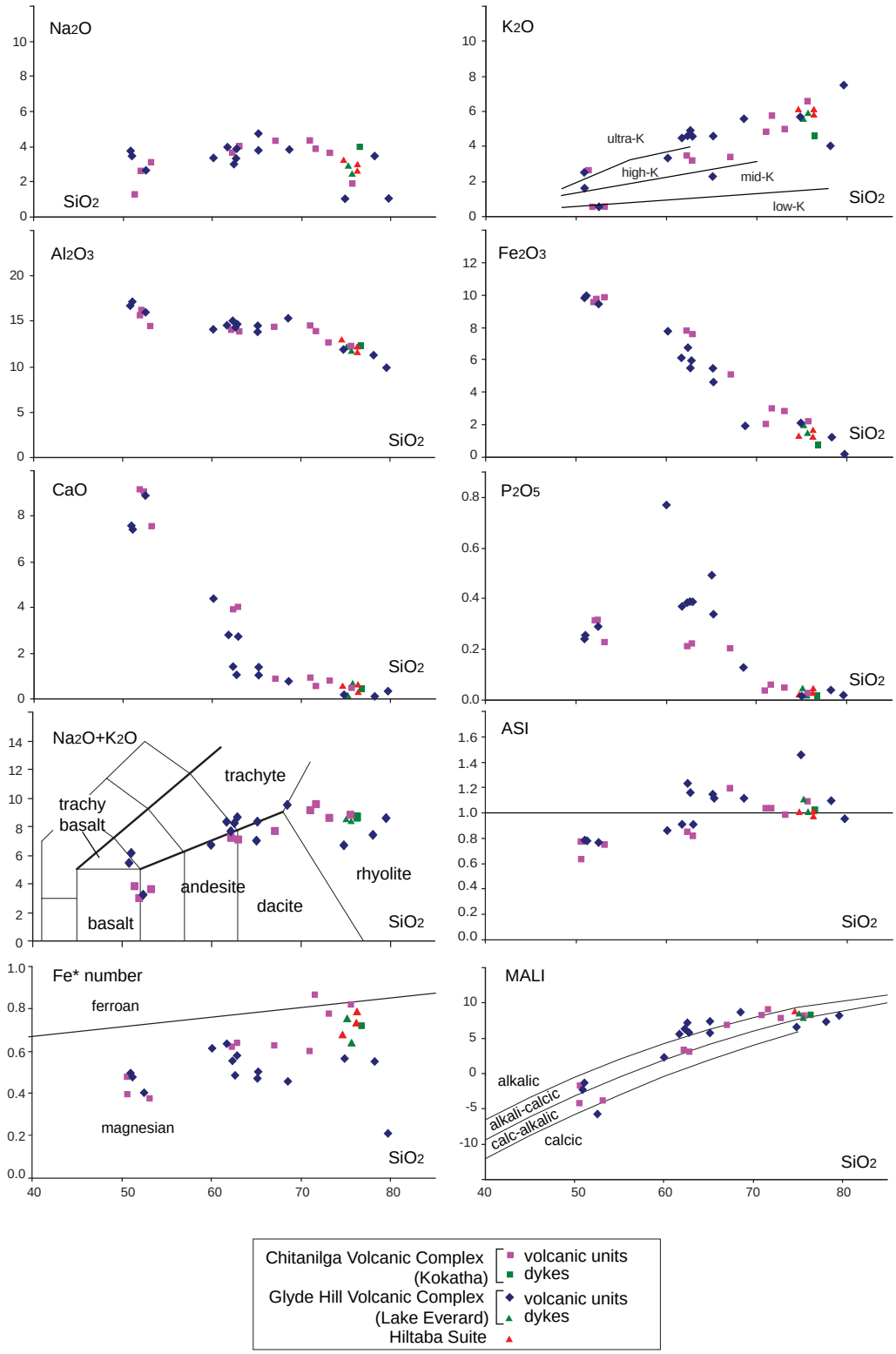

Fig 4.1. Whole-rock major element chemical analyses. Analyses recalculated to anhydrous, concentrations as wt.%. K_2O vs SiO_2 plot after Peccerillo and Taylor (1976); Na_2O + K_2O vs SiO_2 after Le Bas et al. (1986), ASI =Al/(Na +K +Ca -1.67·P) (mol), Fe* number = FeOt/(FeOt+MgO) (mol) and MALI =K_2O +Na_2O -CaO (wt.%) after Frost et al. (2001).

mol) increases with increasing silica. Units from both volcanic complexes are mainly distributed in the magnesian field of Frost et al. (2001).

Alumina saturation index (ASI = (Al/(Na +K +Ca -1.67•P), mol) is between 0.8-1.4, and most samples are mildly peraluminous (ASI >1). Rocks with ASI values below 1, mostly granite samples, are metaluminous (Al_2O_3 >Na_2O+K_2O, mol). A broad decreasing trend is shown in the ASI versus silica plot for intermediate and felsic compositions. Sample GH13 plots above this general trend, mainly because of low Na content. In the modified alkali lime index (MALI = Na_2O+K_2O-CaO, wt.%) versus silica diagram (Frost et al., 2001), intermediate and felsic samples mainly plot into the alkali-calcic and alkalic fields (Fig. 4.1). The rocks can be classified as calc-alkalic to alkali-calcic on the basis of the variations in CaO and alkalis (Peacock, 1931), and as calc-alkaline on the basis of the Fe enrichment in the AFM diagram (Kuno, 1968). Decreasing Al, Fe, Mg, Ca, Ti and P and increasing Na and K with increasing silica can be accounted for by fractional crystallisation of modal minerals (plagioclase, clinopyroxene, Ti-Fe oxide, and apatite).

Trace elements

On primitive mantle-normalised diagrams, significant negative spikes are shown by Sr, P, Ti (Fig. 4.2). These spikes are more pronounced for felsic compositions. Relative depletion is also shown by Nb and Ta (Nb/La = 0.36 and Ta/Nb = 0.03), although it should be noted that Nb and Ta concentrations are not low compared to the average continental crust (e.g. Hu and Gao, 2008). Lead shows wide variations (Pb/Ce = 0.02-0.63) and both positive and negative anomalies are present in some samples. Primitive mantle-normalised rare earth element (REE) diagrams show light REE (LREE) enrichment in comparison with heavy REE (HREE) and a negative Eu anomaly (Fig. 4.3). The Moonamby Dyke Suite shows a more ”evolved” pattern, having higher REE values in comparison to the volcanic units, and a larger negative Eu anomaly (Fig. 4.3). The microgranite dyke intruding the Chitanilga Volcanic Complex at Kokatha (sample GH44) has lower La/YbN compared with the volcanic units and a marked negative Eu peak (Fig. 4.3).

On Harker diagrams, most high field strength (HFS) and RE elements show increasing concentrations with increasing silica (Fig. 4.4, 4.5). These trends indicate incompatible behaviour, leading to high concentrations of HFSE and REE in felsic samples (e.g. Ce ≤200 ppm, Zr ≤500 ppm and Th ≤40 ppm at SiO_2 = 70 wt.%). For silica ≥70 wt.%, some of these elements show steeply increasing trends (Nb, Th, Ta), whereas others increase with silica up to about 70 wt.% and decrease in the most evolved compositions (Zr, Hf and, to a lesser extent, REE). Titanium values define a nearly linear decreasing trend for intermediate and felsic compositions, with the highest values for SiO_2 = 60 wt.%. Mafic samples show variable Ti content (Ti ~4000-7000 ppm, Fig. 4.4). First series transition elements show steep decreasing patterns, with the exception of Mn and Zn which have the highest values for intermediate compositions (Fig. 4.7). Barium is present in concentration up to ~2700 ppm, with the exception of sample GH26 (Whyeela Dacite), containing very fine grained barite.

In comparison with the volcanic rocks, granite and dyke samples show high values of incompatible elements, including some REE, HFSE, Rb, Ta, Th, U, Be and Sn and lower values of compatible elements (Sr, Ba, Sc, V; Figures 4.4, 4.6, 4.7). The quartz-feldspar felsic enclave in the Wheepool Rhyolite (GH32) has similar major and trace

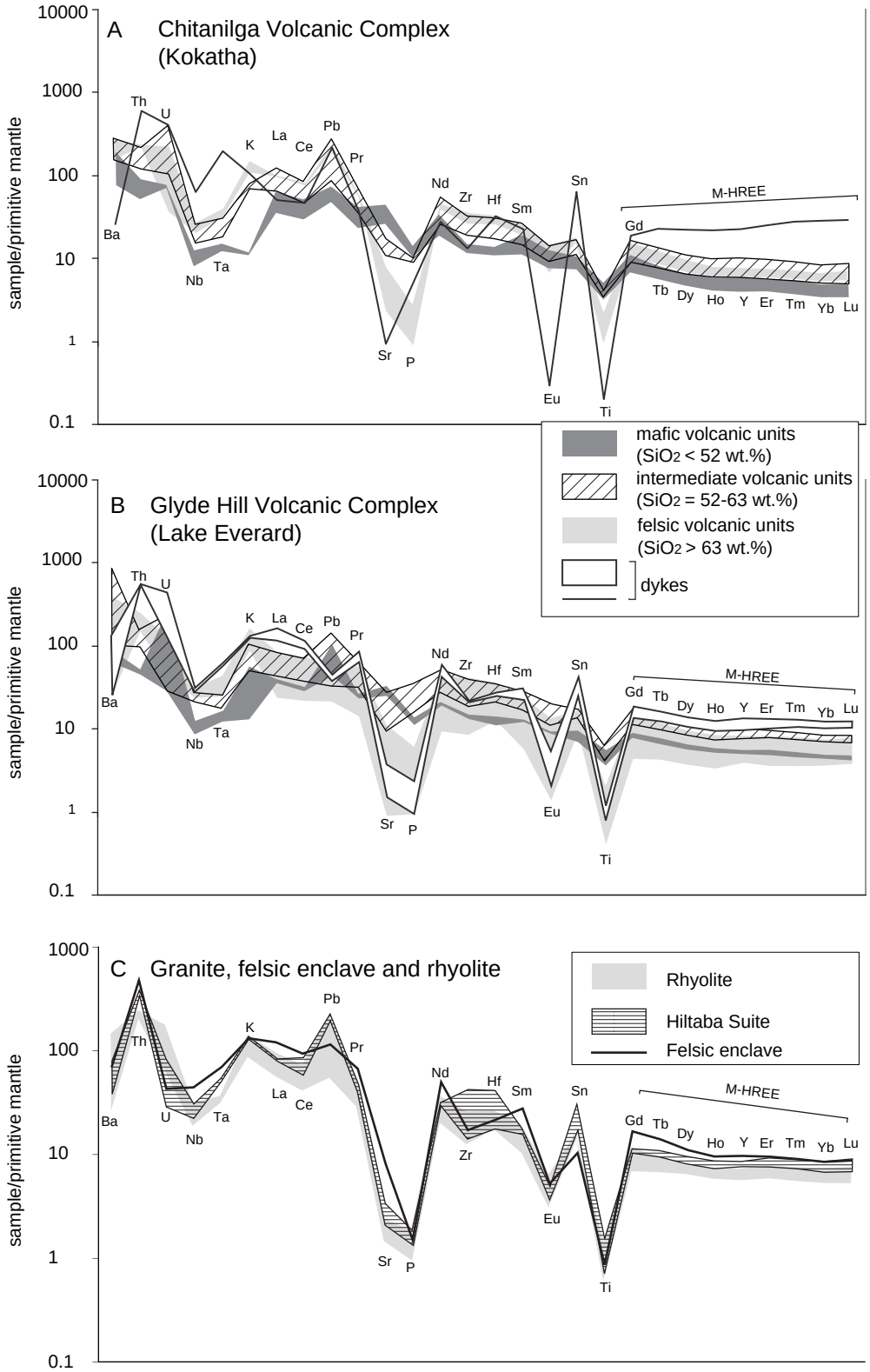

Fig. 4.2. Primitive mantle-normalised incompatible element whole-rock compositions. A- Volcanic units and dykes from the Chitanilga Volcanic Complex. B- Volcanic units and dykes from the Glyde Hill Volcanic Complex. C- Hiltaba Suite and felsic enclave compared with rhyolite units (Wheepool Rhyolite and Lake Gairdner Rhyolite). Normalising values after Sun and McDonough (1989).

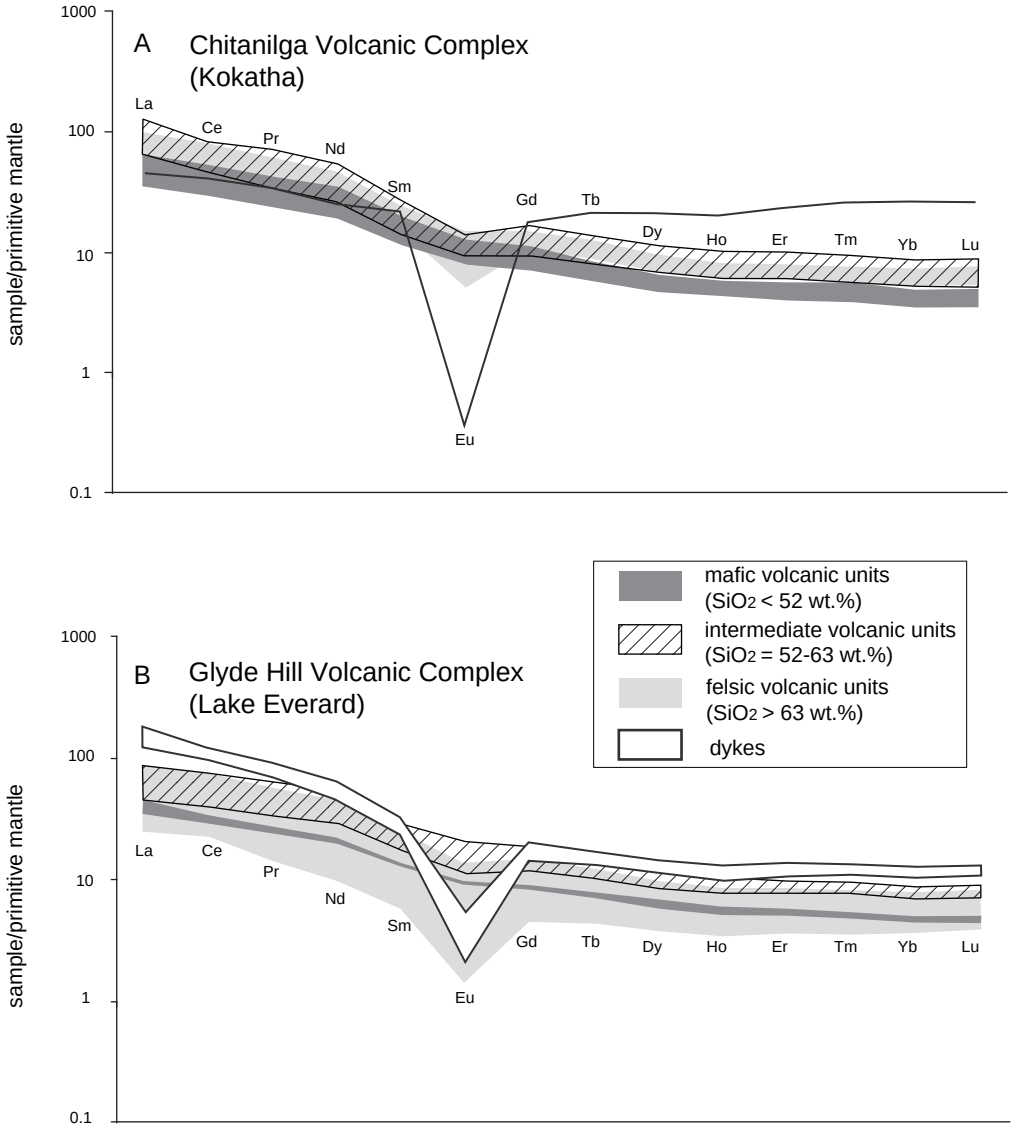

Fig. 4.3. Primitive mantle-normalised REE whole rock analyses. A- Chitanilga Volcanic Complex. B- Glyde Hill Volcanic Complex. Normalising values after Sun and McDonough (1989).

element composition to the samples from the Hiltaba Suite Granite at Kokatha (Fig. 4.2 C), with the exception of higher Ag and, to a lesser extent, Th content.

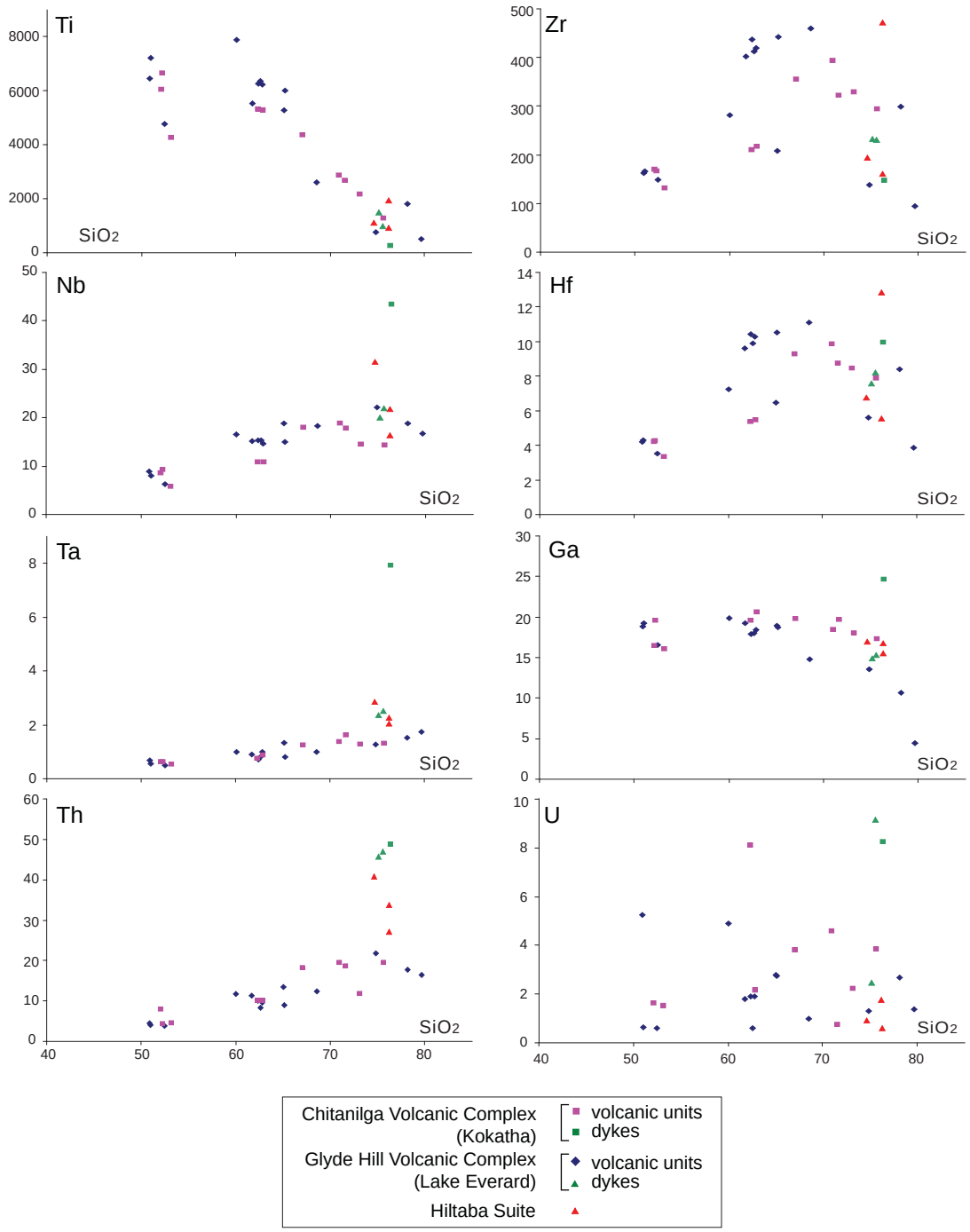

Fig. 4.4. Whole-rock HFSE compositions (ppm) plotted versus SiO_2 (wt.%). ICP-MS and XRF (Nb).

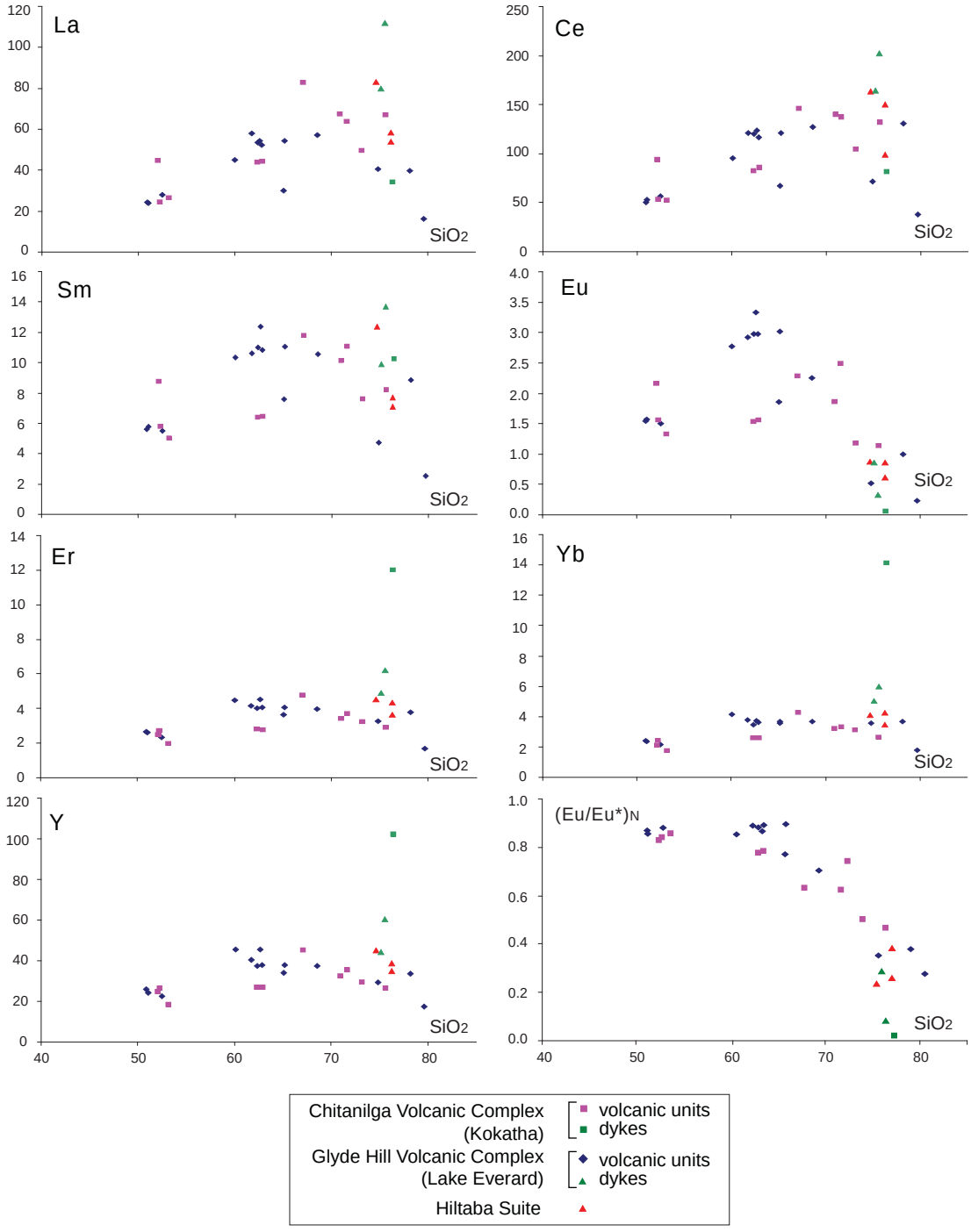

Fig. 4.5. Whole-rock REE compositions (ppm) plotted versus SiO_2 (wt.%). ICP-MS and XRF (La).

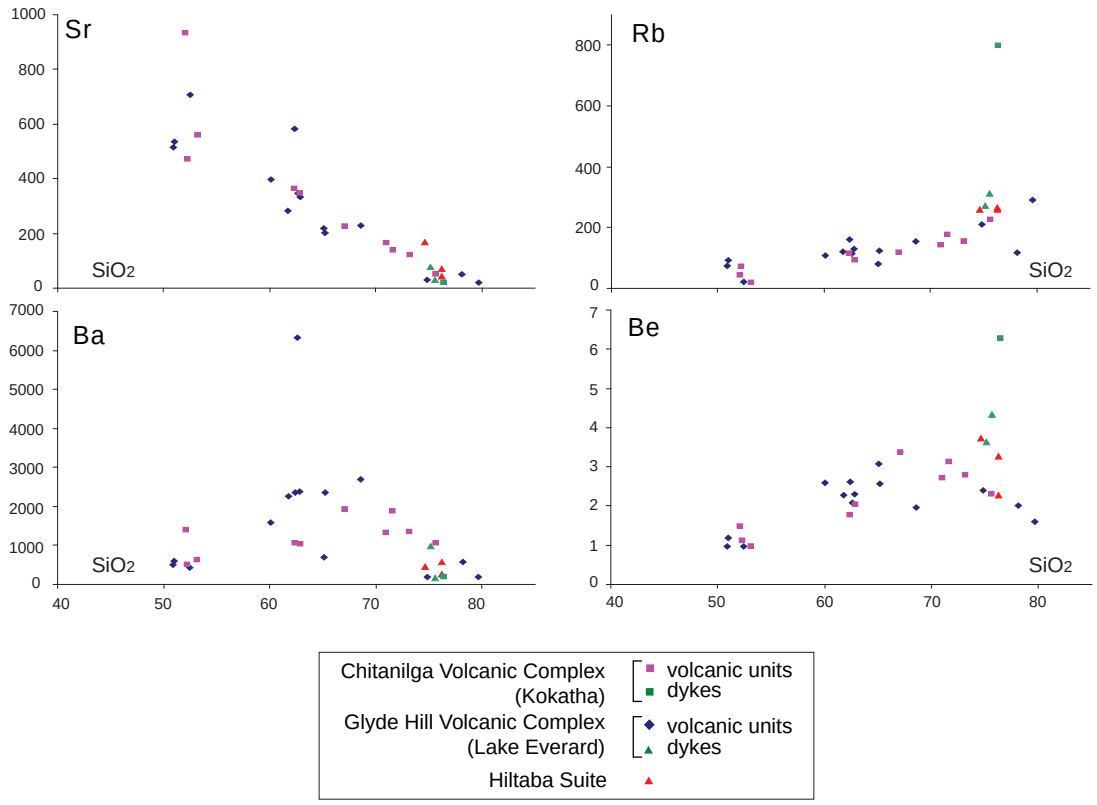

Fig. 4.6. Whole-rock alkali and alkaline earth trace element/LILE compositions (ppm) plotted versus SiO_2 (wt.%). ICP-MS and XRF (Ba, Sr).

4.3.2 Quartz-hosted melt inclusions

Of the nine quartz-bearing units mapped in the Chitanilga and Glyde Hill Volcanic Complexes, three contain well preserved quartz-hosted melt inclusions that were used for this study. These units are the Wheepool Rhyolite, the Waurea Pyroclastics and the Moonamby Dyke Suite, all from the Glyde Hill Volcanic Complex at Lake Everard. Phenocrysts of feldspar are ubiquitous and more abundant than quartz, but feldspar-hosted melt inclusions were not found, possibly because of the moderate but widespread alteration to fine grained products.

Wheepool Rhyolite (samples GH06, 23, 24c, 59)

Melt inclusions are round to negative-crystal-shaped, mostly 5 to 60 µm in diameter, and exceptionally up to 100 µm. Both glassy melt inclusions and crystalline (opaque) to granular-textured (semi-opaque) melt inclusions are present. Glass is mostly preserved in relatively small inclusions (<40 µm, Fig. 4.8 A), whereas larger inclusions tend to be crystalline and opaque (Fig. 4.8 B). Glass-bearing inclusions can be two-phase (glass +vapour bubble, Fig. 4.8 A) or contain small solid phases (Fig. 4.8 C, D). Glass is either colourless or pink to pale brown (Fig. 4.8 A, C, D, E). A bubble is always present and the volumetric proportion between the vapour phase and the inclusions is relatively constant (bubble = 4.6±1.5 vol.% of the inclusion). A colourless mineral phase (relief <glass, K-feldspar?) and a yellow, non-pleochroic phase are locally present. Because of their

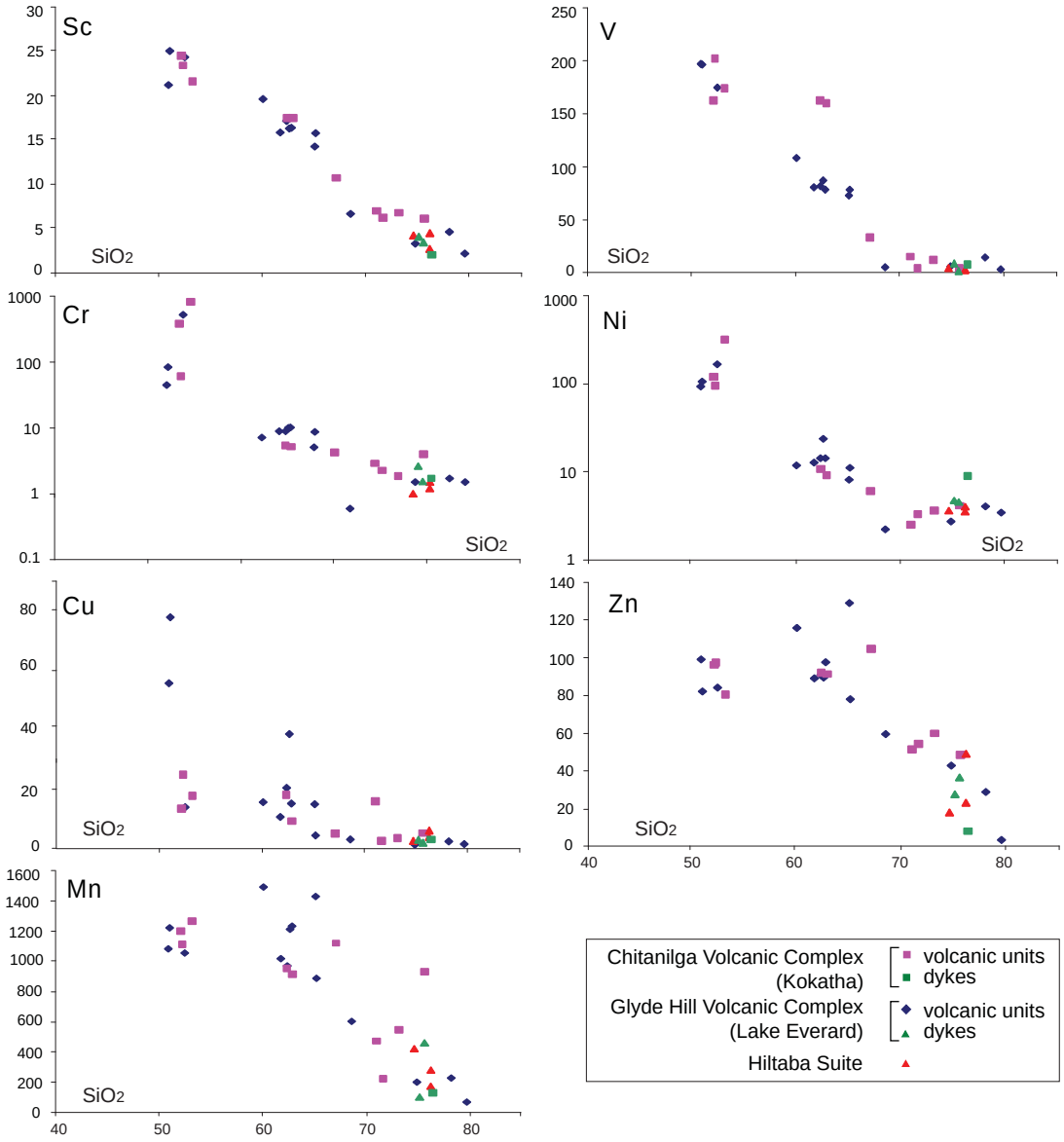

Fig. 4.7. Whole-rock first series transition element compositions (ppm) plotted versus SiO_2 (wt.%). ICP-MS (V, Sc) and XRF (Ni, Cr, Cu, Zn).

uneven distribution and the abundance, these crystals are interpreted as co-trapped, rather than having crystallised after trapping (daughter phase). Melt inclusions occur isolated or in trails. Inclusions along the same trail may show different textures, being either glassy or crystalline and, in the former case, showing different phase associations and abundances. Visibly cracked inclusions are opaque (crystalline, Fig. 4.8 F).

Waurea Pyroclastics (samples GH13, 95)

Melt inclusions are round to negative-crystal-shaped and ≤50-60 µm in diameter. Most are equidimensional, but elongate inclusions are also present (Fig. 4.9 A). Most melt inclusions are clear (glass-bearing); the glass is colourless to pink-yellow. All inclusions

contain a bubble; the ratio of the bubble volume to the volume of the inclusion is relatively constant (bubble/inclusion= 7.4±2.2 vol.%), with some noticeable exceptions (bubble/inclusion >10 vol.%). In several cases the bubble appears to be deformed and flattened on one side (Fig. 4.9 B). Some large (several tens of μm across) and opaque decrepitated melt inclusions show a corona of small fluid inclusions ("sweat" halo) projected from the melt inclusion into the host quartz (Fig. 4.9 C). In addition to glass and a vapour phase, one or more solid phases are locally present (Fig. 4.9 D-F): K-feldspar (colourless, relief <glass) is subhedral; Fe±Ti oxide occurs as both skeletal, opaque crystals and "massive", red crystals. Another elongate to needle-like, non-pleochroic yellow mineral phase up to 20 μm long, was not identified.

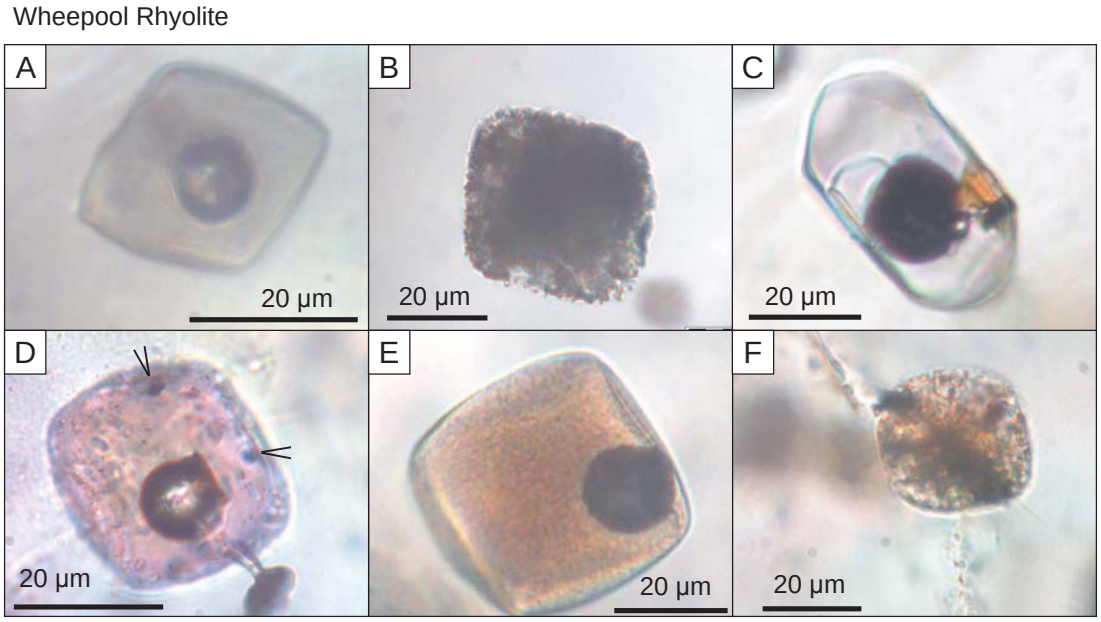

Fig. 4.8. Melt inclusions from the Wheepool Rhyolite. A- Two-phase (glass+vapour) inclusion, sample GH24c. B- Crystalline inclusion, sample GH06. C- Glass-, vapour- and crystal-bearing melt inlusion, sample GH23. D- Glassy inclusion containing a vapour phase and small crystals (arrowed), sample GH59. E- granular-textured semi-opaque melt inclusion, sample GH06. F- Granular-textured melt inclusion crossed by a crack, sample GH59.

Moonamby Dyke Suite (samples GH15, 62, 70, 70B)

All melt inclusions in these samples are completely crystalline (opaque). Their shape varies from round to elongate to subhedral and the size is up to 60 μm (Fig. 4.10 A). Melt inclusions are commonly aligned along curved trapping surfaces (crystal growth planes, Fig. 4.10 B), parallel to CL zones. The white colour of melt inclusions under the binocular microscope makes them distinguishable from embayments, which are brick-red to purple (Fig. 4.10 C).

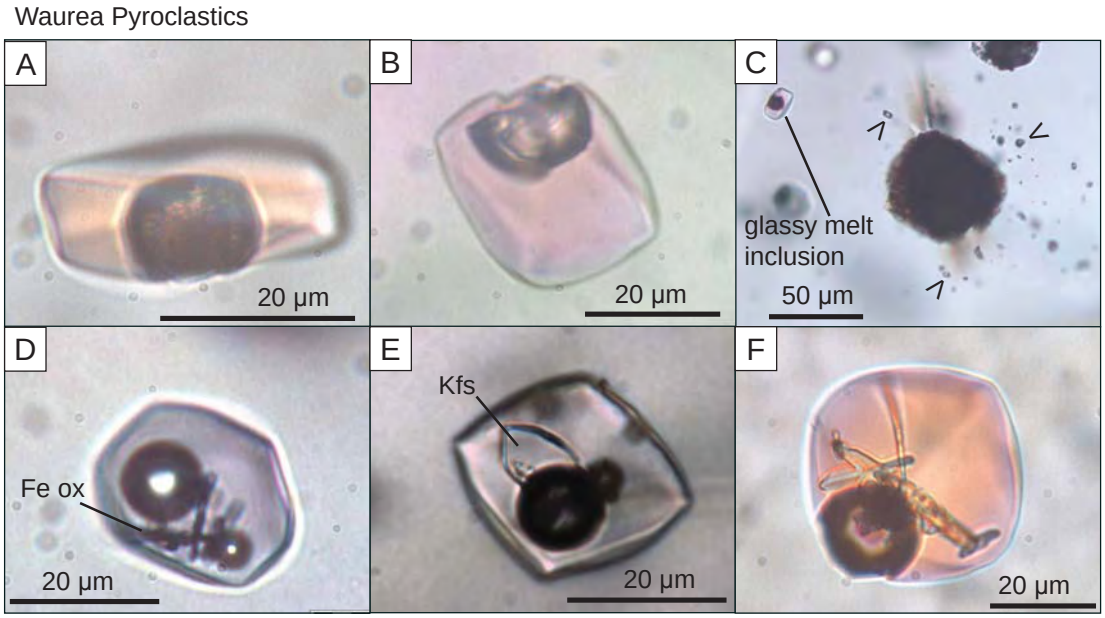

Fig. 4.9. Melt inclusions from the Waurea Pyroclastics. A, B- Two-phase (glass+vapour) melt inclusions (A: sample GH13, B: GH95). The bubble in inclusion B is flattened on the inclusion walls. C- Large decrepitated inclusion surrounded by a corona of fluid inclusions (arrowed) in the host mineral (sample GH95); small melt inclusions to the left are glassy. D- Melt inclusion containing multiple vapour bubbles and dendritic crystals of Fe oxide; E- Negative crystal-shaped melt inclusion containing a crystal of K-feldspar (sample GH13). F- Glass-bearing melt inclusion containing elongate mineral phases (not identified, sample GH13).

4.3.3 Melt inclusion heating experiments

Homogenisation occurred in a wide interval of temperatures. Volcanic units (Wheepool Rhyolite and Waurea Pyroclastics) have homogenisation temperatures in the range 1000-1050°C, whereas the dykes have lower temperatures (800-850°C). In all the samples, small inclusions (≤20 µm) are the most susceptible to homogenisation and no homogenised inclusions bigger than 40 µm were observed. Fractured inclusions, either decrepitated (Fig. 4.11 A) or affected by penetrative cracks (Fig. 4.11 D), show multiple bubbles and a fine grained, semi-opaque solid. A change in melt inclusion shape at high temperature was observed in several cases, including protruding bubbles in incompletely homogenised inclusions and irregular, “bumpy” walls (Fig. 4.11 E, H). Such modifications occurred both below and above minimum homogenisation temperatures.

In the Wheepool Rhyolite, homogenised inclusions are clear and free of cracks. In a few cases, radial cracks were observed only after the inclusions were exposed (compare Fig. 4.12 A, B). Predictably, such fractures do not give any CL response (Fig. 4.12 C), not having undergone healing, whereas other presumably early-formed radial cracks are clearly visible in CL images (Fig. 4.12 E). After heating, melt inclusions larger than 20 µm apparently show a tendency for negative crystal shapes, whereas smaller ones are more likely to be round (Fig. 4.11 B, C). Incompletely homogenised inclusions contain multiple vapour bubbles and microcrystalline, semi-opaque solids (Fig. 4.11 A). Vapour bubbles protruding into the host phase were observed in a limited number of cases. Inclusions crossed by cracks associated with fluid inclusions (Fig. 4.8 F) failed to

Moonamby Dyke Suite

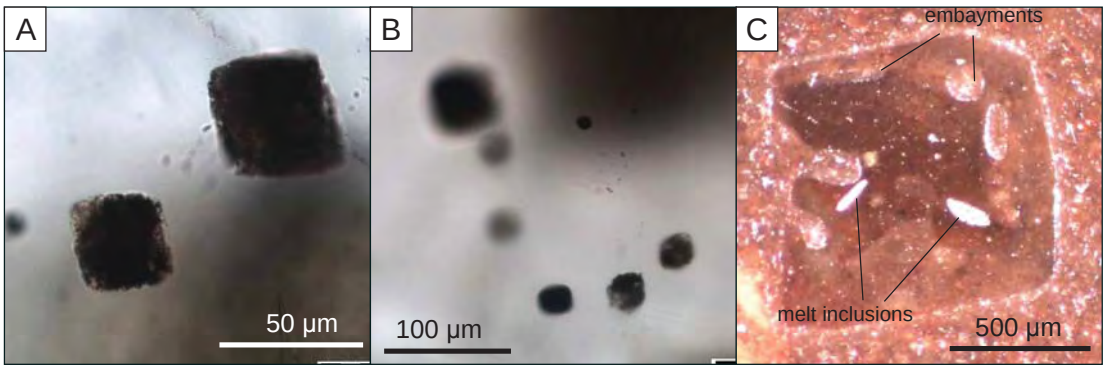

Fig. 4.10. Melt inclusions from the Moonamby Dyke Suite. A- Subhedral negative crystal-shaped, crystalline melt inclusions (sample GH15, transmitted light). B- Trail of crystalline melt inclusions (sample GH15, transmitted light). C- Crystalline melt inclusions are white in reflected light (sample GH70B, binocular microscope).

homogenise.

In the Waurea Pyroclastics, homogenised melt inclusions are smooth to irregular-shaped with “bumpy” walls. Fractured inclusions, both decrepitated (Fig. 4.11D) and affected by pervasive cracks, did not homogenise during heating (Fig. 4.12 D, E). Multiple bubbles and anhedral, semi-opaque solids were observed in these inclusions. Protruding bubbles were observed at T ≥ 900°C (Fig. 4.11 D, E).

In the Moonamby Dyke Suite, melt inclusions show irregular margins after heating, both above (Fig. 4.11 H) and below homogenisation temperature. This behaviour is in contrast with the smooth, round to negative crystal-shaped appearance of unheated melt inclusions (cf. Fig. 4.10).

4.3.4 Melt inclusion analyses

Major elements and comparison with whole-rock composition

The melt inclusion compositions (Tables 4.2, 4.3, 4.4, Fig. 4.13) range from 66 to 83 wt.% SiO_2. With a few exceptions, homogenised inclusions have higher SiO_2 contents than unhomogenised inclusions. Compositions of homogenised melt inclusions are close to the respective whole-rock compositions, except for some differences in alkalis (particularly Na in the Waurea Pyroclastics). Harker diagrams show good agreement between melt inclusion and whole-rock analysis for most elements (Na_2O, K_2O, CaO) and their ratios with Al_2O_3 (Fig. 4.13, Tables 4.2, 4.3), with the exception of the weakly increasing trends of Fe_2O_3, and Fe_2O_3/Al_2O_3 in melt inclusions (Fig. 4.13). Melt inclusion ASI values are between 0.8-1.3. Comparable ASI values were measured in melt inclusions and whole-rock samples, with the exception of the Waurea Pyroclastics, mainly due to a low whole-rock Na content (Fig. 4.13).

Because the melt was silica-saturated at the moment of entrapment, some degree of post-trapping crystallisation on inclusion walls can be expected, with consequent

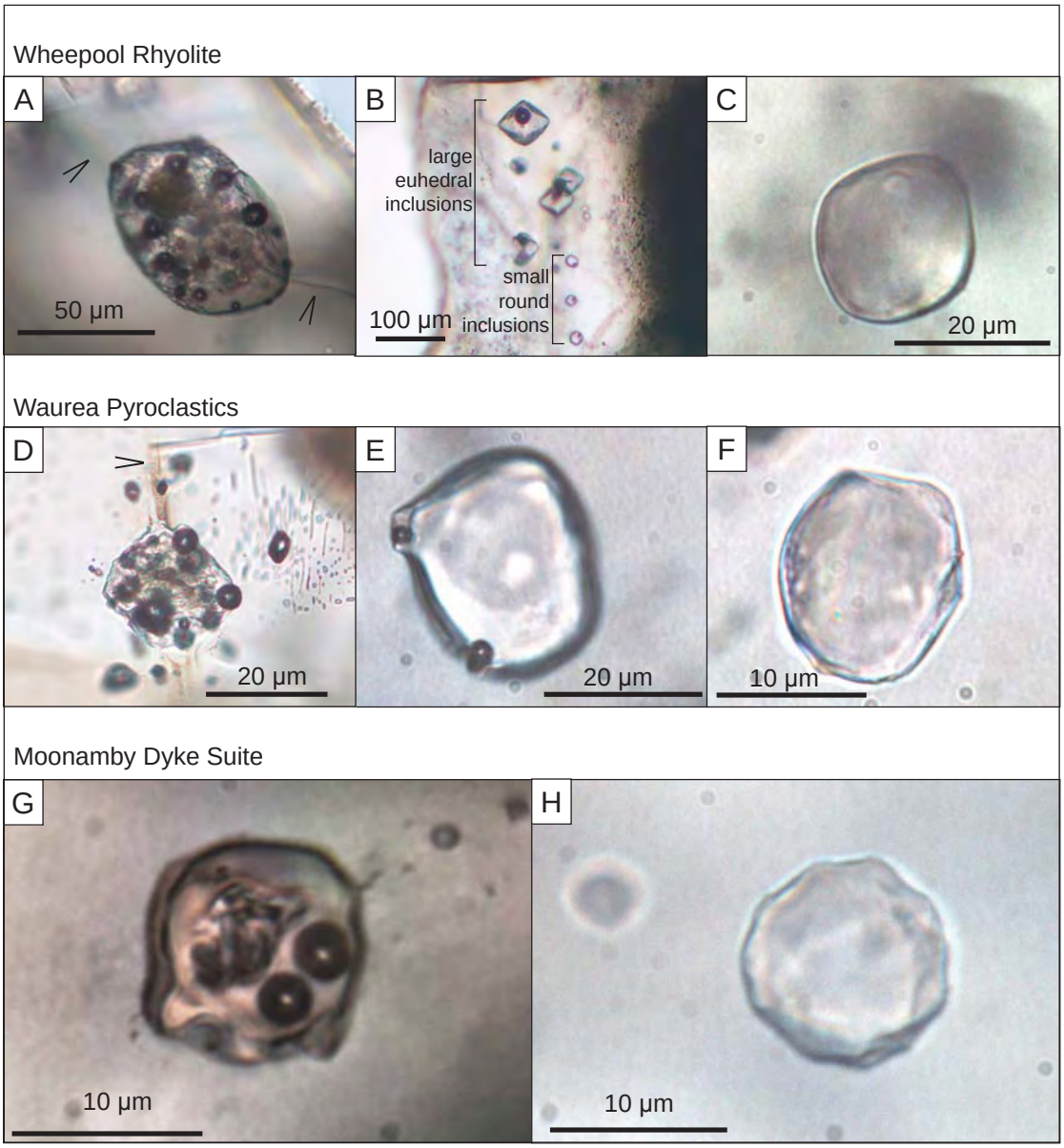

Fig. 4.11. Changes in melt inclusions during homogenisation experiments, comparison between unhomogenised and homogenised inclusions. A, B, C- Wheepool Rhyolite heated at 1000°C (samples GH06, GH23). D, E, F- Waurea Pyroclastics heated at 1000°C (samples GH13, GH95). G, H- Moonamby Dyke Suite heated at 850°C (sample GH15). Melt inclusions crossed by penetrative cracks (A, crack shown by arrows) or radial cracks (D) failed to homogenise at high temperature. Some melt inclusions show bubbles protruding into the host phase (E).

reduction of silica in the included melt. Modifications can also be induced by experimental conditions, as host quartz is melted during heating in the laboratory. In general, heating to temperatures lower than the trapping temperature will result in low silica in the melt inclusions, whereas heating to higher temperatures (overheating) will produce artificially high Si values (Webster et al., 2004). In addition, re-melting of host quartz would have a “dilution” effect on elements other than Si, with a consequent reduction in measured concentration. The negative trends observed in Harker diagrams for most elements,

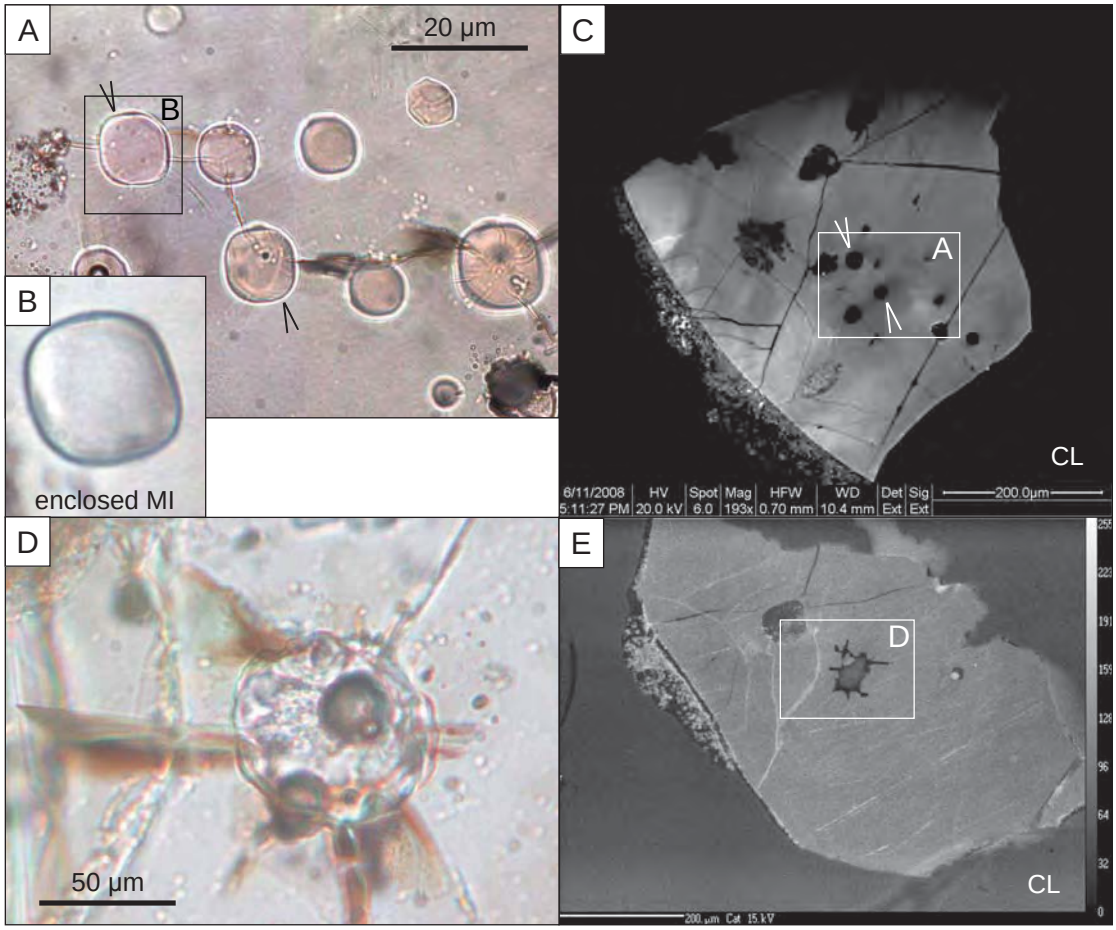

Fig. 4.12. Changes in melt inclusions during homogenisation experiments, homogenised and incompletely homogenised melt inclusions. A, B, C- Wheepool Rhyolite (sample GH59, heated 1000°C). Two exposed inclusions (A, arrowed) appear as dark spots in the CL image (C, arrowed). Some inclusions show radial cracks which were observed only after exposure (cf. still enclosed inclusion, B). These cracks are not visible in CL (C). D, E- Unhomogenised and partly devitrified melt inclusion, Waurea Pyroclastics (sample GH13, heated 1000°C). Decrepitation cracks are clearly visible in both transmitted light (D) and CL (E).

together with higher SiO_2 average values in heated inclusions and the wide span of SiO_2 compositions (Fig. 4.13), are compatible with both post-trapping crystallisation and re-melting of quartz during heating experiments. The dilution effect is proportional to the amount of quartz crystallised or melted. Based on the variations in silica between unheated and homogenised inclusions, the variation of elements other than silica can be estimated in ≤10-15% relative. The dilution effect does not affect ratios of elements. Therefore, variations of element ratios with increasing silica reflect primary magma evolution. It should be noted, however, that silica content and, as a consequence, the steepness of these trends is influenced by these post-trapping processes.

Trace elements

Most trace elements show significant variations in concentration (standard deviation/ average >0.25 for most trace elements and >0.5 for Cu, Ba, Sr, and locally Cs and Li) (Table 4.5 and Figures 4.14 to 4.16). Compositional variability, in terms of both major

and trace elements is more significant in volcanic units (Wheepool Rhyolite and Waurea Pyroclastics) than in subvolcanic samples. Significant variations were also measured among inclusions in the same grain (Ba, Th, REE, Zr and Ta vary by a factor of >3, Nb, Sr and Rb by a factor of 2-2.5). The largest variations were measured in Cu (<9 to 1800 ppm). Such high values should be considered carefully, because Cu contamination can be introduced during sample preparation. Known sources of Cu contamination include: 1) polishing, since Cu and Zn, other than Sn and Pb, can be present in the brass mounts used to carry quartz grains, and 2) diffusion through the quartz lattice during heating in the laboratory (Kamenetsky and Danyushevsky, 2005). However, only minor initial spikes (indices of surface contamination) were observed during ablation in very few samples, and integration intervals were chosen to avoid them. Further, grains were wrapped in Pt foil to avoid diffusion during heating, and the highest Cu was measured in an unheated inclusion. Thus, very high Cu concentrations might not be due to experimental artefacts. One inclusion (13C-b, unhomogenised, Wheepool Rhyolite) shows particularly high K, Rb and low Nb, Zr, Hf, Ta, Pb, Th (with relatively low Si, Sn, U and high Al, Cs, Ba) in comparison with all other inclusions.

A comparison of average melt inclusions and whole-rock compositions (Fig. 4.14) indicates similar trends in primitive mantle-normalised plots. The ratio between average melt inclusion and whole-rock composition is between 0.5 and 2 for most elements (Fig. 4.14 C), but significant depletion in melt inclusions was measured for Ba, Sr, Mg and locally Eu (melt inclusion/whole-rock <0.5) and enrichment for Cu, Pb, Cs and locally U (melt inclusion/whole-rock >2).

In melt inclusions, silica shows weak or no correlation with most trace elements, in agreement with data from whole-rock analyses for the most silicic samples. A good to strong correlation (r^2 = 0.5 – 0.8) was found between Ta, Th, Nb and Rb, confirming their incompatible behaviour also indicated by whole-rock analysis. Such wide compositional variations would imply high degrees of fractionation (80-85% assuming total incompatibility of Th). Good agreement between melt inclusions and felsic whole-rock samples was found in Sr vs. Ba (both elements are strongly compatible in feldspar; White et al., 2003) and Sr vs. incompatible elements (Nb, Rb) plots. However, unlike whole-rock analyses, melt inclusions show positive correlations of U, Pb and Sn with incompatible elements (e.g. Th and Ta, Fig. 4.15), indicating that these elements were also incompatible in the melt.

Ratios of elements with the same ionic charge and similar ion radius (“geochemical twins”), which are expected to show similar geochemical behaviour during magmatic processes, show some significant variations. The largest variations were found in Zr/Hf, Nb/Ta, and Th/U whereas Y/Ho mostly shows near-chondritic values (Fig. 4.16). The deviation from chondritic values generally increases towards felsic compositions. A plot of Zr/Hf versus Zr indicates how this element ratio remains at hyper-chondritic values (Zr/Hf = 40) for mafic to intermediate compositions, or in zircon-undersaturated samples (increasing Zr). For felsic compositions, and decreasing Zr, Zr/Hf decreases. In felsic rocks and melt inclusions, Nb/Ta is negatively correlated with Ta, but not Nb. Melt inclusions show chondritic Th/U values, whereas whole-rock samples show hyper-chondritic values, mainly due to relatively low U values. Y/Ho shows chondritic values, although with significant deviations in some melt inclusions.

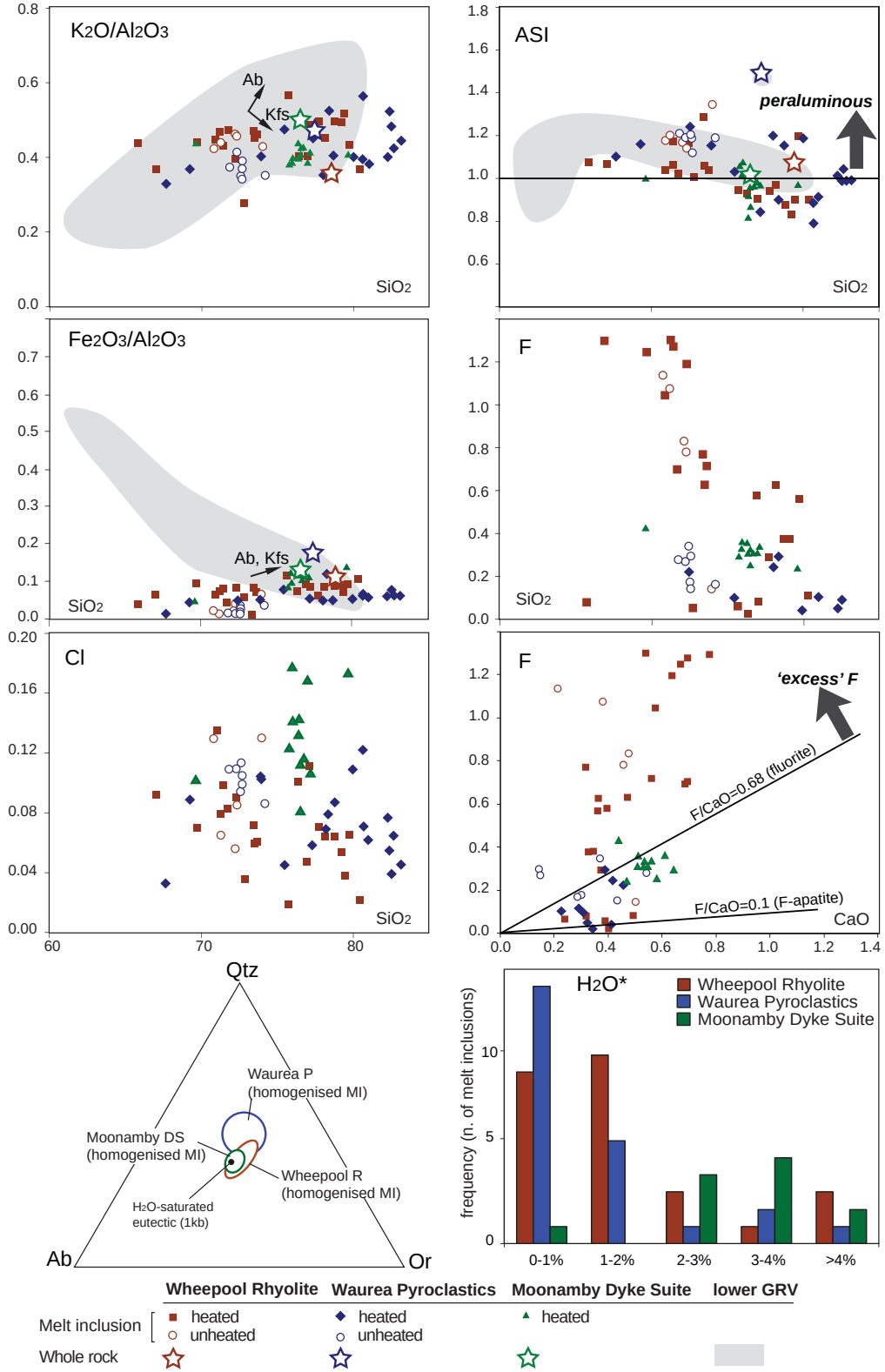

Fig. 4.13. Melt inclusion (EPMA) and whole-rock (XRF) compositions. Data recalculated to anhydrous and plotted as wt.%. Quartz, albite and orthoclase calculated according to the CIPW norm and plotted in the haplogranitic ternary diagram. Arrows indicate melt compositional changes induced by crystallisation of K-feldspar and albite. ASI after Frost et al. (2001). Eutectic composition at P(H_2O) = 1kb after Tuttle and Bowen (1958). H_2O*: water as summation deficit.

Table 4.2: EPMA melt inclusion analyses, Wheepool Rhyolite

Oxide (wt%), recalculated to 100														
MI	comment	sample	Na2O	SiO2	Al2O3	MgO	K2O	CaO	Fe2O3	TiO2	Cl	F	H2O*	ASI
2c (36-50)b (T)	homogenised glass	GH23	4.48	76.96	11.41	0.09	4.58	0.40	1.04	0.21	0.05	0.58	3.62	0.90
21c (14c-34) b	homogenised glass	GH06	4.65	76.40	12.30	0.09	4.94	0.41	0.90	0.19	0.10	<dl	0.81	0.92
7c (35-42)	homogenised glass	GH59	3.32	79.42	10.31	0.06	5.34	0.28	0.76	0.34	0.04	<dl	2.14	0.90
6c (35-24)c (T)	homogenised glass	GH59	3.92	79.20	10.04	0.09	4.93	0.33	0.91	0.15	0.05	0.38	1.15	0.83
6c (35-24)a (T)	homogenised glass	GH59	3.66	78.79	10.39	0.09	5.16	0.34	0.87	0.15	0.06	0.38	1.42	0.87
3c (36-33)	homogenised glass	GH23	4.35	80.41	10.01	0.12	3.69	<dl	1.05	0.16	<dl	0.11	-	0.90
4 (30-27)	homogenised glass	GH59	2.28	79.76	10.92	0.09	4.69	0.36	0.99	0.18	0.06	0.56	1.22	1.19
11c (35-50)	homogenised glass	GH59	3.40	78.17	10.89	0.11	4.95	0.37	0.93	0.15	0.06	0.62	1.91	0.96
9c (35-51)	homogenised glass	GH59	3.40	77.78	11.30	0.11	5.60	0.38	0.68	0.20	0.07	0.29	1.42	0.94
19 (17-20) (T)	(gl+V) heated	GH23	2.89	71.25	15.31	0.12	7.14	0.54	1.13	<dl	0.08	1.30	0.66	1.18
10c (35-48)c (T)	(gl+V) heated	GH59	3.79	71.76	14.85	0.13	7.00	0.69	0.64	0.08	0.08	0.70	1.69	1.03
10c (35-48)d	(gl+V) heated	GH59	3.15	75.71	12.19	0.14	6.94	0.24	1.42	0.15	0.00	<dl	1.47	0.94
10c (35-48)b (T)	(gl+V) heated	GH59	3.52	73.70	13.69	0.09	6.33	0.56	0.98	0.20	0.06	0.71	0.35	1.04
10c (35-48)a (T)	(gl+V) heated	GH59	3.44	73.50	13.97	0.08	6.60	0.47	1.12	0.10	0.06	0.63	1.74	1.06
7 (30-41)	(gl+V) heated	GH59	4.10	70.92	15.13	0.14	6.75	0.58	1.00	0.09	0.13	1.04	2.07	1.04
13c (35-66)b	(gl+V) heated	GH59	5.11	65.81	19.25	0.08	8.47	0.32	0.71	<dl	<dl	<dl	1.31	1.08
13c (35-66)	(gl+V) heated	GH59	3.88	71.39	14.69	0.15	6.32	0.70	1.17	0.16	0.10	1.27	0.32	1.06
17c (17-29)	(gl+V) heated	GH23	5.30	66.98	17.46	0.18	6.42	0.78	1.11	0.28	0.09	1.30	-	1.07
2c (36-50)a (T)	(gl+V) heated	GH23	3.50	72.29	14.69	0.15	5.86	0.64	1.20	0.20	0.09	1.19	1.31	1.16
21c (14c-34)a (T)	(gl+V) heated	GH06	6.21	72.81	15.13	0.10	4.18	0.39	0.84	0.26	0.04	<dl	-	1.00
25 (28-45)	(gl+V) heated	GH59	2.54	73.41	15.48	<dl	6.98	0.32	0.12	<dl	0.07	0.77	-	1.29
average**			3.85	74.59	13.30	0.11	5.85	0.45	0.93	0.18	0.07	0.74	1.45	1.02
std dev			0.93	4.16	2.60	0.03	1.19	0.16	0.27	0.06	0.03	0.38	0.77	0.12
3 (21-60) (T)	(gl+V) unheated	GH06	2.27	73.97	15.05	0.11	6.46	0.51	0.95	0.27	0.13	0.14	4.58	1.35
26d (28-33)	(gl+V) unheated	GH59	3.82	72.30	15.48	<dl	6.33	0.46	0.58	0.12	0.08	0.78	0.03	1.14
27d (28-38) (T)	(gl+V) unheated	GH59	3.78	70.85	16.39	<dl	6.97	0.22	0.39	0.07	0.13	1.13	0.83	1.17
11d (28-37)	(gl+V) unheated	GH59	3.19	72.18	15.61	<dl	7.15	0.48	0.23	0.09	0.06	0.83	2.85	1.16
14d (28-2)	(gl+V) unheated	GH59	3.45	71.23	16.35	<dl	7.14	0.38	0.22	<dl	0.06	1.07	1.68	1.19
average**			3.30	72.11	15.78	0.02	6.81	0.41	0.47	0.14	0.09	0.79	2.00	1.20
std dev			0.63	1.21	0.58		0.39	0.12	0.30	0.09	0.04	0.39	1.78	0.08

*H2O calculated as summation deficit

**average calculated setting to 0 values <dl

(T) also analysed for trace elements

Volatile components

The highest F values (F ≤1.3 wt.%) were measured in the Wheepool Rhyolite (samples GH23 and GH59). Two-phase (both heated and unheated) inclusions have higher F in comparison to homogenised inclusions. Other melt inclusions, however, have lower F concentrations for similar SiO_2 (Fig. 4.13). The other units show F ≤0.4 wt.%. Chlorine is present in concentrations up to ~0.2 wt.%; the highest values were measured in the Moonamby Dyke Suite. Fluorine versus chlorine plots of the Wheepool Rhyolite samples indicate broad positive correlation. Phosphorus and sulfur are consistently below detection limit (275 and 212 ppm, respectively for EPMA), thus these values can be assumed as maxima. These results are in general agreement with whole-rock data showing both P_2O_5 and S values below 0.1 wt.% for the most felsic compositions (≥70 wt.% silica, Table 4.1, Fig. 4.1).

Calculated water (H_2O*) values are widely scattered (Tables 4.2, 4.3, 4.4), but the majority of values fall in the interval 0-2 wt.% for volcanic units and 3-4 wt.% for dykes (Fig. 4.13). Samples from the Wheepool Rhyolite and the Waurea Pyroclastics overlap almost completely.

Unheated inclusions have higher average H2O* contents compared with heated

Table 4.3: EPMA melt inclusion analyses, Waurea Pyroclastics

Oxide (wt%), recalculated to 100														
MI	comment	sample	Na2O	SiO2	Al2O3	MgO	K2O	CaO	Fe2O3	TiO2	Cl	F	H2O*	ASI
12u (10-77)	homogenised glass	GH13	2.92	82.64	9.26	<dl	3.93	0.31	0.61	<dl	0.06	<dl	0.34	0.99
4u 2 (10-16)	homogenised glass	GH13	2.99	78.73	12.10	<dl	4.86	0.38	0.61	<dl	0.09	<dl	0.19	1.15
11 (31-42)	homogenised glass	GH95	4.03	80.65	9.91	0.04	3.90	0.34	0.61	0.08	0.12	<dl	3.21	0.89
5u (10-19) (T)	homogenised glass	GH13	2.34	82.37	9.20	<dl	4.80	0.29	0.58	<dl	0.05	<dl	1.46	0.99
8u (10-52)	homogenised glass	GH13	2.78	83.10	9.04	<dl	4.01	0.25	0.56	<dl	<dl	<dl	1.10	0.99
9 (31-14)	homogenised glass	GH95	4.01	80.95	10.00	<dl	3.81	0.30	0.58	0.09	0.06	<dl	0.61	0.91
10u (10-61)	homogenised glass	GH13	3.58	80.66	9.33	<dl	5.26	0.28	0.57	<dl	0.07	<dl	0.99	0.79
14 (31-3)	homogenised glass	GH95	3.02	82.26	9.47	0.04	3.79	0.32	0.80	<dl	0.08	<dl	0.75	1.01
16u (19-40)	homogenised glass	GH13	3.35	78.39	10.64	0.04	5.55	0.38	1.28	<dl	0.08	0.29	1.52	0.90
15 (31-39)	(gl+V) heated	GH95	3.28	78.05	12.61	0.05	4.46	0.42	0.62	<dl	0.07	0.25	0.16	1.19
15 (31-39) 3	(gl+V) heated	GH95	5.80	67.67	19.40	<dl	6.35	0.41	0.19	<dl	<dl	<dl	0.61	1.10
15 (31-39) 2	(gl+V) heated	GH95	4.00	73.93	14.57	0.06	5.84	0.36	0.81	<dl	0.10	<dl	-	1.16
19u (19-46)b	(gl+V) heated	GH13	4.42	79.97	10.11	0.05	4.02	0.41	0.52	0.13	0.11	<dl	0.64	1.18
19u (19-46)	(gl+V) heated	GH13	2.57	77.19	12.90	0.07	5.80	0.43	0.68	0.15	0.06	<dl	0.77	0.84
14u 2 (10-59)	(gl+V) heated	GH13	4.70	69.23	17.81	0.07	6.58	0.52	0.78	<dl	0.09	<dl	-	1.16
28 (2-86)	(gl+V) heated	GH13	3.83	72.53	16.05	<dl	5.77	0.46	0.77	<dl	0.11	0.22	-	1.24
3u (10-14)	(gl+V) heated	GH13	2.30	82.50	9.21	<dl	4.47	0.30	0.65	0.16	<dl	0.09	2.81	1.04
4u (10-16)	(gl+V) heated	GH13	3.51	75.48	13.11	0.05	6.21	0.22	1.04	<dl	<dl	0.10	-	1.03
average**			3.52	78.13	11.93	0.05	4.97	0.35	0.68	0.12	0.08	0.19	1.08	1.03
std dev			1.08	4.87	3.36	0.01	0.94	0.09	0.23	0.01	0.02	0.08	1.04	0.12
9d (42-25)a	(gl+V) unheated	GH95	3.95	71.81	16.41	<dl	6.11	0.54	0.26	0.10	0.11	0.27	1.51	1.21
9d (42-25) b	(gl+V) unheated	GH95	4.10	74.20	15.16	<dl	5.32	0.29	0.52	0.11	0.09	0.16	-	1.19
18d (42-47) (T)	(gl+V) unheated	GH95	4.31	72.56	16.12	<dl	5.69	0.30	0.52	0.16	0.09	0.17	1.05	1.19
20d (42-50)	(gl+V) unheated	GH95	4.36	72.64	16.10	<dl	5.51	0.44	0.31	0.14	0.10	0.15	0.22	1.19
21d (29-9)	(gl+V) unheated	GH95	4.45	72.64	15.85	<dl	6.19	0.15	0.25	0.00	0.11	0.29	1.26	1.12
22d	(gl+V) unheated	GH95	3.84	72.29	16.13	<dl	6.67	0.15	0.24	<dl	0.11	0.26	8.87	1.18
23d (19-12)	(gl+V) unheated	GH95	4.02	72.59	16.01	<dl	5.88	0.37	0.41	0.16	0.11	0.34	3.55	1.20
average**			4.15	72.67	15.97		5.91	0.32	0.36	0.10	0.10	0.24	2.35	1.18
std dev			0.24	0.80	0.43		0.50	0.16	0.13	0.07	0.01	0.06	3.34	0.03

*H_2O calculated as summation deficit
**average calculated setting to 0 values <dl
(T) also analysed for trace elements

inclusions (Tables 4.2, 4.3). The Wheepool Rhyolite and Waurea Pyroclastics have average H_2O^* = 1.7 ±0.9 wt.% and H2O* = 1.1 ±0.9 wt.%, respectively. The Moonamby Dyke Suite samples have higher average values (H_2O^* = 3.1 ±1.1 wt.%). There is no clear correlation between H_2O and the concentration of major elements.

A plot of F versus CaO reveals a high F/CaO ratio. Melt inclusions from the Wheepool Rhyolite have F/CaO higher than fluorite in most analyses (F_2Ca: F/Ca wt.% = 0.95; F/CaO wt.% = 0.68, Fig. 4.13). In melt inclusions from the other units, F/CaO mostly falls between fluorite and F-apatite (F/CaO wt.% = 0.1 considering an apatite with F = 5 wt.%) and locally higher than fluorite.

Chlorine (EPMA) shows a strong positive correlation with incompatible elements, Pb in particular, with the exception of one spot (Fig. 4.15). A broad positive correlation was also found between F (EPMA) and REE, Y, Zr and Hf in volcanic samples; subvolcanic samples plot on a separate trend.

4.4 Discussion

4.4.1 Melt inclusion textures and heating experiments

Crystalline and glass-bearing inclusions

The crystallisation degree of melt inclusions has been related to several parameters,

Table 4.4: EPMA melt inclusion analyses, Moonamby Dyke Suite

Oxide (wt%), recalculated to 100														
MI	comment	sample	Na2O	SiO2	Al2O3	MgO	K2O	CaO	Fe2O3	TiO2	Cl	F	H2O*	ASI
19c (33-12) (T)	homogenised glass	GH15	4.70	76.52	11.56	<dl	4.69	0.58	1.34	0.22	0.08	0.25	2.48	0.87
18c (33-13)	homogenised glass	GH15	3.82	77.15	11.62	0.02	4.84	0.53	1.31	0.18	0.11	0.33	2.81	0.97
17d (T)	homogenised glass	GH15	3.58	75.99	12.77	0.02	5.07	0.61	1.26	0.17	0.14	0.36	3.98	1.07
01d (33-21)	homogenised glass	GH15	4.93	69.63	16.35	<dl	7.20	0.44	0.82	<dl	0.10	0.43	0.80	1.00
02d (33-23)	homogenised glass	GH15	4.05	76.98	11.86	0.02	4.58	0.51	1.31	0.12	0.17	0.31	2.27	0.98
03d (33-75) (T)	homogenised glass	GH15	4.04	76.71	11.89	<dl	4.83	0.54	1.25	0.17	0.12	0.31	3.08	0.96
05d (33-39)	homogenised glass	GH15	5.23	76.37	11.42	0.03	4.53	0.51	1.35	0.11	0.14	0.36	2.53	0.82
06d (33-72)	homogenised glass	GH15	4.10	76.37	11.80	0.03	5.15	0.53	1.38	0.10	0.13	0.31	3.50	0.92
07d (33-47)	homogenised glass	GH15	3.91	76.53	11.89	0.02	5.07	0.54	1.34	0.18	0.11	0.32	3.27	0.96
12d (32-41)	homogenised glass	GH15	3.82	75.78	12.98	0.04	4.98	0.64	1.13	0.12	0.12	0.29	4.96	1.06
15d (32-51) a	homogenised glass	GH15	3.96	75.96	12.51	<dl	4.86	0.56	1.55	0.12	0.18	0.33	4.14	1.02
15d (32-51) b	homogenised glass	GH15	3.42	79.66	10.29	<dl	4.21	0.47	1.43	0.10	0.17	0.24	3.26	0.97
*average***			*4.13*	*76.14*	*12.24*	*0.02*	*5.00*	*0.54*	*1.29*	*0.13*	*0.13*	*0.32*	*3.09*	*0.97*
std dev			*0.55*	*2.28*	*1.47*	*0.01*	*0.74*	*0.06*	*0.18*	*0.06*	*0.03*	*0.05*	*1.06*	*0.07*

*H_2O calculated as summation deficit

**average calculated setting to 0 values <dl

(T) also analysed for trace elements

including magma cooling rate and the amount of dissolved water. Lowenstern (1994) suggested that slow cooling allows melt inclusions to crystallise, whereas rapid cooling would favour the formation of glass. The lower GRV units confirm this pattern, because melt inclusions from shallow intrusions are entirely crystalline (Fig. 4.10) and those in volcanic rocks are only partly crystalline (Figures 4.8, 4.9). The presence of fluid inclusion coronas around some crystalline melt inclusions (Fig. 4.9 C) suggests that fluid accumulated during post-entrapment crystallisation of volatile-free phases (Fe oxide, feldspar, quartz) was expelled from the melt inclusion and trapped in the host quartz. Water content can also influence crystallisation of melt inclusions. A water-rich melt will be more likely to crystallise than a water-poor one, as a consequence of increased ion diffusivity (Dingwell, 1990). Higher calculated water content in the Moonamby Dyke Suite in comparison with volcanic samples (Tables 4.2, 4.3, 4.4) is consistent with the higher degree of crystallisation.

The processes described above are related to the chemical characteristics and emplacement mechanism of a volume of magma and involve all the inclusions sharing the same emplacement and cooling history. However, glassy and crystalline inclusions can occur in the same grain (Fig. 4.9 C) and along the same trapping plane. Such contrasting behaviour can be explained by selective loss of fluids through leakage or during heating experiments (e.g. Lowenstern and Mahood, 1991; Tait, 1992; Danyushevsky et al., 2002). Some inclusions may have decrepitated at high temperature, when still melted, and lost volatile components (H_2O in particular). Leakage favours quenching to glass, either by increasing the glass transition temperature above the temperature of the system or simply increasing viscosity and reducing ion diffusivity (Dingwell, 1997). Also noteworthy is that loss of volatile components through leakage can have different outcomes, depending on the temperature of the melt inclusion with respect to the glass transition temperature. Cracking and leaking occurring slightly above the glass transition temperature can result in immediate quenching, whereas leakage well above that temperature, will not necessarily result in quenching.

Table 4.5. Melt inclusion analyses (LA-ICP-MS). Major elements as in Tables 4.2-4.4

Melt inclusion	19C 33-12	3D 33-75	17D 32-59	18D 42-47	5u 10-19	2C b 36-50	2C a 36-50	6C c 35-24	6C a 35-24	3 21-60
sample	GH15	GH15	GH15	GH95	GH13	GH23	GH23	GH59	GH59	GH06
unit	MDS	MDS	MDS	WP	WP	WR	WR	WR	WR	WR
Na2O (wt.%)	4.70	4.04	3.58	4.31	2.34	4.48	3.50	3.92	3.66	2.27
SiO2	76.52	76.71	75.99	72.56	82.37	76.96	72.29	79.20	78.79	73.97
Al2O3	11.56	11.89	12.77	16.12	9.20	11.41	14.69	10.04	10.39	15.05
MgO	<dl	<dl	0.02	<dl	<dl	0.09	0.15	0.09	0.09	0.11
K2O	4.69	4.83	5.07	5.69	4.80	4.58	5.86	4.93	5.16	6.46
CaO	0.58	0.54	0.61	0.30	0.29	0.40	0.64	0.33	0.34	0.51
Fe2O3	1.34	1.25	1.26	0.52	0.58	1.04	1.20	0.91	0.87	0.95
TiO2	0.22	0.17	0.17	0.16	<dl	0.21	0.20	0.15	0.15	0.27
Cl	0.08	0.12	0.14	0.09	0.05	0.05	0.09	0.05	0.06	0.13
F	0.25	0.31	0.36	0.17	0.00	0.58	1.19	0.38	0.38	0.14
Be (ppm)	<10.1	4.9	7.2	<6.5	<4.7	4.9	<5.0	<4.4	<10.8	<16.0
B	<108.8	<43.8	26.6	<98.2	<46.7	<54.2	<66.2	<49.4	<90.5	<249.6
Al*	63507.3	63507.3	68799.5	84676.3	47630.4	58215.0	79384.1	52922.7	52922.7	79384.1
P	<218.8	<66.1	56.6	<177.6	<66.6	<67.7	<119.5	<81.8	<207.1	<357.1
Ga	15.4	15.3	19.4	17.2	12.7	13.9	15.8	13.3	13.1	17.0
Cs	8.4	9.7	10.8	10.2	5.8	6.1	6.6	7.5	7.6	8.4
Rb	336.7	370.5	394.2	354.3	253.5	237.2	293.8	233.3	231.2	338.1
Ba	142.1	28.7	14.1	1.9	<1.3	114.1	183.5	48.1	14.4	<10.6
Th	36.6	46.5	46.1	19.7	18.5	17.9	29.0	20.3	20.3	27.3
U	8.8	11.1	11.1	6.0	4.6	4.5	6.3	5.6	6.7	6.4
Nb	21.8	26.2	24.9	31.0	22.0	20.6	30.5	21.7	22.8	33.9
La	79.5	89.9	91.2	12.4	22.7	47.2	76.6	28.6	28.0	41.7
Ce	169.0	205.2	199.0	19.9	52.2	113.5	175.7	74.8	73.4	89.0
Pr	15.7	18.1	19.8	1.7	4.3	11.7	17.1	7.0	7.1	8.8
Pb	41.6	48.6	48.1	43.7	37.6	33.7	43.3	30.8	31.1	50.8
Sr	19.4	8.5	7.1	<0.3	0.4	15.0	21.6	9.2	5.4	0.8
Nd	67.3	64.6	65.8	4.6	13.9	46.0	65.5	27.2	28.9	29.9
Sm	7.9	10.4	12.5	1.3	2.4	8.6	12.5	4.8	7.4	4.2
Zr	200.0	191.8	235.3	145.8	93.8	136.1	234.7	102.9	111.7	162.1
Hf	6.1	6.8	8.7	6.0	4.3	5.4	8.6	4.0	4.4	6.1
Ta	1.4	1.8	2.1	1.9	1.3	1.3	2.1	1.4	1.2	1.7
Eu	0.6	0.3	0.3	<0.2	<0.1	0.4	1.0	0.4	0.5	0.6
Sn	<10.8	9.0	10.1	<9.6	4.3	5.8	7.6	<3.5	<9.9	<21.7
Ti	1333.0	1100.5	1056.5	843.1	638.0	1548.1	2119.0	1079.0	1179.8	1137.2
Gd	10.2	9.7	10.6	0.9	1.7	5.9	10.9	4.7	5.6	7.4
Tb	1.2	1.4	1.7	0.3	0.5	1.0	1.6	0.8	1.0	0.7
Dy	6.9	9.7	10.7	2.2	2.2	7.2	8.7	4.8	5.9	4.5
Li	17.9	11.0	12.1	<5.2	28.1	13.6	6.6	11.9	13.9	53.6
Ho	1.8	1.8	2.0	0.4	0.5	1.3	1.8	1.0	1.0	1.0
Y	43.9	51.9	61.2	18.2	18.0	36.0	54.1	30.2	32.8	33.6
Er	4.4	5.9	6.7	2.6	1.7	3.6	6.0	3.4	3.0	3.1
Tm	0.8	0.9	1.0	0.3	0.4	0.6	1.1	0.5	0.5	0.6
Yb	3.6	6.5	6.4	3.0	2.5	3.9	5.2	2.9	3.4	3.6
Lu	0.7	0.7	1.1	0.3	0.2	0.6	1.0	0.5	0.6	0.7
Cu	121.4	32.4	10.2	<8.7	1154.1	53.5	11.1	167.1	217.8	1818.1
Zn	45.4	44.2	40.6	42.6	64.3	46.4	60.3	42.9	51.7	100.5

MDS: Moonamby Dyke Suite, WR: Wheepool Rhyolite, WA: Waurea Pyroclastics.

Al* internal standard

Table 4.5. (Cont.) Melt inclusion analysis (LA-ICP-MS).

Melt inclusion	13C a 35-66	13C b 35-66	27D 28-38	21C a 14c-34	10C b 35-48	10C a 35-48	10C c 35-48	19 17-20
sample	GH59	GH59	GH59	GH06	GH59	GH59	GH59	GH23
unit	WR	WR	WR	WR	WR	WR	WR	WR
Na2O (wt.%)	3.88	5.11	3.78	6.21	3.52	3.44	3.79	2.89
SiO2	71.39	65.81	70.85	72.81	73.70	73.50	71.76	71.25
Al2O3	14.69	19.25	16.39	15.13	13.69	13.97	14.85	15.31
MgO	0.15	0.08	<dl	0.10	0.09	0.08	0.13	0.12
K2O	6.32	8.47	6.97	4.18	6.33	6.60	7.00	7.14
CaO	0.70	0.32	0.22	0.39	0.56	0.47	0.69	0.54
Fe2O3	1.17	0.71	0.39	0.84	0.98	1.12	0.64	1.13
TiO2	0.16	<dl	0.07	0.26	0.20	0.10	0.08	<dl
Cl	0.10	0.00	0.13	0.04	0.06	0.06	0.08	0.08
F	1.27	0.00	1.13	0.00	0.71	0.63	0.70	1.30
Be (ppm)	5.4	2.8	<15.7	<4.5	3.2	4.5	5.6	<2.5
B	<52.8	<31.3	<214.1	<38.65	<25.09	<9.73	21.2	<13.92
Al*	79384.1	100553.2	84676.3	79384.1	74091.8	74091.8	79384.1	79384.1
P	<106.7	138.2	<303.1	77.3	<33.8	40.9	48.1	<25.7
Ga	17.0	21.9	22.0	17.1	13.0	14.5	15.0	16.1
Cs	6.3	21.7	28.0	3.7	9.0	9.3	9.6	7.7
Rb	294.6	632.0	377.3	203.5	288.0	290.9	311.5	313.0
Ba	252.3	284.8	2.9	90.6	87.4	66.4	111.4	128.0
Th	27.3	8.1	50.2	38.4	28.4	27.5	26.8	25.2
U	6.1	2.9	14.3	7.1	7.0	6.7	7.5	6.9
Nb	25.8	10.5	35.6	31.2	25.0	25.2	21.0	27.1
La	72.1	27.7	41.8	69.5	39.1	37.1	38.3	59.9
Ce	160.1	49.2	72.0	155.0	86.0	81.4	80.2	142.8
Pr	17.5	6.3	5.7	15.8	8.5	8.1	7.8	13.6
Pb	39.6	18.9	54.5	68.1	37.3	39.7	44.0	45.5
Sr	34.0	21.7	8.4	18.7	12.3	10.8	14.2	16.8
Nd	61.2	20.2	11.2	53.7	27.8	26.1	24.9	46.6
Sm	9.5	4.4	2.2	10.2	5.5	5.4	5.1	8.1
Zr	170.7	45.7	128.2	225.0	105.0	109.2	109.7	218.5
Hf	6.1	1.8	5.3	8.2	4.3	4.4	4.5	7.0
Ta	1.8	0.5	2.5	2.3	1.7	1.6	1.6	1.6
Eu	0.7	0.7	<0.3	0.8	0.4	0.4	0.5	0.8
Sn	7.3	2.9	<14.6	5.8	4.2	4.2	4.0	5.1
Ti	1426.3	830.2	564.3	2133.2	1060.9	1169.9	595.9	1294.9
Gd	8.6	3.7	1.6	9.0	4.7	3.8	3.7	6.1
Tb	1.7	0.7	<0.3	1.4	0.6	0.7	0.5	1.0
Dy	8.7	4.0	1.0	9.4	5.2	4.6	3.6	6.8
Li	8.3	12.9	9.3	32.9	9.7	12.7	13.3	2.6
Ho	1.7	0.8	0.2	1.8	1.0	1.0	0.7	1.3
Y	50.1	25.5	13.2	51.1	28.7	28.0	23.2	38.7
Er	5.8	1.8	1.3	5.7	3.3	3.0	2.2	4.1
Tm	0.9	0.3	<0.3	0.8	0.4	0.5	0.4	0.6
Yb	5.8	2.0	2.3	6.5	3.6	3.8	2.5	4.3
Lu	0.8	0.3	0.3	0.7	0.6	0.6	0.4	0.6
Cu	32.9	71.1	<22.2	128.3	75.2	82.6	89.9	55.3
Zn	64.7	60.5	25.4	52.7	45.7	46.1	52.8	67.4

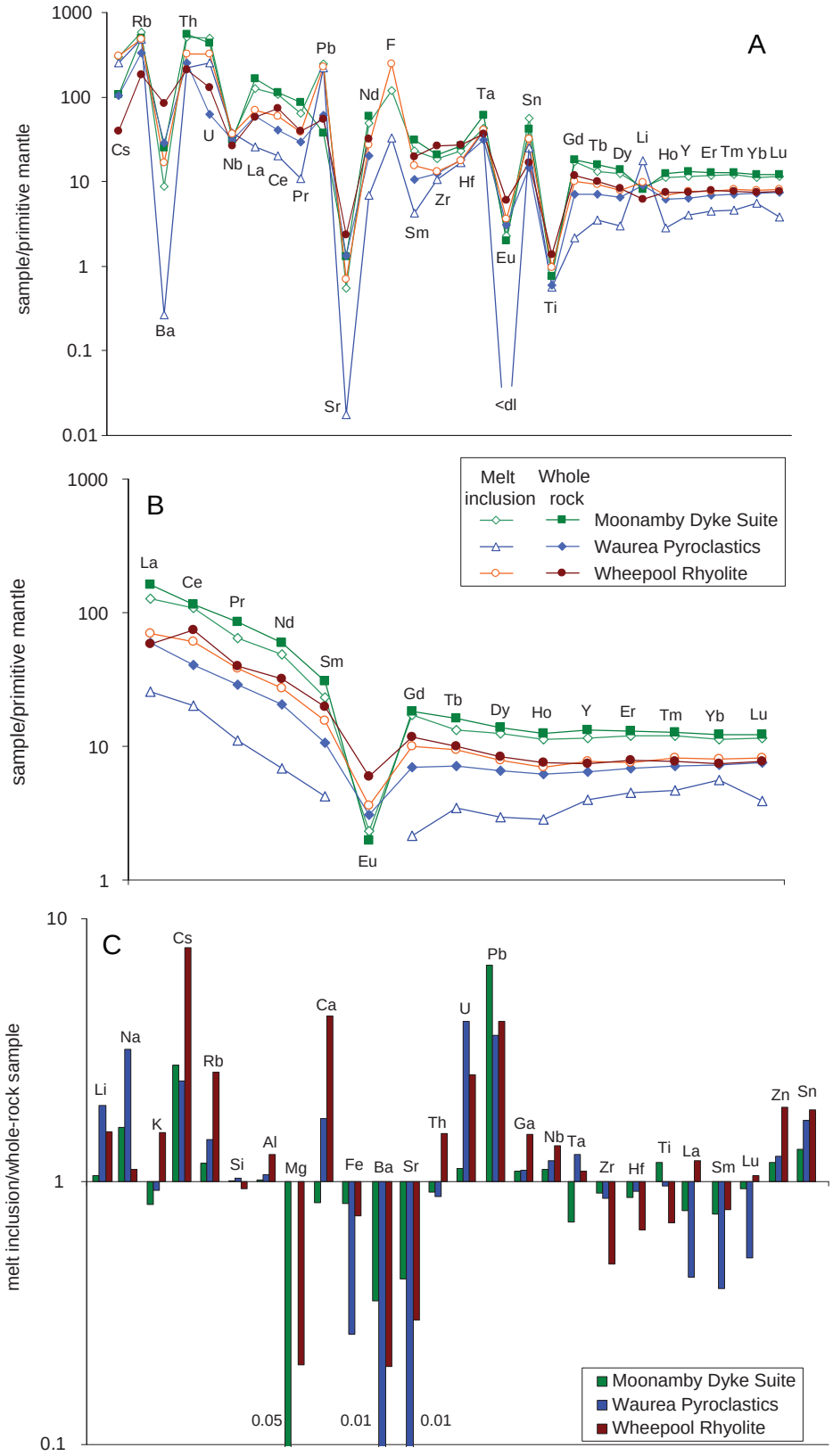

Fig. 4.14. Melt inclusion compositions compared with whole-rock compositions. Primitive mantle-normalised (A- multi-element, B- REE) and relative enrichment (C). Whole rock samples: GH15 (Moonamby Dyke Suite), GH13 (Waurea Pyroclastics) and GH06 (Wheepool Rhyolite).

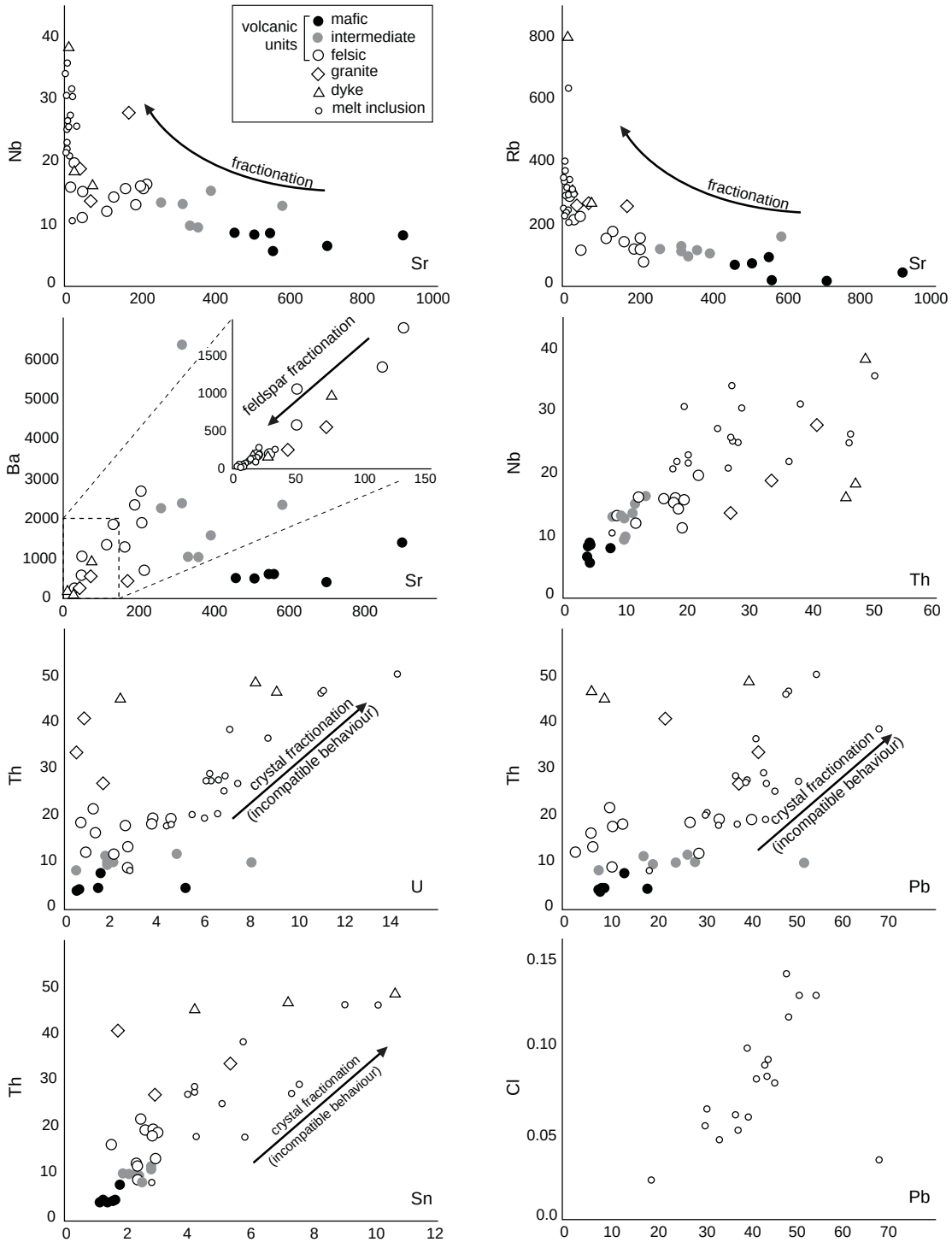

Fig. 4.15. Melt inclusion and whole-rock trace element contents (ppm). Some elements (U, Pb, Sn) show variably depleted whole-rock values compared to melt inclusions.

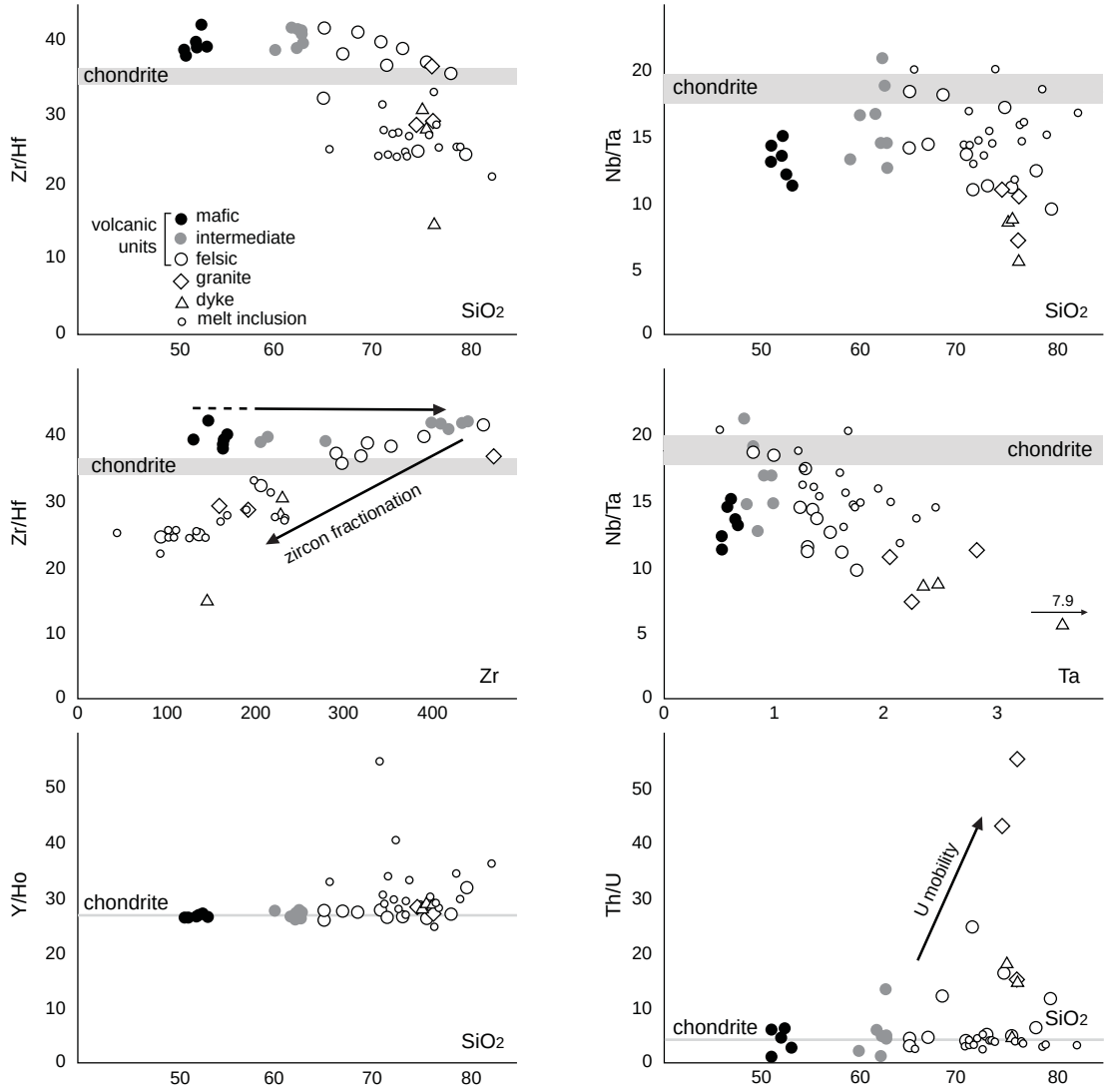

Fig. 4.16. Comparison of trace element ratios in whole-rock and melt inclusion analyses. Chondrite values are added for comparison (Sun and McDonough, 1989; Münker et al., 2003).

Homogenisation temperature

The homogenisation temperature (Th) of a melt inclusion corresponds to the temperature at which glass, vapour bubble and daughter mineral phases homogenise to a single phase (Roedder, 1979). As a consequence of the low compressibility of silicate melts, homogenisation and trapping temperature should be close (Roedder, 1979; Lowenstern, 1994; 1995). Thus, homogenisation temperature can be used to estimate the trapping temperature.

High homogenisation temperatures (1000°C) were measured in the Wheepool Rhyolite and the Waurea Pyroclastics. High Th for rhyolitic melt inclusions are uncommon in the literature, but not unreported. Chabiron et al. (2001) obtained temperatures between 980° and 1045°C in heating stage experiments on F-rich melt inclusions in rhyolites. Thomas (2002) also found a high final homogenisation temperature (950°C)

for quartz-hosted melt inclusions heated in a one-atmosphere furnace. Saito et al. (2001) conducted heating stage experiments on rhyolitic melt inclusions which homogenised between 1100 and 1210°C. Chaigneau et al. (1980) obtained a Th = 1050 ±20°C in quartz-hosted melt inclusions in dacite from the Nijar region, Spain.

In the case of heating stage experiments, rapid heating rate (≤3-4°C/min) may result in overestimation of Th (Lowenstern, 1994; Student, 2002). Student (2002) tested different heating methods on synthetic inclusions and reported that homogenisation temperatures measured on heating stage were systematically higher than those obtained from heating in a furnace. Lowenstern (1994) also found a systematic difference (~75°C) between the two techniques. High homogenisation temperatures obtained through heating stage experiments are in some cases explained by slow kinetics in rhyolitic liquids.

High homogenisation temperatures obtained in long heating runs (several hours) in a furnace cannot be attributed to reaction inertia. They have been explained by loss of volatile components through leakage (Skirius, 1990) or diffusion of H_2 through the host mineral lattice driven by a water pressure difference between the melt inclusion and the external environment during heating experiments (Qin et al., 1992; Danyushevsky et al., 2002; Sobolev and Danyushevsky, 1994). Loss of H_2 leads to a decrease in water pressure within the inclusion and to an increase of melting temperature. Zircon saturation temperatures obtained on melt inclusions (cf. section 4.4.2) indicate lower temperatures (~850-950°C), confirming that homogenisation temperatures are overestimates.

Lowenstern (1994) suggested that in shrinkage bubbles the melt inclusion to bubble ratio should be between 0.2 and 5 vol.% and that higher values are related to leakage. Large bubble-to-melt inclusion ratios were locally measured in inclusions from the Wheepool Rhyolite and the Waurea Pyroclastics (bubble/inclusion ≤5-7 vol.% and ≤10 vol.%, respectively). These values might suggest the local occurrence of leakage, even in inclusions which do not show any evidence of cracks. The observation that the largest inclusions show radial cracks and “sweat” halos (Fig. 4.9 C) indicates that larger inclusions are more susceptible to cracking and leaking, and could explain preferential homogenisation of small inclusions (typically ≤20 µm).

4.4.2 The effect of fractionation and alteration on chemical composition: comparison of whole-rock and melt inclusion data

A comparison between whole-rock composition and unaltered, glassy inclusions allows assessment of the degree of host rock alteration. Harker diagrams show good agreement between melt inclusion and whole-rock analysis for most “mobile”, water-soluble elements (Na_2O, K_2O, CaO) and their ratios with Al_2O_3 (Fig. 4.13, Tables 4.2, 4.3). The ASI can be affected by preferential mobilisation of alkalis compared with the relatively immobile Al. With the exception of a few melt inclusion analyses showing high alkalis, both Na and K widely overlap with whole-rock data. The close similarity in ASI values between whole-rock and melt inclusion analyses (Fig. 4.13) suggests that alteration has not significantly affected the content of alkalis in the rocks, with the notable exception of the Waurea Pyroclastics, which have significantly higher whole-rock ASI values, mainly due to the low Na content of the rock. Locally high ASI values (ASI >1.4) have also been measured by other authors (Giles, 1988; Stewart, 1994; PIRSA, 2006; Fig. 2.3); these values can be explained by alteration of feldspar and mobilisation of alkalis.

The accessory minerals in the lower GRV (apatite, zircon, REE-F-carbonate, Ti-Fe oxide ±monazite ±allanite) are the main carriers of HFSE (Zr, Hf, Nb, Ta, Ti), REE, Y, Th, and U. Textural relationships indicate late crystallisation for most of these phases, in agreement with generally increasing element concentration patterns with increasing fractionation. The presence of accessory phases has a profound influence on the trace element concentration and fractionation of key trace element ratios in the melt (e.g. Bea, 1996). Thus, crystallisation of these minerals can leave a distinctive signature on patterns of element concentration and ratios of elements with similar geochemical behaviour. Concurrent decrease of Zr and Zr/Hf (Fig. 4.16) is the geochemical marker of zircon crystallisation (Linnen and Keppler, 2002; Thomas et al., 2002). Apart from Hf, the most common substitutions in zircon are HREE, Y, Th, and U (Hinton and Upton, 1991; Thomas et al., 2002). Thus, an increase of La/Yb could be expected. The lack of such a geochemical signature can be explained by a low abundance of zircon crystallising (Hinton and Upton, 1991) or concomitant crystallisation of apatite and monazite. Similarly, the effects of zircon fractionation on Th and U seem to be relatively small. Titanium phases (titanite and rutile) are known to be able to partition Nb and Ta (e.g. Schmidt et al., 2004a; Marks et al., 2008). The observed decrease of Nb/Ta with progressing fractionation (increasing silica and increasing Ta) reflects a lower melt activity coefficient for Ta relative to Nb. This feature is the consequence of the fact that, in subaluminous to peraluminous granitic melts, manganotantalite (MnTa2O6) is more soluble than manganocolumbite ($MnNb_2O_6$) (Linnen and Keppler, 1997).

The increasing trend of Zr with increasing silica in whole-rock analyses is consistent with Zr-undersaturation of samples with SiO_2 ≤70 wt.%. This trend is similar to those shown by the so called “high temperature granites” of Chappell et al. (2004). Solubility of Zr in silicate melts is strongly dependent on temperature, and high Zr concentrations suggest high magmatic temperatures (Watson and Harrison, 1983; Rubatto and Hermann, 2007). For SiO_2 >70 wt.%, Zr and the Zr/Hf ratio decrease in both whole-rock and melt inclusion samples. This suggests that the melt reached zircon-saturation in its late stages of crystallisation. Late crystallisation of zircon is in agreement with textural evidence, which indicates that zircon is included in late-crystallised “pockets” of minerals, and includes other minerals such as apatite (e.g. Figures 3.6 E and 3.14 D). The zircon saturation model of Watson and Harrison (1983) can be used as a geothermometer in metaluminous and peraluminous melts. If melt is zircon-undersaturated, the method will yield only minimum estimates of temperature. Application of the zircon saturation model (Watson and Harrison, 1983) on melt inclusions and felsic whole-rock samples indicates temperatures of ~850-950°C. If whole-rock analyses of the lower GRV reported in previous work (Stewart, 1994) are used, even higher maximum temperatures can be estimated (maximum T ~990°C). However, whole-rock analyses may be affected by cumulus zircon, in which case the latter temperature would be overestimates.

Uranium, Pb and Sn are depleted in whole-rock analyses compared to melt inclusions (Fig. 4.15). This depletion is also reflected in the high whole-rock Th/U ratio (Fig. 4.16) and the anomalies observed in plots of normalised whole-rock analyses (Fig. 4.3). Given the solubility of U and Sn in Cl-F-CO_2-bearing aqueous fluids (e.g. Keppler and Wyllie, 1991), either fractionation of a fluid phase in a late-magmatic stage or alteration in the sub-solidus can be envisaged to explain this depletion. Evidence of exsolution of a F-CO_2-bearing fluid has been found in some rhyolite samples in both the Glyde Hill and

Chitanilga Volcanic Complexes in the form of pockets of H_2O-F-CO_2-bearing minerals (discussed further in chapter 6).

It is apparent from plots of whole-rock analyses, that some of the dykes and granite samples show higher concentrations of incompatible elements (e.g. Th, Rb, Ta), lower concentrations of compatible elements (e.g. Sr, Ba) and low (Eu/Eu*)N, Zr/Hf and Nb/Ta, in comparison with felsic volcanic units. This characteristic is consistent with crystallisation of the intrusive samples from a highly fractionated residual melt.

4.4.3 Magma volatile content

Melt inclusion analyses show strong correlation of Cl with the most incompatible elements (Pb, Rb, U, Th) (Fig. 4.15). Incompatible behaviour of Cl suggests that the melt was volatile-undersaturated, since in the presence of a fluid phase the melt would have been depleted in such a volatile element (e.g. Carroll and Webster, 1994). Further, this behaviour of Cl represents a point against leakage of fluids from the melt inclusions.

The behaviour of F is somewhat more complex and could be related to fractionation of F-bearing phases, such as F-apatite and fluorite. Due to the high F-Ca ratios (Fig. 4.13), F content cannot be wholly buffered, even if crystallisation of magmatic fluorite is admitted. Since fluorite is the mineral phase which contains the highest F content observed during petrographic examinations, no mineral phase capable of accommodating the observed amount of F was identified. Even assuming fluorite as the only Ca-bearing mineral, most melt inclusions from the Wheepool Rhyolite and some inclusions from the Waurea Pyroclastics and the Moonamby Dyke Suite show an “excess” in F.

The lower H_2O* in heated inclusions could be explained by diffusion of H_2 through the host mineral lattice during heating experiments (Qin and Anderson, 1992; Danyushevsky et al., 2002; Sobolev and Danyushevsky, 1994). Therefore, unheated inclusions should be considered more representative of the original water composition. The observed anhydrous parageneses (cf. chapter 3) are in agreement with relatively low water content and melt volatile-undersaturation.

4.4.4 Possible source rocks of the lower GRV magmas

Enrichment in LILE and LREE and depletion in Nb and Ta are common throughout the compositional spectrum in both volcanic complexes (Fig. 4.3). These geochemical features clearly distinguish the mafic rocks (basalt s.l.) from typical asthenospheric basalts (ocean island and mid-oceanic ridge basalts, OIB and MORB, Sun and McDonough, 1989). Stewart (1994) showed that obtaining the lower GRV basalt compositions starting from OIB or MORB would require either protracted fractionation or extensive crustal assimilation, neither of which is compatible with the primitive characteristics of these rocks, indicated for example by high Cr, and MgO contents (≤800-100 ppm and ≤8-11 wt.%, respectively). Therefore, a LILE- and LREE-enriched lithospheric mantle source seems likely.

A common origin for the mafic and the intermediate-felsic magmas of the entire GRV, and evolution through mechanisms of assimilation and fractional crystallisation has been invoked on the basis of geochemical and isotopic data (Stewart, 1994).

However, simple considerations based on the bimodal compositions of the lower GRV (compositions around 55 wt.% SiO_2 have not been found) and the amount of mafic magma required to obtain the large volumes of rhyolite observed are difficult to reconcile with this interpretation. Giles (1988) proposed that the mafic and intermediate-felsic rocks had different sources. The source of andesites, dacites and rhyolites was considered to be the lower continental crust. A recent Lu/Hf and U/Pb isotopic study of detrital zircons (Belousova et al., 2009) has found mainly crustal isotopic signatures and minor mantle contribution for a magmatic event at ~1595Ma, correlated with the GRV-Hiltaba Suite magmatism.

4.4.5 Comparison with the upper GRV and other SLIP

Whole-rock composition

The Glyde Hill and Chitanilga Volcanic Complexes of the lower GRV show very similar whole-rock compositions in terms of both major and trace elements, and similar trends with increasing silica (Figures 4.1 to 4.7). The upper GRV have a narrower compositional range (dacite-rhyolite-trachydacite, e.g. Giles, 1988) than the lower GRV. Both the lower and upper GRV have high K_2O, K/Na ratio and are peraluminous to metaluminous. The upper GRV have similar major elements, but generally higher Fe* number, and higher incompatible trace elements (Nb, Rb, REE, Y, Th) than samples of the lower GRV with equivalent silica (Fig. 4.17). The upper GRV meet most major and trace element compositional discrimination criteria for A-type magmas, including high Fe* number, HFSE, Ga/Al and low CaO (Collins, 1982; Whalen et al., 1987; Eby et al., 1990). For instance, the upper GRV plot in the A-type magma field of the incompatible element vs Ga/Al diagrams (Fig. 4.17), whereas the lower GRV plot across the boundary between I-type and A-type magmas. Furthermore, the upper GRV plot in the within-plate field of Pearce (1984), whereas the lower GRV are transitional between the field for convergent margin and within-plate granites. The lower GRV share several chemical characteristics with other SLIP magmas (Fig. 4.17, Cameron, 1980; Pankhurst and Rapela, 1995; Riley et al., 2001; Bryan, 2007).

Melt inclusion composition. The role of volatiles in the emplacement of large-volume felsic volcanic units

Melt inclusions were studied in the quartz-bearing Paney Rhyolite member of the Eucarro Rhyolite of the upper GRV by Kamenetsky et al. (2000) and Bath (2005). The Eucarro Rhyolite is a large-volume unit (>500 km^3) extending for >200 km along strike underneath the Yardea Dacite. A recent investigation (Allen and McPhie, 2003) interpreted it to be a single lava, approximately 300 m thick. The Eucarro Rhyolite is one of the three extensive felsic lavas forming the upper GRV, together with the Pondanna Dacite Member and the Moonaree Dacite Member of the Yardea Dacite (Allen and McPhie, 2003, Allen et al., 2008). In comparison with the Wheepool Rhyolite, it has a similar whole-rock composition, but a higher phenocryst content (15-21 vol.% against ~10 vol.%). Melt inclusion analyses in the Eucarro Rhyolite indicate comparable concentrations of most major elements (Al_2O_3, Na_2O, K_2O, TiO_2 and CaO) with the data presented here for the lower GRV. Normalised trace elements show similar patterns (Fig. 4.18), but some concentrations are higher in the Eucarro Rhyolite (REE, Y, Th, U, Zr). In the Eucarro Rhyolite, all these elements show positive correlations, indicating

incompatible behaviour. Volatile components also show several similarities, including:

1. similar concentrations of fluorine and the same broad negative correlation with silica;

2. low Cl/F ratio, although comparatively higher values were measured in the Eucarro Rhyolite;

3. similarly low values of calculated water; and

4. very low concentrations of P_2O_5 and S.

The Cl/F ratio has been related to the tectonic setting (Lowenstern, 1995; Aiuppa et al., 2009) and low values seem to be associated with intracontinental settings. Previous estimates of volatile content in the GRV were based on the paragenesis stability that suggested a low content of water (H_2O ≤1-2 wt.% in the Yardea Dacite of the upper GRV, Creaser and White, 1991).

Exsolution of a fluid phase, and therefore vesiculation, is a critical step in explosive eruptions. Explosive eruptions have been responsible for emplacement of most large-volume felsic units worldwide throughout geological history. Relatively large examples (~12 km^3 erupted, bulk volume) in historic times are the 1912 Katmai eruption and the 1883 Krakatau eruption (Hildreth, 1983; Self, 2006). Typically, the remainder of magma left volatile-depleted following an explosive eruption phase, tends to erupt effusively forming small-volume domes (<few km^3), which reflect the high viscosity of degassed rhyolite (Walker, 1973). In the case of the GRV, the volatile-undersaturated composition (and consequent general absence of vesiculation), coupled with high temperature and high concentrations of de-polymerising and viscosity-reducing halogens (Manning, 1981; Giordano et al., 2004) created the favourable conditions for large-volume effusive eruption. Large volumes of magmas (up to several hundreds of km^3) were erupted mostly non-explosively, and the probable high eruption rate allowed the lava to spread widely (several tens of km).

Based on mineralogy and mineral chemistry, significant amounts of F and water-understaturated compositions have been inferred in the source magmas of other extensive felsic lavas and strongly rheomorphic ignimbrites (Snake River Plain, e.g. Christiansen and McCurry, 2008; Keweenawan Midcontinent Rift plateaux volcanics, Green and Fitz, 1993; Etendeka, Namibia, Ewart et al., 1998b; 2004b).

4.5 Conclusions

Comparison of whole-rock and melt inclusion analyses suggests that only moderate alteration of major elements (Na in particular) has occurred, despite partial sericitisation of feldspar. High whole-rock K concentrations (K_2O ≤7-8 wt.%) are matched by melt inclusion compositions and are a primary characteristic of the magma. However, local alteration and mobilisation of elements resulted in high values of alumina saturation index of some samples (ASI ≥1.3, Fig. 2.3 and 4.1).

Some trace elements (U, Pb, and Sn) exhibiting good correlation with incompatible

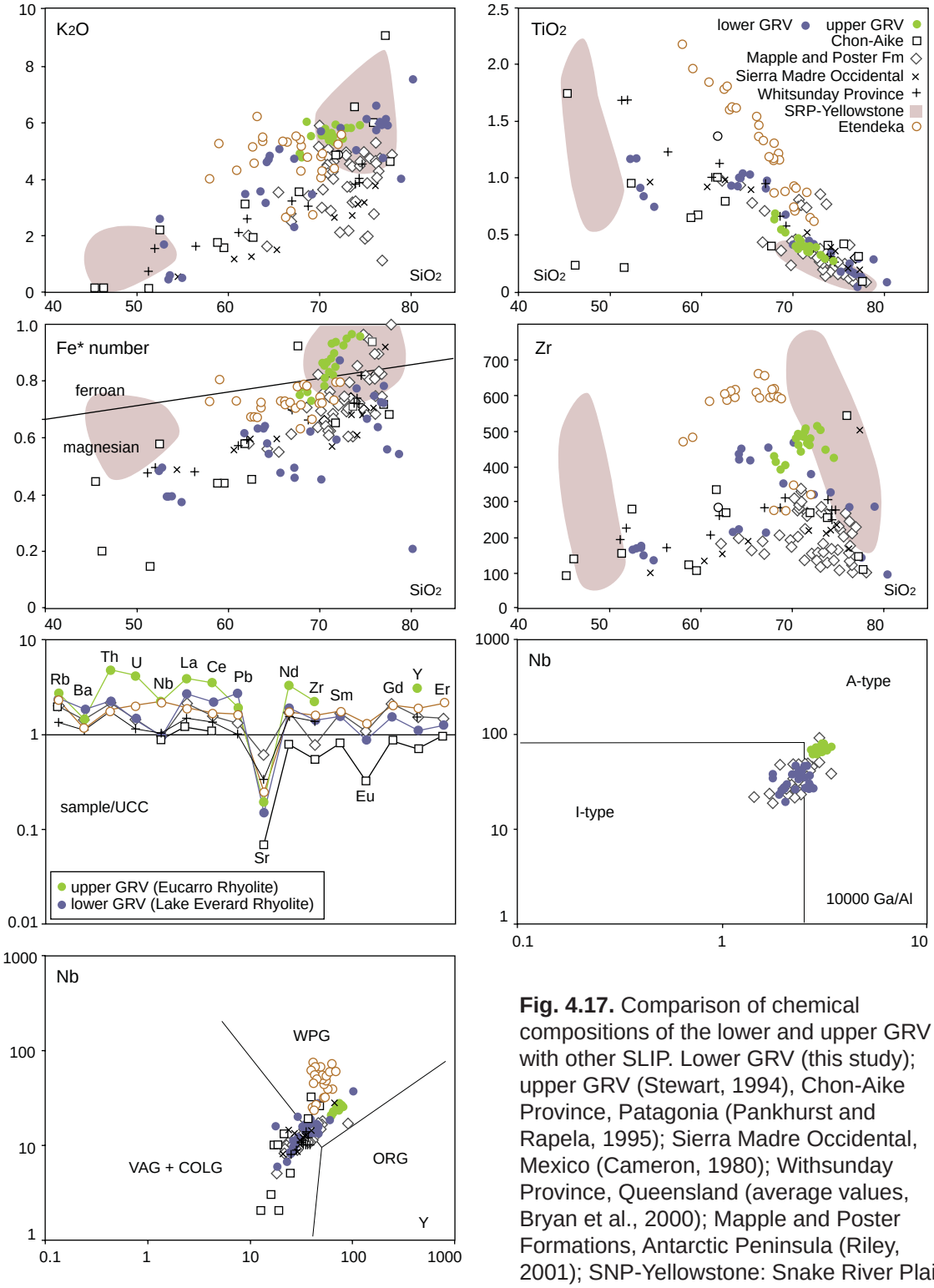

Fig. 4.17. Comparison of chemical compositions of the lower and upper GRV with other SLIP. Lower GRV (this study); upper GRV (Stewart, 1994), Chon-Aike Province, Patagonia (Pankhurst and Rapela, 1995); Sierra Madre Occidental, Mexico (Cameron, 1980); Withsunday Province, Queensland (average values, Bryan et al., 2000); Mapple and Poster Formations, Antarctic Peninsula (Riley, 2001); SNP-Yellowstone: Snake River Plain and Yellowstone, west USA (Christiansen and McCurry, 2008); Etendeka, Namibia (Ewart et al., 2004b). Modified iron number (Fe* number = FeOt/(FeOt+MgO)) after Frost et al. (2001). UCC: upper continental crust (Hu and Gao, 2008). Nb vs 10000·Ga/Al after Whalen et al. (1987). Nb vs Y diagram after Pearce (1984), WPG: within-plate granite, VAG: volcanic arc granite, COLG: collisional granite, ORG: orogenic granite.

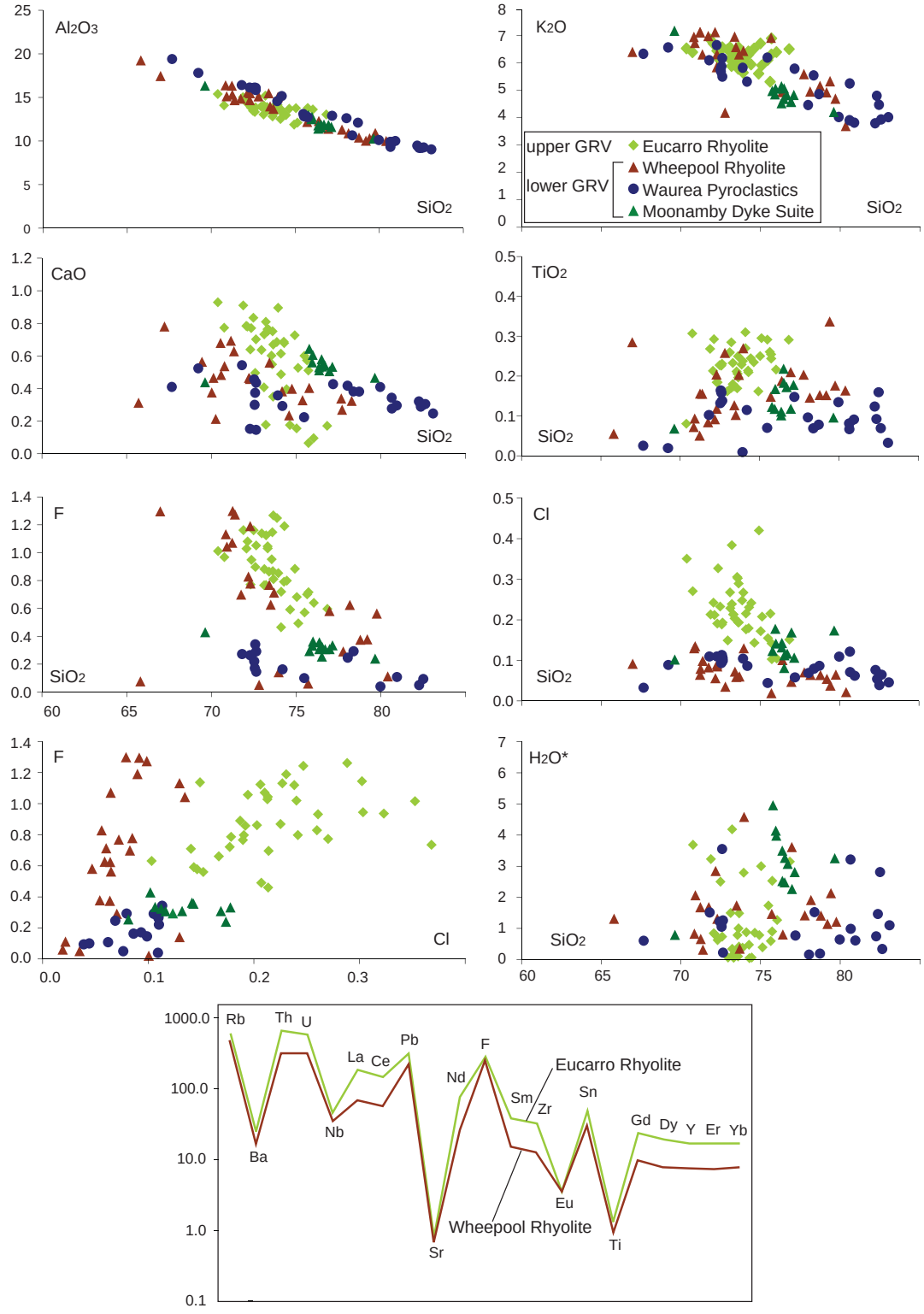

Fig. 4.18. Comparison between melt inclusion compositions in the lower GRV and upper GRV (Eucarro Rhyolite, Kamenetsky et al., 2000; Bath, 2005). Data recalculated as anhydrous and plotted as wt.%. H_2O^*: water calculated by difference (Devine et al., 1995).

elements (e.g. Th) in melt inclusion analyses, show low and scattered concentrations in whole-rock compositions (Fig. 4.15). This relationship implies that whole-rock samples were depleted in these trace elements and do not represent melt compositions.

Melt inclusion and whole-rock compositions plot on the same evolution trends. Melt inclusions show higher average contents of the more incompatible elements (e.g. Th, Ta, Nb, Rb) and lower concentrations of the more compatible elements (e.g. Ba, Sr). Thus, melt inclusions appear to be “more evolved”. Large compositional variations (even measured in melt inclusions hosted in single grains) are consistent with crystal-liquid fractionation of the modal minerals and mechanisms of magma mixing need not be invoked.

Wide variations of trace elements in melt inclusions with minor variation in SiO_2 suggest that these magmas remained at eutectic composition, fractionating quartz and feldspar as major phases, together with ±zircon (indicated by Zr-Hf fractionation) and ±Ti phases (Nb-Ta fractionation). Both protracted crystal fractionation and variable degrees of partial melting may have occurred and contributed to variable concentrations of incompatible trace elements (e.g. Th, Nb, Ta, U, Pb).

Melt inclusions and felsic whole-rock samples show evidence for zircon-saturation (Fig. 4.16). The zircon saturation model of Watson and Harrison (1983) applied on these samples indicates temperatures of 850-950°C.

Up to 1.3 wt.% F was measured in melt inclusions from the Wheepool Rhyolite. These values are consistent with F abundances found in melt inclusions from the Eucarro Rhyolite of the upper GRV (Bath, 2005), indicating high F concentrations throughout the volcanic province. Chlorine is present in moderate concentrations (Cl <0.2 wt.%) and correlates with incompatible elements (e.g. Th, Pb). This correlation is interpreted as evidence for volatile-undersaturation of the melt. Sulfur and phosphorus concentrations are low (<a few hundred ppm). Average values of calculated water contents in homogenised inclusions (EPMA, difference method) are relatively low for felsic magmas (H_2O^* = 2.0 - 2.3 wt.% for the volcanic units and = 3.1 wt.% for the dykes). Low water content is consistent with the anhydrous parageneses (feldspar, ±quartz, ±pyroxene, apatite, zircon) observed in the lower GRV (cf. chapter 3). Low water contents (H_2O ≤2 wt.%) have also been previously estimated for the upper GRV (Creaser and White, 1991; method of Nekvasil, 1991).

High F and low water contents, together with high magmatic temperatures help to account for the occurrence of large-volume, widespread rhyolite lavas in both the lower and upper GRV.

CHAPTER 5

Magma chamber dynamics revealed by quartz textures and trace element chemistry

5.1 Introduction

Crystal zoning and other disequilibrium textures (mineral rims, resorption textures) of different mineral species (plagioclase, biotite, amphibole, olivine), have been used to gain insight into magmatic processes (e.g. Anderson, 1984; Ginibre et al., 2002; Streck, 2008). Disequilibrium textures and metastable assemblages are evidence of the occurrence of reactions, and are essential to the reconstruction of the history of a magma. These features represent responses to changing magmatic conditions and can be preserved in intra-granular textures and successive growth zones of minerals. The sequence of growth zones defines a "crystal stratigraphy" (Wiebe, 1968), which can yield information on the relative timing of magmatic processes. For example, such textures have been used to identify processes of magma mixing and contamination, considered to occur in the formation and evolution of many intermediate and felsic magmas, even when the mixing is complete (hybridisation) or when the magmas involved are similar in composition (e.g. Tepley et al., 2000; Shane et al., 2008; Streck, 2008).

Quartz in silicate magmas is stable under a wide range of compositions and P-T conditions. Despite its abundance, it has not been commonly used as a source of petrological information. This is because quartz, due to its single end-member composition, does not readjust its stoichiometric substitutions with changing (P, T, X) conditions during crystallisation and subsequent re-equilibration. However, a wealth of information can be recorded in a variety of characteristics of quartz, including habit, non-stoichiometric substitutions in growth zones, inclusions and coronas (e.g. Sato, 1975; Müller et al., 2003; Wark et al., 2007). The main advantages of quartz in comparison with other minerals are its chemical stability and physical strength. In ancient and altered rocks, quartz may be the only well preserved mineral.

This chapter is focussed on the characterisation of the quartz population in the lower GRV on the basis of texture, cathodoluminescence, and trace element content. The study involves a wide array of quartz occurrences in different volcanic and intrusive rocks (lavas, ignimbrites, shallow and deeper intrusions) to assess the information that can be obtained from such characteristics of quartz and its implications for the magma dynamics. A brief review of CL applications to quartz is also given.

5.2 Methods and analytical techniques

Electron microprobe trace element analysis

Trace element concentrations in quartz were determined by a Cameca SX100 electron microprobe operating at 15 kV and 200 nA with a beam diameter of 5 µm. Analyses

were performed for Al, Ti and Fe. Prolonged counting time (12 minutes per analysis) was needed to reach low detection limits, does not allow the measurement of alkalis, for which diffusion can be expected during such long electron bombardment. Analyses were carried out along core-to-rim traverses, based on cathodoluminescence zones. In order to test the repeatability of the measurements, each traverse was repeated in two closely spaced parallel lines. The calculated detection limits ranged from conservative values of 9 ppm for Al, to 14 ppm for Ti, to 23 ppm for Fe. Calculated standard deviations are: Al 8 ppm, Ti 12 ppm, Fe 19 ppm.

Scanning electron microscope cathodoluminescence (SEM-CL) images

Cathodoluminescence (CL) images were obtained on polished carbon-coated samples with a FEI Quanta 600 scanning electron microscope (SEM) operated at 10 kV and equipped with a Gatan PanaCLF CL detector. All CL images are polychromatic (including all wavelengths) 8 bit bitmap (grey scale values in the range 0-255). Core to rim CL intensity profiles were obtained by measuring the local grey value in an area approximately 20 X 20 µm wide. CL profiles were obtained in areas free of healed fractures, inclusions and surface irregularities.

5.3 Sample description

Ten quartz-phyric units in the lower GRV were analysed: 1) the Wheepool Rhyolite, 2) the Lake Gairdner Rhyolite, 3) the Waurea Pyroclastics, 4) the Yantea Rhyolite-dacite,5) the Whyeela Dacite, 6) the Andesite I (Lake Everard), 7) the Andesite (Kokatha), 8) the Moonamby Dyke Suite, 9) microgranite dykes intruded at the base of the sequence at Kokatha, and 10) the Hiltaba Suite Granite. Relevant petrographic characteristics are summarised below and in Table 5.1. Detailed field and petrographic descriptions of these rocks are given in chapter 3.

5.3.1 Volcanic units

Three ubiquitously quartz-phyric volcanic units (Wheepool Rhyolite, Waurea Pyroclastics and Lake Gairdner Rhyolite) are present in the Glyde Hill and Chitabilga Volcanic Complexes of the lower GRV. Quartz occurs as subhedral to anhedral crystals and crystal fragments, up to a few mm in size. In other volcanic units (Whyeela Dacite, Yantea Rhyolite-dacite and the andesites), quartz is only locally present in very low abundances (Table 5.1 and chapter 3). In these units, quartz is anhedral (round or lobate) and may be surrounded by a corona of other minerals.

Wheepool Rhyolite (samples GH06, 23, 24c, 59)

The Wheepool Rhyolite includes massive or banded porphyritic rocks. Phenocrysts (~10 vol.%) include euhedral to subhedral plagioclase (albite) and K-feldspar (perthite), up to 5 mm in size, and minor (≤1 vol.%) subhedral to anhedral quartz, up to 1 mm and in some cases 2-3 mm in diameter. The microcrystalline, and locally micropoikilitic, groundmass (<10 to 50 µm) is mainly composed of quartz, K-feldspar and albite.

Table 5.1: Textural and compositional characteristics of quartz-bearing units in the lower GRV

unit	Wheepool Rhyolite	Lake Gairdner Rhyolite	Waurea Pyroclastics	Yantea Rhyolite-dacite	Whyeela Dacite	Andesite I	Andesite	Moonamby Dyke Suite	Microgranite Dykes	Hiltaba Suite Granite
locality	Lake Everard	Kokatha	Lake Everard	Lake Everard	Lake Everard	Lake Everard	Kokatha	Lake Everard	Kokatha	Kokatha
emplacement mode	lava	pyroclastic	pyroclastic	lava	lava	lava	lava	shallow intrusion	shallow intrusion	intrusion
texture	porphyritic	massive-eutaxitic	massive-eutaxitic	porphyritic	porphyritic	porphyritic	porphyritic-glomerophyric	porphyritic	seriate-equigranular	equigranular-seriate
Max grain size	≤5 mm	≤2 mm	≤2 mm	≤5 mm	≤2 mm	≤2 mm (locally ≤2 cm)	≤2 mm	≤3 cm	≤2 mm	≤10 mm
phenocrysts/ crystals	Ab, Kfs, Qtz	Qtz, Kfs, Ab	Kfs, Qtz, Ab	Ab, ±Qtz	Ab, ±Qtz	Pl, (Am-altered) Cpx, ±Qtz	Pl, (Am-altered) Cpx, Kfs, ±Qtz	Qtz, Ab, Kfs	Qtz, Ab, Kfs (perthite), Bt	Qtz, Kfs, Ab, Bt
groundmass	Qtz, Kfs, Ab	Kfs, Qtz, Fe ox	Qtz, Kfs	Ab, Kfs, Qtz	Ab, Kfs, Qtz	Pl, Qtz, Cpx, ±Qtz	Qtz, Pl, Kfs, ±Qtz	Qtz, Ab, Kfs		
accessory minerals	F-Ap, Zrn, Fe-Ti ox, ±REE-F-Cb, ±Mnz	Ttn, Zrn, Fe-Ti ox	Fe ox, Ti ox, Fl, Zrn	Fe-Ti ox, F-Ap, Zrn, ±Ep, ±Chl, ±REE-F-Cb	Fe-Ti ox, Ap, Fl, Zrn, ±Chl, ±Cc	Mag, Ap, Ttn, REE-F-Cb	Mag	Fe-Ti ox, Fl, Ap, Zrn, REE-F-Cb	(Y-)Fl, Nb-Ti ox, REE-F-Cb, Fe ox, ±Ep, ±Aln, ±Bt, ±Ms, ±Zrn, ±Ap, ±Mnz, ±Toz	Fe ox, Fl, Zrn, Ap
groundmass/ matrix texture	microcrystalline (< 50 µm)	vitriclastic (≤ 500 µm)	vitriclastic (≤ 300 µm)	microcrystal-line-microp-oikilitic (≤ 50 µm)	microcrystal-line-granophy-ric (≤ 50 µm)	microcrystalline (≤ 20 µm)	microcrystalline (≤ 20 µm)	microcrystalline (≤ 100 µm), poikilitic Qtz, radially ori-ented Kfs around Qtz phenocrysts	Qtz-Kfs granophyric texture	-
phenocryst abundance/ crystal proportion	10%	20%	<20%	10%	<10%	<1%	<1%	10-20%	-	-
quartz abundance	≤1% (phenocryst)	10% (crystal)	5-10% (crystal)	<1% (uneven distribution)	<1% (uneven distribution)	<1% (uneven distribution)	<1% (uneven distribution)	5-10% (phenocryst)	20-30%	20-30%
felsic enclaves				X	X	X	X			
TAS chemical classification (Le Bas et al., 1986)	rhyolite	rhyolite	rhyolite	rhyolite-dacite	dacite	andesite	andesite	rhyolite	rhyolite	rhyolite

Abbreviations: Ab albite, Aln allanite, Am amphibole, Ap apatite, Bt biotite, Cb carbonate, Cc calcite, Chl chlorite, Cpx clinopyroxene, Ep epidote, Fl fluorite, Kfs K-feldspar, Mag magnetite, Mnz monazite, Ms muscovite, ox oxide, Qtz quartz, Toz topaz, Ttn titanite, Zrn zircon.

Lake Gairdner Rhyolite (samples GH51, 87)

The Lake Gairdner Rhyolite contains quartz, K-feldspar (perthite) and plagioclase (albite) crystals and crystal fragments (≤2 mm in size, ~ 20 vol.%), and minor lithic fragments in fine-grained eutaxitic-textured matrix. Quartz crystals are sub- to euhedral and bipyramidal. The matrix is mainly composed of platy and cuspate devitrified glass shards, <500 μm in size.

Waurea Pyroclastics (samples GH13, 95)

The Waurea Pyroclastics include several different volcaniclastic facies. One facies, relatively poorly sorted crystal tuff, includes quartz as a main component (5-10 vol.%), other than K-feldspar and minor albite and lithic fragments (<5 vol.%). Quartz occurs as anhedral (round to lobate) to subhedral crystals and angular crystal fragments, up to 1-2 mm in diameter, either as separate crystals or included in lithic fragments. Crystals and lithic fragments are embedded in fine grained (≤0.3 mm) matrix, mainly composed of devitrified glass shards.

Yantea Rhyolite-dacite (samples GH09, 24, 56B)

The Yantea Rhyolite-dacite includes feldspar-phyric, massive or banded to fiamme-bearing lithologies. Phenocrysts (~10 vol.%) include plagioclase (albite) and minor quartz set in a microcrystalline to micropoikilitic, and locally spherulitic, groundmass. Quartz forms globules, ≤5 mm in diameter, surrounded by a rim of fine-grained phyllosilicate minerals. The groundmass is composed of albite tablets surrounded by K-feldspar and quartz. Medium- to coarse-grained felsic enclaves occur next to the base of the unit; they are up to several metres in size and have gradational margins (described below, section 5.3.4).

Whyeela Dacite (samples GH26, 33)

The Whyeela Dacite contains phenocrysts of albite and, locally, quartz set in a microcrystalline to granophyric-textured groundmass. The texture is heterogeneous: the size and abundance of phenocrysts varies considerably between outcrops. Quartz crystals are anhedral, up to a few mm in size, and unevenly distributed (sample GH33). Medium- to coarse-grained felsic enclaves are unevenly distributed in the unit (described below, section 5.3.4). In the area surrounding these enclaves, the host rock is enriched in anhedral, embayed quartz and K-feldspar crystals, up to 2 cm across.

Andesite I (Lake Everard) (sample GH72) and Andesite (Kokatha) (samples GH39, 52)

Andesites are massive and sparsely porphyritic with scattered phenocrysts (<1 vol.%) of plagioclase, amphibole-altered clinopyroxene and locally K-feldspar in a microcrystalline groundmass. Anhedral quartz grains (a few mm across) that show wavy extinction are locally present. These quartz grains are surrounded by a mineral rim (corona) composed of clinopyroxene, calcite and opaques (Cu-Fe±Zn sulfides and magnetite, sample GH72, Fig. 5.1 A) or green amphibole (sample GH52, Fig. 5.1 B).

5.3.2 Dykes

Moonamby Dyke Suite (samples GH15, 70, 70B, 92)

The volcanic sequence at Lake Everard is intruded by several porphyritic dykes, up to tens of metres wide. The dykes are mostly homogeneous in texture and contain medium- to coarse-grained phenocrysts of K-feldspar, quartz and minor sodic plagioclase. The quartzo-feldspathic groundmass is microcrystalline (grain size ≤50 μm) to micropoikilitic. Quartz phenocrysts are anhedral and deeply embayed (or "vermicular"). In one of the dykes (sample GH15) K-feldspar and albite form a thin (0.1-0.2 mm) rim around quartz crystals. Minerals in the rim are fine-grained, needle-shaped and radially oriented (Fig. 5.1 C, D). Fluorite-F-apatite-Ti-oxide-REE-fluoro-carbonate-bearing aggregates (micromiarolitic cavities) are locally present (Fig. 5.1 C).

Microgranite dykes (samples GH44, 91)

These dykes show a seriate texture and are composed of quartz, K-feldspar, albite and a complex accessory assemblage (Table 1). Quartz and K-feldspar (microperthite) form anhedral to subhedral crystals, up to 2-3 mm across, locally showing micro-granophyric intergrowth.

5.3.3 Granite

Hiltaba Suite granite at Kokatha (samples GH37, 38)

The Hiltaba Suite granite at Kokatha includes leucocratic, equigranular- to seriate-textured rocks, mainly composed of quartz, K-feldspar, plagioclase and biotite. The granite is medium to coarse-grained (≤10 mm, sample GH37), and locally finer grained (≤2 mm, sample GH38). Quartz and K-feldspar show mutual inclusion and intergrowth (granophyric) textures.

5.3.4 Felsic enclaves (sample GH29, 32, 52B)

Felsic enclaves occur close to the base of the Yantea Rhyolite-dacite, in the Whyeela Dacite and in the Andesite at Kokatha (Fig. 5.1 E, F). The enclaves are centimetres to several metres in size and have a massive or foliated texture. The enclaves are associated with the occurrence of anhedral quartz and K-feldspar grains, up to 2 cm across, in the host rocks.

Massive-textured enclaves

Massive-textured, medium-grained enclaves have round and gradational margins with the host rock, and contain crystals of K-feldspar and amoeboid quartz, separated by a microcrystalline quartz + K-feldspar + albite groundmass. Feldspar crystals are commonly surrounded by a granophyric rim, up to 0.5 mm-thick, formed by an intergrowth of K-feldspar and quartz growing perpendicular to the margins of phenocrysts (Fig. 5.1 E). These intergrowths make up 10-20 % of the groundmass and only occur around K-feldspar. Quartz is present as single anhedral crystals, <0.5 mm across, or as round to lobate aggregates, 0.5 to 1 mm in size, associated with epidote, calcite and minor fluorite and chlorite.

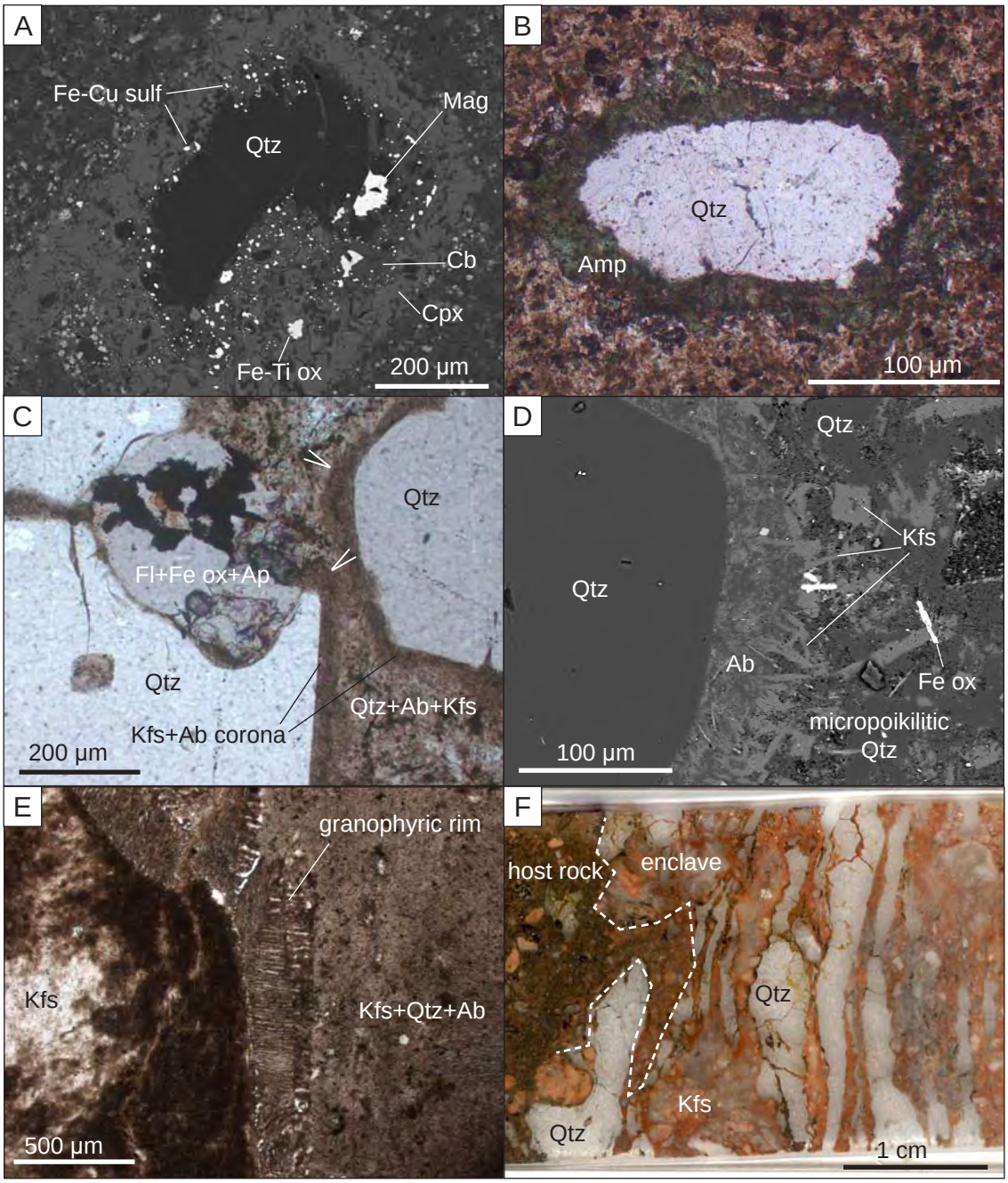

Fig. 5.1. Coronas around quartz crystals in the lower GRV. A: Clinopyroxene-carbonate-oxide-sulfide corona around a quartz grain in the Andesite I at Lake Everard; sample GH72, BSE. B: Amphibole corona in the Andesite at Kokatha; sample GH52, plane polarised transmitted light. C, D: K-feldspar +albite corona around quartz phenocrysts; Moonamby Dyke Suite, sample GH15. C: The feldspathic corona is almost continuous around quartz phenocrysts (arrowed). The corona is absent or significantly reduced at the contact between a phenocryst and an aggregate of fluorite, Fe oxide and apatite within an embayment; plane polarised transmitted light. D: Detail of the corona, composed of radially oriented skeletal crystals of K-feldspar and albite; BSE. E: Granophyric textures around a K-feldspar crystal in a felsic enclave in the Whyeela Dacite at Lake Everard, sample GH29, plane polarised transmitted light. F. Contact between a foliated felsic enclave and the host rock (Andesite, Kokatha, sample GH52B). Abbreviations: Ab - albite, Amp - amphibole, Ap - apatite, Cb - carbonate, Cpx - clinopyroxene, Fl - fluorite, Kfs - K-feldspar, Qtz - quartz, Mag - magnetite, ox - oxide, sulf - sulfide.

Foliated enclaves

Medium-grained, quartz- and feldspar-bearing felsic enclaves, showing a mm-scale foliation, occur in the Andesite at Kokatha (Fig. 5.1 F), together with massive-textured enclaves (Fig. 3.21). These inclusions are up to a few tens of centimetres across and occur near the upper contact of the unit. Quartz in these enclaves shows wavy extinction and triple junction contacts.

5.4 The application of CL to the study of quartz

Cathodoluminescence (CL) images can highlight cryptic intra-granular textures, undetectable in both optical and back-scattered electron (BSE) microscopy. These textures include: 1) growth-related textures (growth zones), twinning, grain shapes and growth modes (euhedral, anhedral; e.g. D'Lemos et al., 1997); 2) resorption-related textures, indicated by intersection relationships between growth surfaces (discordant boundaries or "unconformities"); and 3) healed brittle deformation structures. Other than being an intrinsic characteristic of each mineral, cathodoluminescence is strongly dependent on defects in the crystal lattice, particularly point defects induced by trace element substitutions (e.g. Götze et al., 2001). Elements enhancing CL response of minerals are commonly referred to as activators. Therefore, CL can be used as a proxy for trace element distribution (e.g. Perny et al., 1992; Watt et al., 1997; Müller et al., 2000).

CL textures are referred to as primary or secondary, in reference to textures formed during and after crystallisation, respectively. Among primary textures, oscillatory and step zones are defined by similarity with compositional zones in plagioclase (Sibley et al., 1976; Watt et al., 1997). Oscillatory zones are periodic, small-scale (μm-scale) and small amplitude variations in CL and considered to be due to slow, diffusion-controlled crystallisation under conditions of low undercooling (Bottinga et al., 1966; Sibley et al., 1976; Shore and Fowler, 1996). These conditions are possible in relatively static magma which preserves diffusive boundary layers at the crystal-liquid interface (Allègre et al. 1981; Sibley et al., 1976). Thus, oscillatory zones are interpreted to be the result of local self-organisation of trace elements at the interface between melt and crystal. Conversely, step zones are defined as wide, non-periodic and larger-scale (≥tens of μm) variations in CL intensity. Unlike oscillatory zones, these are interpreted to be due to "external" or "extrinsic" factors independent of local crystallisation and reflect variations in intensive parameters (P, T) and magma composition caused by processes such as crystal settling, magma convection, mixing, and reservoir replenishment (Shore and Fowler, 1996). As such, step zones can give information about the environment of formation of quartz.

The most common secondary textures include healed fractures, healed radial cracks around melt and fluid inclusions and modifications (smudging) of primary zoning due to redistribution of lattice defects (e.g. Boiron et al., 1992; Götze, 2005).

Comparison of CL images allows groups of crystals with similar zoning patterns to be identified. Zones can be correlated among crystals in the same group. The classification of CL textures is subjective. The following criteria, mainly based on primary textures, have been adopted: presence of step zones and oscillatory zones, intersection between CL textures, CL intensity and shape of step zone margins. Crystals from each unit show

one or more CL zoning patterns (Figures 5.2, 5.3, 5.4).

5.5 Quartz cathodoluminescence textures

5.5.1 Volcanic units (GH06, 23, 59, 13, 95, 51, 87)

In the three ubiquitously quartz-phyric volcanic units (Wheepool Rhyolite, Waurea Pyroclastics and Lake Gairdner Rhyolite), quartz is present as subhedral (bipyramidal) to anhedral (round and embayed) crystals, up to 2 mm in size. Angular quartz fragments are also common in the two pyroclastic units (Waurea Pyroclastics and Lake Gairdner Rhyolite).

Comparison of approximately 120 grains reveals three main CL step zones (zones a-c, Fig. 5.2). Zone A is CL-dark, homogeneous or progressively darker towards the rim, and locally oscillatory zoned. Zone (a) occurs as anhedral cores discordantly rimmed by zone (c). Zone (b) is CL-bright, and oscillatory zoned. Zone (b) shows round margins and occurs either as cores discordantly surrounded by zone (c) or forms the whole crystal. Zone (c) is relatively CL-bright and oscillatory zoned, and has euhedral to subhedral concordant margins. Zones (a) and (b) were not found in contact. Crystals apparently formed by zone (c) only (Fig. 5.2 C, G) can be artefacts of sectioning. The oscillatory zones are mostly planar and parallel (Fig. 5.2 C), indicating that the crystals maintained euhedral shapes throughout most of their growth. In addition to zones (a)-(c), thin (<100 μm), irregular-bordered bright rims, similar to the groundmass quartz, are locally present around both step-zoned and non-step-zoned phenocrysts (Fig. 5.2 A).

Other volcanic units (Andesites from Kokatha and Lake Everard and Yantea Dacite-rhyolite) are only very locally quartz-phyric and show low-contrast CL textures. These units are described below, in section 5.5.4.

5.5.2 Hypabyssal rocks (dykes)

Moonamby Dyke Suite

More than 120 CL images were compared. Unlike the volcanic units, the main textures can be correlated among crystals in single dykes, although significant differences can be seen between different intrusions (Fig. 5.3). The quartz phenocrysts are anhedral (embayed to vermicular), up to 2 mm, and occasionally 10 mm, in size. Step zones are evident in two of the dykes, and superimposed by planar (euhedral) to irregular and convoluted oscillatory zones (Fig. 5.3 A-E). Lobate growth surfaces are also common. Some lobes extend outwards and result in embayments at the grain margin or have been overgrown resulting in the formation of melt inclusions (Fig. 5.3 E). Local inward bending of growth structures (embayments), indicating differential growth rate, was also observed. Both oscillatory and step zones fit the embayments, indicating that these embayments are growth features, rather than the result of resorption (e.g. Fig. 5.2 E).

In some cases, CL step zones and oscillatory zones are curved towards the core forming cuspidal (chevron) textures, coupled on opposite sides of a crystal and connected by fractures crossing the entire crystal (Fig. 5.3 A). Locally, phenocrysts are overgrown by a thin (<20 μm) and texture-less external layer of quartz, similar to the microcrystalline

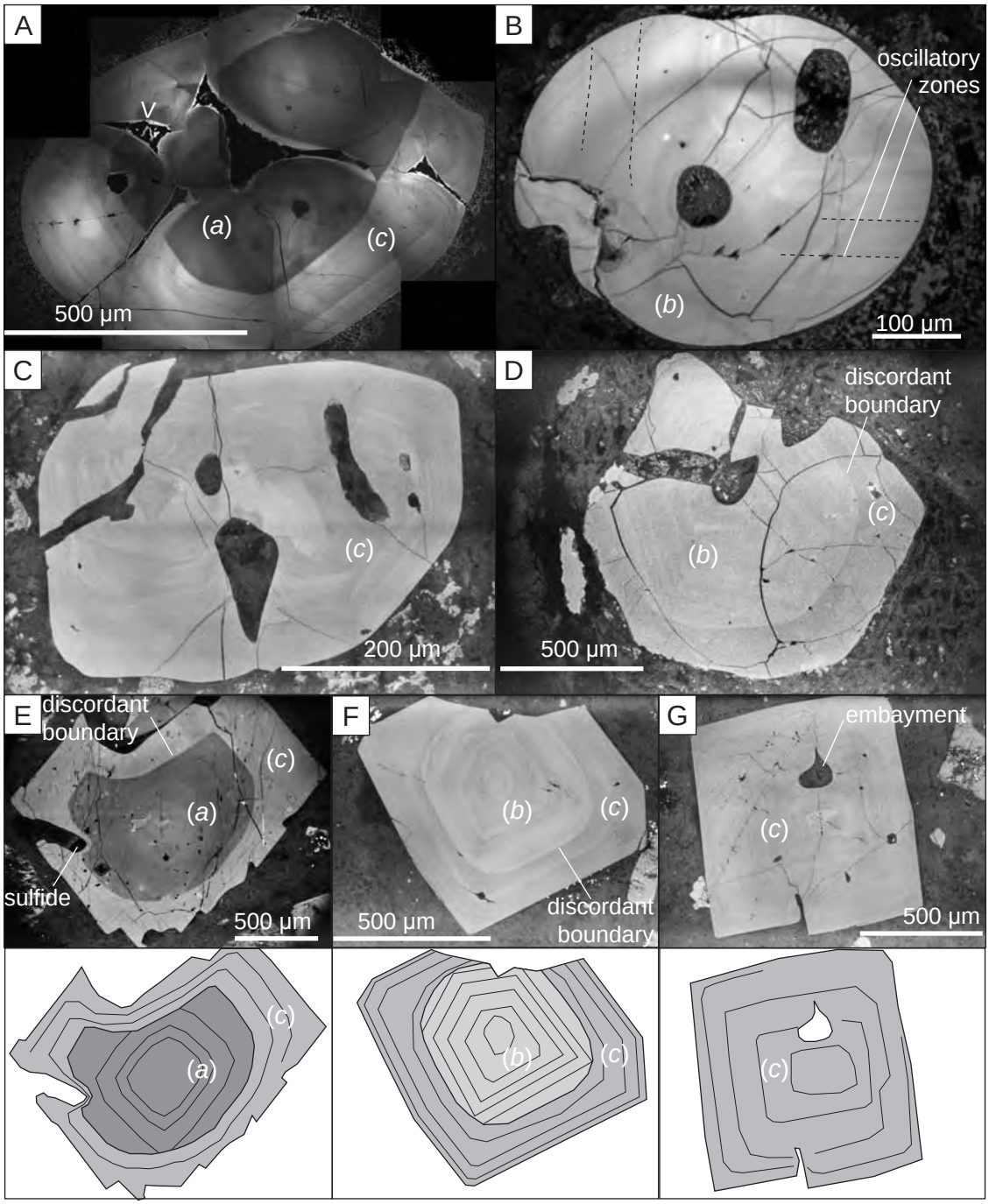

Fig. 5.2. Cathodoluminescence textures in the volcanic units from the lower GRV. A, B: Quartz from the Wheepool Rhyolite (sample GH23). A thin bright overgrowth is locally present (arrowed). C, D: Fractured crystals in the Waurea Pyroclastics (sample GH13). E-G: Quartz from the Lake Gairdner Rhyolite (sample GH51). A sulfide crystal constituted a mechanical growth impediment (E). For E-G, growth textures are highlighted. Zones (*a*), (*b*) and (*c*) were not found together in the same grain. Growth textures (oscillatory zones) are parallel to subhedral grain margins in zone (*c)*, except where fractured (top of F), but are truncated by round zone boundaries or grain margins in zones (*a*) and (*b*).

groundmass quartz.

In dyke 1 (GH70, 70B), three main CL step zones, separated by sharp boundaries, can be distinguished (Fig. 5.3 A-C). The core is bright and anhedral with lobate margins. The core is discordantly surrounded by a CL-dark mantle, in which there are oscillatory zones that decrease in luminescence towards the rim. The mantle-rim boundary truncates the internal textures in the mantle, and in a few cases, in the core (Fig. 5.3 B). The rim is relatively bright and homogeneous.

In dyke 2 (GH15), three main, broadly concentric zones with gradual variations in CL brightness are recognisable in most phenocrysts (Fig. 5.3 D-E). A relatively bright, oscillatory zoned core is commonly visible. The core grades into a darker, oscillatory zoned and locally discontinuous mantle up to 100-150 μm thick. The mantle is surrounded by a rim that is similar to the core in brightness and oscillatory zones. Lobate growth surfaces are mainly limited to discrete intervals, commonly in the rim and, in some cases, in the core. Minor truncation surfaces, not associated with abrupt CL changes, occur in different zones. These surfaces cannot easily be correlated between crystals.

In dyke 3 (GH92), the phenocrysts show weakly contrasted oscillatory zones defining euhedral growth textures without step zones (Fig. 5.3 F). The “smudging” of oscillatory zones makes the relationship between habit and growth textures unclear. CL-dark areas characterised by irregular shape and sharp borders are present.

Microgranite Dykes (GH91, GH44)

Quartz occurs as anhedral crystals up to a few mm in size and finer-grained interstitial crystals intergrown with K-feldspar. Review of approximately 40 CL images revealed complex intra-granular textures with different step and oscillatory zones. The relatively dark, rounded core has irregular and “smudged” zones (Fig. 5.3 G). The core is separated from the rim by a sharp, round contact. The rim exhibits oscillatory zones, sub-parallel to the core-rim boundary. In a few cases, an internally weakly zoned bright core is visible (Fig. 5.3 H). Other crystals have a weak luminescence with “smudged” concentric parallel zones, and subhedral and relatively bright core surrounded by a darker mantle. Quartz intergrown with K-feldspar has an extremely weak CL emission and no internal CL zones.

5.5.3 Hiltaba Suite granite (GH37)

Quartz is present as mostly anhedral crystals up to 3 mm across. Comparison of 15 CL images shows weakly contrasted CL emission with a rather irregular distribution. Two zoning patterns were distinguished. The first zoning pattern (Fig. 5.4 A) is nearly concentric, and composed of a bright homogeneous core and a rim becoming progressively darker towards the grain margin. The core-rim boundary is gradational. The core does not show internal textures, whereas the rim contains weakly contrasted oscillatory zones. The anhedral grain margins cut across the internal textures. The second pattern is characterised by weakly contrasted to homogeneous, non-concentric luminescence. Quartz crystals exhibit weak growth zones, which do not allow detailed characterisation. “Smudged” CL is also common in both interstitial and fine-grained quartz (Fig. 5.4 B).

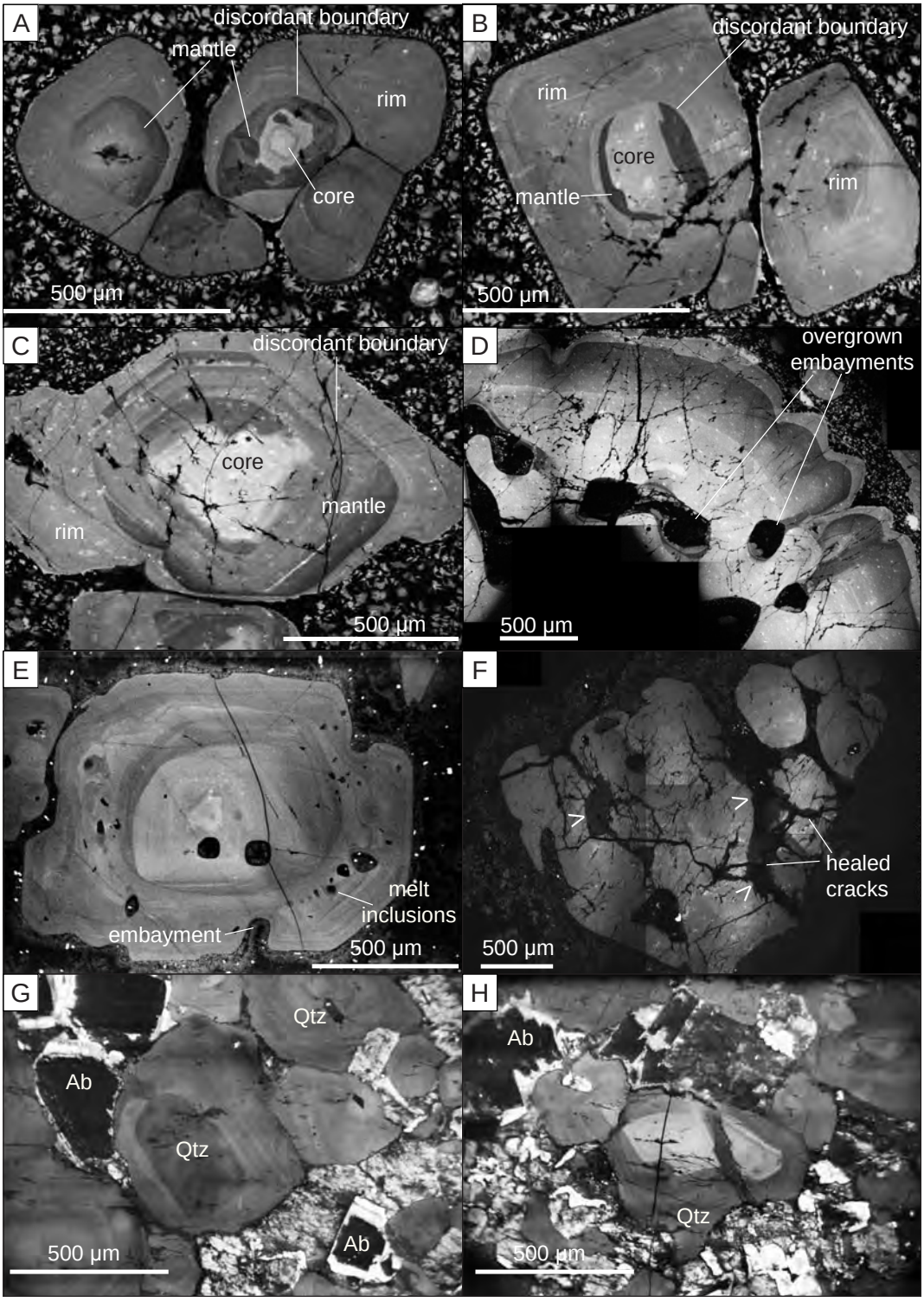

Fig. 5.3. Contrasting cathodoluminescence textures in dykes intruded in the Glyde Hill (A-F) and Chitabilga (G, H) Volcanic Complexes of the lower GRV. A-C: A round mantle-rim boundary truncates the internal growth textures, sample GH70 (dyke 1). In B, the core is surrounded by a discontinuous mantle. D-E: Wavy CL zones (disturbances of growth) coincide with melt inclusions or embayments, sample GH15 (dyke 2). Crystal core in D (black) was not imaged . F: Smudged primary CL textures. The crystal is crossed by secondary CL-dark areas related to healed cracks (arrowed), sample GH92 (dyke 3). G-H: Subhedral, concentrically zoned quartz crystals, sample GH91. H: concentrically zoned crystal with a bright core.

5.5.4 Felsic enclaves

Whyeela Dacite (GH29, 33) and Yantea Rhyolite-Dacite (GH56B)

Quartz grains are anhedral (lobate to round) and up to several mm in size. Major variations in CL emission (step zones) were not observed. Weakly contrasted oscillatory zones are cross-cut by the grain margin (Fig. 5.4 C). A thin CL-bright overgrowth has similar characteristics to the groundmass, and discontinuously rims the quartz crystals. In other crystals, CL textures are “smudged” and no concentric zones were observed (Fig. 5.4 D). Dark homogeneous areas related to cracks are visible.

Andesite I (Lake Everard) (GH72) and Andesite (Kokatha) (GH52)

Rare anhedral quartz grains up to several mm in size are present. Quartz grains are surrounded by amphibole- or pyroxene-bearing coronas. In all grains, CL is weak and shows no contrasted textures (Fig. 5.4 E). Quartz is intensely fractured and healed fractures appear as dark µm-scale bands. A thin and discontinuous CL-bright rim locally surrounds the grain.

5.5.5 Secondary textures

Healed fractures are clearly distinguishable in CL as low emission (dark grey-black) bands, up to a few tens of µm wide. In several cases, trails of fluid inclusions are aligned along fracture traces. In the pyroclastic units (Waurea Pyroclastics and Lake Gairdner Rhyolite), angular quartz fragments show a jigsaw-fit arrangement, not clearly visible in transmitted light, providing evidence for in situ fragmentation (Fig. 5.2 C, D), when the pyroclastic deposit was still unconsolidated. In the granite and some of the dykes intruded in the Glyde Hill Volcanic Complex, cracks form a dense network throughout quartz crystals. In the Microgranite dykes, healed fractures are several tens µm-thick and may cut different grains or only single grains (Fig. 5.3 H), but not through the surrounding grains and groundmass, indicating that the fracturing occurred at different stages, before or after the rock was completely solidified. Angular jigsaw-fit fragments are cemented within the fractures. In some cases, fractures are lined by Fe oxide. Weakly luminescent areas characterised by irregular (mostly lobate) shape and sharp borders are present in the granite, dykes and felsic enclaves (Fig. 5.3F, 5.4 A-D). These areas are spatially unrelated to the primary concentric zones and appear to be, at least partially, related to grain boundaries and cracks. Apparently similar textures were previously reported by D’Lemos et al. (1997) and Van den Kerkhof and Hein (2001).

5.6 Quartz trace element content

To further characterise the zones in quartz, trace element concentrations in different crystallisation stages (defined by CL zones) were determined in core-to-rim microprobe profiles (Fig. 5.5). The results were compared with CL relative intensity to assess the relationships between CL behaviour and trace element content. Trace element analyses confirm the subdivision of zones based on CL, although some overlap between zones exists in the volcanic units (Fig. 5.6).

Titanium is present in concentrations between approximately 25 and 130 ppm.

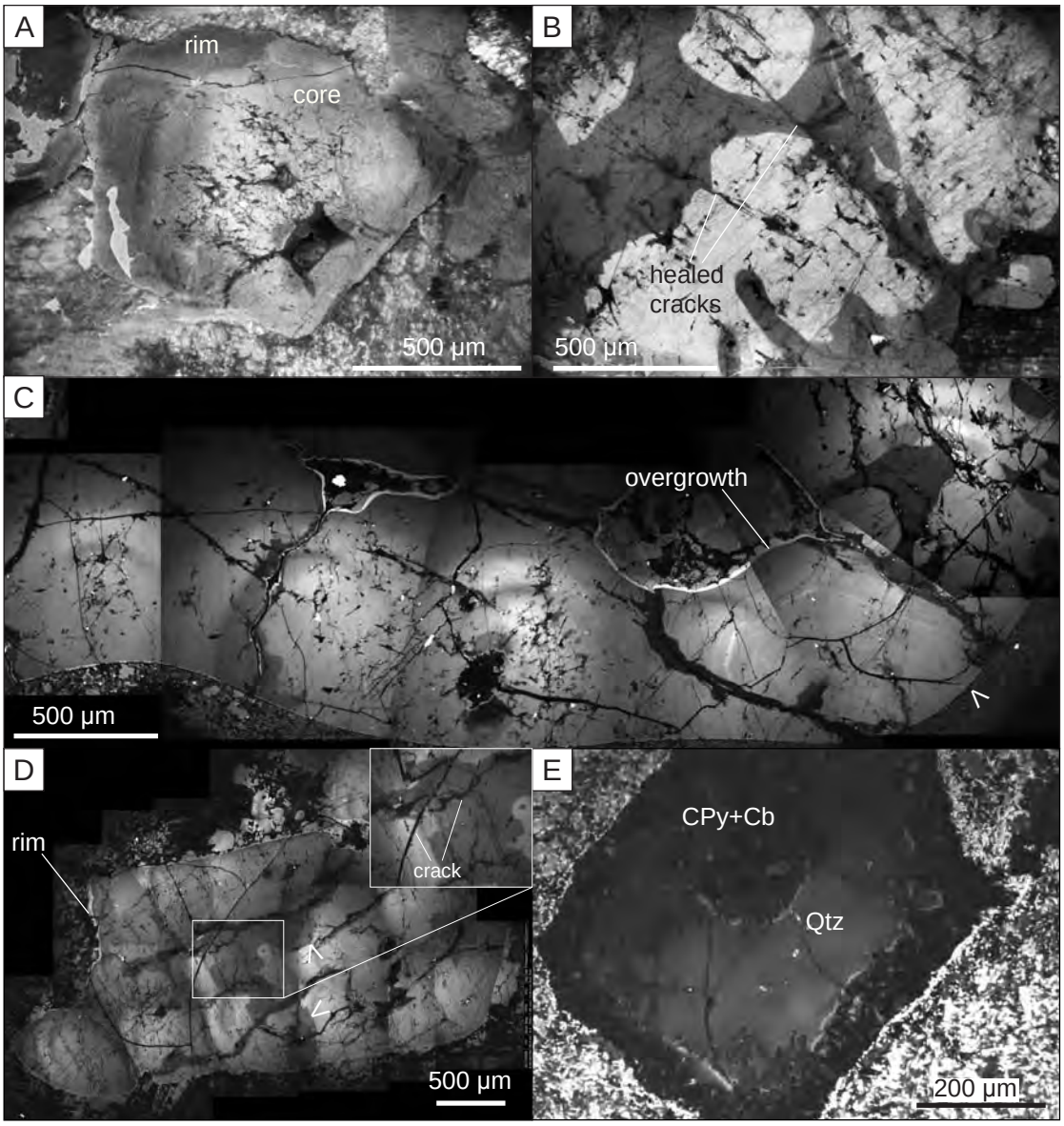

Fig. 5.4. Cathodoluminescence textures in the Hiltaba Suite granite and felsic enclaves from the lower GRV. A: "Smudged" CL zones, Hiltaba Suite (sample GH37). B: Dark homogeneous secondary CL textures with sharp borders are partly related to cracks (sample GH37). C: Quartz grain from a felsic enclave in the Whyeela Dacite shows weak oscillatory zones cross-cut by grain margin (arrowed), dark lobate areas associated with fractures and a thin discontinuous bright rim (sample GH29). D: "Smudged" CL textures. Dark homogeneous areas (arrowed) are distributed around fractures, see inset for detail (Whyeela Dacite, sample GH33). E: Weak CL emission in a quartz grain in andesite (Andesite I, sample GH72).

Titanium profiles show a clear correlation with CL intensity (Fig. 5.5), as found in other studies (e.g. Müller et al., 2000; 2005; Wark and Watson, 2006) and justifies the use of CL brightness as a proxy for Ti distribution. Iron content is in the range 10-330 ppm, Al in the range 100-680 ppm and in places above 3000 ppm. Aluminium and Fe show no evident correlation with CL, and no clear correlation was found between trace elements. A comparison of parallel traverses shows good correspondence in Ti and Fe values

between adjacent analyses, with variations in the order of the ppm (comparable with or less than the standard deviation of EPMA). Conversely, aluminium content locally shows a significant mismatch, in the order of several tens to hundreds of ppm. Such a difference could be accounted for by the presence of micro-inclusions or surface contamination during the polishing process with alumina powder.

5.7 Discussion

5.7.1 Crystallisation history of quartz recorded by crystal stratigraphy

CL zones record successive stages of crystal growth. Parallel CL textures indicate that the crystals were euhedral and their facets remained parallel during crystallisation (Fig. 5.2 C). In some cases, CL textures are bent into wavy and lobate shapes, indicating that the growth was "disturbed" and the crystal did not maintain a euhedral habit throughout (Fig. 5.3 D-E). These lobes can be preserved at the crystal margin as embayments, and are especially abundant in dykes in the lower GRV (Fig. 5.3 D-E). Deeply embayed ("vermicular") quartz has been reported in other shallow intrusions such as porphyries (e.g. Chang and Meinert, 2004). Embayments have been mostly interpreted as evidence of resorption resulting from temperature increase, depressurisation or compositional variations (magma mixing) (e.g. Nekvasil, 1991; Bachmann et al., 2002). However, the fact that the some embayments reflect CL growth textures, rather than truncating them, suggests that this could be not always the case, as also suggested by other studies (e.g. Lowenstern, 1995; Müller et al., 2000).

Growth-related irregular or lobate textures may be due to a physical impediment (a mineral or fluid phase stuck on the surface of the quartz crystal, Fig. 5.2.E). However, in most cases an impediment is not apparent (Fig. 5.3). During crystal growth in the magma, "topographic" highs on the crystal surface will be advantaged in comparison with the embayments because of a higher degree of exposure to the elements necessary for crystallisation (SiO2 in the case of quartz). Therefore, small irregularities in the surface, once created, can be enhanced by further crystallisation and evolve into wavy and lobate textures.

While quartz embayments can be shown to be not always due to resorption, there other indicators of quartz resorption. In particular, discordant CL textures and grain margins (Fig. 5.2, 5.3) indicate that quartz phenocrysts underwent multiple resorption episodes implying that the magma experienced several shifts from silica-saturated to silica-undersaturated conditions during crystallisation. Assuming equilibrium crystallisation, trace element uptake of quartz is controlled by 1) magma composition, and 2) quartz-melt distribution coefficients (ratio between element concentration in quartz and concentration in the melt, $K_{Qtz/melt} = C_{Qtz/Cmelt}$), in their turn influenced by the intensive parameters (P, T) and by melt bulk composition. Therefore, progressive changes in quartz trace element content are expected as a consequence of normal evolution of composition and thermal conditions, even in a magma crystallising as a closed system. Titanium content, in particular, has been related to the equilibration temperature of quartz (Ti-in-quartz or TitaniQ geothermometer; Wark and Watson, 2006). Because of the relationship between Ti content and crystallisation temperature and the correlation between Ti content and CL intensity, CL zones of each quartz grain can be used as an indicator of the crystallisation

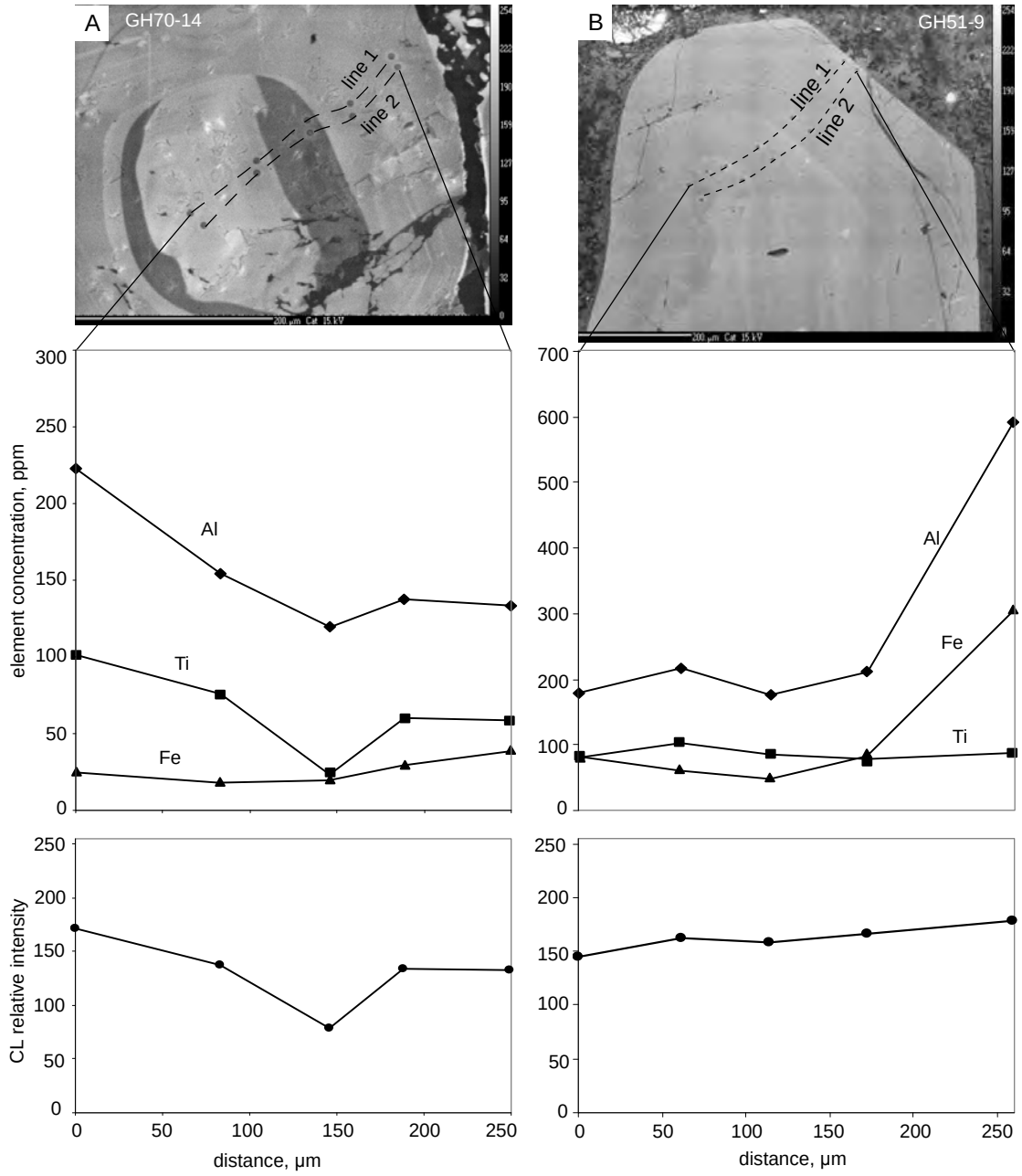

Fig.5.5. Trace element distribution in quartz grains from the Moonamby Dyke Suite (A) and Lake Gairdner Rhyolite (B) compared with CL intensity. Titanium values show a good correlation with CL emission. Trace elements are averaged between parallel traverses (lines 1 and 2) and expressed as ppm, CL as panchromatic 8 bit 0-255 grey scale.

history of quartz. In this regard, the main challenge is distinguishing between the effects of temperature and melt composition on quartz Ti content. However, the abrupt variations of Ti in quartz (step zones) that are associated with textural features (resorption surfaces), reflect discrete events rather than a continuous compositional and thermal evolution of the melt, and require a sudden change in the crystallisation environment.

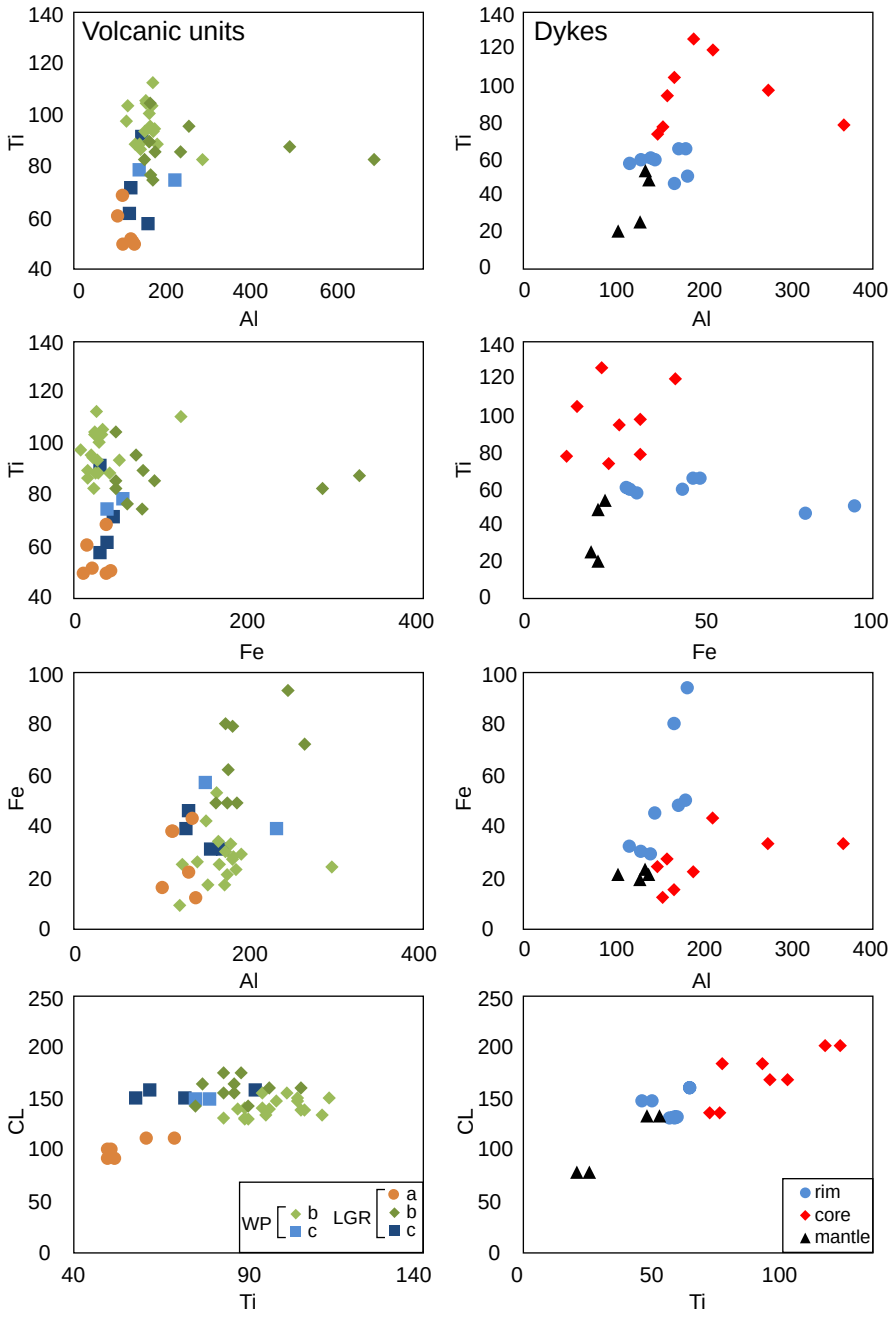

Fig. 5.6. Trace element composition and CL relative emission intensity of quartz in the volcanic units and the Moonamby Suite Dykes. LGR: Lake Gairdner Rhyolite, WP: Waurea Pyroclastics, a-c: quartz zones (see text).

Quartz crystallisation temperature and evidence for a temperature increase

Although the geothermometer of Wark and Watson (2006) was calibrated on the Ti intake of quartz in a Ti-saturated melt (in equilibrium with rutile), it can also be used for Ti-undersaturated magmas, provided that the activity of Ti in the melt is known. The temperature is related to the Ti content of quartz by the equation:

$$T(^{o}C) = -3765/(\log (XTi/aTi)-5.69)-273,$$

where XTi is the content of Ti in quartz and aTi is the activity of Ti in the melt.

Most rhyolitic magmas are Ti-undersaturated (aTi <1) (e.g. Hayden and Watson, 2007; Wiebe et al., 2007). In the lower GRV, Ti oxide occurs as exsolved domains in Fe-Ti oxide or as anhedral grains interstitial between groundmass crystals, and was not found as inclusions in quartz. Thus, the application of the geothermometer assuming aTi = 1 would give underestimated (minimum) crystallisation temperatures. If aTi = 0.6 is assumed, for the volcanic units, the calculated temperature values are in the interval T = 725-829°C, and for the Moonamby Dyke Suite in the interval T = 635-845°C.

Although aTi has a profound influence on the estimates of crystallisation temperature, it has only a minor effect on estimates of difference of temperature between zones (ΔT, Fig. 5.7). Some quartz phenocrysts show luminescent rims around relatively dark cores (reverse zoning, e.g. Fig. 5.2 A, E). These CL-bright rims cross-cut internal growth zones and are associated with an increase in Ti content. Under the assumption of a constant Ti activity and assuming a value of aTi = 0.6 (Hayden and Watson, 2007), this Ti increase translates into a core-rim temperature increase of up to 190 °C for the volcanic units (zones a to c). In the Moonamby Dyke Suite, core-mantle and mantle-rim ΔT can be estimated in -145°C and 112°C, respectively.

Reverse zoning in quartz has been previously interpreted as evidence for either an increase in Ti and/or crystallisation temperature due to the injection of hotter and more Ti-rich mafic magma (mafic recharge) in the magma chamber (Müller et al., 2003; Wark and Wolff, 2006; Wark et al., 2007; Wiebe et al., 2007; Shane et al., 2008). Basalt magmas are considered the main heat carriers in volcanically active areas, causing crust melting and prolonging the lifespan of felsic plutons, and are an important means of triggering eruptions (e.g. Bachmann et al., 2002; Hildreth and Wilson, 2007). In the lower GRV, mafic rocks crop out at Kokatha (>1 km thick sequence of mafic lavas) and very locally at Lake Everard (Blissett et al., 1993). Mafic igneous inclusions were described by Stewart (1994) and Allen et al. (2003) in the upper GRV rhyolitic units, providing evidence of interaction of such magmas with the GRV felsic magmas.

5.7.2 Coexisting quartz populations with different origins

The comparison of large amounts of crystals allows identification of crystal populations with distinct features. One of the most prominent characteristics emerging from the study of quartz in the lower GRV volcanic units is the coexistence, in the same unit and even in the same thin section, of crystals showing contrasting zoning patterns and trace element content (Figures 5.2, 5.3). This observation suggests that quartz crystals formed under different conditions and were later mixed and implies a dynamic regime of the magma chamber (Fig. 5.8). In the volcanic units, CL-dark, low-Ti (zone a) and bright high-Ti (zone b) quartz (Fig. 5.2) must have crystallised separately. Subsequently, quartz crystals underwent partial resorption (truncation of growth textures), either independently or after being juxtaposed. Finally, resorbed crystals of both types underwent Si-(over)saturated conditions and crystallisation was resumed (zone c). Not all the crystals underwent the last phase of crystallisation (Fig. 5.2).

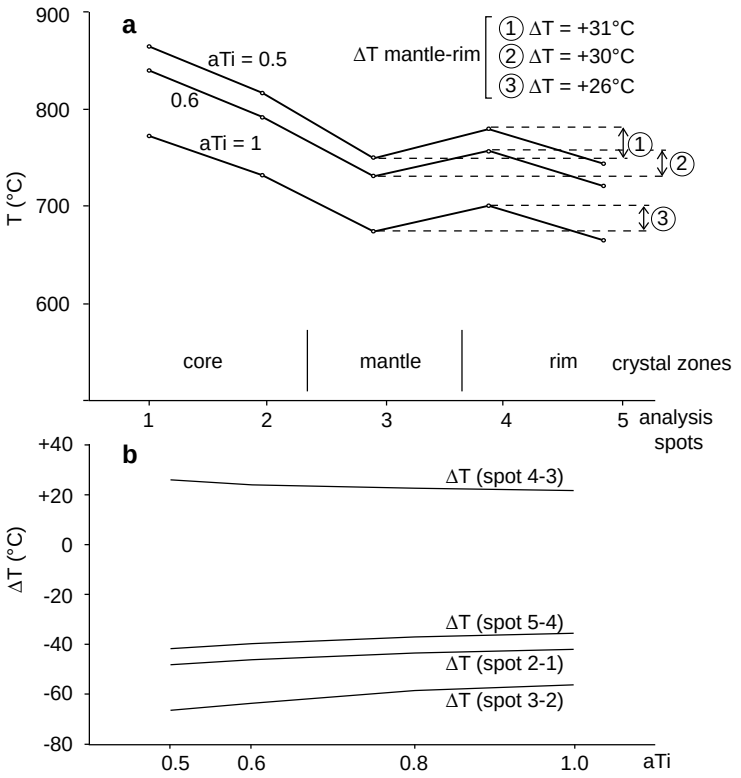

Fig. 5.7. Influence of Ti activity a_{Ti} on the estimates of quartz crystallisation temperature (Ti-in-quartz geothermometer, Wark and Watson, 2006). Titanium activity has a significant influence on crystallisation temperature (A), but only a minor influence on ΔT between crystal zones (B). Moonamby Dyke Suite, sample GH70, grain 70-10.

The question can be asked whether these quartz populations were carried by magmas with different composition. Melt inclusions offer the opportunity to analyse the melt coexisting with those quartz crystals. As shown in chapter 4, plots of melt inclusion compositions define trends consistent with evolution by fractional crystallisation of a single melt. Therefore, based on the available evidence, trace element zones and resorption textures in quartz crystals were not related to mixing of different melts. An alternative explanation is re-heating and convective stirring of the magma chamber (self-mixing, Couch et al., 2001), rather than open system processes. Mingled felsic lavas were described in the Eucarro Rhyolite of the upper GRV. Different portions of the lava can be distinguished by mineral abundances and texture (Morrow and McPhie, 2000), and have been interpreted to originate by accumulation of different amounts of crystals in a similar melt (Kamenetsky et al., 2000).

In contrast to the volcanic units, quartz zones and textures in single dykes can be correlated between crystals, which implies common crystallisation conditions and a shared crystallisation history. Quartz in dykes probably crystallised in a relatively stable, non-convecting portion of the magma, possibly roughly in situ (in the dykes).

5.7.3 Preservation of CL textures and cooling history

Preservation of sharp primary CL textures associated with abrupt Ti variations (tens of ppm) over short distances (μm to a few tens of μm, Figures 5.2, 5.3, 5.5) has implications for the cooling history of the magma after quartz crystallisation. Experimental work by Cherniak et al. (2007) indicated that diffusion of Ti in quartz operates at the mm-scale in 102-104 years at 800-900°C. Therefore, the Ti gradients observed between

zones in the volcanic units and the dykes could have been preserved only for a short time at high temperature and cooling must have happened shortly after crystallisation, either by eruption or intrusion at shallow levels. A further implication is that the absence of sharp CL textures in the Hiltaba Suite granite, Whyeela Dacite, Yantea Rhyolite-dacite and the andesites (Fig. 5.4), could be a secondary (post-crystallisation) feature and is consistent with a long residence at high temperature. Some phenocryst cores (e.g. Wheepool Rhyolite, Fig. 5.2 A) also show smudged CL textures in comparison with the rims. This feature could reflect partial re-equilibration (solid state diffusion) of the cores favoured by longer residence at high temperatures (e.g. in the magma chamber) and rapid cooling shortly after the crystallisation of the rims.

Other secondary modifications of CL textures include healed cracks and dark CL areas (e.g. Fig. 5.4 B-D), which are readily distinguishable from primary textures.

5.7.4 Quartz textures that record disequilibrium conditions: mineral rims (coronas)

The presence of mineral rims (coronas) around quartz grains indicates thermal or thermal-chemical disequilibrium between the quartz and the surrounding melt, or decompression/devolatilisation-driven disequilibrium.

Clinopyroxene- and amphibole-bearing reaction coronas: chemical-thermal disequilibrium

In the Andesite (Chitanilga Volcanic Complex) and Andesite I (Glyde Hill Volcanic Complex), quartz grains are unevenly distributed, anhedral and surrounded by reaction coronas (Fig. 5.1 A, B). The presence of such coronas, together with an anhedral habit and the common association with foliated enclaves (metamorphic xenoliths), points to

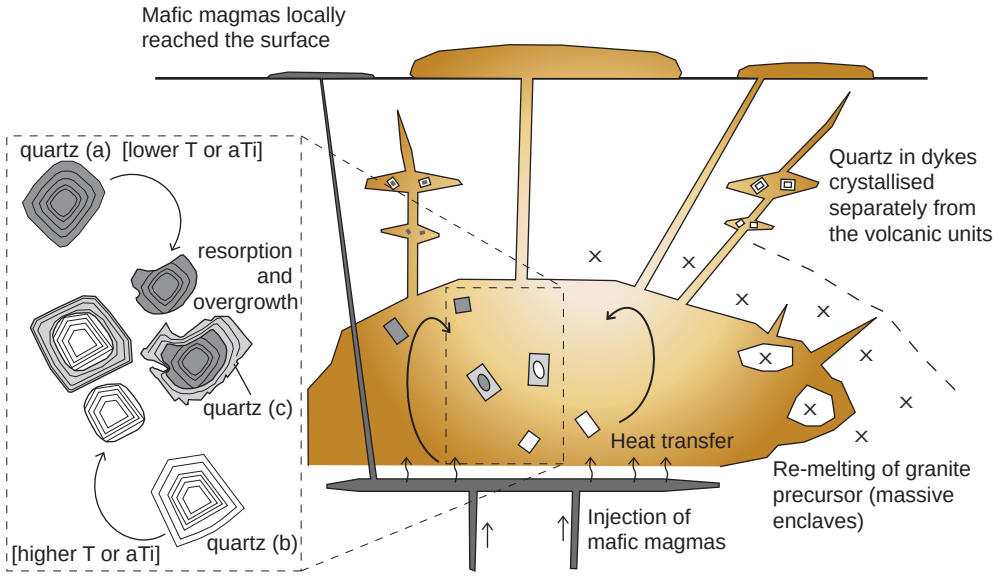

Fig. 5.8. Conceptual model for the crystallisation of quartz in the lower GRV magma chamber.

a xenocrystic origin for the quartz population. Reaction coronas form when the host magma composition is significantly different from the magma where the crystal originally formed. Several authors (Sato, 1975; Stimac and Pearce, 1992; Watt et al., 1997) used Ca-pyroxene-bearing coronas to prove a xenocrystic origin of quartz crystals and as an evidence of magma mixing or crustal assimilation.

Skeletal K-feldspar-albite corona around quartz phenocrysts: de-compression-driven disequilibrium

The K-feldspar-albite coronas around quartz phenocrysts in the Moonamby Dyke Suite (Fig. 5.1 C, D) can be interpreted in the quartz-K-feldspar-albite haplogranitic ternary system. Crystallisation of the coronas indicates a sudden shift from the stability of quartz±feldspar, crystallising as phenocrysts, to the stability field of feldspar. The nucleation on quartz crystals (heterogeneous nucleation) and the skeletal growth of K-feldspar and albite suggest rapid crystallisation under conditions of significant oversaturation (Lofgren, 1971). Such a shift can be achieved by 1) a change in composition; 2) a decrease in volatile pressure; 3) a decrease in melt volatile content.

A compositional change can hardly be obtained instantaneously, whereas depressurisation can be easily envisaged in an intrusive environment (e.g. upward flow of magma in a dyke). A decrease in pressure would shift the eutectic towards higher temperature and away from the quartz apex in the ternary haplogranitic system (Manning, 1981). A decrease in volatile solubility will accompany a decrease in pressure and, if the magma was close to saturation, unmixing of a fluid phase is expected. Water content of this dyke, estimated on the basis of melt inclusion analysis, is higher than in the volcanic units (chapter 4, Fig. 4.13). In the studied sample (GH15), the presence of fluorite- and ±biotite-bearing micromiarolitic cavities (Fig. 5.1 C, discussed further in chapter 6) suggests that a H_2O-F-bearing fluid was exsolved.

The coronas are almost continuous around quartz grains, with rare exceptions where a micromiarolitic cavity is in contact with a phenocryst (Fig. 5.1 C). Embayments in quartz crystals in these dykes can be shown to be mostly primary (growth-related) textures (Fig. 5.3 D-E). These textural relationships suggest the following sequence of events: 1) crystallisation of embayed crystals, 2) decompression (rise of magma in the dyke) and exsolution of volatiles into micromiarolitic cavities with consequent shift in equilibrium, 3) crystallisation of skeletal feldspar around quartz phenocrysts, 4) crystallisation of the surrounding groundmass. The events at points 2 and 3 are both consequences of de-compression and must have occurred nearly simultaneously. In this case, although quartz was destabilised by decompression, it was not resorbed because the coronas crystallising around it isolated and protected it. Finally, crystallisation of quartz in the surrounding groundmass indicates that, after the crystallisation of feldspar coronas, the magma became once again silica-saturated, even under the new lower-fluid pressure conditions. According to some experimental work (e.g. Lofgren, 1971), micropoikilitic texture forms under lower degrees of oversaturation in comparison with skeletal crystals. This relationship is consistent with a progressive shift towards the eutectic composition and near-equilibrium crystallisation.

Quartz-K-feldspar granophyric overgrowth in felsic enclaves

Blocks of medium-coarse grained quartzo-feldspathic igneous rock (granite) included in volcanic units show evidence of partial melting, followed by a rapid cooling. Evidence of melting includes the anhedral and lobate quartz and K-feldspar, truncation of growth textures in quartz, and the presence of fine-grained groundmass between the quartz and feldspar (Fig. 5.4 C). They are also variably dismembered adding to the quartz and feldspar population of the host. Evidence for rapid crystallisation includes the granophyric rim around K-feldspar, other than the microcrystalline groundmass (Fig. 5.1 E). Granophyric rims indicate eutectic growth of quartz and K-feldspar in conditions of significant oversaturation. Similar textures in the Fish Canyon Tuff and the Alid volcanic field were explained by rapid depressurisation and devolatilisation (Lipman et al., 1997; Lowenstern et al., 1997). Crystallisation of the granophyric rims most likely occurred during or after eruption of the host volcanic units. Because of the similar mineralogy and major and trace element composition to the Hiltaba Suite granite (chapter 4, Fig. 4.2 C), the felsic enclaves are interpreted as the product of partial re-melting of an early-crystallised portion (plutonic precursor) of the GRV-HS magma.

Similar enclaves were found in the Yardea Dacite (Garner and McPhie, 1999) and in the Eucarro Rhyolite (Allen et al., 2003). Their presence in the lower and in the upper GRV testifies that the process of re-melting of granite continued throughout the volcanic history of the province.

5.8 Conclusions

Primary (syn-crystallisation) CL textures in quartz tend to be better preserved in volcanic and hypabyssal units of the lower GRV than in granite samples. Varying degrees of complexity can be observed in quartz phenocryst CL primary textures (step zones), from the simplest case in the dykes, where zones can be correlated among quartz phenocrysts, to the volcanic units, where multiple populations of crystals coexist in the same sample. Each of these populations records a complex history of crystallisation and resorption events. The homogeneity of quartz populations in single dykes is interpreted as evidence that all quartz crystals shared the same crystallisation history and probably crystallised largely after isolation of these small magma batches in intrusions. The volcanic units tapped a larger part of the magma characterised by a dynamic regime which resulted in juxtaposition of different quartz populations, each with different crystallisation histories.

Alternating events of crystallisation and resorption, reverse zoning (rimward increase of Ti content) of quartz, and melting of already crystallised portions of the magma chamber (felsic enclaves) are consistent with a non-monotonous thermal evolution of the GRV-HS magma and suggest the occurrence of different thermal “pulses”. Plausible mechanisms to explain these features are re-heating and convective stirring of the magma chamber (self-mixing of Couch et al., 2001), rather than open system processes. The “engine” for convection is identified in heat input, possibly supplied by underplating mafic magma. Therefore, the magma chamber did not behave as an isolated system, and exchange of energy, if not mass, occurred.

Embayments are common in quartz in the dykes and are mirrored by the CL textures suggesting that, in many cases, embayments had a primary (growth-related, rather than resorption-related) origin.

CHAPTER 6

The role of fluorine in the concentration and transport of lithophile trace elements in felsic magmas: insights from the Gawler Range Volcanics, South Australia

6.1.Introduction

Fluorine (F) plays an important role in several processes occurring in magmas and associated fluids. Experimental studies indicate that F dissolved in silicate liquids strongly influences phase equilibria by decreasing solidus temperature and shifting the eutectic composition away from quartz in the granitic ternary diagram (Manning, 1981). Fluorine reduces viscosity and increases ion diffusivity in silicate melts (Dingwell et al., 1985; Giordano et al., 2004). Fluorine has also been shown to have a major influence on the activity coefficients of trace elements in magmas by increasing the solubility of zirconium and other high field strength elements (HFSE) (Keppler, 1993). The capacity of halogens (F and Cl) to bond with and to transport lithophile elements (e.g. REE, Nb, Th, U, Ba), commonly considered as immobile in an aqueous fluid (e.g. Cullers et al., 1973; Lesher et al., 1986; Michard and Albarède, 1986; Möller et al., 2003), has been confirmed by experimental data (Keppler and Wyllie, 1990; 1991; Webster et al., 1989; London et al., 1988). Evidence indicating the association of these elements and F-bearing mineralising fluids has been reported by several authors in different natural systems, including felsic magmatic systems (Charoy and Raimbault, 1994; Gieré, 1986; Audétat et al., 2000; Webster et al., 2004; Schönenberger et al., 2008), and metamorphic rocks (Gieré and Williams, 1992; Pan and Fleet, 1996; Rubatto and Hermann, 2003). This paper reports the presence of late-formed aggregates of F-, REE (lanthanides, U, Th)-, Y- and HFSE (Ti, Zr, Nb)-rich minerals filling vesicles, micromiarolitic cavities and lithophysal vugs in rhyolitic units of the Gawler Range Volcanics of South Australia. These minerals indicate mobility of such elements in the late magmatic stage. We also discuss (1) the characteristics of the phase (here referred to as late-stage magmatic fluid) that transported these elements, as inferred from mineralogical and textural data, (2) the role of complexing agents in the transport of REE and HFSE and (3) the capacity for F-rich magmas to produce distinctive trace element-rich late-stage magmatic fluids.

6.2.Vesicles, micromiarolitic cavities and lithophysal vugs

Despite textural differences, vesicles, micromiarolitic cavities and lithophysal vugs share a common origin as a consequence of magmatic volatile element concentration and imply the presence of a volatile-rich, alumino-silicate-poor fluid phase (Roedder, 1981; London, 1986). This phase can be permanently entrapped on solidification and crystallise in situ, and evidence of its characteristics can be preserved by minerals

precipitating in these cavities.

Vesicles form in lavas, shallow intrusions and densely welded pyroclastic facies as a result of exsolution of a volatile phase (McPhie et al., 1993). Miarolitic cavities (miaroles) can be found in shallow intrusions and comprise crystals of magmatic, super-solidus minerals projecting into either a cavity or a mass of hydrothermal minerals (London, 1986; Candela, 1997; Kile and Eberl, 1999). Such “external” nucleation of super-solidus minerals (nucleation on the former fluid phase interface) determines the irregular shape of these cavities (Candela and Blevin, 1995; Candela, 1997). Lithophysae consist of radially oriented crystallites, sometimes concentrically chambered, distributed around a circular to star shaped vug (McArthur et al., 1998). They occur in lavas and welded pyroclastic deposits and can reach a few tens of centimetres in diameter. The central vug forms during crystallisation and it may remain open or be lined or filled with minerals (McPhie et al., 1993). Although the origin is debated, ductile or ductile-brittle deformation of lithophysae provides evidence for high-temperature crystallisation within the melt (Cas and Wright, 1987; McArthur et al., 1998 and ref. therein).

6.3.Sample description

Four units locally containing either vesicles, micromiaroles or lithophysae were examined in thin sections and rock slabs for this study (Table 6.1, Fig. 6.1, cf. chapter 3 for detailed sample description). These include both volcanic and subvolcanic rocks, all rhyolitic in composition. The samples are generally fresh, despite a minor to moderate sericitisation of feldspar. Whole rock chemical analyses indicate decreasing CaO, MgO, P_2O_5 and Sr and increasing K_2O, REE, HFSE (Zr, Nb, Rb, Ga) and Y with increasing silica (Fig. 6.2, chapter 4). Some of these elements show continuously increasing trends (Nb, Th), whereas other elements increase with silica up to about 70 wt.% and decrease in the most evolved compositions (Zr and, to a lesser extent, Ce, Fig. 6.2, cf. chapter 4). The generally positive evolution trends of most lithophile trace elements indicate incompatible behaviour, leading to high concentrations of HFSE and REE in felsic compositions (e.g. Ce ≤200 ppm, Zr ≤650-700 ppm and Th ≤40 ppm at SiO_2 = 70 wt.%).

6.4.Analytical techniques

Selected samples were crushed in a tungsten carbide mill for X-ray fluorescence (XRF) and inductively coupled plasma mass spectrometry (ICP-MS) whole rock analysis at the University of Tasmania. Samples were digested in HF/H_2SO_4 with the PicoTrace high pressure digestion equipment and analysed with a Philips PW1480 X-ray Fluorescence Spectrometer and an Agilent 4500 ICP-MS. Detection limits for trace elements in ICP-MS are ≤0.01 ppm (REE) and ≤0.5 ppm for other elements, except As (5 ppm). A comparison of XRF and ICP-MS trace element data indicates a good correlation between the two methods, the difference being <20 % relative. See chapter 4 for a more detailed description of chemical analyses.

Laser ablation ICP-MS traverses were carried out in order to compare the distribution of REE (La-Lu), Y, Th, Nb, Pb, U, Cu, Zn, Mo, Cs, Rb, Ba, W, Si, Al, Ti, Fe, Ca and P in vesicles and in the surrounding groundmass from the Rhyolite-dacite (sample GH35). A

Table 6.1. Textural and compositional characteristics of the samples

unit	Rhyolite-dacite (Mi2)	Baldry Rhyolite	Moonamby Dyke Suite	Microgranite Dykes
locality	Kokatha	Lake Everard	Lake Everard	Kokatha
samples	GH34, GH35*	GH67, GH68*	GH15*, GH70, GH70B, GH92	GH44*, GH91*
emplacement	lava	lava	shallow intrusion	shallow intrusion
texture	porphyritic ±vesicular	porphyritic ±lithophysal	porphyritic ±micromiarole-bearing	seriate-equigranular
phenocryst grainsize	≤1-2 mm	≤2 mm	≤3 cm	≤2 mm
phenocryst	albite	K-feldspar, quartz	quartz, albite, K-feldspar	quartz, albite, K-feldspar (perthite), biotite
groundmass	quartz, albite, K-feldspar	quartz, albite, K-feldspar	quartz, albite, K-feldspar	
accessory minerals	Fe oxide, Ti oxide, fluorite, apatite, REE-F-carbonate, ±monazite	Fe oxide, Ti oxide, fluorite, zircon	Fe oxide, Ti oxide, fluorite, apatite, REE-F-carbonate	(Y-)fluorite, Nb-Ti oxide, REE-F-carbonate, Fe oxide, ±epidote, ±allanite, ±biotite, ±muscovite, ±zircon, ±apatite, ±monazite, ±topaz
groundmass texture	microcrystalline (< 20 μm)	microcrystalline (≤ 20 μm), "herring bone-like" quartz and K-feldspar	microcrystalline (≤ 100 μm), poikilitic quartz, radially oriented K-feldspar around quartz phenocrysts	quartz-K-feldspar granophyric texture
phenocryst modal abundance	≤10%	<1%	10-20%	-
chemical classification (Le Bas et al., 1986)	rhyolite-dacite	rhyolite	rhyolite	rhyolite

*Vesicle-/micromiarole-/lithophysa-bearing sample

New Wave UP-213 Laser and an Agilent 4500 ICP-MS mass spectrometer were used. The laser was operated at a frequency of 10 Hz and at 3.6-3.7 J/cm^2. A large spot size (100 μm) in comparison with the average grain size in the groundmass (~10 μm) was used in order to obtain “average” multi-grain values. Glass NIST 612 was used as the primary standard. The results of laser ablation traverses are used in two ways: (1) To map the distribution of trace elements and to identify trace element-bearing mineral phases by comparing concurrent peaks (qualitative use). It is possible, for instance, to identify a titanite grain by locating concurrent Ti and Ca peaks and to assess its contribution to the trace element signal. (2) To quantify the trace element contents of the groundmass and vesicles.

Electron microprobe (EPMA) compositional maps were produced to show the distribution of major elements around vesicles in the Rhyolite-dacite. Maps were obtained using a five spectrometer-equipped Cameca X100 microprobe. A 15 KV accelerating

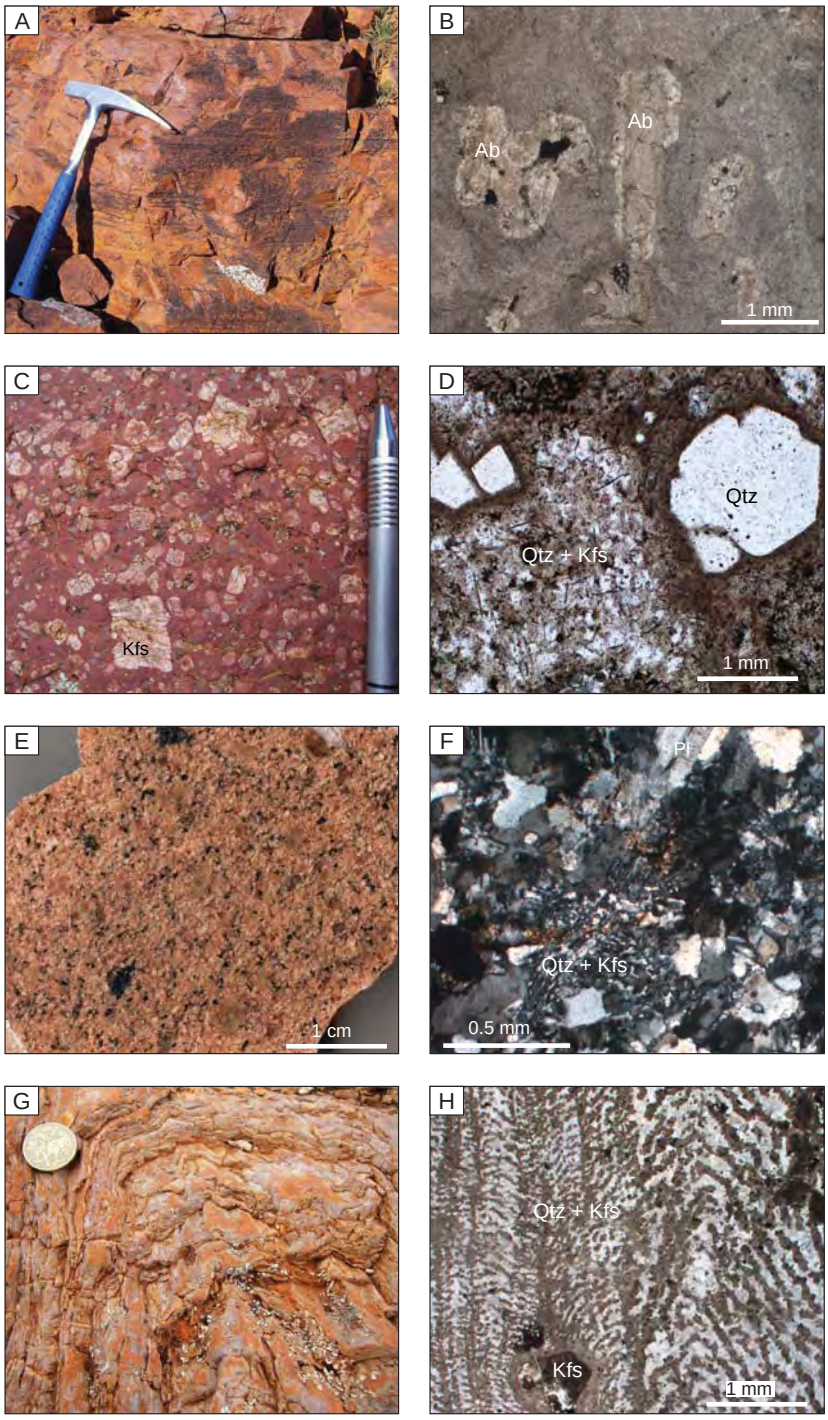

Fig. 6.1. A, B: Rhyolite-dacite Mi2. A: mm-scale flow bands; B: sericite-altered albite phenocrysts in a microcrystalline groundmass (sample GH34, transmitted plane polarised light). C, D: Moonamby Dyke Suite. C: Centimetre-scale phenocrysts of K-feldspar and quartz and (D) phenocrysts of quartz in a micropoikilitic quartzo-feldspathic groundmass (sample GH15, transmitted plane polarised light). E, F: Microgranite dyke. E: specimen and (F) seriate texture with K-feldspar, albitic plagioclase and quartz (sample GH44, transmitted light, crossed nichols). G, H: Baldry Rhyolite. G: Flow-folded flow-bands and (F) phenocryst of K-feldspar and a µm-scale quartz and K-feldspar layers in the groundmass (sample GH67B, transmitted plane polarised light). Abbreviations: Ab: albite, Kfs: K-feldspar, Pl: plagioclase, Qtz: quartz.

voltage and a spatial resolution of 3 µm were used. Measured elements include Si, Ti, Al, Fe, Ca, K, Na and La.

Cathodoluminescence (CL) images were obtained on polished carbon-coated samples with a FEI Quanta 600 scanning electron microscope (SEM) operated at 10 kV and equipped with a Gatan PanaCLF CL detector.

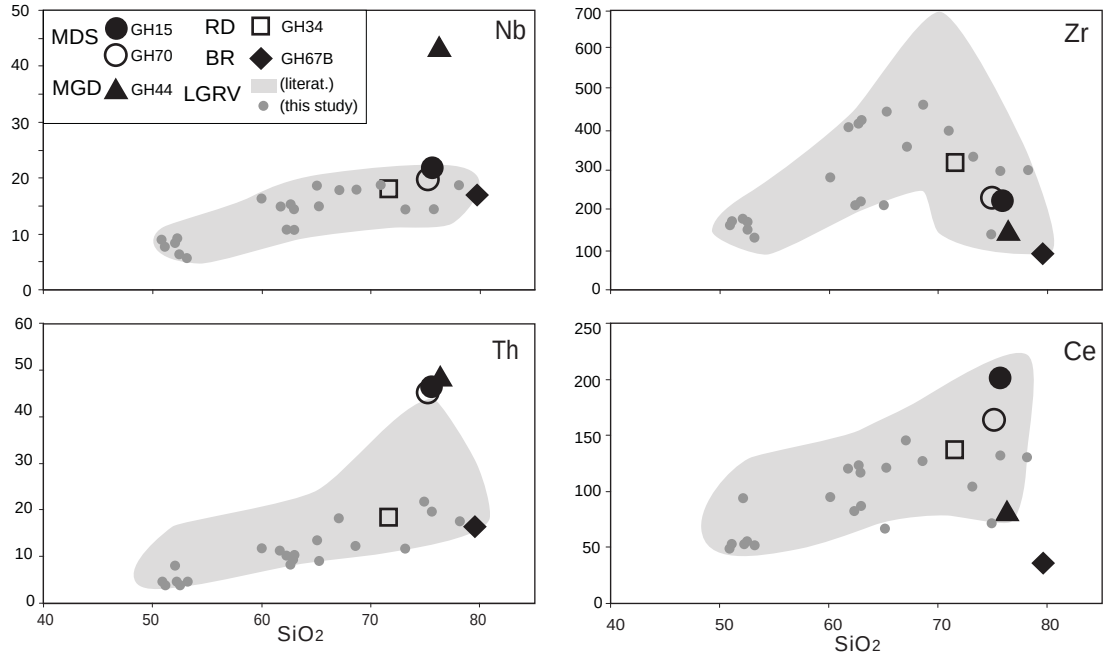

Fig. 6.2. Harker diagrams of selected whole rock trace element compositions from the lower GRV at Kokatha and Lake Everard. MDS: Moonamby Dyke Suite, RD: Rhyolite-dacite, MGD: Microgranite Dyke, BR: Baldry Rhyolite. LGRV literature data from Giles (1988).

6.5.Mineral assemblages in vesicles, micromiaroles and lithophysae

Vesicle-filling assemblage. Elongate and aligned vesicles, <5 vol.% of the sample (GH35), are lined with quartz and filled with epidote (pistacite), Y-bearing fluorite, fibrous Mn-bearing chlorite, ±titanite, ±REE-fluoro-carbonate (synchysite-(Ce)?, Ca(Ce,La) $F(CO_3)_2$), ±barite (Fig. 6.3 A, B). Cathodoluminescence images allow distinction of euhedral quartz from fan-shaped aggregates of needle-like silica crystals, both growing inwards from the walls (Fig. 6.3 C). Although the vesicles are elongate, crystals within the vesicles show no preferential orientation implying a static growth. The groundmass of the rock is very fine grained (≤10 μm) and displays concentric zones of minerals around the vesicles (Fig. 6.3 D).

Micromiaroles. Irregular-shaped aggregates with jagged margins form approximately 5 vol.% of the sample (GH15) and include Y-bearing fluorite, Nb-bearing Ti oxide (identified as anatase for its optically negative character), zircon, REE-F-carbonate (synchysite-(Ce)?), F-apatite, quartz and chlorite-altered biotite (Fig. 6.4 A, B). Titanium oxide and apatite form euhedral prismatic crystals growing towards the centre of the cavity. These aggregates, ≤1mm in size, have sharp borders without any alteration halo and are not interconnected by or related to fractures.

Interstitial accessory assemblage. The Microgranite dykes (samples GH44, GH91) show a complex accessory mineral assemblage including fluorite, a Th-bearing REE-fluoro-carbonate, Nb-bearing Ti oxide, Fe oxide, chlorite-altered biotite, ±epidote, ±allanite, ±zircon, ±muscovite, ±topaz, ±monazite and ±titanite. All the accessory minerals occur in interstitial positions between the major phases (Fig. 6.4 C, D), with the

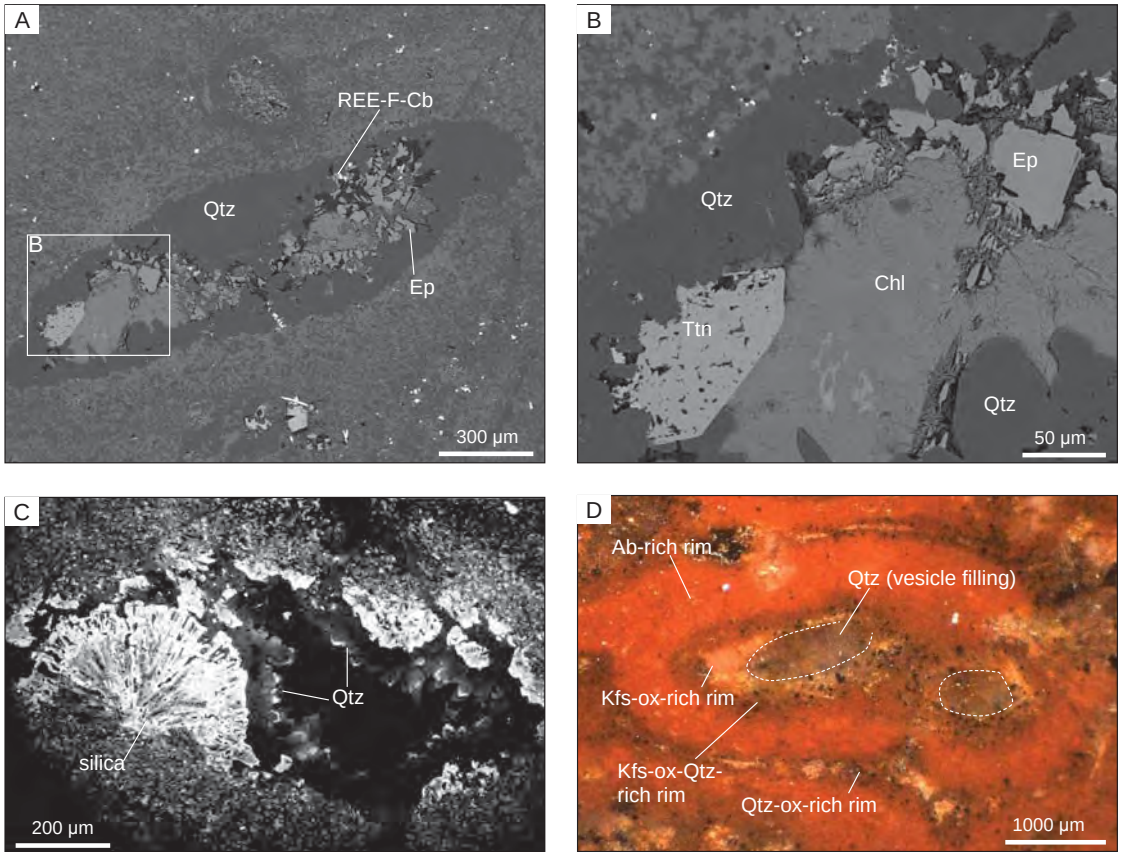

Fig. 6.3. Vesicle-filling assemblage in the Rhyolite-dacite (Mi2), Kokatha. A, B: Concentric zones with quartz inside the rim. Euhedral quartz and titanite contrast with the anhedral habit of epidote and chlorite. C: Silica occurs as euhedral quartz crystals perpendicular to the vesicle walls and needle-like crystals in fan-shaped aggregates. D: Mineralogical zones in the groundmass around vesicles, vesicle outline is indicated by dashed lines. Sample GH35, A, B: back scattered electron (BSE), C: cathodoluminescence (CL) and D: binocular microscope. Abbreviations: Chl: chlorite, Ep: epidote, ox: oxide, REE-F-Cb: REE-fluoro carbonate, Ttn: titanite.

exception of zircon, topaz and monazite. In these samples, zircon occurs as inclusions in quartz. For topaz and monazite, textural relationships are obscured by sericite localised around the margin and along fractures, and by a pleochroic (radiation damage) halo in the surrounding minerals, respectively.

Lithophysae. Lithophysal vugs (sample GH68) are partly filled with quartz, thinly layered amorphous silica, Y-bearing fluorite and minor amounts of Ca-Mg carbonate, Fe-oxide and barite. The minerals are roughly concentrically arranged: quartz is directly deposited in contact with the walls and fluorite deposited in a later stage in the internal portions of the vug (Fig. 6.5). Three types of silica can be distinguished by combining CL and back scattered electron (BSE) images (type I- highly CL-contrasted euhedral quartz, type II- µm-scale layered silica blanketing type I silica, type III-elongate prismatic crystals showing patchy CL (Fig. 6.5 B). Type III silica is present within the CL-banded quartz (type I) and between the latter and the vug walls. Fine grained Fe-oxide and Sr-bearing barite aggregates occur along the contact between the first and second types of silica. Fluorite overgrew layered silica, as shown by truncation relationships.

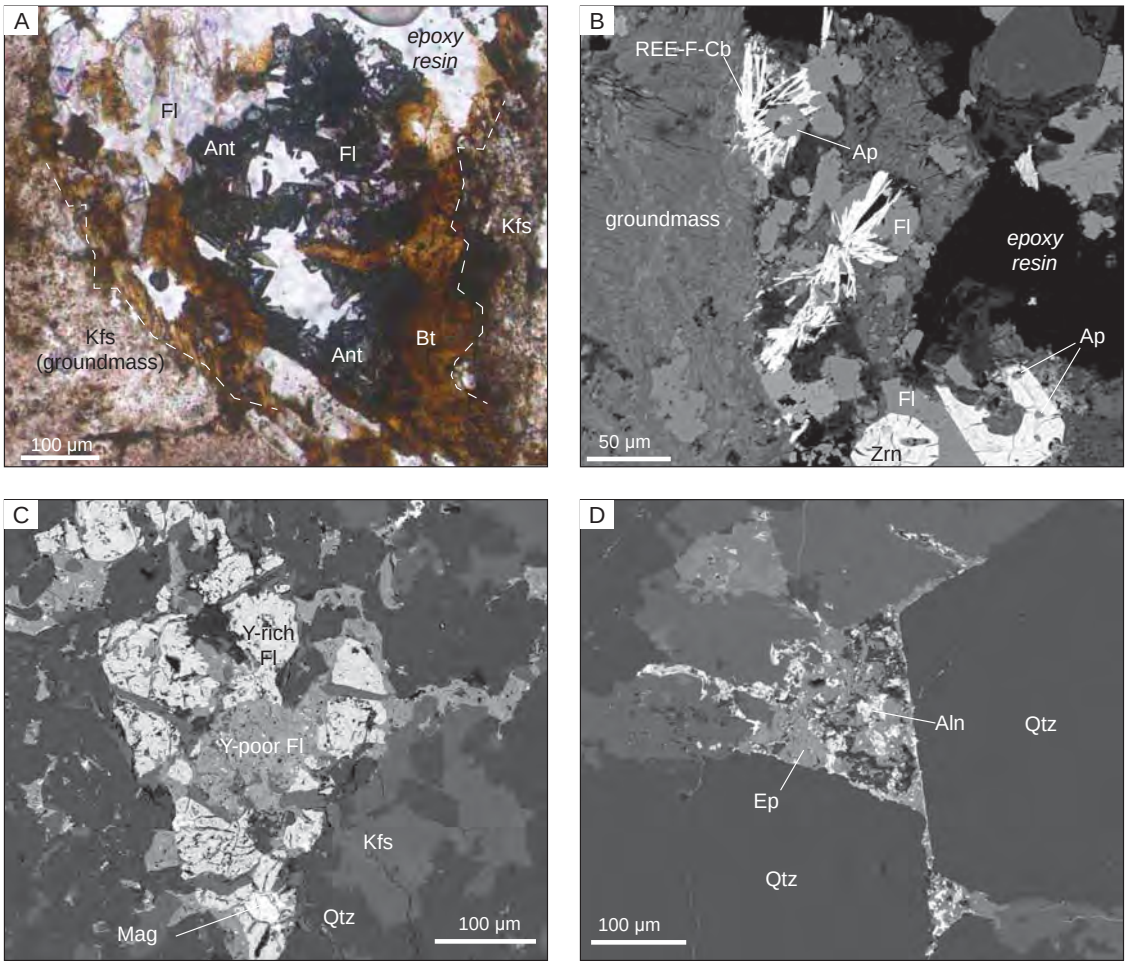

Fig. 6.4. Micromiarolitic cavity-filling assemblages in the Moonamby Dyke Suite at Lake Everard (A, B) and interstitial aggregates of accessory phases in microgranite dykes at Kokatha (C, D). A: Aggregate of Y-bearing fluorite, euhedral Nb-bearing anatase and biotite infilling a micromiarolitic cavity (the walls are indicated). Assuming a growth from the walls inwards, substantiated by the orientation of crystals of anatase, anatase overgrew fluorite and biotite. B: Zircon is subhedral and completely to partially includes apatite. Needle-like crystals of REE-F-carbonate are distributed around and within fractures in apatite and fluorite. The carbonate (synchysite?) shows a predominance of LREE over HREE and locally contains Th. Textural relationships suggest the following crystallisation sequence: apatite-zircon-fluorite-F-carbonate. C: An Y-rich (BSE-bright) and an Y-poor (BSE-dark) type of fluorite can be distinguished. D: Fine grained epidote and allanite form an aggregate in an interstital position between quartz grains. A, B: Sample GH44, optical microscope plane-polarised light and BSE; C, D: sample, GH91 BSE. Abbreviations: Aln: allanite, Ant: anatase, Ap: apatite, Bt: biotite, Fl: fluorite, Mag: magnetite, Zrn: zircon.

6.6.Chemical composition and systematics of vesicles and surrounding groundmass

Zones in the groundmass around vesicles were studied with a combination of optical microscopy, BSE images and compositional maps. Starting from an inner position (next to the vesicle walls), the concentric zones are (Fig. 6.6 B, cf. 6.3 D):

1) 0-150-µm-thick zone enriched in K-feldspar ±Fe oxide ±Ti oxide, quartz

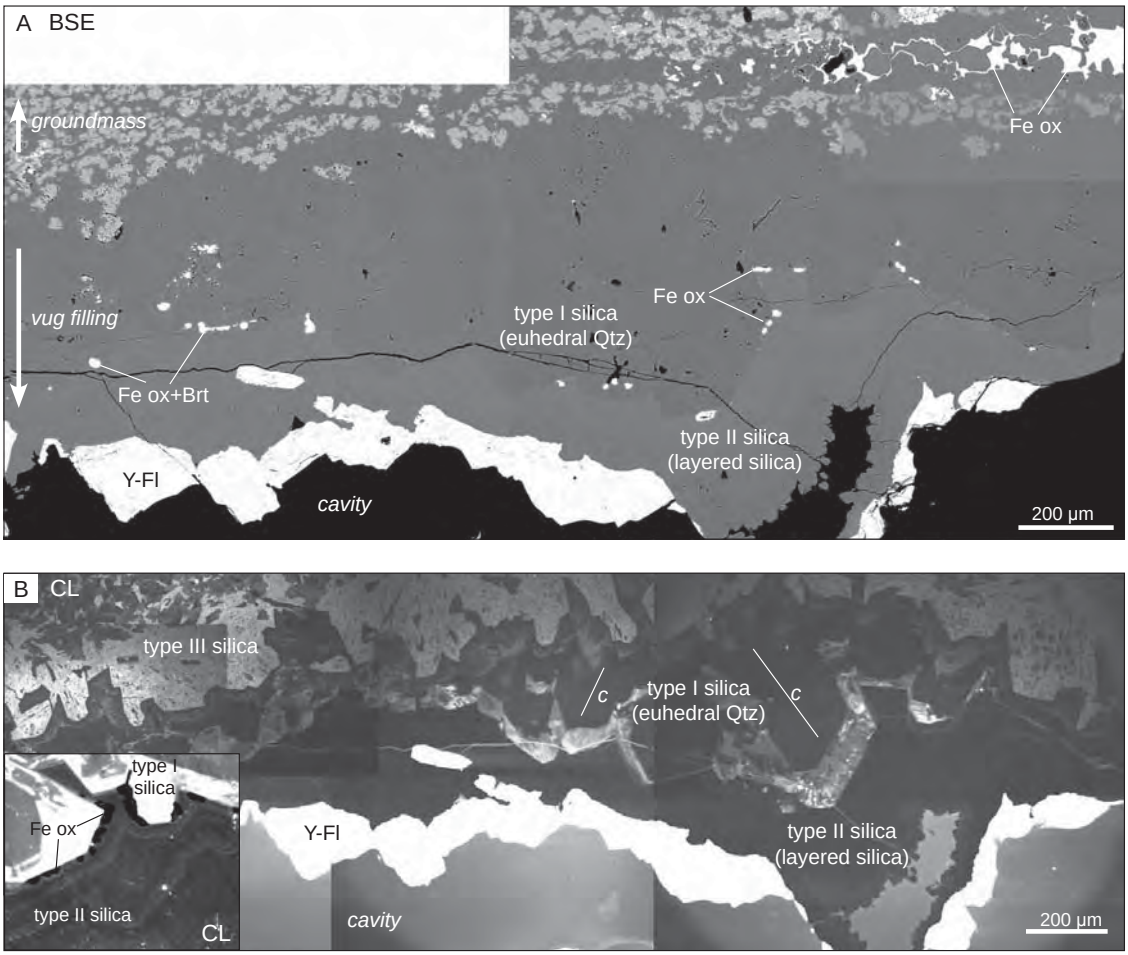

Fig. 6.5. Lithophysal vug-filling assemblage. Euhedral quartz is overgrown by thinly layerd silica (inset). Fine grained Fe oxide and Sr-barite aggregates are located between the two types of silica (A and inset). CL-zoned euhedral quartz (*c* axis of quartz is indicated) is mantled by CL-dark layered silica (B and inset). Fluorite overgrows type II silica. Sample GH68, BSE (A) and CL (B). Abbreviations: Brt: barite.

±titanite;

2) 100-µm-thick, quartz, albite, K-feldspar (feldspars <20-30%) zone;

3) 200-300-µm-thick, albite-rich zone;

4) outer zone relatively rich in quartz, K-feldspar, Fe oxide and Ti oxide.

Laser ablation traverses were carried out across the vesicles and into the groundmass (Fig. 6.6 A). A comparison of peaks in LA-ICP-MS traverses gives qualitative information on the trace element content of mineral phases. In both vesicles and groundmass, peaks in trace elements (REE, Y, U, Th, Nb, Zr, W and Pb) commonly occur together with peaks in Ti and Ca (related to titanite), whereas P (phosphates) appears to be less correlated. However, the largest peaks in REE, ±Y ±U, are related to the presence of fine grained REE-fluoro-carbonate. Lead, despite some correlation with Ti-Ca peaks (titanite), is less sensitive to variations in other elements and is mainly concentrated within the vesicles, irrespective of the mineral phase.

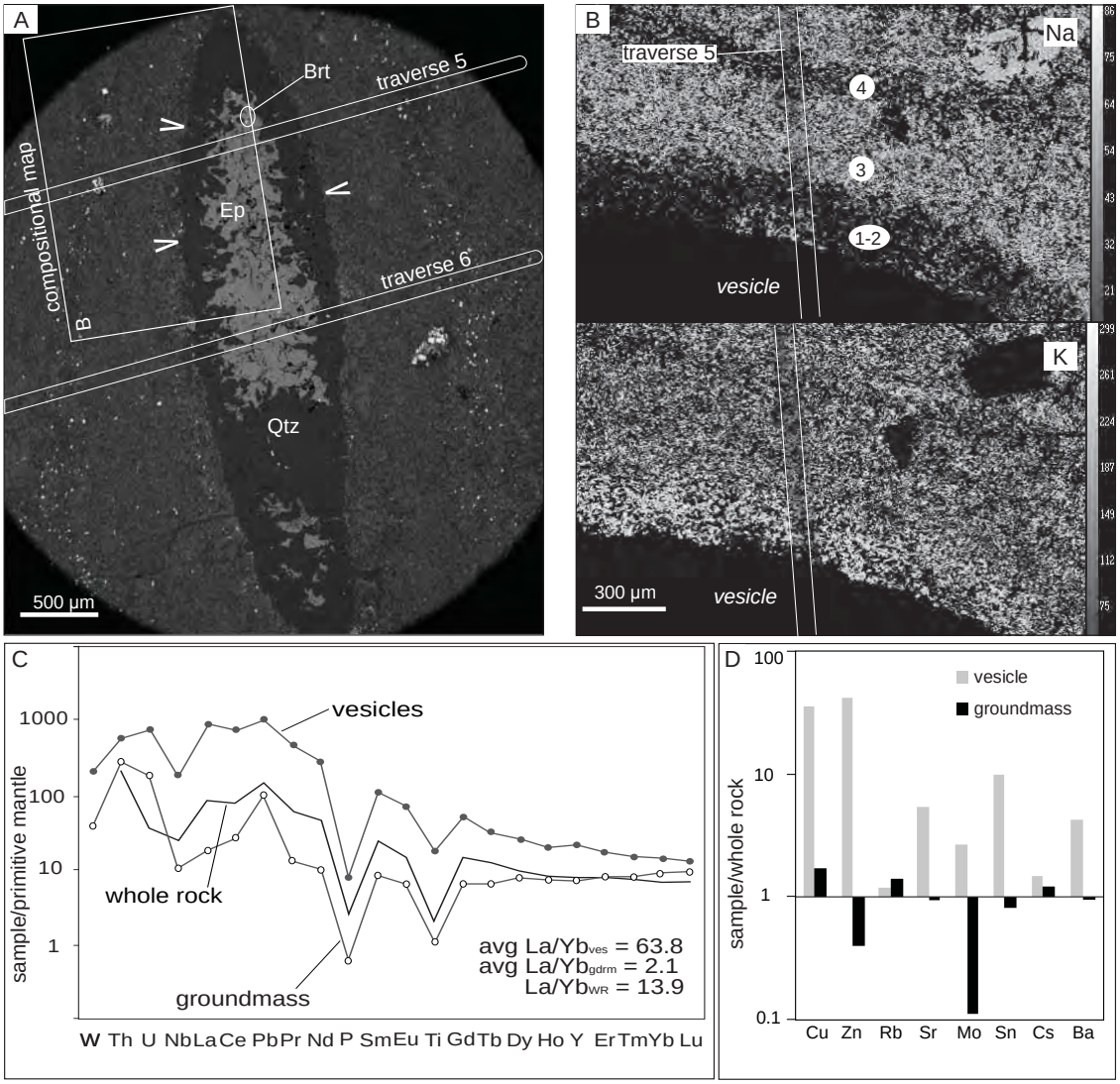

Fig. 6.6. Major and trace element distribution around vesicles and between the vesicles and the groundmass in the Rhyolite-dacite Mi2. A. Position of LA-ICP-MS traverses (BSE image, vesicle walls arrowed). B. Major elements (Na and K) zones around a vesicle (zones are indicated, see section 5 for details). C. Primitive mantle-normalised trace element concentrations in the vesicle fills, groundmass (LA-ICP-MS average values, sample GH35) and whole rock (ICP-MS, non-vesicular sample GH34) show generally similar patterns, distinguished by a different La/Yb ratio. D. Whole rock (GH34)-normalised LILE and base metals. Normalising values after Sun and McDonough (1989).

Vesicles are enriched in all the analysed trace elements, including REE (especially LREE and MREE), HFSE and transition elements (Cu, Zn, Mo, W), as well as Ca and Fe, compared to both the surrounding groundmass and whole rock (Fig. 6.6 C, D). The highest degrees of enrichment between vesicles and groundmass were measured for Pb, Zn, Cu and LREE. Primitive mantle-normalised diagrams show generally similar patterns for vesicle filling and groundmass, with LREE enriched in comparison with HREE and negative peaks for P and Ti. However, the vesicles exhibit a more fractionated trend (average La/Yb groundmass < average La/Yb vesicle; Fig. 6.6 C).

Concentric zones of minerals in the groundmass around vesicles are confirmed by major element (Si, Al, Ti, Fe) variations in LA-ICP-MS profiles. However, although a symmetrical decrease of trace element concentrations towards the vesicles was locally found, there seems to be no systematic distribution according to concentric zones.

6.7.Discussion

6.7.1.The role of accessory minerals in the fractionation of trace elements

Accessory minerals (fluorite, zircon, REE-fluoro-carbonate, Ti oxide, titanite and, to a lesser extent, apatite, monazite and allanite) are the main trace element-bearing phases. Some of these crystallised early (they occur as inclusions in major minerals) and played a role in the fractionation of trace elements in the melt. The evolution trends shown by trace elements are in agreement with the modal mineralogy and the observed textures. The sharp decrease of P and Zr, occurring between 60-65 wt.% silica and above 70 wt.% silica, respectively, reflects the crystallisation of apatite and zircon and their inclusion relationship. Crystallisation of zircon, apatite and minor monazite may have also partially reduced the concentration of REE in the melt, and are consistent with the weakly decreasing trends observed (Fig. 6.2). Continuously increasing trends shown by other trace elements (e.g. Nb, Th, Ta) indicate that these elements behaved as incompatible in the magma.

6.7.2.Late-stage crystallisation of accessory minerals

The fact that trace element-bearing accessory minerals mostly occupy interstitial positions in the groundmass, infill cavities and occur in spaces between major phases (Fig. 6.3, 6.4, 6.5), implies a late crystallisation (Fig. 6.7). As mentioned, zircon and apatite occur as both early-formed inclusions in the major minerals, and as late-formed crystals in micromiaroles (Fig. 6.4 B). Other accessory phases (anatase, titanite, fluorite, REE-F-carbonate, allanite and barite) only occur in vesicles, micromiaroles and lithophysae (Fig. 6.3, 6.4, 6.5) or in an interstitial position in the groundmass, implying a late origin (Fig. 6.7).

REE-fluoro-carbonate (synchysite-(Ce)?) is the main trace element-bearing phase, having high concentrations of REE, Y, U, ±Th. Total REE in REE-F-carbonate are three orders of magnitude higher than the whole rock content (semi-quantitative electron microprobe analysis). Normalised values show a light REE-enriched composition. Given such high concentrations, less than 0.1 wt.% of this mineral could be responsible for the whole rock REE content.

The formation of REE-fluoro-carbonates in felsic igneous rocks has been interpreted as a result of: (1) post-magmatic high-temperature alteration of accessory phases such as allanite, monazite, apatite and zircon, and remobilisation of REE by means of F- and CO_2-rich fluids (Bea, 1996; Förster, 2001). (2) Crystallisation from a vapour, as suggested by Gilbert and Williams-Jones (2008), who reported the presence of REE-F-carbonate in fumarolic encrustations in a carbonatitic lava of Lengai volcano, Tanzania. (3) Crystallisation from silicate magma. Chabiron et al. (2001) reported the presence of

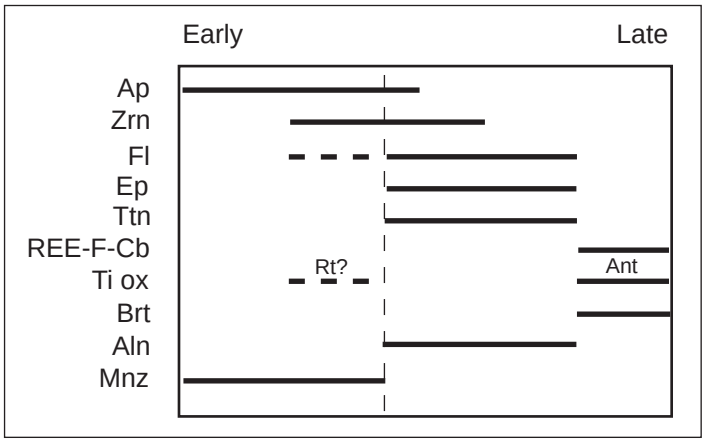

Fig. 6.7. Crystallisation sequence for the accessory minerals in the LGRV. Apatite and zircon are common in the groundmass of most samples and also occur in the micromiarolitic cavities. Fluorite occurs in interstitial position in the groundmass, and in vesicles, micromiarolitic cavities and lithophysae. Epidote occurs in vesicles and in interstitial aggregates in the groundmass of the Microgranite dyke, in association with allanite. Titanite is present in the vesicles in the Rhyolite-dacite Mi2. REE-F-carbonate is common in micromiaroles and vesicles, and as late-formed crystals in the groundmass. Ti oxide in the form of anatase occurs in the micromiaroles as a late-crystallising phase overgrowing fluorite. Ti oxide (rutile?) also occurs in the groundmass of all the units. Barite occurs in minor amounts in the vesicles and in the lithopysae. Monazite occurs in minor amounts as inclusions in the major phases of the Microgranite dykes.

parisite ($Ca(Ce,La)_2F_2(CO_3)_2$) as daughter crystals in melt inclusions from the rhyolites of the Streltsovka caldera (Russia).

In the rocks described here, none of these hypotheses seems applicable. Firstly, there is no evidence of alteration of magmatic accessory minerals. Therefore, an origin of REE-F-carbonate by alteration of magmatic accessory phases and remobilisation of trace elements is not likely. Secondly, a fumarolic (subaerial) environment described by Gilbert and Williams-Jones (2008) does not fit the described samples. Furthermore, a magmatic origin is not supported by textures. Instead, the hypothesis of direct crystallisation from a late-stage magmatic fluid is preferred.

6.7.3.Characteristics of the late-stage fluid

Because no fluid inclusions were found in the accessory minerals in the studied samples, direct evidence of the phase from which these minerals were deposited is not preserved. However, inferences on its physico-chemical characteristics can be made on the basis of textures and compositions of the minerals present:

1) Volatile-rich composition, as indicated by the widespread occurrence of F-bearing minerals (fluorite, REE-F-carbonate, F-apatite), CO_2-bearing minerals (carbonate), hydrous minerals (epidote), and the local presence of phosphates (apatite), and sulfate (barite).

2) Capacity to transport lithophile, “immobile” elements (REE, Y and HFSE), indicated by the presence of accessory minerals containing these elements.

3) Low viscosity. A growth from a low-viscosity phase is indicated by textures described above (Fig. 6.3, 6.4, 6.5), with minerals growing in cavities proceeding from the walls inwards (euhedral crystals of quartz, layered silica, fluorite, Ti-oxide and titanite).

The role of halogens (F and Cl) as complexing agents for REE, Y and HFSE has

been mentioned earlier (e.g. Keppler and Wyllie, 1990; 1991; Webster et al., 1989; Charoy and Raimbault, 1994; Gieré, 1986; Audétat et al., 2000; Webster et al., 2004; Schönenberger et al., 2008; Pan and Fleet, 1996). A mobility of these elements is shown by both experimental studies and evidence from natural systems. Hydrothermal systems enriched in these elements occur in different geological environments and the enrichment can reach ore grades (e.g. Metz et al., 1985; Gieré, 1986; Gieré and Williams, 1992; Oreskes and Einaudi, 1990; Monecke et al., 2002; Rubatto and Hermann, 2003). Thermodynamic calculations (Wood, 1990a, b; Lee and Byrne, 1992) and experimental work (Webster et al., 1989; Bau, 1991; Bau and Möller, 1992; Haas et al., 1995) show that complexation of trace elements with ligands such as F^- and Cl^-, but also OH^-, CO_3^{2-}, PO_4^{3-}, and SO_4^{2-} can significantly increase the solubility of these elements and is potentially important in natural systems. The stability of the complexes formed by these ligands with trace elements increases with temperature (Haas et al., 1995; Migdisov et al., 2009).

Fluorine was found to form complexes with REE, U and Th, whereas it appears to have little or no influence on Cu and Sn (Keppler and Wyllie, 1990; 1991). Wendlant and Harrison (1979) found that REE partition significantly in favour of a CO_2 vapour in equilibrium with a silicate liquid, and that the distribution coefficients are several orders of magnitude higher than for the silicate melt-H_2O vapour equilibrium (Mysen, 1979). Experimental work by Keppler and Wyllie (1991) indicates that CO_2 and Cl form complexes with U, but not with Th. Copper and tin are essentially non soluble in pure water, even at high temperature (750°C), and their fluid/melt distribution is enhanced by Cl, but not by F (Keppler and Wyllie, 1991). Solubility of Mo and W, on the contrary, is pH-sensitive. These elements (W and Mo) are more soluble in H_2O fluids, and become less soluble if HF and HCl are added, as a consequence of the decrease in pH of the fluid (Keppler and Wyllie, 1991). In nature, a high and variable degree of enrichment in REE and HFSE (Th, U, Nb), other than Sr, F and P, of carbonatitic melts and other CO2-rich melts is well known (Lentz, 1999). Furthermore, Pili et al. (2002) showed evidence for a mobility of trace elements (including REE, Ta, Nb and Y) during brittle deformation of carbonates, thus proving that CO_2-H_2O fluids can mobilise these elements, even at low temperatures. Fluorine and CO_2 have been invoked as complexing agents in the formation of REE-U-Th-rich deposits (e.g. Oreskes and Einaudi, 1990; McLennan and Taylor, 1979; Simpson, 1979), consistently with fluorite-carbonate mineralisation commonly found in these deposits.

Because of the semi-volatile nature of fluorine, unlike water and CO_2, the F-rich composition is another characteristic of this fluid that should be discussed. Fluorine is highly soluble in silicate liquids and is generally incompatible with most minerals and the fluid phase (Dolejš and Baker, 2007a). A fluid-silicate melt distribution coefficient DF (Ffluid/Fmelt) of 0.1-0.4 has been measured for moderately high F concentrations (F~1 wt.%, London et al., 1988). However, the distribution coefficient depends on F abundance: high concentrations (≥7-8 wt.% F in the melt) will result in DF > 1 and in F preferentially partitioning into the fluid phase (Carroll and Webster, 1994; Webster, 1990). Such high concentrations are not common in nature. Values of F = 2.9 wt.%, (Audétat et al., 2000), 3.2 wt.% (Chabiron et al., 2001), 5 wt.% (Webster et al., 2004), 6.4 wt.% (Thomas et al., 2005) have been measured in melt inclusions and high whole rock F values (1.6 wt.%) were reported in highly evolved topaz-bearing rhyolite (ongonite, Štemprok,

1991). In the lower GRV, we measured F ≤1.3 w.t% in melt inclusions (unpublished data). However, considering the high F-Ca ratios in melt inclusions (F/CaO (wt.%) ≤ 1.8), it becomes apparent that F content in some units cannot be accommodated by the observed paragenesis (F-apatite, fluorite and fluoro-carbonates), even if crystallisation of fluorite (F/CaO = 0.68) from the magma is admitted. Therefore, protracted crystallisation would lead to high concentrations of F in the last fractions of residual melt. Such "excess F", unbuffered by crystallising phases, could have eventually exsolved in a F-rich fluid phase upon volatile saturation. Significant enrichments in F were as also reported in experiments on F-bearing haplogranitic systems (Dolejš and Baker, 2007b).

6.7.4.Origin of the fluid

Whole rock analyses indicate a moderate-high concentration of REE and HFSE in the magma and increasing trends with progressing fractionation (increasing Si). Therefore, the magma itself is the most obvious source of REE and HFSE. Further, high concentrations of F in quartz-hosted melt inclusions (F ≤1.3 wt.%, Cl ≤0.2 wt.%; unpublished data) provide a likely origin for F.

However, an outstanding question is whether the fluid had a magmatic (or primary) origin or a much later, secondary origin. In the second hypothesis, a hot hydrothermal fluid, unrelated to the magma, could have leached the trace elements from the host rocks. We favour a magmatic origin, based on geochemical and micro-structural evidence. A first criterion to distinguish between these two hypotheses is geochemical. Primitive mantle-normalised trace element plots show close similarities between vesicle fillings, groundmass around vesicles and non-vesicular whole rock composition (Fig. 6.6 C). The main difference lies in the steepness of the normalised trends, with patterns for the vesicle-filling minerals and the surrounding groundmass distributed symmetrically with respect to the non-vesicular samples (Fig. 6.6 C).

The increase in La/Yb ratio of vesicles can be explained by the fractionation of modal minerals (quartz, feldspar, Fe-Ti oxide, zircon and apatite) and the preference of feldspar and zircon for HREE over LREE (e.g. Hinton and Hupton, 1991). A slightly higher Rb concentration and lower Sr and Ba in the groundmass (Fig. 6.6 D) is also consistent with fractionation of alkali-feldspar in the groundmass. A second criterion to distinguish between a magmatic or a secondary origin of the fluid is based on micro-structural evidence. A secondary fluid would either flow along cracks, depositing veins, or diffuse pervasively the rock. As shown, no evidence of a hydrothermal system or veins at any scale, and no significant alteration were found in the rocks, apart from a moderate sericitisation of feldspar. Furthermore, as mentioned, alteration of magmatic accessory phases would be needed to remobilise REE and HFSE (e.g. Förster, 2001), but this was not found.

6.7.5.Formation of vesicles

We propose a three-stage model for the formation of the vesicles that can also be applied to micromiaroles and lithophysae. This model is based on the following considerations: 1. Vesicle fillings and groundmass show similar trace element patterns,

pointing to a common origin. Differences include a higher La/Yb ratio, (Fig. 6.6 C) in the vesicles, compatible with the crystallisation of modal minerals in the groundmass and the formation of a highly fractionated residual melt. 2. The vesicles are not interconnected by veinlets or visible cracks, so that a late (secondary) ingress of fluid seems unlikely. 3. The concentric zoning of major elements, but not trace elements, in the groundmass around the vesicles (Fig. 6.3 D) suggests a contemporaneous formation of the zoning and the vesicles. We hypothesise that, during the formation of vesicles, a chemical zonation was created in the melt by a boundary layer effect (selective uptake of elements by the exsolving phase). During subsequent rapid crystallisation, this zonation was translated into an uneven mineral distribution (Fig. 6.3 D, 6.6 B), as crystals of quartz, feldspar and oxides formed according to the local availability of elements. Trace elements, incompatible with respect to the crystallising phases, were concentrated in the interstitial residual liquid. 4. Zonation of minerals within vesicles (Fig. 6.3) indicates that quartz crystallised first and then the other minerals at the centre.

The first stage of the model is the exsolution of a fluid from the silicate liquid resulting in the formation of vesicles (Fig. 6.8-I). Quartz adjacent to the vesicle walls may have crystallised from this fluid. In a second stage, crystallisation of major minerals in the groundmass around the vesicles forms a residual liquid containing high concentrations of volatile and trace elements. A fluid phase exsolves from such an “enriched” residual melt (Fig. 6.8-II). Alternatively, a very evolved and volatile-rich residual melt could meet the required characteristics (e.g. Keppler and Willey, 1991). This fluid moves through a framework of fine grained quartz and feldspars in an already mostly crystallised rock and concentrates within the vesicles previously formed (open system behaviour of the vesicles). The core assemblage of minerals, rich in F, REE, Y and HFSE, crystallises from such a fluid (Fig. 6.8-III).

Smith (1967), Bloomer (1994) and De Hoog and van Bergen (2000) reported the presence of vesicle fillings and veins enriched in incompatible trace elements in volcanic rocks from different environments. They interpreted these aggregates, termed segregations by Smith (1967), to have crystallised from a residual liquid. According to the mechanism proposed by Smith (1967) and adopted by Bloomer (1994), a residual liquid was mobilised and injected into the vesicles by fluid overpressure developed during crystallisation of the groundmass.

6.7.6.Implications on the transport of REE, Y and HFSE in the late magmatic stage

We have shown that the GRV magmas produced volatile-rich, F-bearing phase at a late stage of evolution. A distinctive assemblage of REE-, HFSE- and F-bearing minerals (including REE-F-carbonate, REE phosphates and fluorite) crystallised from this phase where it filled vesicles, micromiaroles and lithophysal vugs. A similar mineral association and the same high REE and F abundances are characteristic of the U-bearing iron oxide copper-gold deposits in the Olympic Dam province, which is hosted in associated rocks of the Hiltaba Suite Granite (Oreskes and Einaudi, 1990; Skirrow et al., 2007). This similarity could imply a genetic link, largely overlooked in the literature, between GRV-HS magmas and the mineralising hydrothermal system at Olympic Dam.

6.8.Conclusions

Accessory mineral assemblages contained in micromiaroles, vesicles and lithophysal vugs or occupying interstitial positions in the GRV include significant amounts of REE (lanthanides, U, Th), Y, HFSE (Ti, Zr, Nb) and transition metals (Cu, Zn, Mo, W). These elements are mainly concentrated in REE-fluoro-carbonate, zircon, niobian Ti oxide, fluorite, titanite and, to a lesser extent, apatite and allanite. Textures and mineral associations indicate that these accessory minerals formed at a late-magmatic stage, rather than in super-solidus conditions and that they crystallised from a volatile (F, H_2O, CO_2, ±P, ±S)-rich low-viscosity (fluid) phase. It is inferred that fluorine played the dual role of promoting incompatible behaviour and concentration of lithophile trace elements in the residual magmatic liquid and, together with other complexing agents (CO_2, OH^-, P), allowing the transport of the same “immobile” elements in a fluid in the late magmatic stage.

Experimental data (London et al., 1988; Webster, 1990; Keppler and Willey, 1991) and melt inclusion studies in pegmatites (Thomas et al., 2000; 2009) have shown that silicate melts can contain very high amounts of water. Such a high solubility of silicate and volatile component allows the existence of fluid phases with intermediate properties between an aqueous fluid and a silicate melt in terms of both composition and physical characteristics. The presence of REE- and HFSE-bearing minerals (e.g. zircon, xenotime, fluorite, fluoro-carbonate) described by Thomas et al. (2009) in pegmatites, implies that this kind of fluids are able to transport significant amounts of lithophile elements. Such a volatile- and silicate-rich fluid phase could account for the textural, mineralogical and compositional data described here.

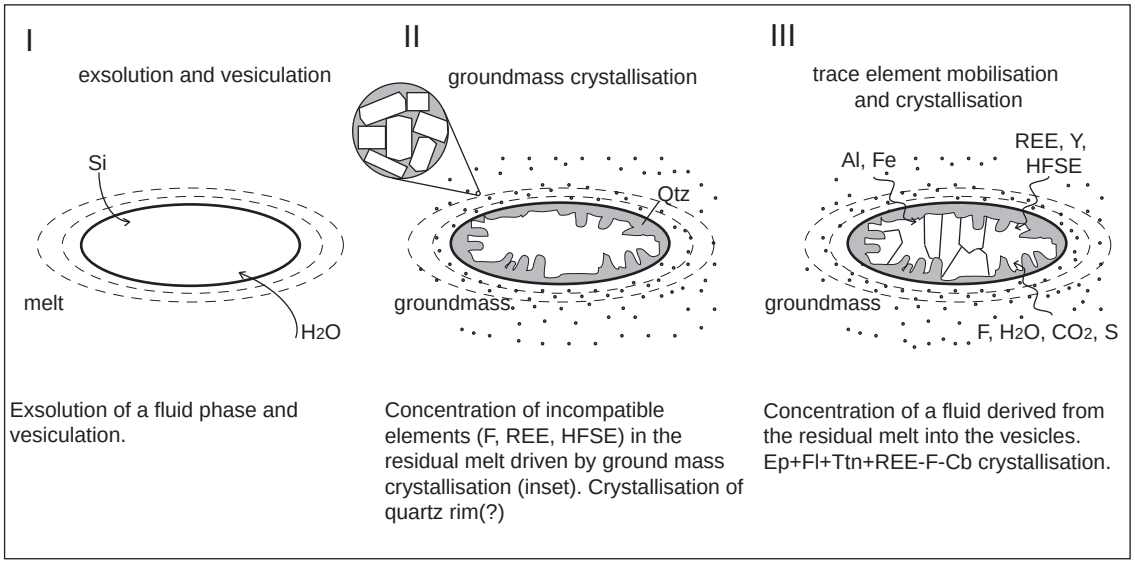

Fig. 6.8. A model for the formation of vesicles and vesicle-filling mineral assemblages in the Rhyolite-dacite (Mi2), Kokatha.

CHAPTER 7

Summary and conclusions

7.1 Volcanology of the Gawler SLIP

The lower Gawler Range Volcanics (GRV) include several small to moderate volume (up to >100 km^3) and moderately extensive (up to several hundreds of km^2) felsic units. The Glyde Hill and the Chitanilga Volcanic Complexes are the best exposed sequences in the lower GRV.

The Glyde Hill Volcanic Complex includes a 1-km-thick sequence of mostly felsic (dacite and rhyolite) units. Felsic ignimbrites and intermediate-mafic lavas are areally and volumetrically subordinate. Some of the felsic lavas were probably emplaced as multiple flows erupted from point or linear sources, and are interpreted to lie near their vents. The succession dips gently towards the centre of the outcrop area.

The Chitanilga Volcanic Complex is 3-km-thick and includes a thick (~1 km) but localised pile of mafic lavas interbedded with minor felsic ignimbrites, followed by localised to extensive (up to several tens of km across) felsic lavas and ignimbrites. The sequence dips southeast at a moderate angle (~30°), partly due to tilting. Lavas are interpreted to lie near their vents, whereas location of sources of the ignimbrites remains uncertain.

Mineral assemblages in intermediate to felsic units include phenocrysts of feldspar, and locally quartz and ±altered clinopyroxene in a quartzo-feldspathic groundmass. Mafic lavas include phenocrysts of clinopyroxene and local altered olivine in a feldspar-clinopyroxene groundmass. Textures are homogeneous across units, with local variations associated with enclaves and xenocrysts, mostly occurring in andesites.

Several of the felsic units in the Glyde Hill and Chitanilga Volcanic Complex have been previously interpreted as ashflow tuffs (Giles, 1977; Blissett, 1993). Evidence of an explosive eruption mechanism is very clear in some of these units, such as in the case of the bubble-wall shard-rich matrix of the Lake Gairdner Rhyolite, which justifies interpretation as an ignimbrite. However, other extensive felsic units have combinations of characteristics such as evenly porphyritic texture, lack or absence of lithic fragments and fragmented crystals, and the presence of flow-folded flow bands and autobreccia domains. These characteristics suggest effusive or mildly explosive (lava fountain) eruption mechanism and long-distance lava-like emplacement mechanism (viscous flow) for several of these units.

Other volcanic complexes in the lower GRV include: 1) the hydroexplosive rhyolitic centre of Menninnie Dam in the southern GRV (Roach et al., 2000), 2) the Tarcoola-Kingoonya succession, which includes ignimbrite and minor basalt lava (Creaser et al., 1993), and 3) the Myall Creek succession, mostly composed of felsic lava and ignimbrite (Daly, 1985; Blissett et al., 1993; Allen et al., 2008).

As a whole, the lower GRV are characterised by a volumetrical predominance of felsic lavas in comparison with ignimbrite (lavas represent more than 90% of the erupted volume). However, ignimbrite can be conspicuous or even predominant in single volcanic complexes: for instance, ~45 vol.% of the felsic units in the Chitanilga Volcanic Complex (Table 3.2) and most of the rhyolitic centre at Menninnie dam are composed of ignimbrite.

The upper GRV are composed of flat-lying to gently north-dipping, thick and extensive (up to a few hundred km across) felsic lavas with a combined volume exceeding 4000 km^3 and very minor ignimbrite (Allen and McPhie, 2002; Allen et al, 2008). Mineral assemblages are essentially anhydrous and include phenocrysts of plagioclase, K-feldspar, pyroxene and locally quartz in a fine grained quartz-feldspar groundmass.

Based on the available U-Pb zircon dating (Fanning et al., 1988), the GRV were emplaced over a short time span of ~2 Ma. Thus, if the volume of 25000 km^3 is assumed, the average emplacement rate must have been approximately 0.0125 km^3/a (Table 7.1). This intense eruption activity compares with average extrusion rates of 0.001 km3/a (peak 0.012 km^3/a) of the subduction-related flare-up magmatism of the Altiplano-Puna volcanic complex, central Andes (De Silva and Gosnold, 2007), and 0.010 km3/a of the Paraná volcanic province, according to recent geochronological data (Pinto et al., 2011). Other SLIP have been emplaced over wider time periods, although most of their activity occurred in short-lived pulses separated by periods of minor activity. For example, the Chon-Aike province of Patagonia and Antarctic Peninsula was emplaced in three main pulses (V1 to V3) of ≤10 Ma each, which collectively cover 30-40 Ma (average emplacement rate 0.007 km^3/a, Pankhurst et al., 2000), the Sierra Madre occidental

Table 7.1. Volume and emplacement rate of some large felsic volcanic provinces

Province	Primary emplacement mechanism	Phenocrysts	Volume (km3)	Age (Ma)	Time span (Ma)	Extrusion rate (km3 / year)	Reference
GRV	lava	anhydrous mineralogy	25000	1591–1592	2	0.0125	Blissett et al., 1993; Fanning, 1988
Paraná-Etendeka province (silicic component)	lava	anhydrous mineralogy	20000	135–134	2	0.010	Ewart et al., 1998; Pinto et al., 2011
Southern Rocky Mountain volcanic field	ignimbrite		15000	37–22	15	0.0010 (peak 0.008)	Lipman, 2007
Whitsunday	ignimbrite	hydrous mineralogy	2200000	132–95	37	0.0595	Bryan et al., 2000
Chon-Aike, Patagonia and Anctartic Peninsula	ignimbrite	hydrous mineralogy	230000	188–153	35	0.0066	Pankhurst et al., 1998; 2000
Sierra Madre Occidental, Mexico	ignimbrite	hydrous mineralogy	390000	38–20	18	0.0217	Ferrari et al., 2000; Bryan et al., 2008
Taupo Volcanic Zone	ignimbrite		20000	1.6–0	1.6	0.0125	Wilson et al., 1995
Yellowstone-Snake River Plain (silicic component)	lava, ignimbrite	anhydrous mineralogy	x10000	16–0	16		Branney et al., 2008; Bonnichsen et al., 2008

(3.9·105 km^3) had two main pulses over a total 18 Ma time period (Ferrari et al., 2000).

The GRV represent an end-member in a spectrum of felsic large volcanic provinces ranging between lava-dominated and ignimbrite-dominated provinces. Anther example of felsic lava-dominated provinces is the felsic component of the Paraná-Etendeka (Ewart et al., 1998b), whereas the Whitsunday province is an example of ignimbrite-dominated SLIP (Bryan, 2000). The Snake River Plain and Keweenawan volcanics include both lavas and ignimbrites, and the ignimbrites tend to be strongly rheomorphic (Branney et al., 2008; Bonnichsen et al., 2008). [The lava-dominated end-member provinces tend to have anhydrous parageneses and high magmatic temperatures, whereas the ignimbrite-dominated provinces contain hydrous mineral phases (amphibole and biotite) and are mostly lower-temperature.]

7.2 Chemical characteristics of the Gawler SLIP

7.2.1 Summary of geochemistry

The GRV and HS are a silicic-dominated SLIP characterised by high K_2O, REE (except Eu), Y, HFSE, Ga/Al and K/Na, and moderate to high Fe#, and by low CaO, Sr, Ba, Ni, and Cr. In primitive mantle-normalised plots, strong negative anomalies of Sr, Ba and Eu are shown in rhyolites. The GRV are metaluminous to peraluminous (chapter 4, Table 7.2), and alkali-calcic to calc-alkalic (Peacock, 1931; Frost et al., 2001).

Quartz-hosted melt inclusions from the lower GRV (this study) and upper GRV (Bath, 2005) have generally similar compositions to the rhyolites, but have lower contents of compatible elements (Sr, Ba, Eu, and Ti), and locally higher incompatible elements (Th, Nb, and Rb). Melt inclusions have high concentrations of F (up to 1.3 wt.%), moderate Cl (up to 0.4 wt.%) and low S and P (<a few hundreds ppm). Water contents calculated by difference method (Devine et al., 1995) is low for felsic magmas (average ~1-3 wt.% in homogenised inclusions). The water-poor magma composition is also indicated by the mostly anhydrous phenocryst parageneses (feldspar, ±quartz, ±clinopyroxene, Fe-Ti oxide, apatite in intermediate to felsic rocks). Good correlation between Cl – a highly volatile element (Carroll and Webster, 1994) – and incompatible elements (e.g. Pb, U, Th) in melt inclusions is compatible with volatile-undersaturation of the magma.

Comparison of whole-rock and melt inclusion data indicates that, despite weak to moderate alteration of feldspar and pyroxene, major elements have only partially been modified in whole-rock compositions (Na in particular). Mobility of some trace elements (Pb, U, and Sn) is suggested by erratic distributions and variable depletion of whole-rock analyses in comparison with melt inclusions.

Fluorine and F/Cl of the melt are typically high (F ≤1.3 wt.%, Cl ≤0.2-0.4 wt.%), and inferred water content is low, as suggested by high melt inclusion microprobe totals and anhydrous parageneses. Feldspar crystallised between hyper- and sub-solvus conditions, originating either one alkali-feldspar or two-feldspar assemblages.

The passage between the lower and upper GRV is marked by an increase of REE and HFSE (Th, Zr, Hf) content, and Fe# (Table 7.1). Plots of Ga/Al, HFSE, and Fe# indicate that the long-term compositional evolution of the GRV marked an evolution from

Table 7.2. Main chemical and petrographic characteristics of the GRV and HS at Kokatha

	Lower GRV	Upper GRV	Hiltaba Suite (Kokatha)
Paragenesis	feld ±Qtz ±Cpx +Zrn +Fe-Ti ox +Ap	feld ±Cpx ±Qtz +Zrn +Fe-Ti ox +Ap (5)	feld +Qtz +Fe-Ti ox +Ap +Fl +Zrn +Bt (8)
ASI	metaluminous to peraluminous (increasing with increasing SiO2)	metaluminous to peraluminous (increasing with increasing SiO2) (1, 2, 3)	metaluminous to peraluminous (3)
FeO#	magnesian to ferroan (Frost et al., 2001)	ferroan (Frost et al., 2001) (1, 2, 3)	magnesian to ferroan (Frost et al., 2001) (3)
K2O	high- to ultra-K, K/Na >1	high- to ultra-K, K/Na >1 (1, 2, 3)	high- to ultra-K, K/Na >1 (3)
Tot Alkali	silica-undersaturated to saturated (TAS, Le Bas et al., 1986)	silica-undersaturated to saturated (TAS, Le Bas et al., 1986) (1, 2, 3)	silica-undersaturated to saturated (TAS, Le Bas et al., 1986) (3)
Alkali versus CaO	Calc-alkalic to alkali-calcic (Peacock, 1931)		
REE and HFSE	moderate	high (WPG of Pearce, 1984; A-type of Whalen et al., 1987) (1, 2, 3)	high (WPG of Pearce, 1984; A-type of Whalen et al., 1987) (3)
Other trace elements (primitive mantle-normalised)	Sr, Ba, Ti, P, ±Eu, Nb, Ta negative spikes; Th, ±Pb, ±Sn positive spikes	Sr, Ba, Ti, P, ±Eu, Nb, Ta negative spikes, Pb positive spikes (1, 2, 3)	Sr, Ba, Ti, P, ±Eu, Nb, Ta negative spikes
Volatile components	high F (≤1.3 wt%), moderate Cl (≤0.2 wt%), low H2O (≤2 wt% by difference)	high F (≤1.3 wt%), moderate Cl (≤0.4 wt%), low H2O (≤2 wt% by difference and paragenesis) (6, 7)	
Temperature	≤950°C (Zrn saturation)	≤1050°C (Zrn saturation)	≤°C (Zrn saturation)
		900-1100°C (two pyroxene) (7)	
Emplacement mechanism	felsic (+mafic) lavas, felsic ignimbrites	felsic lavas	

References: (1) Giles, 1988; (2) Stewart, 1994; (3) PIRSA, unpublished dataset; (4) Giles, 1988; (5) Blissett, 1993; (6) Bath, 2005; (7) Creaser and White, 1991; (8) Flint, 1993

transitional to A-type.

7.2.2 Halogen content of magmas and implications on the geodynamic setting of the Gawler SLIP

Abundances of F and Cl of magmas vary significantly according to the tectonic environment. Arc magmas typically have low F/Cl, as shown by degassing volcanos and melt inclusion data (e.g. Aiuppa, 2009; Dunbar et al., 1989; Symonds et al., 1990; Wallace, 2005; Witter et al., 2005). This is believed to be the consequence of Cl introduced by recycling of subducted sediments and dehydration of the subducting slab into the mantle wedge (Aiuppa et al., 2009). Furthermore, arc magmas tend to have high water contents and high oxygen fugacity, both characteristics that do not fit the Gawler SLIP and other intracontinental, “A-type” magmas.

Conversely, magmas produced in extensional and continental settings are known to be water-poor, high in F/Cl and low in oxygen fugacity (Aiuppa et al., 2009). For example, high F/Cl ratios are typical of the Proterozoic rapakivi granites of Finland and

Cenozoic topaz rhyolites of the US (e.g. Christiansen et al., 2007). Ratios of F/Cl >1 have been measured in continental peralkaline rhyolites (Bailey, 1980), F/Cl >3 have been measured in topaz rhyolites (Christiansen et al., 1983), and F/Cl ≥10 have been measured in tin- and topaz-rhyolites and tin-granites (Webster et al., 2004).

Hypotheses for the high halogen contents and high F/Cl ratios in these rocks may involve source rock characteristics, magma fractionation, degassing during eruption, or a combination of these.

In the Gawler SLIP, melt inclusions indicate that high halogens and high F/Cl are primary characteristics of the magma, and are not related to preferential devolatilisation of Cl during eruption/emplacement (e.g. Christiansen et al., 1986; Webster, 1992). Thus the hypothesis of a degassing-related depletion of Cl (hypothesis 1) can be discarded.

Concentrations of F and Cl of igneous rocks are also controlled by fractionation processes (e.g. Christiansen, 2007). Fluorine mostly behaves as an incompatible element during crystal fractionation, and tends to partition in the silicate melt during separation of a fluid phase (Carroll and Webster, 1994; Webster, 1990). Thus, F will concentrate in the melt with progressing crystallisation and, because of its high solubility in silicate melts (Dolejs and Baker, 2007), it can reach high abundances (e.g. tin- and topaz-rhyolites, and pegmatites; Webster and Duffield, 1994; Thomas et al., 2005). Chlorine is also incompatible with respect to most crystal phases, but has a preference for the fluid phase in equilibrium with the melt (e.g. Webster and Holloway, 1990). The highest values of Cl concentration (>1 wt.%) occur in intermediate to felsic alkaline rocks (e.g. Lowenstern, 1994), with the exception of the even higher values of kimberlites (Kamenetsky et al., 2007).

This fractionation-induced enrichment in halogens is also valid for the Gawler SLIP in general, as shown by melt inclusion data. In the Gawler SLIP magmas, Cl was more incompatible than F, as shown by correlations with other incompatible trace elements (cf. Cl vs Pb plot, Fig. 4.15). During fractionation, F content was partially buffered by crystallisation of F-apatite, ±fluorite, and possibly other F-bearing magmatic phases. Therefore increase of F/Cl cannot be a result of protracted fractionation. This requires that the magma in its less evolved stages of fractionation, and possibly the source rocks, had a high F/Cl ratio.

This introduces the problem of how a high-F and high-F/Cl source rock can be produced in the crust. Christiansen (2007) pointed out that, during the process of emplacement and crystallisation of magmas, F is preferentially retained by phosphates and silicates, whereas Cl is lost to a high extent in hydrothermal fluids. Further, preferential degassing of Cl over F is observed in modern volcanic systems (e.g. Nicotra et al., 2010), in agreement with higher distribution coefficient between gas phase and melt for Cl than that for F (e.g., Kilinc & Burnham, 1972; Webster & Holloway, 1988). Thus, even magmas with a low F/Cl may crystallise to form rocks with higher F/Cl ratio values. Remelting of these rocks can produce magmas with high F/Cl; and the halogen concentrations of these magmas could then be enhanced by crystallisation.

7.3 Emplacement mechanism of large felsic lavas

As a whole, the GRV were emplaced in two main stages of volcanic activity (Blissett, 1985; Blissett et al., 1993; Stewart, 1994). The first stage involved emplacement of several small to moderate volume units of variable chemical composition emplaced as non-fragmented flows (lavas and domes) or fragmented (pyroclastic flows). Overall, lavas predominate (>90 vol.%), but ignimbrites can be locally conspicuous. In the second stage, a limited number of large, phenocryst-rich, and chemically relatively homogeneous dacitic-rhyolitic units were emplaced as lavas and very minor ignimbrites.

Controls on eruption and emplacement mechanisms

Explanation for the emplacement of extensive lava units can be given by taking into account several parameters: temperature, dissolved volatiles, eruption rate, and bulk composition. High magmatic temperatures and high F contents would have reduced magma viscosity, whereas low inferred water contents would have caused low vesiculation, expansion and explosivity.

Further explanation for the vast extent of felsic lavas may be provided by vent geometry and areal distribution. For some units in both the lower and upper GRV, eruption from multiple point or line sources (fissures) has been proposed (Giles, 1977; Allen and McPhie, 2002). This would have favoured widespread flow, and seems likely, based on the elongate outcrop of some lava units (e.g. Rhyolite-dacite Mi2 in the Chitanilga Volcanic Complex and Wheepool Rhyolite in the Glyde Hill Volcanic Complex, Fig. 3.2 and 3.18). Positions of units in the lower GRV indicate that source vents were scattered over a vast area (several tens of km across).

It has been shown (chapter 4 and Table 7.1) that felsic rocks in the lower and upper GRV have very similar chemical characteristics in terms of major elements and volatile components. Therefore, different emplacement mechanisms observed (Table 7.1) cannot be explained by invoking the effect of bulk composition and dissolved volatile elements on magma viscosity. Instead, different magmatic temperatures and eruption rate may be responsible.

Application of the zircon saturation model (Watson and Harrison, 1983) on melt inclusion compositions in the lower GRV yields T ~ 850-950°C. Available melt inclusion data from the Eucarro Rhyolite in the upper GRV (Bath, 2005), indicates zircon-saturation T ~ 930-1050°C. It should be noted that zircon solubility in silicate melt is increased by the presence of dissolved F (Keppler, 1993). If this is the case, temperatures would be overestimates. Error in the overestimation would occur roughly to the same extent in the lower and upper GRV, given the similar F content. However, zircon saturation temperatures in the upper GRV are in broad agreement with previous temperature estimates for the Eucarro Rhyolite and Yardea Dacite based on two-pyroxene, pigeonite-augite equilibrium geothermometry and apatite saturation (T = 900-1100°C; Creaser and White, 1991; Stewart, 1994). Thus, magmas that formed the upper GRV were hotter than the lower GRV magma by ~100°C. A similar temperature difference can reduce viscosity of a rhyolite (SiO_2 = 76 wt.%) containing a moderate amount of water (H_2O = 3 wt.%) by approximately 3 orders of magnitude (Giordano et al., 2008), promoting effusive eruption and viscous flow.

The other difference between lower and upper GRV is the size of units. The largest units in the lower GRV are 100-200 km^3 in volume (Yantea Rhyolite-dacite, Lake Gairdner Rhyolite, and Wheepool Rhyolite, Tables 3.1 and 3.2); whereas all the three units forming the upper GRV exceed 1000 km^3 (Allen at al., 2008). All the units in the upper GRV are believed to be single flow units. Erupted volume and eruption rate are also considered to strongly affect the emplacement mechanism by favouring viscous flow and extending the length of lavas (Walker, 1973).

7.4 Nature of crustal magma storage and magma chamber dynamics

7.4.1 Magma chamber models

Modern models of felsic igneous systems agree on the fact that magma chambers are composed of largely solid crystal mush with interstitial melt (Bachmann and Bergantz, 2008). Large crustal intrusions are assembled incrementally, via successive injections of magma and do not exist as large volumes of molten rock at one time (Glazner et al., 2004). Geophysical studies and drilling campaigns (Detrick et al., 1990) have failed to identify large pools of molten rock underneath volcanic systems. In oceanic spreading zones, this has led to the notion that mid ocean rift volcanos do not have large, mostly liquid-state magma chambers, but rather diffused plumbing systems. Popular models for felsic intrusions propose a zoned structure with largely solid margins, an intermediate crystal mush, and a mostly melted core-top (Hildreth, 2004; Hildreth and Wilson, 2007). Boundaries between these zones shift inwards and outwards, or “wax and wane”, according to the thermal regime (Bachmann et al., 2002).

7.4.2 Dynamics and formation of a large felsic magma chamber

Succession of quartz zones (step zones) with different compositions and textures represent a “crystal stratigraphy” that records information on the crystallisation history of the GRV magma. Primary (syn-crystallisation) CL textures in quartz are better preserved in rapidly cooled volcanic units and dykes of the lower GRV than in slowly cooled granite samples. Preservation of sharp Ti profiles in volcanic units and dykes suggests short residence time of quartz crystals at high temperature: eruption (or shallow emplacement of dykes) occurred shortly (10^2-10^3 years) after quartz crystallisation (Chakraborty, 2008).

In the dykes, zones can be correlated among quartz phenocrysts. This homogeneity of quartz populations in single dykes is interpreted as evidence that all quartz crystals shared the same crystallisation history and probably crystallised largely after isolation of these small magma batches in intrusions.

In the volcanic units, multiple quartz populations coexist in the same sample. Each of these populations records a complex history of crystallisation and resorption events. The volcanic units tapped a larger part of the magma characterised by a dynamic regime, which resulted in juxtaposition of different quartz populations, each with different crystallisation histories. Geothermometric estimates based on Ti content of quartz zones suggest significant differences of quartz crystallisation temperatures (ΔT up to >100°C) between adjacent zones.

Alternating events of crystallisation and resorption (truncation of growth textures), reverse zoning (rimwards increase in Ti content) of quartz, and melting of already crystallised portions of the magma chamber (enclaves or igneous inclusions) are consistent with non-monotonous thermal evolution of the GRV-HS magma and suggest the occurrence of different thermal "pulses".

The described textural features can be explained by re-heating, reactivation, and convective stirring of the magma chamber (self-mixing; Couch et al., 2001). Heat input represented both the "engine" for convection and the cause of re-melting of previously crystallised magma, and was possibly supplied by underplating of mafic magma. Open-system processes, such as injection of basalt magma at the base of the magma chamber, are common in intermediate-felsic magmas (e.g. Murphy et al., 2000; Davidson et al., 2007) and can have played a role.

The mechanism proposed for the lower GRV is only apparently in conflict with existing models that propose zoned, largely solid magma chambers (crystal mush), incapable of bulk flow (e.g. Bachmann and Bergantz, 2004; Glazner et al., 2004; Hildreth, 2004; Vigneresse et al., 1996). In fact, mixing of crystal populations does not need the entire magma chamber to be largely molten at one time, and may happen locally in hotter volumes of magma located at the top or core of the chamber or in hot, rising plumes. Evidence for pulsating conditions, with temperature increase and re-melting of crystal mush (waxing and waning magma chamber) has been found in other felsic provinces (Charlier et al., 2005; Hildreth and Wilson, 2007).

Because Ti diffusion in quartz is relatively fast (Cherniak et al., 2007), CL features observed in the lower GRV must have formed shortly ($\leq 10^2$-10^4 years) before being "quenched" by emplacement on the surface or at shallow depth. Thus, sharp gradients and resorption textures recorded relatively short, episodic events – in comparison with the estimated life span of the Gawler SLIP (Fanning et al., 1988; Flint, 1993) of ~10 Ma.

7.5 Petrogenesis and tectonic circumstances of the Gawler SLIP

Two petrogenetic models can be envisaged in the production of felsic magmas in bimodal mafic-felsic igneous provinces: 1) production of rhyolite via fractionation of a mantle-derived parental basaltic magma, and 2) coeval melting of separate mantle and crustal sources to give mafic and felsic magmas, respectively.

7.5.1 Production of basalt in the GRV

The first objection to mafic to felsic evolution via fractionation is that approximately 90% fractionation is necessary to produce rhyolite from a basaltic parental magma. Because >95 vol.% of outcropping rocks in the GRV are felsic, an improbably large volume of femic magma (~10^6 km^3) should have been produced. The vast majority of this would be concealed deep in the crust. It should be recognised, however, that the overall felsic/mafic ratio could be different from what is revealed by exposure. Denser mafic magmas are more likely than felsic magmas to be trapped during their ascent through the crust at levels where buoyancy is reached. Geochemical arguments can also be

used to test a possible derivation of rhyolites from basalts. Fractionation of basalt would imply extensive feldspar crystallisation, which would give marked negative anomalies in Sr, Ba and Eu (White et al., 2003) in the andesites and dacites. This is not observed (chapter 4, Fig. 4.2). Major and trace element geochemical modelling failed to identify a fractionation line between basalt and andesite of the lower GRV. In particular, Ni, Sc, Cr, and V are too low in the andesites, implying that intermediate and felsic magmas of the GRV were not derived from extensive fractionation of basalt (Giles, 1988). Furthermore, the compositional gap between mafic and intermediate samples also argues against fractionation across the compositional spectrum, and is more easily explained by separate sources. Whole-rock isotopic compositions are not conclusive, because of a lack of precise constraints on the composition of Archean and Paleoproterozoic rocks (Stewart, 1994), and because the method is only reliable in presence of a clear isotopic contrast between source rocks. Thus, separate sources for mafic and intermediate-felsic magmas appear more likely.

For the basalt (and basaltic andesite, SiO_2 <54-55 wt.%), partial melting of a mantle source must be envisaged. Given the relatively high and variable LILE contents in comparison to typical MORB or continental rift basalt (chapter 4), a metasomatised source has been proposed (Giles, 1988). This is also in agreement with the variable $^{143}Nd/^{144}Nd$ isotopic ratios measured for the lower part of the Chitanilga Volcanic Complex (Stewart, 1994). Causes of this metasomatism cannot be easily identified, but it can be noted that the Gawler craton was affected by the emplacement of subduction-related 1620-1610 Ma St. Peter Suite ~30-40 Ma before emplacement of the GRV (Ferris et al., 2002; Betts and Giles, 2006). Subduction is known to be capable of adding elements to the mantle, especially water-soluble LILE. Thus, some of the geochemical characteristics of the GRV could be inherited from previous tectonic events.

Having excluded the mantle origin, two hypotheses can be advanced for the production of the voluminous felsic, A-type magmas that characterise the Gawler SLIP: 1) melting of residual granodioritic (quartzo-feldspathic) continental crust; left after a previous melting event (Collins et al., 1982; Whalen et al., 1987; Giles, 1988; Creaser and White, 1991), melting occurred at high temperature because the crust was made refractory by a previous extraction of melt or because of the low water content (King et al., 2001) or 2) melting of recent basaltic magmas emplaced at the base of the crust (Patiño Douce, 1997; Frost and Frost, 2001). Both these hypotheses can be complemented by subsequent various degrees of crustal assimilation and fractionation.

To address these hypotheses, it is useful to summarise the characteristics and petrogenetic hypotheses of felsic magmas with similar geochemical composition as the Gawler SLIP, the “A-type”.

7.5.2 Chemical characteristics and origin of A-type magmas

Loiselle and Wones (1979) defined A-type granites as mildly alkaline, with low CaO and Al_2O_3, high Fe#, high K_2O, K_2O/Na_2O and F, and low H_2O and low oxygen fugacity. Trace elements incompatible with feldspar and mafic silicates (REE except Eu, Zr, Nb, Ta) are high, compatible elements (Ba, Sr, Eu) are low. Values of the $^{87}Sr/^{86}Sr$ ratio are low (0.703-0.712). Examples of A-type granite provided by Liselle and Wones (1979) are the Pikes Peak batholith, the White Magma Series of New Hampshire, US, the Nigerian

Younger granites and the Gardar Province, Greenland. The proposed genetic mechanism is fractionation of alkali basalt, with or without interaction of lower granulitic crust in rift zones or intracontinental settings.

Successive work aimed at defining distinctive trace element content of A-type magmas. Collins (1982) distinguished the A-type Gabo and Mumbulla Suites of southeast Australia from I-type plutons of the same area mainly on the basis of trace elements (REE, Nb, and Ga). Collins et al. (1982) also pointed out that the southeast Australian granites are homogeneous and contain interstitial annite. The proposed genetic mechanism is melting of a granulitic source after extraction of a previous granite melt. This second melting would occur under high temperature, H_2O-undersatured conditions, generating a H_2O-poor, F- and Cl-rich, high-incompatible element magma with low-viscosity.

Clemens et al. (1986) performed experiments on the Watergums Granite of southeast Australia. They infer high temperature (830°C to >900°C), moderate water contents (~2-4 wt.%) and high F contents for the Watergums Granite magma. They concluded that the granite was originated by high temperature melting of a residual source after extraction of an I-type granite. Given the homogeneous composition and texture of the granite, they also proposed that the granite was emplaced at a wholly molten state.

Other studies of the A-type granites of the Lachlan Fold Belt of southeast Australia (Wangrah Suite; King et al., 2001) also prefer an origin by partial melting of quartzo-feldspathic crust.

Whalen et al. (1987) created trace element discrimination plots based on Ga/Al versus various HFSE (Nb, Y, and Zr), and alkalis. Eby et al. (1990) and Eby (1992) pointed out that the rocks classified as A-type included a variety of granitoid suites and their volcanic equivalents. These authors proposed a further distinction based on the Y/Nb ratio, considered indicative of the source rocks. A-type suites with Y/Nb <1.2 (A1) are derived from sources chemically similar to those of oceanic island basalts, suites with Y/Nb <1.2 (A2) are derived from sources similar to island arc or continental margin basalt. Some authors (e.g. Frost and Frost, 1997; Dall'Agnol et al., 1999) have described magnetite- and hornblende-bearing high-Fe# granites, and called them "reduced" A-type, in reference to the inferred higher oxygen fugacity in comparison with other A-type granites.

Multiple classifications involving different parameters have led to somewhat conflicting and misleading terms. Therefore, some authors have cautioned from the use of A-type, and have proposed that the term A-type be dropped (Creaser et al., 1991; Frost and Frost, 2011).

Three main mechanisms have been proposed for the genesis of A-type magmas: 1) fractional crystallisation of mantle magmas and assimilation of crust (e.g. Loiselle and Wones, 1979); 2) evolution by melting of underplated mantle-derived mafic rocks (e.g. Hildreth, 1991; Frost and Frost, 1997; Frost et al., 1999); 3) partial melting of granulitic refractory quartzo-feldspathic crustal rocks (e.g. Collins et al., 1982; Clemens et al., 1986; Whalen et al., 1987; King et al., 2001);.

7.5.3 Production of intermediate-felsic magmas in the GRV

The hypothesis of production of rhyolite by fractionation of basalt has already been discussed. The hypothesis of melting of a residual quartzo-feldspathic source involves high temperature vapour-absent melting of granulitic crust in which biotite and hornblende have been previously enriched in F by a previous melting event. Fluoro end members of hydrous minerals are more thermally stable compared to their F-poor equivalents (Holloway and Ford, 1975; Holloway, 1977; Manning and Pichavant, 1983). High REE and HFSE are the result of melting of accessory minerals in the source rock.

Because not all A-type magmas are believed to be F-rich, melting of a refractory, but unfractionated quartz source has also been proposed (King et al., 2001). Melting of a similar quartzo-feldspathic source rock was proposed by Patiño Douce (1997) and Skjerlie and Johnston (1993), who have experimentally proven that production of a melt with A-type characteristics does not require previous extraction of a melt.

Creaser et al. (1991) have pointed out that a rock that has undergone partial melting should be depleted in K and should have its Fe/Mg reduced, both characteristics which are contrary to A-type definition. They proposed water-undersaturated partial melting of a tonalitic rock as the petrogenetic mechanism.

As mentioned, the GRV magmatism records a compositional and thermal evolution through time – from the lower to the upper GRV – that includes increase in temperature, Fe#, Ga/Al, and REE-HFSE compositions, and decrease in the abundance of ignimbrite and mafic rocks. [Whole-rock geochemical analyses of the lower GRV indicate a scatter in Harker diagrams and the presence of multiple lines of descent, whereas the upper GRV has much narrower compositional ranges and well defined lines of liquid evolution (Giles, 1988). Neodymium isotopic values also show more scattered values in the lower GRV (Giles, 1988; Stewart, 1994).] The GRV evolved from transitional between I- and A-type in HFSE vs. Ga/Al discrimination diagrams (Whalen et al., 1987) and from transitional between arc and intraplate to intraplate in tectonic setting diagrams (Pearce et al., 1984). A similar chemical evolution is also shown by other SLIP, such as the Chon-Aike province (Riley et al., 2001).

The compositional and thermal secular evolution between lower and upper GRV can be explained by a petrogenetic model that involves melting of continental crust. As melting proceeds, the lower melting-temperature components are progressively removed, and the source becomes more refractory. As a consequence, melting occurs at higher temperature, with increasing melting of zircon and other high-temperature melting accessory minerals and consequent increase of HFSE and REE in the melt. The increase in temperature results in extensive melting, and eruption of large volumes of felsic lavas at high emplacement rates.

7.5.4 Tectonic circumstances

Production of such a large amount of felsic magma in the Gawler SLIP (estimated ~100 000 km^3) from a comparatively refractory lower crust in an intracontinental setting requires a high influx of heat, and implication of the mantle is necessary. This can be achieved by mantle uprise, such as the mantle diapir described by Giles (1988). Mafic

magma generated in the uprising mantle would move upwards and intrude the crust or take place at the base of the crust. Evidence of magmatic magmatism in the first phase of the GRV activity is represented by eruption of basalt in the lower GRV. The increase of geothermal gradient induced by these processes may have caused extensive high-temperature metamorphism and melting of the crust. Betts et al. (2009) proposed mantle rise via a plume mechanism. They explained the progressively younging magmatism of central Australia as the result of drift of the continent over a mantle plume.

An alternative mechanism that has been proposed to explain build-up of heat in the mantle in intracontinental setting is thermal insulation by an overlying continental mass (Hofmann, 1989). This mechanism has been proposed to explain the occurrence of the 1.6-1.3 Ga global-scale magmatic event and high-temperature low-pressure metamorphism following accretion of Laurentia-Baltica (Anderson and Morrison, 2005), and also affected Brazil (Dall'Agnol et al., 1999). According to some reconstructions (e.g. Hofmann, 1989), Australia was adjoined to the western margin of Laurentia in the Early Proterozoic, forming a super continent. Thus, it might have shared the same tectonic and thermal-magmatic history as the modern North America.

7.6 A link between Gawler SLIP magmatism and mineralisation at Olympic dam?

The GRV show evidence of the presence of a F-rich fluid, which is interpreted to have exsolved from the F-rich GRV source magmas (chapter 6). This fluid deposited aggregates of REE- and HFSE-bearing minerals (fluorite, REE-F-carbonate, zircon, anatase, apatite), also enriched in Pb, U, and Cu. This implies that the fluid was capable of transporting these elements in solution. This capacity of transport can be attributed to the presence of complexing agents, primarily F, CO_2, OH^-, and P.

A similar F- and REE-bearing mineral association and the same high REE and F abundances are characteristic of the U-bearing iron oxide copper-gold deposits in the Olympic Dam province, which is hosted in associated granites of the Hiltaba Suite (Oreskes and Einaudi, 1990; Skirrow et al., 2007). This similarity could indicate that the granites are not only a "passive host" (e.g. Oreskes and Einaudi, 1990), and imply a genetic link, sometimes overlooked in the literature, between GRV-HS magmas and the mineralising hydrothermal system at Olympic Dam, as also suggested by Johnson and Cross (1995).

A simple calculation can be used to assess the amount of F released during the emplacement and crystallisation of the Gawler SLIP. Using the estimate of 100 000 km^3 for the volume of magma involved, and an average F concentration value of 0.5 wt.% in the melt, the total F "available" in the province was ~$1.3 \cdot 10^{17}$ kg (assuming a granite density of 2700 kg/m3). Whole-rock measures of 0.1 wt.% F (Bath, 2005) suggest that 0.9 wt.% F may have been lost during crystallisation. This corresponds to a mass of ~$1.1 \cdot 10^{15}$ kg of F potentially exsolved by the Gawler SLIP magma in its emplacement and crystallisation stage. Although evidence of this fluid was found very locally in the lower GRV, it can be envisaged that the same process could have happened at a much larger scale, as suggested by extensive F-mineralisation at Olympic dam.

Melt inclusions provide evidence for melt volatile-undersaturation in relatively early

stages of magma evolution (during crystallisation of quartz phenocrysts). The presence of "pockets" of minerals such as micromiaroles, vesicles and vugs in lithophysae implies that a volatile (F, H_2O, $\pm SO_4^{2-}$, $\pm CO_2$)-rich phase formed in the late-stages of solidification.

REFERENCES CITED

Aiuppa, A., 2009. Degassing of halogens from basaltic volcanism: Insights from volcanic gas observations. Chemical Geology, 263(1-4): 99-109.

Aiuppa, A., Baker, D.R. and Webster, J.D., 2009. Halogens in volcanic systems. Chemical Geology, 263(1-4): 1-18.

Allègre, C.J., Provost, A. and Jaupart, C., 1981. Oscillatory zoning - a pathological case of crystal-growth. Nature, 294(5838): 223-228.

Allen, S.R. and McPhie, J., 2002. The Eucarro Rhyolite, Gawler Range Volcanics, South Australia: a > 675 km3, compositionally zoned lava of Mesoproterozoic age. Geological Society of America Bulletin, 114(12): 1592-1609.

Allen, S.R., McPhie, J., Ferris, G., Simpson, C., 2008. Evolution and architecture of a large felsic Igneous Province in western Laurentia: The 1.6 Ga Gawler Range Volcanics, South Australia. Journal of Volcanology and Geothermal Research, 172(1-2): 132-147.

Allen, S.R., Simpson, C.J., McPhie, J., Daly, S.J., 2003. Stratigraphy, distribution and geochemistry of widespread felsic volcanic units in the Mesoproterozoic Gawler Range Volcanics, South Australia. Australian Journal of Earth Sciences, 50(1): 97-112.

Anderson, A.T., 1984. Probable relations between plagioclase zoning and magma dynamics, Fuego Volcano, Guatemala. American Mineralogist, 69(7-8): 660-676.

Anderson, A.T., Davis, A.M. and Lu, F.Q., 2000. Evolution of Bishop Tuff rhyolitic magma based on melt and magnetite inclusions and zoned phenocrysts. Journal of Petrology, 41(3): 449-473.

Anderson, A.T., Newman, S., Williams, S. N., Druitt, T. H., Skirius, C., and Stolper, E., 1989. H2O, CO2, Cl, and Gas in Plinian and Ash-Flow Bishop Rhyolite. Geology, 17(3): 221-225.

Andrews, G.D.M., Branney, M.J., Bonnichsen, B. and McCurry, M., 2008. Rhyolitic ignimbrites in the Rogerson Graben, southern Snake River Plain volcanic province: volcanic stratigraphy, eruption history and basin evolution. Bulletin of Volcanology, 70(3): 269-291.

Audétat, A., Günther, D. and Heinrich, C.A., 2000. Magmatic-hydrothermal evolution in a fractionating granite: A microchemical study of the Sn-W-F-mineralized Mole Granite (Australia). Geochimica et Cosmochimica Acta, 64(19): 3373-3393.

Bachmann, O. and Bergantz, G.W., 2008. Rhyolites and their source mushes across tectonic settings. Journal of Petrology, 49(12): 2277-2285.

Bachmann, O. and Bergantz, G.W., 2008. Rhyolites and their source mushes across tectonic settings. Journal of Petrology, 49(12): 2277-2285.

Bachmann, O., Dungan, M.A. and Lipman, P.W., 2002. The Fish Canyon magma body, San Juan volcanic field, Colorado: Rejuvenation and eruption of an upper-crustal batholith. Journal of Petrology, 43(8): 1469-1503.

Bailey, D.K., 1980. Volcanism, earth degassing andreplenished lithosphere mantle. Philosophical Transactions of the Royal Society of London. Series A, Mathematical and Physical Sciences, 297(1431): 309-322.

Bath, A., 2005. Petrography and geochemistry of the Mesoproterozoic Gawler Range Volcanics, South Australia, University of Tasmania, Hobart, 101 pp.

Bau, M., Möller, P., 1992. Rare earth element fractionation in metamorphogenic hydrothermal calcite, magnesite and siderite. Contributions to Mineralogy and Petrology, 45: 231-246.

Bea, F., 1996. Residence of REE, Y, Th and U in granites and crustal protoliths; Implications for the chemistry of crustal melts. Journal of Petrology, 37(6): 1601-1601.

Belousova, E.A., Reid, A.J. , Griffin, W.L. , O'Reilly, S.Y. (2009) Rejuvenation vs. recycling of Archean crust in the Gawler Craton, South Australia: Evidence from U–Pb and Hf isotopes in detrital zircon. Lithos, 113, 570-582.

Belperio, A. and Freeman, H., 2004. Common geological characteristics of Prominent Hill and Olympic Dam - Implication for iron oxide copper-gold exploration models. Pacrim 2004 Congress, 2004(5): 115-125.

Belperio, A., Flint, R. and Freeman, H., 2007. Prominent Hill: A hematite-dominated, iron oxide copper-gold system. Economic Geology, 102(8): 1499-1510.

Betts, P.G. and Giles, D., 2006. The 1800-1100 Ma tectonic evolution of Australia. Precambrian Research, 144(1-2): 92-125.

Betts, P.G., Giles, D., Foden, J., Schaefer, B.F., Mark, G., Pankhurst, M.J., Forbes, C.J., Williams, H.A., Chalmers, N.C., Hills, Q., 2009. Mesoproterozoic plume-modified orogenesis in eastern Precambrian Australia. Tectonics, 28(3): TC3006.

Betts, P.G., Giles, D., Lister, G.S. and Frick, L.R., 2002. Evolution of the Australian lithosphere. Australian Journal of Earth Sciences, 49(4): 661-695.

Blewett, R.S., Black, L. P., Sun, S. S., Knutson, J., Hutton, L. J., Bain, J. H. C., 1998. U-Pb zircon and Sm-Nd geochronology of the Mesoproterozoic of North Queensland: implications for a Rodinian connection with the Belt supergroup of North America. Precambrian Research, 89(3-4): 101-127.

Blissett, A.H., 1975. Rock units in the Gawler Range Volcanics, South Australia. Geological Survey of South Australia, Quarterly Geological Notes, 55: 2-14.

Blissett, A.H., 1977. Childara, Sheet SH/53-14, 1:250000 geological series. Geological Survey of South Australia, Adelaide.

Blissett, A.H., 1980. Childara, South Australia. Sheet SH/53-14. 1:250 000 geological series. Explanatory notes. Geological Survey of South Australia, Adelaide.

Blissett, A.H., 1985. Gairdner, South Australia. Sheet SH/53-15, 1:250 000 geological series. Explanatory notes, Geological Survey of South Australia, Adelaide.

Blissett, A.H., Creaser, R.A., Daly, S.J., Flint, R.B., Parker, A.J., 1993. Gawler Range Volcanics. In: J.F. Drexel, Preiss, W. V., Parker, A. J. (Editor), The geology of South Australia. Geological Survey of South Australia, Adelaide.

Bonnichsen, B., Kauffman, D.F., 1987. Physical features of rhyolite lava flows in the Snake River Plain volcanic province, Southwestern Idaho. Geological Society of America, 212 (Special Paper): 119-145.

Bonnichsen, B., Leeman, W.P., Honjo, N., McIntosh, W.C. and Godchaux, M.M., 2008. Miocene silicic volcanism in southwestern Idaho: geochronology, geochemistry, and evolution of

the central Snake River Plain. Bulletin of Volcanology, 70(3): 315-342.

Borg, S.G., and DePaolo, D.J., 1994. Laurentia, Australia and Antarctica as a Late Proterozoic supercontinent: constraints from isotopic mapping. Geology, 22: 307-310.

Branch, C.D., 1978. Evolution of the middle Proterozoic Chandabooka Caldera, Gawler range acid volcano-plutonic province, South Australia. Journal of the Geological Society of Australia, 25(4): 199-216.

Branney, M.J., Barry, T.L. and Godchaux, M., 2004. Sheathfolds in rheomorphic ignimbrites. Bulletin of Volcanology, 66(6): 485-491.

Branney, M.J., Bonnichsen, B., Andrews, G. D. M., Ellis, B., Barry, T. L., McCurry, M., 2008. 'Snake River (SR)-type' volcanism at the Yellowstone hotspot track: distinctive products from unusual, high-temperature silicic super-eruptions. Bulletin of Volcanology, 70(3): 293-314.

Branney, M.J., Kokelaar, B.P, 1992. A reappraisal of ignimbrite emplacement: particulate to non-particulate flow transition during progressive aggradation of high-grade ignimbrite. Bulletin of Volcanology, 54, 504-520.

Branney, M.J., Kokelaar, B.P. and Mcconnell, B.J., 1992. The Bad Step Tuff - a Lava-Like Rheomorphic Ignimbrite in a Calc-Alkaline Piecemeal Caldera, English Lake District. Bulletin of Volcanology, 54(3): 187-199.

Branney, M.J., Kokelaar, B.P., 2003. Pyroclastic density currents and the sedimentation of ignimbrites, Memoirs 2003. Geological Society, London, pp. 152.

Bryan, S., 2007. Silicic Large Igneous Provinces. Episodes, 30(1): 20-31.

Bryan, S.E. and Ernst, R.E., 2008. Revised definition of large igneous provinces (LIPs). Earth-Science Reviews, 86(1-4): 175-202.

Bryan, S.E., Ewart, A., Stephens, C.J., Parianos, J., Downes, P.J., 2000. The Whitsunday Volcanic Province, Central Queensland, Australia: lithological and stratigraphic investigations of a silicic-dominated large igneous province. Journal of Volcanology and Geothermal Research, 99(1-4): 55-78.

Bryan, S.E., Ferrari, L., Reiners, P. W., Allen, C. M., Petrone, C. M., Ramos-Rosique, A., Campbell, I. H., 2008. New insights into crustal contributions to large-volume rhyolite generation in the mid-Tertiary Sierra Madre Occidental province, Mexico, revealed by U-Pb geochronology. Journal of Petrology, 49(1): 47-77.

Bryan, S.E., Riley, T.R., Jerram, D. A., Leat, P.T. & Stephens, C.J., 2002. Silicic volcanism: an under-valued component of large igneous provinces and volcanic rifted margins. In: M.A. Menzies, Klemperer, S. L., Ebinger, C. J. & Baker, J. (Editor), Magmatic Rifted Margins. Geological Society of America, Special Papers. Geological Society of America, pp. 99-120.

Budd, A.R. and Fraser, G.L., 2004. Geological relationships and Ar-40/Ar-39 age constraints on gold mineralisation at Tarcoola, central Gawler gold province, South Australia. Australian Journal of Earth Sciences, 51(5): 685-699.

Budd, A.R. and Skirrow, R.G., 2007. The nature and origin of gold deposits of the Tarcoola goldfield and implications for the central Gawler gold province, south Australia. Economic Geology, 102(8): 1541-1563.

Bull, K.F. and McPhie, J., 2007. Fiamme textures in volcanic successions: Flaming issues of definition and interpretation. Journal of Volcanology and Geothermal Research, 164(4): 205-

216.

Cameron, M., Bagby, W.C., Cameron, K.L., 1980. Petrogenesis of Voluminous Mid-Tertiary Ignimbrites of the Sierra-Madre Occidental, Chihuahua, Mexico. Contributions to Mineralogy and Petrology, 74(3): 271-284.

Candela, P.A. and Blevin, P.L., 1995. Do some miarolitic granites preserve evidence of magmatic volatile phase permeability? Economic Geology and the Bulletin of the Society of Economic Geologists, 90(8): 2310-2316.

Candela, P.A., 1997. A review of shallow, ore-related granites: Textures, volatiles, and ore metals. Journal of Petrology, 38(12): 1619-1633.

Carroll, M.R. and Webster, J.D., 1994. Solubilities of Sulfur, Noble-Gases, Nitrogen, Chlorine, and Fluorine in Magmas. Volatiles in Magmas, 30: 231-279.

Cas, R.A.F., 1978. Silicic Lavas in Paleozoic Flysch-Like Deposits in New-South-Wales, Australia - Behavior of Deep Subaqueous Silicic Flows. Geological Society of America Bulletin, 89(12): 1708-1714.

Cas, R.A.F., Wright, J.V., 1987. Volcanics successions modern and ancient. Alan & Unwin, London, 528 pp.

Chabiron, A., Alyoshin, A. P., Cuney, M., Deloule, E., Golubev, V. N., Velitchkin, V. I., Poty, B., 2001. Geochemistry of the rhyolitic magmas from the Streltsovka caldera (Transbaikalia, Russia): a melt inclusion study. Chemical Geology, 175(3-4): 273-290.

Chaigneau, M., Massare, D., Clocchiatti, R., 1980. Contribution à l'étude des inclusions vitreuses et des éléments volatils contenus dans les phénocristaux de quartz de roches volcaniques acides. Bulletin of Volcanology, 41(1): 233-240.

Chakraborty, S., 2008. Diffusion in solid silicates: a tool to track timescales of processes comes of age. Annual Review of Earth and Planetary Sciences, 36(1): 153-190.

Chappell, B.W., 2004. Towards a unified model for granite genesis. Fifth Hutton Symposium on the Origin of Granites and Related Rocks, 389: 1-10.

Chappell, B.W., White, A.J.R., Williams, I.S., Wyborn, D. , 2004. Low- and high-temperature granites. Transactions of the Royal Society of Edinburgh: Earth Sciences, 95: 125-140.

Charlier, B.L.A., Wilson, C. J. N. Lowenstern, J. B. Blake, S. Van Calsteren, P. W. Davidson, J. P., 2005. Magma generation at a large, hyperactive silicic volcano (Taupo, New Zealand) revealed by U-Th and U-Pb systematics in zircons. Journal of Petrology, 46(1): 3-32.

Charoy, B. and Raimbault, L., 1994. Zr-rich, Th-rich, and REE-rich biotite differentiates in the A-type granite pluton of Suzhou (Eastern China) - the key role of fluorine. Journal of Petrology, 35(4): 919-962.

Cherniak, D.J., Watson, E.B. and Wark, D.A., 2007. Ti diffusion in quartz. Chemical Geology, 236(1-2): 65-74.

Christiansen RL (1984) Yellowstone magmatic evolution: its bearing on understanding large-volume explosive volcanism In: Boyd FR et al. (eds), Explosive volcanism: inception, evolution and hazards. National Research Council Studies in Geophysics, National Academy Press, Washington DC, 84–95.

Christiansen, E.H., Burt, D.M., and Sheridan, M.F., 1986. The geology of topaz rhyolites

from the western United States. Geological Society of America Special Paper 205, 82 pp.

Christiansen, E.H., Burt, D.M., Sheridan, M.F. and Wilson, R.T., 1983. The petrogenesis of topaz rhyolites from the western United States. Contributions to Mineralogy and Petrology, 83(1): 16-30.

Christiansen, E.H., Haapala, I. and Hart, G.L., 2007. Are Cenozoic topaz rhyolites the erupted equivalents of Proterozoic rapakivi granites? Examples from the western United States and Finland. Lithos, 97(1-2): 219-246.

Christiansen, E.H. and McCurry, M., 2008. Contrasting origins of Cenozoic silicic volcanic rocks from the western Cordillera of the United States. Bulletin of Volcanology, 70(3): 251-267.

Clarke, G.L., Guiraud, M., Powell, R. and Burg, J.P., 1987. Metamorphism in the Olary Block, South-Australia - Compression with cooling in a Proterozoic fold belt. Journal of Metamorphic Geology, 5(3): 291-306.

Clough, B.J., Wright, J.V. and Walker, G.P.L., 1982. Morphology and dimensions of the young comendite lavas of La-Primavera volcano, Mexico. Geological Magazine, 119(5): 477-485.

Coffin, M.F., Eldholm, O., 1994. Large igneous provinces: crustal structure, dimensions and external consequences. Reviews of Geophysics, 32, 1-36.

Collins, W.J., Beams, S.D., White, A.J.R. and Chappell, B.W., 1982. Nature and origin of A-type granites with particular reference to southeastern Australia. Contributions to Mineralogy and Petrology, 80(2): 189-200.

Couch, S., Sparks, R.S.J. and Carroll, M.R., 2001. Mineral disequilibrium in lavas explained by convective self-mixing in open magma chambers. Nature, 411(6841): 1037-1039.

Creaser, R.A. and Fanning, C.M., 1993. A U-Pb zircon study of the Mesoproterozoic Charleston Granite, Gawler Craton, South-Australia. Australian Journal of Earth Sciences, 40(6): 519-526.

Creaser, R.A., 1989. The geology and petrology of Middle Proterozoic felsic magmatism of the Stuart Shelf, South Australia, La Trobe University, Victoria, 434 pp.

Creaser, R.A., 1995. Neodymium isotopic constraints for the origin of Mesoproterozoic felsic magmatism, Gawler-Craton, South Australia. Canadian Journal of Earth Sciences, 32(4): 460-471.

Creaser, R.A., Price, R.C., Wormald, R.J., 1991. A-type granites revisited - Assessment of a residual-source model. Geology, 19(11): 163-166.

Creaser, R.A., White, A.J.R., 1991. Yardea Dacite - Large-volume, high-temperature felsic volcanism from the Middle Proterozoic of South-Australia. Geology, 19(1): 48-51.

Dall'agnol, R., Scaillet, B. and Pichavant, M., 1999. An experimental study of a Lower Proterozoic A-type granite from the eastern Amazonian Craton, Brazil. Journal of Petrology, 40(11): 1673-1698.

Detrick, R.S., Mutter, J.C., Buhl, P. and Kim, I.I., 1990. No evidence from multichannel reflection data for a crustal magma chamber in the MARK area on the Mid-Atlantic Ridge. Nature, 347(6288): 61-64.

D'Lemos, R.S., Kearsley, A.T., Pembroke, J.W., Watt, G.R. and Wright, P., 1997. Complex

quartz growth histories in granite revealed by scanning cathodoluminescence techniques. Geological Magazine, 134(4): 549-552.

Daly, S.J., 1985. Tarcoola, SH53-10, 1:250 000 Geological Series. Geological Survey of South Australia.

Daly, S.J., 1993. Sediments associated with the Gawler Range Volcanics. In: J.F. Drexel, Preiss, W.V., Parker, A.J. (Editor), The geology of South Australia. Geological Survey of South Australia, pp. 124-127.

Daly, S.J., Fanning, C.M., Fairclough, M.C., 1998. Tectonic evolution and exploration potential of the Gawler Craton, South Australia. AGSO Journal of Australian Geology and Geophysics, 17(3): 145-168.

Danyushevsky, L.V., McNeill, A.W. and Sobolev, A.V., 2002. Experimental and petrological studies of melt inclusions in phenocrysts from mantle-derived magmas: an overview of techniques, advantages and complications. Chemical Geology, 183(1-4): 5-24.

Davidson, J.P., Morgan, D.J., Charlier, B.L.A., Harlou, R. and Hora, J.M., 2007. Microsampling and isotopic analysis of igneous rocks: Implications for the study of magmatic systems. Annual Review of Earth and Planetary Sciences, 35: 273-311.

Davidson, P. and Crawford, A.J., 2006. Coexisting melt and fluid inclusions at Batu Hijau: Evidence for primary magmatic aqueous fluids and their relationship to mineralisation. Geochimica et Cosmochimica Acta, 70(18): A131-A131.

Davidson, P. and Kamenetsky, V.S., 2001. Immiscibility and continuous felsic melt-fluid evolution within the Rio Blanco porphyry system, Chile: Evidence from inclusions in magmatic quartz. Economic Geology and the Bulletin of the Society of Economic Geologists, 96(8): 1921-1929.

Davidson, P., Davidson, P., Kamenetsky, V., Cooke, D. R., Frikken, P., Hollings, P., Ryan, C., Van Achterbergh, E., Mernagh, T., Skarmeta, J., Serrano, L., Vargas, R., 2005. Magmatic precursors of hydrothermal fluids at the Rio Blanco Cu-Mo deposit, Chile: Links to silicate magmas and metal transport. Economic Geology, 100(5): 963-978.

Davidson, P., Kamenetsky, V., Hollings, P., Cooke, D. and Frikken, P., 2002. Magmatic fluids coexisting with felsic melts: an example from Rio Blanco rhyolite, Chile. Geochimica et Cosmochimica Acta, 66(15A): A169-A169.

Detrick, R.S., Mutter, J.C., Buhl, P. and Kim, I.I., 1990. No evidence from multichannel reflection data for a crustal magma chamber in the MARK area on the Mid-Atlantic Ridge. Nature, 347(6288): 61-64.

Devine, J.D., Gardner, J.E., Brack, H.P., Layne, G.D. and Rutherford, M.J., 1995. Comparison of microanalytical methods for estimating H2O contents of silicic volcanic glasses. American Mineralogist, 80(3-4): 319-328.

Dingwell, D.B. and Hess, K.U., 1998. Melt viscosities in the system Na-Fe-Si-O-F-Cl: Contrasting effects of F and Cl in alkaline melts. American Mineralogist, 83(9-10): 1016-1021.

Dingwell, D.B. and Mysen, B.O., 1985. Effects of water and fluorine on the viscosity of albite melt at high-pressure - a preliminary investigation. Earth and Planetary Science Letters, 74(2-3): 266-274.

Dingwell, D.B., 1989. Effect of fluorine on the viscosity of diopside liquid. American Mineralogist, 74(3-4): 333-338.

Dingwell, D.B., 1990. Effects of structural relaxation on cationic tracer diffusion in silicate melts. Chemical Geology, 82(3-4): 209-216.

Dingwell, D.B., 1997. The brittle-ductile transition in high-level granitic magmas: material constraints. Journal of Petrology, 38(12): 1635-1644.

Dingwell, D.B., Scarfe, C.M. and Cronin, D.J., 1985. The effect of fluorine on viscosities in the system Na2O-Al2O3-SiO2 - Implications for phonolites, trachytes and rhyolites. American Mineralogist, 70(1-2): 80-87.

Dolejš, D. and Baker, D.R., 2007. Liquidus equilibria in the system K2O-Na2O-Al2O3-SiO2-F2O-1-H2O to 100 MPa: I. Silicate-fluoride liquid immiscibility in anhydrous systems. Journal of Petrology, 48(4): 785-806.

Dolejš, D. and Baker, D.R., 2007. Liquidus equilibria in the system K2O-Na2O-Al2O3-SiO2-F2O-1-H2O to 100 MPa: II. Differentiation paths of fluorosilicic magmas in hydrous systems. Journal of Petrology, 48(4): 807-828.

Dunbar, N.W., Hervig, R.L. and Kyle, P.R., 1989. Determination of pre-eruptive H2O, F and Cl contents of silicic magmas using melt inclusions: examples from Taupo volcanic center, New Zealand. Bulletin of Volcanology, 51(3): 177-184.

Ernst, R., E., Buchanan, K. L., Campbell, I. H., 2005. Frontiers in large igneous province research. Lithos, 79, 271-297.

Ewart, A. Marsh, J. S., Milner, S. C., Duncan, A. R., Kamber, B. S., III, Armstrong, R. A., 2004a. Petrology and geochemistry of Early Cretaceous bimodal continental flood volcanism of the NW Etendeka, Namibia. Part 1: Introduction, mafic lavas and re-evaluation of mantle source components. Journal of Petrology, 45(1): 59-105.

Ewart, A. Marsh, J. S., Milner, S. C., Duncan, A. R., Kamber, B. S., III, Armstrong, R. A., 2004b. Petrology and geochemistry of Early Cretaceous bimodal continental flood volcanism of the NW Etendeka, Namibia. Part 2: Characteristics and petrogenesis of the high-Ti latite and high-Ti and low-Ti voluminous quartz latite eruptives. Journal of Petrology, 45(1): 107-138.

Ewart, A., Milner, S.C., Armstrong, R.A., Duncan, A.R., 1998a. Etendeka volcanism of the Goboboseb Mountains and Messum Igneous Complex, Namibia. Part I: Geochemical evidence of early cretaceous Tristan plume melts and the role of crustal contamination in the Paraná-Etendeka CFB. Journal of Petrology, 39(2): 191-225.

Ewart, A., Milner, S.C., Armstrong, R.A. and Duncan, A.R., 1998b. Etendeka volcanism of the Goboboseb Mountains and Messum Igneous Complex, Namibia. Part II: Voluminous quartz latite volcanism of the Awahab Magma System. Journal of Petrology, 39(2): 227-253.

Fanning, C.M., Flint, R.B., Parker, A.J., Ludwig, K.R., Blissett, A.H., 1988. Refined Proterozoic evolution of the Gawler Craton, South-Australia, through U-Pb zircon geochronology. Precambrian Research, 40-1: 363-386.

Ferrari, L., Lopez-Martinez, M., Rosas-Elguera, J., 2002. Ignimbrite flare-up and deformation in the southern Sierra Madre Occidental, western Mexico: implications for the late subduction history of the Farallon plate. Tectonics, 21(4): 17/1-17/24.

Ferris, G., 2003. Volcanic textures within the Glyde Hill Volcanic Complex. Quarterly Earth Resources Journal of Primary Industries and Resources, South Australia 29: 36-41.

Ferris, G.M., 2001. The geology and geochemistry of granitoids in the Childara region, western Gawler craton, South Australia—implications for the Proterozoic tectonic history of

the western Gawler craton and the development of lode-style gold mineralization at Tunkillia, University of Tasmania, Hobart, 175 pp.

Ferris, G.M., Schwarz, M.P., Heithersay, P., 2002. The geological framework, distribution, and controls of Fe-oxide Cu–Au mineralization in the Gawler Craton, South Australia: Part 1—Geological and tectonic framework. In: Porter, M.T. (Ed.), Hydrothermal Iron Oxide Copper–Gold and Related Deposits: A Global Perspective, 2, 9–32.

Flint, R.B., 1993. Hiltaba Suite. In: J.F. Drexel, Preiss, W.V., Parker, A.J. (Editor), The geology of South Australia. Geological Survey of South Australia, Adelaide, pp. 127-131.

Förster, H.J., 2001. Synchysite-(Y)-synchysite-(Ce) solid solutions from Markersbach, Erzgebirge, Germany: REE and Th mobility during high-T alteration of highly fractionated aluminous A-type granites. Mineralogy and Petrology, 72(4): 259-280.

Fraser, G., McAvaney, S., Neumann, N., Szpunar, M. and Reid, A., 2010. Discovery of early Mesoarchean crust in the eastern Gawler Craton, South Australia. Precambrian Research, 179(1-4): 1-21.

Fraser, G.L. and Lyons, P., 2006. Timing of Mesoproterozoic tectonic activity in the northwestern Gawler Craton constrained by Ar-40/Ar-39 geochronology. Precambrian Research, 151(3-4): 160-184.

Fraser, G.L., Skirrow, R.G. and Budd, A.R., 2006. Geochronology of Mesoproterozoic gold mineralization in the Gawler Craton, and temporal links with the Gawler Range Volcanics. Geochimica et Cosmochimica Acta, 70(18): A185-A185.

Fraser, G.L., Skirrow, R.G., Schmidt-Mumm, A. and Holm, O., 2007. Mesoproterozoic gold in the central Gawler craton, South Australia: Geology, alteration, fluids, and timing. Economic Geology, 102(8): 1511-1539.

Frost, B.R., Barnes, C. G., Collins, W. J., Arculus, R. J., Ellis, D. J., Frost, C. D., 2001. A geochemical classification for granitic rocks. Journal of Petrology, 42(11): 2033-2048.

Frost, C.D. and Frost, B.R., 1997. Reduced rapakivi-type granites: The tholeiite connection. Geology, 25(7): 647-650.

Frost, C.D. and Frost, B.R., 2011. On Ferroan (A-type) granitoids: their compositional variability and modes of origin. Journal of Petrology, 52(1): 39-53.

Frost, C.D., Frost, B.R., Chamberlain, K.R. and Edwards, B.R., 1999. Petrogenesis of the 1.43 Ga Sherman Batholith, SE Wyoming, USA: a reduced, rapakivi-type anorogenic granite. Journal of Petrology, 40(12): 1771-1802.

Garner, A. and McPhie, J., 1999. Partially melted lithic megablocks in the Yardea Dacite, Gawler Range Volcanics, Australia: implications for eruption and emplacement mechanisms. Bulletin of Volcanology, 61(6): 396-410.

Gieré, R., 1986. Zirconolite, allanite and hoegbomite in a marble skarn from the Bergell contact aureole - Implications for mobility of Ti, Zr and REE. Contributions to Mineralogy and Petrology, 93(4): 459-470.

Gieré, R., Williams, C.T. , 1992. REE-bearing minerals in a Ti-rich vein from the Adamello contact aureole (Italy). Contributions to Mineralogy and Petrology 112: 83-100.

Gifkins, C.C., Allen, R.L. and McPhie, J., 2005. Apparent welding textures in altered pumice-rich rocks. Journal of Volcanology and Geothermal Research, 142(1-2): 29-47.

Gilbert, C.D. and Williams-Jones, A.E., 2008. Vapour transport of rare earth elements (REE) in volcanic gas: Evidence from encrustations at Oldoinyo Lengai. Journal of Volcanology and Geothermal Research, 176(4): 519-528.

Giles, C.W., 1977. Rock units in the Gawler Range Volcanics, Lake Everard area, South Australia. Geological Survey of South Australia, Quarterly Geological Notes, 51: 7-16.

Giles, C.W., 1988. Petrogenesis of the Proterozoic Gawler Range Volcanics, South-Australia. Precambrian Research, 40-1: 407-427.

Ginibre, C., Wörner, G. and Kronz, A., 2002. Minor- and trace-element zoning in plagioclase: implications for magma chamber processes at Parinacota volcano, northern Chile. Contributions to Mineralogy and Petrology, 143(3): 300-315.

Giordano, D., Romano, D.B., Dingwell, D.B., Poe, B. and Behrens, H., 2004. The combined effects of water and fluorine on the viscosity of silicic magmas. Geochimica et Cosmochimica Acta, 68(24): 5159-5168.

Glazner A.F., Bartley J.M., Coleman D.S., Gray W., Taylor R.Z., 2004. Are plutons assembled over millions of years by amalgamation from small magma chambers. GSA Today 14, 4-11.

Green, J.C. and Fitz, T.J., 1993. Extensive felsic lavas and rheoignimbrites in the Keweenawan Midcontinent Rift Plateau Volcanics, Minnesota - Petrographic and field recognition. Journal of Volcanology and Geothermal Research, 54(3-4): 177-196.

Gurenko, A.A. and Chaussidon, M., 1995. Enriched and depleted primitive melts included in olivine from Icelandic tholeiites - Origin by continuous melting of a single mantle column. Geochimica et Cosmochimica Acta, 59(14): 2905-2917.

Gurenko, A.A., Belousov, A.B., Trumbull, R.B. and Sobolev, A.V., 2005. Explosive basaltic volcanism of the Chikurachki volcano (Kurile arc, Russia): Insights on pre-eruptive magmatic conditions and volatile budget revealed from phenocryst-hosted melt inclusions and groundmass glasses. Journal of Volcanology and Geothermal Research, 147(3-4): 203-232.

Hamilton, M.A. and Buchan, K.L., 2010. U-Pb geochronology of the Western Channel Diabase, northwestern Laurentia: Implications for a large 1.59 Ga magmatic province, Laurentia's APWP and paleocontinental reconstructions of Laurentia, Baltica and Gawler craton of southern Australia. Precambrian Research, 183(3): 463-473.

Hand, M., Reid, A. and Jagodzinski, L., 2007. Tectonic framework and evolution of the Gawler craton, southern Australia. Economic Geology, 102(8): 1377-1395.

Hand, M.P., Reid, A.J., Szpunar, M.A., Direen, N., Wade, B., Payne, J., Barovich, K.M. , 2008. Crustal architecture during the early Mesoproterozoic Hiltaba-related mineralisation event: are the Gawler Range Volcanics a foreland basin fill? MESA Journal 51: 19-24.

Hayden, L.A. and Watson, E.B., 2007. Rutile saturation in hydrous siliceous melts and its bearing on Ti-thermometry of quartz and zircon. Earth and Planetary Science Letters, 258(3-4): 561-568.

Haynes, D.W., Cross, K.C., Bills, R.T. and Reed, M.H., 1995. Olympic Dam ore genesis - a fluid-mixing model. Economic Geology and the Bulletin of the Society of Economic Geologists, 90(2): 281-307.

Head, J.W., III and Coffin, M.F., 1997. Large igneous provinces: a planetary prospective. In: M.F. Coffin and O. Eldholm (Editors), Large igneous provinces: crustal structure, dimensions and external consequences. American Geophysical Union.

Henry, C.D. and Wolff, J.A., 1992. Distinguishing strongly rheomorphic tuffs from extensive silicic lavas. Bulletin of Volcanology, 54(3): 171-186.

Henry, C.D., Price, J. G., Rubin, J. N., Parker, D. F., Wolff, J. A., Self, S., Franklin, R., Barker, D. S., 1988. Widespread, lava-like silicic volcanic-rocks of Trans-Pecos Texas. Geology, 16(6): 509-512.

Hildreth, W., 1981. Gradients in silicic magma chambers - Implications for lithospheric magmatism. Journal of Geophysical Research, 86(Nb11): 153-192.

Hildreth, W.E.S., Halliday, A.N. and Christiansen, R.L., 1991. Isotopic and chemical evidence concerning the genesis and contamination of basaltic and rhyolitic magma beneath the Yellowstone Plateau volcanic field. Journal of Petrology, 32(1): 63-138.

Hildreth, W., 2004. Volcanological perspectives on Long Valley, Mammoth Mountain, and Mono Craters: several contiguous but discrete systems. Journal of Volcanology and Geothermal Research, 136(3-4): 169-198.

Hildreth, W., Wilson, C.J.N., 2007. Compositional zoning of the Bishop Tuff. Journal of Petrology, 48(5): 951-999.

Hinton, R.W. and Upton, B.G.J., 1991. The Chemistry of zircon - variations within and between large crystals from syenite and alkali basalt xenoliths. Geochimica et Cosmochimica Acta, 55(11): 3287-3302.

Hoffman, P.F., 1989. Speculations on Laurentia's first gigayear (2.0 to 1.0 Ga). Geology, 17(2): 135-138.

Holtz, F., Roux, J., Behrens, H., Schulze, F., 1999. The effects of silica and water on the viscosity of hydrous quartzofeldspathic melts. American Mineralogist, 84, 27-36.

Hu, Z.C. and Gao, S., 2008. Upper crustal abundances of trace elements: a revision and update. Chemical Geology, 253(3-4): 205-221.

Johan, V. and Johan, Z., 1994. Accessory minerals of the Cinovec (Zinnwald) Granite cupola, Czech-Republic. 1. Nb-bearing, Ta-bearing and Ti-bearing oxides. Mineralogy and Petrology, 51(2-4): 323-343.

Johan, Z. and Johan, V., 2005. Accessory minerals of the Cinovec (Zinnwald) granite cupola, Czech Republic: indicators of petrogenetic evolution. Mineralogy and Petrology, 83(1-2): 113-150.

John, D.A., 2008. Supervolcanoes and metallic ore deposits. Elements, 4(1): 22.

Johnson, J.P. and Cross, K.C., 1995. U-Pb geochronological constraints on the genesis of the Olympic Dam Cu-U-Au-Ag deposit, South Australia. Economic Geology, 90(5): 1046-1063.

Kamenetsky, V.S. and Danyushevsky, L.N., 2006. Exceptional mobility of Cu and Ag inferred from experiments with rhyolitic melt inclusions in quartz. Geochimica et Cosmochimica Acta, 70(18): A302-A302.

Kamenetsky, V.S. and Danyushevsky, L.V., 2005. Metals in quartz-hosted melt inclusions: Natural facts and experimental artifacts. American Mineralogist, 90(10): 1674-1678.

Kamenetsky, V.S., Morrow, N. and McPhie, J., 2000. Origin of high-Si dacite from rhyolitic melt: evidence from melt inclusions in mingled lavas of the 1.6 Ga Gawler Range Volcanics, South Australia. Mineralogy and Petrology, 69(3-4): 183-195.

Kamenetsky, V.S., Naumov, V.B., Davidson, P., van Achterbergh, E. and Ryan, C.G., 2004. Immiscibility between silicate magmas and aqueous fluids: a melt inclusion pursuit into the magmatic-hydrothermal transition in the Omsukchan Granite (NE Russia). Chemical Geology, 210(1-4): 73-90.

Keppler, H. and Wyllie, P.J., 1990. Role of fluids in transport and fractionation of uranium and thorium in magmatic processes. Nature, 348(6301): 531-533.

Keppler, H. and Wyllie, P.J., 1991. Partitioning of Cu, Sn, Mo, W, U, and Th between melt and aqueous fluid in the systems haplogranite-H2O HCl and haplogranite-H2O HF. Contributions to Mineralogy and Petrology, 109(2): 139-150.

Keppler, H., 1993. Influence of fluorine on the enrichment of high-field strength trace-elements in granitic-rocks. Contributions to Mineralogy and Petrology, 114(4): 479-488.

Kile, D.E. and Eberl, D.D., 1999. Crystal growth mechanisms in miarolitic cavities in the Lake George ring complex and vicinity, Colorado. American Mineralogist, 84(5-6): 718-724.

Kilinc, I.A. and Burnham, C.W., 1972. Partitioning of chloride between a silicate melt and coexisting aqueous phase from 2 to 8 kilobars. Economic Geology, 67(2): 231-235.

King, P.L., Chappell, B.W., Allen, C.M. and White, A.J.R., 2001. Are A-type granites the high-temperature felsic granites? Evidence from fractionated granites of the Wangrah Suite. Australian Journal of Earth Sciences, 48(4): 501-514.

Kuno, H., 1968. Differentiation of basalt magma. In: H.H. Hes, Poldervaart, A.A. (Editor), the Poldervaart treatise on rocks of basaltic composition. Interscience, New York, pp. 623-688.

Lebas, M.J., Lemaitre, R.W., Streckeisen, A., Zanettin, B., 1986. A chemical classification of volcanic-rocks based on the total alkali silica diagram. Journal of Petrology, 27(3): 745-750.

Lesher, C.M., Gibson, H.L. and Campbell, I.H., 1986. Composition-volume changes during hydrothermal alteration of andesite at Buttercup-Hill, Noranda-District, Québec. Geochimica et Cosmochimica Acta, 50(12): 2693-2705.

Linnen, R.L. and Keppler, H., 1997. Columbite solubility in granitic melts: consequences for the enrichment and fractionation of Nb and Ta in the Earth's crust. Contributions to Mineralogy and Petrology, 128(2-3): 213-227.

Linnen, R.L. and Keppler, H., 2002. Melt composition control of Zr/Hf fractionation in magmatic processes. Geochimica et Cosmochimica Acta, 66(18): 3293-3301.

Lipman, P., Dungan, M., Bachmann, O., 1997. Comagmatic granophyric granite in the Fish Canyon Tuff, Colorado: implications for magma-chamber processes during a large ash-flow eruption. Geology, 25(10): 915-918.

Lofgren, G., 1971. Experimentally produced devitrification textures in natural rhyolitic glass. Geological Society of America Bulletin, 82(1): 111-&.

London, D., 1986. Formation of tourmaline-rich gem pockets in miarolitic pegmatites. American Mineralogist, 71(3-4): 396-405.

London, D., Hervig, R.L. and Morgan, G.B., 1988. Melt-vapor solubilities and elemental partitioning in peraluminous granite-pegmatite systems - Experimental results with Macusani glass at 200 Mpa. Contributions to Mineralogy and Petrology, 99(3): 360-373.

Lowenstern, J.B. and Mahood, G.A., 1991. New data on magmatic H2O contents of

pantellerites, with implications for petrogenesis and eruptive dynamics at Pantelleria. Bulletin of Volcanology, 54(1): 78-83.

Lowenstern, J.B., 1994. Chlorine, fluid Immiscibility, and degassing in peralkaline magmas from Pantelleria, Italy. American Mineralogist, 79(3-4): 353-369.

Lowenstern, J.B., 1995. Applications of silicate melt inclusions to the study of magmatic volatiles. In: J.F.H. Thompson (Editor), Magmas, fluids and ore deposits. Mineralogical Association of Canada Short Course, pp. 71-99.

Lowenstern, J.B., Clynne, M.A. and Bullen, T.D., 1997. Comagmatic A-type granophyre and rhyolite from the Alid volcanic center, Eritrea, northeast Africa. Journal of Petrology, 38(12): 1707-1721.

Lowenstern, J.B., Smith, R.B. and Hill, D.P., 2006. Monitoring super-volcanoes: geophysical and geochemical signals at Yellowstone and other large caldera systems. Philosophical Transactions of the Royal Society A: Mathematical, Physical and Engineering Sciences, 364(1845): 2055-2072.

Lu, F.Q., Anderson, A.T. and Davis, A.M., 1992. Melt inclusions and crystal-liquid separation in rhyolitic magma of the bishop tuff. Contributions to Mineralogy and Petrology, 110(1): 113-120.

Mahoney, M.F., Coffin, M.F., 1997. Large igneous provinces: continental, oceanic and planetary flood volcanism. Geophysical Monograph 100.

Manley, C.R., 1996. In situ formation of welded tuff-like textures in the carapace of a voluminous silicic lava flow, Owyhee County, SW Idaho. Bulletin of Volcanology, 57(8): 672-686.

Manning, D.A.C., 1981. The Effect of fluorine on liquidus phase-relationships in the system Qz-Ab-Or with excess water at 1Kb. Contributions to Mineralogy and Petrology, 76(2): 206-215.

Marks, M.A.W., Coulson, I. M., Schilling, J., Jacob, D. E., Schmitt, A. K., Markl, G., 2008. The effect of titanite and other HFSE-rich mineral (Ti-bearing andradite, zircon, eudialyte) fractionation on the geochemical evolution of silicate melts. Chemical Geology, 257(1-2): 153-172.

Marsh, J.S., Ewart, A., Milner, S.C., Duncan, A.R. and Miller, R.M., 2001. The Etendeka Igneous Province: magma types and their stratigraphic distribution with implications for the evolution of the Paraná-Etendeka flood basalt province. Bulletin of Volcanology, 62(6): 464-486.

Mason, B.G., Pyle, D.M. and Oppenheimer, C., 2004. The size and frequency of the largest explosive eruptions on Earth. Bulletin of Volcanology, 66(8): 735-748.

Mathez, E.A. and Webster, J.D., 2004. Partitioning of chlorine and fluorine in the system apatite - silicate melt - aqueous fluid. Geochimica et Cosmochimica Acta, 68(11): A638-A638.

Mathez, E.A. and Webster, J.D., 2005. Partitioning behavior of chlorine and fluorine in the system apatite-silicate melt-fluid. Geochimica et Cosmochimica Acta, 69(5): 1275-1286.

McArthur, A.N., Cas, R.A.F. and Orton, G.J., 1998. Distribution and significance of crystalline, perlitic and vesicular textures in the Ordovician Garth Tuff (Wales). Bulletin of Volcanology, 60(4): 260-285.

McPhie, J., DellaPasqua, F., Allen, S.R., Lackie, M.A., 2008. Extreme effusive eruptions: palaeoflow data on an extensive felsic lava in the Mesoproterozoic Gawler Range Volcanics. Journal of Volcanology and Geothermal Research, 172(1-2): 148-161.

McPhie, J., Doyle, M., Allen, R., 1993. Volcanic textures: a guide to the Interpretation of textures in volcanic rocks. University of Tasmania Centre for Ore Deposit and Exploration Studies, Hobart, 198 pp.

Métrich, N. and Clocchiatti, R., 1989. Melt inclusion investigation of the volatile behavior in historic alkali basaltic magmas of Etna. Bulletin of Volcanology, 51(3): 185-198.

Michard, A., Albarède, F., 1986. The REE contents of some hydrothermal fluids. Chemical Geology 55: 51-60.

Milner, S.C., Duncan, A.R., Ewart, A., 1992. Quartz latite rheoignimbrite flows of the Etendeka Formation, North-Western Namibia. Bulletin of Volcanology, 54(3): 200-219.

Möller, P., Dulsky, P., Morteani, G., 2003. Partitioning of rare earth elements, yttrium, and some major elements among source rocks, liquid and vapor of Larderello-Travale Geothermal Field, Tuscany (Central Italy). Geochimica et Cosmochimica Acta 67(2): 171-183.

Morrow, N. and McPhie, J., 2000. Mingled silicic lavas in the Mesoproterozoic Gawler Range Volcanics, South Australia. Journal of Volcanology and Geothermal Research, 96(1-2): 1-13.

Müller, A., Breiter, K., Seltmann, R. and Pecskay, Z., 2005. Quartz and feldspar zoning in the eastern Erzgebirge volcano-plutonic complex (Germany, Czech Republic): evidence of multiple magma mixing. Lithos, 80(1-4): 201-227.

Müller, A., Rene, M., Behr, H.J. and Kronz, A., 2003. Trace elements and cathodoluminescence of igneous quartz in topaz granites from the Hub Stock (Slavkovsky Les Mts., Czech Republic). Mineralogy and Petrology, 79(3-4): 167-191.

Müller, A., Seltmann, R. and Behr, H.J., 2000. Application of cathodoluminescence to magmatic quartz in a tin granite - case study from the Schellerhau Granite Complex, Eastern Erzgebirge, Germany. Mineralium Deposita, 35(2-3): 169-189.

Müller, A., Wiedenbeck, M., Van den Kerkhof, A.M., Kronz, A. and Simon, K., 2003. Trace elements in quartz - a combined electron microprobe, secondary ion mass spectrometry, laser-ablation ICP-MS, and cathodoluminescence study. European Journal of Mineralogy, 15(4): 747-763.

Murphy, M.D., Sparks, R.S.J., Barclay, J., Carroll, M.R. and Brewer, T.S., 2000. Remobilization of andesite magma by intrusion of mafic magma at the Soufriere Hills Volcano, Montserrat, West Indies. Journal of Petrology, 41(1): 21-42.

Nicotra, E., Viccaro, M., Ferlito, C. and Cristofolini, R., 2010. Influx of volatiles into shallow reservoirs at Mt. Etna volcano (Italy) responsible for halogen-rich magmas. European Journal of Mineralogy, 22(1): 121-138.

Oreskes, N. and Einaudi, M.T., 1990. Origin of rare-earth element-enriched hematite breccias at the Olympic-Dam Cu-U-Au-Ag deposit, Roxby Downs, South Australia. Economic Geology and the Bulletin of the Society of Economic Geologists, 85(1): 1-28.

Oreskes, N. and Einaudi, M.T., 1992. Origin of hydrothermal fluids at Olympic Dam – Preliminary results from fluid inclusions and stable isotopes. Economic Geology and the Bulletin of the Society of Economic Geologists, 87(1): 64-90.

Pankhurst, R.J., Leat, P. T., Sruoga, P., Rapela, C. W., Marquez, M., Storey, B. C., Riley, T. R., 1998. The Chon Aike province of Patagonia and related rocks in West Antarctica: a silicic large igneous province. Journal of Volcanology and Geothermal Research, 81(1-2): 113-136.

Pankhurst, R.J., Rapela, C.R., 1995. Production of Jurassic rhyolite by anatexis of the lower crust of Patagonia. Earth and Planetary Science Letters, 134(1-2): 23-36.

Pankhurst, R.J., Riley, T.R., Fanning, C.M. and Kelley, S.P., 2000. Episodic silicic volcanism in Patagonia and the Antarctic Peninsula: chronology of magmatism associated with the break-up of Gondwana. Journal of Petrology, 41(5): 605-625.

Parker, A.J. and Lemon, N.M., 1982. Reconstruction of the early Proterozoic stratigraphy of the Gawler Craton, South-Australia. Journal of the Geological Society of Australia, 29(1-2): 221-238.

Parker, D. and White, J., 2008. Large-scale silicic alkalic magmatism associated with the Buckhorn Caldera, Trans-Pecos Texas, USA: comparison with Pantelleria, Italy. Bulletin of Volcanology, 70(3): 403-415.

Patiño Douce, A.E., 1997. Generation of metaluminous A-type granites by low-pressure melting of calc-alkaline granitoids. Geology, 25(8): 743-746.

Pearce, J. A. (1996). A users guide to basalt discrimination diagrams. In:Wyman, D. A. (eds) Trace element geochemistry of volcanic rocks: applications for massive sulphide exploration. Geological Association of Canada, Short Course Notes 12, 79-113.

Pearce, J.A., Harris, N.B.W. and Tindle, A.G., 1984. Trace element discrimination diagrams for the tectonic interpretation of granitic rocks. Journal of Petrology, 25(4): 956-983.

Peate, D.W., 1997. The Paranà-Etendeka province. In: M.F. Mahoney and M.F. Coffin (Editors), Large igneous provinces: continental, oceanic and planetary flood volcanism. Geophysical Monograph, pp. 217-245.

Peccerillo, A. and Taylor, S.R., 1976. Geochemistry of Eocene calc-alkaline volcanic-rocks from Kastamonu area, northern Turkey. Contributions to Mineralogy and Petrology, 58(1): 63-81.

Peppard, B.T., Steele, I.M., Davis, A.M., Wallace, P.J. and Anderson, A.T., 2001. Zoned quartz phenocrysts from the rhyolitic Bishop Tuff. American Mineralogist, 86(9): 1034-1052.

Perny, B., Eberhardt, P., Ramseyer, K., Mullis, J. and Pankrath, R., 1992. Microdistribution of Al, Li, and Na in alpha-quartz - Possible causes and correlation with short-lived cathodoluminescence. American Mineralogist, 77(5-6): 534-544.

Peucat, J.J. Capdevila, R., Fanning, C. M., Menot, R. P., Pecora, L. Testut, L., 2002. 1.60 Ga felsic volcanic blocks in the moraines of the Terre Adelie Craton, Antarctica: comparisons with the Gawler Range Volcanics, South Australia. Australian Journal of Earth Sciences, 49(5): 831-845.

Primary Industries and Resources of South Australia (PIRSA), 2006. South Australia MGA geoscientific geographic information system, DVD-ROM. Primary Industries and Reasources of South Australia.

Pyle, D.M. and Mather, T.A., 2009. Halogens in igneous processes and their fluxes to the atmosphere and oceans from volcanic activity: A review. Chemical Geology, 263(1-4): 110-121.

Qin, Z.W., Lu, F.Q. and Anderson, A.T., 1992. Diffusive reequilibration of melt and fluid inclusions. American Mineralogist, 77(5-6): 565-576.

Roache, M.W., Allen, S.R., McPhie, J., 2000. Surface and subsurface facies architecture of a small hydroexplosive, rhyolitic centre in the Mesoproterozoic Gawler Range Volcanics, South Australia. Journal of Volcanology and Geothermal Research, 104(1-4): 237-259.

Robertson, R.S., Preiss, W.V., Crooks, A.F., Hill, P.W., Sheard, M.J., 1998. Review of the Proterozoic geology and mineral potential of the Curnamona Province in South Australia. AGSO Journal of Australian Geology and Geophysics, 17: 169–182.

Roedder, E., 1979. Origin and significance of magmatic inclusions. Bulletin De Mineralogie, 102(5-6): 487-510.

Romano, C., Poe, B., Mincione, V., Hess. K. U., Dingwell, D. B., 2001. The viscosities of dry and hydrous XAlSi3O8 (X = Li, Na, K, Ca0.5, Mg0.5) melts. Chemical Geology, 174, 115-132.

Rubatto, D. and Hermann, J., 2003. Zircon formation during fluid circulation in eclogites (Monviso, Western Alps): implications for Zr and Hf budget in subduction zones. Geochimica et Cosmochimica Acta, 67(12): 2173-2187.

Rubatto, D. and Herman, J., 2007. Experimental zircon/melt and zircon/garnet trace element partitioning and implications for the geochronology of crustal rocks. Chemical Geology 241 (2007) 38-61

Rubatto, D., Williams, I.S. and Buick, I.S., 2001. Zircon and monazite response to prograde metamorphism in the Reynolds Range, central Australia. Contributions to Mineralogy and Petrology, 140(4): 458-468.

Rubenach, M.J. and Barker, A.J., 1998. Metamorphic and metasomatic evolution of the Snake Creek Anticline, Eastern Succession, Mt Isa Inlier. Australian Journal of Earth Sciences, 45(3): 363-372.

Saito, G., Kazahaya, K., Shinohara, H., Stimac, J. and Kawanabe, Y., 2001. Variation of volatile concentration in a magma system of Satsuma-Iwojima volcano deduced from melt inclusion analyses. Journal of Volcanology and Geothermal Research, 108(1-4): 11-31.

Salvi, S., Fontan, F., Monchoux, P., Williams-Jones, A.E. and Moine, B., 2000. Hydrothermal mobilization of high field strength elements in alkaline igneous systems: evidence from the Tamazeght complex (Morocco). Economic Geology and the Bulletin of the Society of Economic Geologists, 95(3): 559-575.

Sato, H., 1975. Diffusion coronas around quartz xenocrysts in andesite and basalt from Tertiary volcanic region in Northeastern Shikoku, Japan. Contributions to Mineralogy and Petrology, 50(1): 49-64.

Scaillet, B. and Macdonald, R., 2004. Fluorite stability in silicic magmas. Contributions to Mineralogy and Petrology, 147(3): 319-329.

Schmidt, M.W., Dardon, A., Chazot, G. and Vannucci, R., 2004. The dependence of Nb and Ta rutile-melt partitioning on melt composition and Nb/Ta fractionation during subduction processes. Earth and Planetary Science Letters, 226(3-4): 415-432.

Schönenberger, J., Köhler, J. and Markl, G., 2008. REE systematics of fluorides, calcite and siderite in peralkaline plutonic rocks from the Gardar Province, South Greenland. Chemical Geology, 247(1-2): 16-35.

Self, S., 2006. The effects and consequences of very large explosive volcanic eruptions. Philosophical Transactions of the Royal Society a-Mathematical Physical and Engineering Sciences, 364(1845): 2073-2097.

Shane, P., Smith, V.C. and Nairn, I., 2008. Millennial timescale resolution of rhyolite magma recharge at Tarawera volcano: insights from quartz chemistry and melt inclusions. Contributions to Mineralogy and Petrology, 156(3): 397-411.

Sibley, D.F., Vogel, T.A., Walker, B.M. and Byerly, G., 1976. Origin of oscillatory zoning in plagioclase - diffusion and growth controlled model. American Journal of Science, 276(3): 275-284.

Skirius, C.M., Peterson, J.W. and Anderson, A.T., 1990. Homogenizing rhyolitic glass inclusions from the Bishop Tuff. American Mineralogist, 75(11-12): 1381-1398.

Skirrow, R.G. Bastrakov, E. N., Baroncii, K., Fraser, G. L., Creaser, R. A., Fanning, C. M., Raymond, O. L. and Davidson, G. J., 2007. Timing of iron oxide Cu-Au-(U) hydrothermal activity and Nd isotope constraints on metal sources in the Gawler craton, south Australia. Economic Geology, 102(8): 1441-1470.

Skirrow, R.G., Bastrakov, E., Davidson, G.J., Raymond, O., Heithersay, P., 2002. Geological framework, distribution and controls of Fe-oxide Cu- Au deposits in the Gawler craton. Part II. Alteration and mineralization. In: T.M. Porter (Editor), Hydrothermal iron oxide copper-gold and related deposits. Porter GeoConsultancy, Adelaide, pp. 33-47.

Skjerlie, K.P. and Johnston, A.D., 1993. Fluid-absent melting behavior of an F-rich tonalitic gneiss at mid-crustal pressures: implications for the generation of anorogenic granites. Journal of Petrology, 34(4): 785-815.

Sobolev, A.V. and Danyushevsky, L.V., 1994. Petrology and geochemistry of boninites from the North Termination of the Tonga Trench - Constraints on the generation conditions of primary high-Ca boninite magmas. Journal of Petrology, 35(5): 1183-1211.

Sparks, R.S.J., Self, S., Walker, G.P.L. , 1973. Products of ignimbrite eruptions. Geology, 1: 115-118.

Štemprok, M., 1991. Ongonite from Ongon Khairkhan, Mongolia. Mineralogy and Petrology, 43(4): 255-273.

Stewart, K.P., 1994. High temperature silicic volcanism and the role of mantle magmas in Proterozoic crustal growth: the Gawler Range Volcanic Province, University of Adelaide, Adelaide.

Stimac, J.A. and Pearce, T.H., 1992. Textural evidence of mafic-felsic magma interaction in dacite lavas, Clear-Lake, California. American Mineralogist, 77(7-8): 795-809.

Straub, S.M. and Layne, G.D., 2003. The systematics of chlorine, fluorine, and water in Izu arc front volcanic rocks: implications for volatile recycling in subduction zones. Geochimica et Cosmochimica Acta, 67(21): 4179-4203.

Streck, M.J., 2008. Mineral textures and zoning as evidence for open system processes. Minerals, inclusions and volcanic processes, 69: 595-622.

Student, J.J., 2002. Silicate melt inclusions in igneous petrogenesis. Unpublished PhD thesis, Virginia Polytechnic Institute and State University, 119 pp.

Sun, S.S., McDonough, W.F., 1989. Chemical and isotopic systematics of oceanic basalts: implications for mantle composition and processes. In: A.D. Saunders, Norry, M. J. (Editor), Magmatism in the ocean basins. Geological Society of London, London, pp. 313-345.

Symonds, R.B., Rose, W.I., Gerlach, T.M., Briggs, P.H. and Harmon, R.S., 1990. Evaluation of gases, condensates, and SO2 emissions from Augustine volcano, Alaska: the degassing of a Cl-rich volcanic system. Bulletin of Volcanology, 52(5): 355-374.

Tait, S., 1992. Selective preservation of melt inclusions in igneous phenocrysts. American

Mineralogist, 77(1-2): 146-155.

Tepley, F.J., Davidson, J.P., Tilling, R.I. and Arth, J.G., 2000. Magma mixing, recharge and eruption histories recorded in plagioclase phenocrysts from El Chichon Volcano, Mexico. Journal of Petrology, 41(9): 1397-1411.

Thomas, J.B., 2002. Melt inclusion geochemistry. Unpublished PhD thesis. Virginia Polytechnic Institute and State University, 89 pp.

Thomas, R., Davidson, P., Rhede, D. and Leh, M., 2009. The miarolitic pegmatites from the Konigshain: a contribution to understanding the genesis of pegmatites. Contributions to Mineralogy and Petrology, 157(4): 505-523.

Thomas, R., Förster, H.J., Rickers, K. and Webster, J.D., 2005. Formation of extremely F-rich hydrous melt fractions and hydrothermal fluids during differentiation of highly evolved tin-granite magmas: a melt/fluid-inclusion study. Contributions to Mineralogy and Petrology, 148(5): 582-601.

Thomas, R., Webster, J.D. and Heinrich, W., 2000. Melt inclusions in pegmatite quartz: complete miscibility between silicate melts and hydrous fluids at low pressure. Contributions to Mineralogy and Petrology, 139(4): 394-401.

Tuttle, O.F., Bowen, N.L., 1958. Origin of granite in the light of experimental studies in the system NaAlSi3O8 - KAiSi3O8 - SiO2H2O. Geological Society of America Memoirs, 74, xi. Geological Society of America.

Twist, D. and French, B.M., 1983. Voluminous acid volcanism in the Busheveld Complex: a review of the Rooiberg Felsite. Bulletin Volcanologique, 46(3): 225-242.

Van den Kerkhof, A.M. and Hein, U.F., 2001. Fluid inclusion petrography. Lithos, 55(1-4): 27-47.

Vigneresse, J.L., Barbey, P. and Cuney, M., 1996. Rheological transitions during partial melting and crystallization with application to felsic magma segregation and transfer. Journal of Petrology, 37(6): 1579-1600.

Wallace, P.J., 2005. Volatiles in subduction zone magmas: concentrations and fluxes based on melt inclusion and volcanic gas data. Journal of Volcanology and Geothermal Research, 140(1-3): 217-240.

Walker, G.P.L., 1973. Lengths of lava flows. Philosophical Transactions of the Royal Society of London A, 274: 107-118.

Walker, G.P.L., 1980. Low aspect ratio ignimbrites. Nature, 283: 286-287.

Walker, G.P.L., 1983. Ignimbrite types and ignimbrite problems. Journal of Volcanology and Geothermal Research, 17(1-4): 65-88.

Walker, G.P.L., Heming, R.F. and Wilson, C.J.N., 1980. Ignimbrite veneer deposits or pyroclastic surge deposits - Reply. Nature, 286(5776): 912-912.

Wark, D.A. and Spear, F.S., 2005. Ti in quartz: cathodoluminescence and thermometry. Geochimica et Cosmochimica Acta, 69(10): A592-A592.

Wark, D.A. and Watson, E.B., 2006. TitaniQ: a titanium-in-quartz geothermometer. Contributions to Mineralogy and Petrology, 152(6): 743-754.

Wark, D.A., Hildreth, W., Spear, F.S., Cherniak, D.J. and Watson, E.B., 2007. Pre-eruption recharge of the Bishop magma system. Geology, 35(3): 235-238.

Watson, B.E., Harrison, M.T., 1983. Zircon saturation revisited: temperature and composition effects in a variety of crustal magma types. Earth and Planetary Science Letters 64, 295-304.

Watt, G.R., Wright, P., Galloway, S. and McLean, C., 1997. Cathodoluminescence and trace element zoning in quartz phenocrysts and xenocrysts. Geochimica et Cosmochimica Acta, 61(20): 4337-4348.

Webster, J., Thomas, R., Förster, H.J., Seltmann, R. and Tappen, C., 2004. Geochemical evolution of halogen-enriched granite magmas and mineralizing fluids of the Zinnwald tin-tungsten mining district, Erzgebirge, Germany. Mineralium Deposita, 39(4): 452-472.

Webster, J.D. and Holloway, J.R., 1988. Experimental constraints on the partitioning of Cl between topaz rhyolite melt and H2O and H2O + CO2 fluids - New implications for granitic differentiation and ore deposition. Geochimica et Cosmochimica Acta, 52(8): 2091-2105.

Webster, J.D., 1990. Partitioning of F between H2O and CO2 fluids and topaz rhyolite melt - Implications for mineralizing magmatic-hydrothermal fluids in F-rich granitic systems. Contributions to Mineralogy and Petrology, 104(4): 424-438.

Webster, J.D., 1992. Water solubility and chlorine partitioning in Cl-rich granitic systems: effects of melt composition at 2 kbar and 800°C. Geochimica Et Cosmochimica Acta, 56(2): 679-687.

Webster, J.D., 2007. Experimental constraints on fluorine and chlorine partitioning in the pseudosystem apatite-silicate melt-fluid(s) and applications to magmatic degassing. Geochimica et Cosmochimica Acta, 71(15): A1096-A1096.

Webster, J.D., Holloway, J.R. and Hervig, R.L., 1989. Partitioning of lithophile trace-elements between H2O and H2O + CO2 fluids and topaz rhyolite melt. Economic Geology, 84(1): 116-134.

Webster, J.D., Tappen, C.M. and Mandeville, C.W., 2009. Partitioning behavior of chlorine and fluorine in the system apatite-melt-fluid. II: Felsic silicate systems at 200 MPa. Geochimica et Cosmochimica Acta, 73(3): 559-581.

Whalen, J.B., Currie, K.L. and Chappell, B.W., 1987. A-type granites - Geochemical characteristics, discrimination and petrogenesis. Contributions to Mineralogy and Petrology, 95(4): 407-419.

White, J.C., Holt, G.S., Parker, D.F. and Ren, M.H., 2003. Trace-element partitioning between alkali feldspar and peralkalic quartz trachyte to rhyolite magma. Part I: Systematics of trace-element partitioning. American Mineralogist, 88(2-3): 316-329.

Wiebe, R.A., Wark, D.A. and Hawkins, D.P., 2007. Insights from quartz cathodoluminescence zoning into crystallization of the Vinalhaven granite, coastal Maine. Contributions to Mineralogy and Petrology, 154(4): 439-453.

Winchester, J.A. and Floyd, P.A., 1977. Geochemical discrimination of different magma series and their differentiation products using immobile elements. Chemical Geology, 20: 325-343.

Witter, J.B., Kress, V.C. and Newhall, C.G., 2005. Volcán Popocatépetl, Mexico. Petrology, magma mixing, and immediate sources of volatiles for the 1994-present eruption. Journal of Petrology, 46(11): 2337-2366.

Wright, J.V., Smith, A.L. and Self, S., 1980. A working terminology of pyroclastic deposits. Journal of Volcanology and Geothermal Research, 8(2-4): 315-336.

Appendix I - Sample list

sample n.	locat. X	locat. Y	Unit	Complex	Sampling date	Thin section	Rock mount	WR chemical analysis	Melt inclusion analysis	Qtz CL	Qtz trace element profiles
GH39	525051	6540439	Andesite	CVC	15/10/06	X		ME+TE		X	
GH52	524820	6542202	Andesite	CVC	19/10/06	X		ME+TE		X	
GH52B	524825	6542207	Andesite + foliated enclave	CVC	19/10/06						
GH41	518655	6543479	Basalt	CVC	16/10/06	X		ME+TE			
GH45	519971	6543857	Basalt	CVC	16/10/06	X		ME+TE			
GH49	519979	6544918	Basalt	CVC	18/10/06	X		ME+TE			
GH50	520440	6544626	Basalt	CVC	18/10/06	X		ME+TE			
GH80	521273	6543210	Basalt	CVC	03/08/07						
GH81	510067	6543836	Basalt	CVC	04/08/07						
GH88	519405	6544631	Basalt	CVC	11/08/07						
GH42	520055	6543542	Basalt	CVC	16/10/06	X		ME		X	
GH90	520051	6543913	Basalt	CVC	11/08/07						
GH46	533107	6546128	Chandabooka Dacite	CVC	17/10/06	X		ME+TE			
GH47	530716	6545911	Chandabooka Dacite	CVC	17/10/06						
GH53	525658	6542899	Chandabooka Dacite	CVC	19/10/06						
GH51	524145	6542610	Lake Gairdner Rhyolite	CVC	19/10/06	X		ME+TE		X	X
GH16	524102	6542654	Lake Gairdner Rhyolite	CVC	6/08/06						
GH82B	524029	6542642	Lake Gairdner Rhyolite	CVC	05/08/07						
GH87	523820	6542839	Lake Gairdner Rhyolite	CVC	10/08/07	X				X	
GH44	519864	6543748	Microgranite dyke	CVC	16/10/06	X		ME+TE		X	
GH79	519933	6543460	Microgranite dyke	CVC	03/08/07						
GH91	519948	6543638	Microgranite dyke	CVC	12/08/07	X				X	
GH34	524277	6543641	Rhyolite-dacite (Mi2)	CVC	12/10/06	X		ME+TE			
GH34B	524277	6543641	Rhyolite-dacite (Mi2)	CVC	12/10/06					X	
GH35	524220	6543611	Rhyolite-dacite (Mi2)	CVC	12/10/06		X			X	
GH43	520134	6543607	Volcaniclastic deposit interbedded with Basalt	CVC	16/10/06	X		ME+TE		X	
GH48	519533	6433203	Volcaniclastic deposit interbedded with Basalt	CVC	18/10/06						
GH48B	519538	6433208	Volcaniclastic deposit interbedded with Basalt	CVC	18/10/06						
GH82	520303	6543691	Volcaniclastic deposit interbedded with Basalt	CVC	04/08/07	X					
GH40	525031	6540512	Rhyolite-dacite (Mi5)	CVC	15/10/06	X		ME+TE			
GH40B	525009	6540602	Rhyolite-dacite (Mi5)	CVC	15/10/06						
GH83	525046	6541144	Rhyolite-dacite (Mi5)	CVC	08/08/07	X					
GH84	525152	6541147	Rhyolite-dacite (Mi5)	CVC	08/08/07						
GH85	525157	6541152	Rhyolite-dacite (Mi5)	CVC	08/08/07						
GH86	523942	6542662	Sandstone in L. Gairdner Rhyolite	CVC	10/08/07						
GH89	520046	6543908	Volcaniclastic deposit interbedded with Basalt	CVC	11/08/07						
GH17	520050	6483395	Andesite II	GHVC	05/10/06	X		ME+TE			
GH18	519166	6482749	Andesite II	GHVC	05/10/06						
GH22	515779	6482266	Andesite II	GHVC	08/10/06						
GH22B	515948	6481690	Andesite II	GHVC	08/10/06						
GH72	484559	6495596	Andesite I	GHVC	27/10/06	X		ME+TE			
GH13	515415	6501451	Waurea Pyroclastics	GHVC	5/08/06	X		ME+TE	X	X	X
GH54B	515607	6501226	Waurea Pyroclastics	GHVC	21/10/06	X		ME			
GH55	516003	6501766	Waurea Pyroclastics	GHVC	22/10/06						
GH56	514629	6501608	Waurea Pyroclastics	GHVC	21/10/06	X		ME			
GH65	517867	6501874	Waurea Pyroclastics	GHVC	25/10/06						
GH65B	517872	6501879	Waurea Pyroclastics	GHVC	25/10/06						
GH95	515415	6501451	Waurea Pyroclastics	GHVC	15/08/07				X	X	

Appendix I - Sample list (cont.)

sample n.	locat. X	locat. Y	Unit	Complex	Sampling date	Thin section	Rock mount	WR chemical analysis	Melt inclusion analysis	Qtz CL	Qtz trace element profiles
GH11	496919	6490477	Bunburn Dacite	GHVC	4/08/06						
GH25	521540	6490673	Bunburn Dacite	GHVC	09/10/06		X				
GH27	521899	6491165	Bunburn Dacite	GHVC	10/10/06	X		ME+TE			
GH57	506849	6490628	Bunburn Dacite	GHVC	23/10/06						
GH60	509773	6491435	Bunburn Dacite?	GHVC	23/10/06		X				
GH31	520150	6480997	Childera Dacite	GHVC	11/10/06		X				
GH76	486560	6500658	Childera Dacite	GHVC	28/10/06	X		ME+TE			
GH93	486689	6500667	Childera Dacite	GHVC	15/08/07	X					
GH20	516088	6485851	Mangaroongah Dacite	GHVC	07/10/06	X		ME+TE			
GH20B	515806	6485186	Mangaroongah Dacite	GHVC	07/10/06						
GH21	515440	6484867	Mangaroongah Dacite	GHVC	07/10/06		X				
GH24B	522475	6487690	Mangaroongah Dacite	GHVC	09/10/06						
GH73	487389	6496156	Mangaroongah Dacite	GHVC	28/10/06	X		ME+TE			
GH74	487394	6496160	Mangaroongah Dacite	GHVC	27/10/06	X	X				
GH75	487641	6499134	Mangaroongah Dacite	GHVC	28/10/06						
GH77	484874	6492331	Mangaroongah Dacite	GHVC	30/10/06		X				
GH78	506562	6486719	Mangaroongah Dacite	GHVC	30/10/06						
GH07	493342	6489464	Nuckulla Basalt	GHVC	3/08/06	X		ME+TE			
GH94	492668	6489230	Nuckulla Basalt	GHVC	15/08/07						
GH69	492468	6489230	Nuckulla Basalt	GHVC	26/10/06	X		ME+TE			
GH71	491465	6490512	Nuckulla Basalt	GHVC	26/10/06	X		ME+TE			
GH08	484545	6493681	Moonamby Dyke Suite	GHVC	4/08/06						
GH15	509965	6502023	Moonamby Dyke Suite	GHVC	5/08/06	X		ME+TE	X	X	
GH62	509701	6502089	Moonamby Dyke Suite	GHVC	24/10/06						
GH70	491376	6490439	Moonamby Dyke Suite	GHVC	26/10/06	X		ME+TE		X	X
GH70B	491381	6490444	Moonamby Dyke Suite	GHVC	26/10/06		X			X	
GH92	486550	6489826	Moonamby Dyke Suite	GHVC	14/08/07		X				
GH61	508334	6503487	Yantea Rhyolite-dacite	GHVC	24/10/06						
GH66	509489	6506208	Yantea Rhyolite-dacite	GHVC	25/10/06						
GH67	506205	6502560	Baldry Rhyolite	GHVC	25/10/06					X	
GH67B	506082	6502444	Baldry Rhyolite	GHVC	25/10/06	X		ME+TE		X	
GH68	506087	6502449	Baldry Rhyolite	GHVC	25/10/06		X			X	
GH06	515196	6488706	Wheepool Rhyolite	GHVC	3/08/06	X		ME+TE	X	X	
GH23	517647	6488394	Wheepool Rhyolite	GHVC	08/10/06		X		X	X	
GH59	506968	6488733	Wheepool Rhyolite	GHVC	23/10/06		X		X	X	
GH24C	523300	6487800	Wheepool Rhyolite	GHVC	09/10/06				X		
GH26	522957	6494580	Whyeela Dacite	GHVC	09/10/06	X		ME+TE			
GH30	523955	6495281	Whyeela Dacite	GHVC	10/10/06						
GH33	523710	6495243	Whyeela Dacite	GHVC	11/10/06		X				
GH64	517843	6500771	Whyeela Dacite	GHVC	25/10/06						
GH09	489331	6492457	Yantea Rhyolite-dacite	GHVC	4/08/06		X				
GH10	494537	6491393	Yantea Rhyolite-dacite	GHVC	4/08/06						
GH24	523013	6493194	Yantea Rhyolite-dacite	GHVC	08/10/06	X		ME+TE			
GH28	522105	6492857	Yantea Rhyolite-dacite	GHVC	10/10/06		X				

Appendix I - Sample list (cont.)

sample n.	locat. X	locat. Y	Unit	Complex	Sampling date	Thin section	Rock mount	WR chemical analysis	Melt inclusion analysis	Qtz CL	Qtz trace element profiles
GH56B	514138	6501269	Yantea Rhyolite-dacite	GHVC	22/10/06		X			X	
GH63	514040	6501725	Yantea Rhyolite-dacite	GHVC	24/10/06						
GH32	523705	6495238	Granite enclave	HS	11/10/06	X	X	ME+TE		X	
GH29	524305	6495515	Granite enclave	HS	10/10/06					X	
GH19	516472	6486536	Yandoolka Rhyolite	GHVC	06/10/06		X				
GH36	518402	6545323	Hiltaba suite Granite	HS	13/10/06						
GH37	517317	6546439	Hiltaba suite Granite	HS	13/10/06	X		ME+TE		X	
GH38	518870	6545808	Hiltaba suite Granite	HS	13/10/06	X		ME+TE			

ME: major elements; TE: trace elements; CVC: Chitanilga Volcanic Complex; GHVC: Glyde Hill Volcanic Complex; HS: Hiltaba Suite. X and Y: grid reference GDA94.

Appendix II - Quartz trace element analysis

Analysis n.	Sample n.	Al	Al det limit	Fe	Fe det lim	Ti	Ti det lim	CL relative intensity
Qtz 13-13 line1	GH13	0.3347	0.0009	0.0123	0.0023	0.0111	0.0014	136
		0.0167	0.0009	0.0025	0.0023	0.0105	0.0014	141
		0.0125	0.0009	0.0025	0.0023	0.0104	0.0014	150
		0.0174	0.0009	0.0030	0.0023	0.0101	0.0014	158
		0.0232	0.0009	0.0039	0.0023	0.0075	0.0014	152
Qtz 13-13 line2	GH13	0.0186	0.0009	0.0023	0.0023	0.0095	0.0014	136
		0.0166	0.0009	0.0034	0.0023	0.0106	0.0014	141
		0.0122	0.0009	0.0009	0.0023	0.0098	0.0014	150
		0.0183	0.0009	0.0028	0.0023	0.0094	0.0014	158
		0.0151	0.0009	0.0057	0.0023	0.0079	0.0014	152
Qtz 13-6 line1	GH13	0.0173	0.0009	0.0017	0.0023	0.0090	0.0014	132
		0.0180	0.0009	0.0033	0.0023	0.0104	0.0014	153
		0.0154	0.0009	0.0017	0.0023	0.0087	0.0014	142
		0.0142	0.0009	0.0026	0.0023	0.0089	0.0014	133
		0.0152	0.0009	0.0042	0.0023	0.0089	0.0014	143
Qtz 13-6 line2	GH13	0.0192	0.0009	0.0029	0.0023	0.0089	0.0014	132
		0.0182	0.0009	0.0027	0.0023	0.0113	0.0014	153
		0.0176	0.0009	0.0021	0.0023	0.0096	0.0014	142
		0.0295	0.0009	0.0024	0.0023	0.0083	0.0014	133
		0.0164	0.0009	0.0053	0.0023	0.0094	0.0014	143
Qtz 51-9 line1	GH51	0.0174	0.0009	0.0080	0.0023	0.0090	0.0014	145
		0.0264	0.0009	0.0072	0.0023	0.0096	0.0014	163
		0.0163	0.0009	0.0049	0.0023	0.0083	0.0014	158
		0.0245	0.0009	0.0093	0.0023	0.0086	0.0014	167
		0.0685	0.0009	0.0284	0.0023	0.0083	0.0014	178
Qtz 51-9 line2	GH51	0.0182	0.0009	0.0079	0.0023	0.0075	0.0014	145
		0.0176	0.0009	0.0049	0.0023	0.0105	0.0014	163
		0.0187	0.0009	0.0049	0.0023	0.0086	0.0014	158
		0.0177	0.0009	0.0062	0.0023	0.0077	0.0014	167
		0.0493	0.0009	0.0326	0.0023	0.0088	0.0014	178
Qtz 51-4 line1	GH51	0.0102	0.0009	0.0016	0.0023	0.0061	0.0014	113
		0.0132	0.0009	0.0022	0.0023	0.0052	0.0014	93
		0.0114	0.0009	0.0038	0.0023	0.0050	0.0014	102
		0.0157	0.0009	0.0031	0.0023	0.0092	0.0014	161
		0.0171	0.0009	0.0031	0.0023	0.0058	0.0014	153
Qtz 51-4 line2	GH51	0.0113	0.0009	0.0038	0.0023	0.0069	0.0014	113
		0.0140	0.0009	0.0012	0.0023	0.0050	0.0014	93
		0.0136	0.0009	0.0043	0.0023	0.0051	0.0014	102
		0.0129	0.0009	0.0039	0.0023	0.0062	0.0014	161
		0.0132	0.0009	0.0046	0.0023	0.0072	0.0014	153
Qtz 70-14 line1	GH70	0.0278	0.0009	0.0033	0.0023	0.0098	0.0014	171
		0.0158	0.0009	0.0012	0.0023	0.0078	0.0014	138
		0.0107	0.0009	0.0021	0.0023	0.0021	0.0014	79
		0.0133	0.0009	0.0030	0.0023	0.0060	0.0014	134
		0.0120	0.0009	0.0032	0.0023	0.0058	0.0014	133
Qtz 70-14 line2	GH70	0.0171	0.0009	0.0015	0.0023	0.0105	0.0014	171
		0.0152	0.0009	0.0024	0.0023	0.0074	0.0014	138
		0.0132	0.0009	0.0019	0.0023	0.0026	0.0014	79
		0.0144	0.0009	0.0029	0.0023	0.0061	0.0014	134
		0.0149	0.0009	0.0045	0.0023	0.0060	0.0014	133
Qtz 70-10 line1	GH70	0.0193	0.0009	0.0022	0.0023	0.0126	0.0014	205
		0.0364	0.0009	0.0033	0.0023	0.0079	0.0014	187
		0.0138	0.0009	0.0023	0.0023	0.0054	0.0014	135
		0.0176	0.0009	0.0048	0.0023	0.0066	0.0014	163
		0.0171	0.0009	0.0080	0.0023	0.0047	0.0014	150
Qtz 70-10 line2	GH70	0.0215	0.0009	0.0043	0.0023	0.0120	0.0014	205
		0.0163	0.0009	0.0027	0.0023	0.0095	0.0014	187
		0.0142	0.0009	0.0021	0.0023	0.0049	0.0014	135
		0.0184	0.0009	0.0050	0.0023	0.0066	0.0014	163
		0.0186	0.0009	0.0094	0.0023	0.0051	0.0014	150

Concentrations and detection limits as wt.%, CL intensity as 1-255 scale